SIFT-MS: DEVELOPMENT OF INSTRUMENTATION AND APPLICATIONS

Gregory James Francis
Department of Chemistry

A thesis presented for the Degree of Doctor of Philosophy at the

University of Canterbury,
Christchurch, New Zealand.

December 2007

"*I decorated it myself.*
Thank you, you're too much.
Honestly, it was nothing."

-Keith Buckley

Dedicated to Esmé Margaret Colville who sadly passed away while this thesis was in preparation. A generous, wise and loving grandmother who was guiding light in my life and proved that the world through an artists eyes is a beautiful place.

TABLE OF CONTENTS

ACKNOWLEDGEMENTS

I wish to extent my gratitude to my academic supervisor Prof. Murray McEwan, for without whom, this thesis would not be possible. In early 2003, Murray was gracious enough to accept me into his research group as a BSc(Hons) student, even though I had recently neglected to hand-in an undergraduate assignment he had set. To this day I am still reminded about that assignment on a regular occasion! Murray's wisdom and sharp wit have helped me resolve many issues during the course of this research and made the process very enjoyable; to him I am forever indebted. Furthermore, many thanks to my assistant supervisors Dr. Daniel Milligan, Dr. Barry Prince, Dr. Vaughan Langford and Dr. Paul Wilson. Each has had a large role in the day-to-day supervision of the research presented herein and without their expert input, many research avenues would not have been pursued or explored to their full potential.

Gratitude is extended to the employees of Syft Technologies, where the majority of the research presented herein was undertaken. I could not ask for a more pleasant group of people to spend 40-50 hours per week (and sometimes a few hours in the weekend) with. All of the 61 employees who I have encountered in the previous three and a half years have had some part to play in this thesis and for that I am very thankful. Particular gratitude is reserved for CEO Geoff Peck, who has provided me many tremendous opportunities that few Ph.D. students even dream of, let alone accomplish. Because of Syft Technologies and Geoff, I have learned to see science from both an academic and commercial point-of-view, as well as being able to travel the world.

I also wish to thank staff and students at the University of Canterbury Chemistry Department. Particular thanks go to Dr. Robert Maclagan for advice on computational studies, Dr. Colin Freeman for general advice on gas-phase ion-molecule chemistry and Robert McGregor for blowing the glassware discussed herein (and then repairing that glassware when I had broken it). Also thanks are given to the University of Canterbury based SIFT group, Sam Edwards and Dr. Brett Davis, for allowing me to share laboratory and office space, and a few good laughs.

I wish to acknowledge the researchers involved in the chemical warfare program at the Defence Science and Technology Organisation in Melbourne, Australia for their time and involvement in work presented herein.

Special thanks go to Prof. Diethard Bohme for welcoming me into his research group at York University (Toronto, ON, Canada) in 2003 and for his guidance and support during the six months I spent in Toronto as a research assistant. I would also like to extent thanks to the remainder of the Bohme group for their support and friendship.

I thank the Foundation for Research Science and Technology for the award of a Technology for Industry Fellowship, that not only provided the funding for the current research, but also provided the opportunity to work in an industrial setting during the previous three and half years.

Finally and most importantly, I wish to express tremendous gratitude to my family and friends. Dad, Mum, Rob and Sharon have provided me with the tools I need to not just complete a Ph.D. thesis, but to get through life. Your support, both moral and financial, has helped me to get to where I am now and I hope I have made you proud. And Dad, I'm sorry I didn't end up as a physicist or mathematician, I hope you can cope with me being a chemist! To my grandparents, Grandad and Grandma, you have both been important role models to me in your own very special ways. Your wisdom, kindness and generosity I will treasure in my heart forever. You are an inspiration. To Nan, thank you for being so supportive and kind-hearted. I have been very lucky to be so close to someone as special as you over the past three and half years.

I wish to thank members of all the bands I have been involved in over the course of researching the information discussed herein. My musical ventures have been an excellent outlet to offset my academic pursuits and therefore I give thanks to the members of Sixlip, A Bridge Between, The Red Corner and Yesterday's Model. I also wish to thank Christopher Jerram, Peter Gaukrodger, Simon Fullick and David Pearson for being excellent friends and flatmates. Also thank you (and I'm sorry) to anyone I have accidentally omitted.

Last of all I want to thank Claire Waghorn for being by my side over the last 12 months. Claire is the most important person in my life and her support and love means everything to me. So to Claire, I love you and thank you.

LIST OF TABLES

LIST OF FIGURES

PUBLICATIONS

The following is a list of publications, that are peer-reviewed journal articles or patents, by Gregory J. Francis.

Gregory J. Francis, Daniel B. Milligan, Paul F. Wilson, Vaughan S. Langford, and Murray J. McEwan.
Int. J. Mass Spectrom., **268**:38–46, 2007.
GeoVOC: A SIFT-MS Method for the Analysis of Small Linear Hydrocarbons of Relevance to Oil Exploration.

Gregory J. Francis, Daniel B. Milligan, and Murray J. McEwan.
J. Phys. Chem. A, **111**:9670–9679, 2007.
Gas-Phase Reactions and Rearrangements of Alkyl Esters with H_3O^+, NO+, and O_2^+: A Selected Ion Flow Tube Study.

Murray J. McEwan, Paul F. Wilson, Gregory J. Francis, and T.H. Morton.
Int. J. Mass Spectrom., **267**:81–88, 2007.
Transfer of F^+ Versus Fluoronium Metathesis: Competing Reactivities of the Gaseous Fluoroformyl Cation.

Daniel B. Milligan, Gregory J. Francis, Barry J. Prince, and Murray J. McEwan.
Anal. Chem., **79**:2537-2540, 2007.
Demonstration of Selected Ion Flow Tube MS Detection in the Parts per Trillion Range

Gregory J. Francis and Daniel B. Milligan.
New Zealand Patent Application 549242, 18 August **2006**.
Improvements in or related to SIFT-MS instruments.

Gregory J. Francis, Matthew Forbes, Dietrich A. Volmer, and Diethard K. Bohme.
The Analyst, **130**:508–513, 2005.
Periodicity in Collision-Induced and Remote-Bond Activation of Alkali Metal Ions Attached to Polyether Ionophores.

Matthew Forbes, Dietrich A. Volmer, Gregory J. Francis, and Diethard K. Bohme.
J. Am. Soc. Mass Spectrom., **16**:779–791, 2005.
A Comparison of Data Analysis Methods for Determining Gas Phase Stabilities by CID: Alkali Metal Complexes of Polyether Ionophore Antibiotics.

Gregory J. Francis, Paul F. Wilson, Robert G.A.R. Maclagan, Colin G. Freeman, Michael Meotner (Mautner), and Murray J. McEwan.
J. Phys. Chem. A, **108**:7548–7553, 2004.
Ionic Reactions Between Formaldehyde and Hydrocarbons. H_2 Transfer as a Hydrogenation Mechanism in Astrochemistry.

ABSTRACT

Data is presented for a range of experiments that have been performed using a selected ion flow tube (SIFT) instrument operated at room temperature (~ 298K) with carrier gas pressures typically in the range of 0.3 – 0.6 Torr. The majority of the experiments discussed are performed on a Voice100 instrument that has not been described in detail previously. The Voice100 is a novel instrument that has been designed particularly for quantitative trace gas analysis using the SIFT-MS technique.

A mixture of helium and argon carrier gases are employed in the Voice100 flow tube. By mixing carrier gases, the flow dynamics and diffusion characteristics of a flow tube are altered when compared to classic single carrier gas models. Therefore firstly, optimal flow conditions for the operation of a Voice100 are characterised. The diffusion of an ion in a mixture of carrier gases is then characterised using theoretical models and experimental techniques. This research requires that a new parameter M_P be defined regarding the mass discrimination of an ion in the non-field-free region near the downstream ion sampling orifice. Furthermore, a new method is described for the simultaneous measurement of rate coefficients for the reactions of $H_3O^+.(H_2O)_n$ (n = 1, 2, 3) ions with analytes.

Rate coefficients and branching ratios for the reactions of SIFT-MS precursor ions with specific analytes related to four individual applications are presented. For each application, the kinetic parameters are determined so as to facilitate the quantitative detection of the analytes relevant to that application. The GeoVOC application involves the measurement of hydrocarbon concentrations in the headspace of soil and water across a range of humidities. Alkyl esters are investigated to allow for the quantitative detection of each compound in fruits and vegetables. Chemical warfare agents, their surrogates and precursor compounds are studied which allows for the quantitative or semi-quantitative detection of a range of highly toxic compounds. Finally, 17 compounds classified by the US-EPA as hazardous air pollutants are studied that enables SIFT-MS instruments to replicate sections of the TO-14A and TO-15 methods.

This entire document was written and compiled using the open-source software packages *OpenOffice.org, Inkscape* and *KBibTex* that were running on a *Kubuntu Linux* platform.

CHAPTER 1

GAS-PHASE ION-MOLECULE KINETICS MEETS ANALYTICAL CHEMISTRY

1.1 A Common Thread

On an initial perusal of the table of contents of this thesis, one may be forgiven for querying the relevance of many of the chapter titles to one another. “GeoVOC: Geochemical Volatile Organic Compounds” and “Reactions and Rearrangements of Alkyl Esters” seem to be far removed from each other, and the chapter title “Chemical Warfare Agents” does not seem to echo titles of previous thesis chapters in this field. One may therefore ask “what is the common thread that brings such a diverse range of topics together?” The common thread of this thesis is the selected ion flow tube - mass spectrometry (SIFT-MS) technique, which is a technique for the quantitative analysis of trace analytes in whole air samples. First described by Spanel and Smith in 1996, [1] the SIFT-MS technique uses prior knowledge of the gas-phase ion-molecule chemistry to quantitatively measure the concentrations of many analytes simultaneously in whole air samples.

The current number of analytes which can be quantified by SIFT-MS is less than 500, such that expanding the 'compound database' is very important for the advancement of the technique both from an academic and a commercial point of view. Furthermore, the concurrent development of new SIFT-MS instrumentation requires a fundamental understanding of the dynamics and flow characteristics of the carrier gases in the flow tube. All chapters in this thesis work toward either expanding the size of the compound database on an application-by-application basis or to gain a greater understanding of the flow tube dynamics associated with SIFT-MS instrumentation. Examples of applications which will be discussed in this thesis are: the quantitative detection of hydrocarbons in soil and water samples to optimise the oil exploration process, the quantification of chemical warfare agents and agent surrogates in the parts-per-trillion-by-volume concentration range, and the measurement of alkyl ester concentrations in fruit.

The SIFT-MS technique is an intersection between gas-phase physical chemistry (ion-

molecule kinetics), computational chemistry (gas-phase mechanistic understanding) and analytical research (determination of analyte concentrations). Because of this intersection, the information which is covered herein broaches a wide range of topics, such as the transport properties of ions in mixed carrier gases, the quantitative detection of volatile compounds and the gas-phase rearrangement pathways determined by quantum chemical methods. However, the type of instrumentation used for this technique was not originally developed for this purpose, but instead for research into elucidating the chemistry of the atmosphere of earth, terrestrial bodies, comae and the interstellar medium. [2]

1.2 Historical Review

1.2.1 Flowing Afterglow – Mass Spectrometer

In 1963, in the laboratory of Prof. H.P. Broida, a discovery was made when studying the optical spectroscopy of neutral molecules in a helium afterglow down the course of a glass tube. [3] The researchers found that ions were affecting the observed neutral chemistry as far as 1 m downstream of an electrical discharge when the gas velocity was ~100 m s^{-1}. Because the mass spectrometer had become a commonly used piece of instrumentation, [4] it was a natural step to attempt to observe the ions postulated to occur in an afterglow, and understand their gas-phase chemistry.

In 1969, using a flowing afterglow mass spectrometer developed at the Environmental Science Services Administration (ESSA; now known as NOAA – the National Oceanographic and Atmospheric Administration) laboratory in Boulder, Colorado, USA, the first quantitative measurement of an ion-molecule reaction rate in a flowing system was published by Ferguson and co-workers. [5] The flowing afterglow mass spectrometer (FA) is quite simply a long tube connected to a quadrupole mass spectrometer, where the two regions are separated by an electrostatic ion sampling orifice. Gases are introduced at one end of the long tube (usually 1 m length) and pulled to the other end by a mechanical pump designed for large gas loads (known as a roots blower). By ionising the gas at the upstream end of the tube in an electrical discharge or by electron bombardment, and introducing other reactant gases downstream of the ionisation region, the reactions of ions with neutrals can be probed by the mass spectrometer. [6-8] When the concentration (number density) of the reactive neutral analyte entering the flow tube is known, the reaction rate coefficient can be determined (discussed

further in section 1.3). The instrumentation affords a simple, but extraordinarily useful outcome, in that all reactions which are studied are occurring at thermal energy. This outcome is due to inelastic collisions of the ionised species with the surrounding carrier atoms (such as helium) removing any excess vibrational, rotational and electronic energy which an ion may have following the ionisation process. Because of this feature, processes which are occurring in atmospheric environments, such as the ionosphere, could be modelled and studied by the FA.

The FA was found to be an excellent technique for studying the ion-neutral chemistry of the earth's upper atmosphere, and over the ensuing 10 years the majority of the reactions which are critical in explaining the behaviour of the terrestrial ionosphere were understood from a chemical kinetic point-of-view. [2] Other laboratories also built FA instruments for their own ion-molecule investigations including York University (Canada) [9], University of Birmingham (UK) [10] and the University of Canterbury. [11]

However, even though the FA was substantially better than other instrumentation available at the time of inception, it had two major drawbacks such that the study of complex chemistries was found to be difficult. [2] The first drawback was the presence of unwanted reactant ions observed in the mass spectra. These ions were found to be present due to impurities in the gases being ionised or secondary unwanted chemistry occurring in the reaction tube. The impurity ions could be minimised by introducing 'scavenging' gases, however these ions were often still present in relatively high concentrations. The second drawback was the presence of electrons in the flow tube. The electrons are an obvious product when forming cations, however in the reaction region electrons lead to ion-electron recombination and ambipolar diffusion. Ion electron recombination reactions are often found to be 100 to 1000 times faster than ion-neutral reactions [12] such that, where possible, an ion will react with an electron preferentially over a neutral species. Ambipolar diffusion results in rapid and mass dependent losses of ions toward the flow tube walls, [13] which is an issue as only those ions in the centre of the flow tube are sampled into the mass spectrometer. Both drawbacks are due to the ion creation region (where the ionisation occurs) being inside the flow tube. This observation was apparent to Adams and Smith who, in 1976, first published the SIFT technique. [14]

1.2.2 Selected Ion Flow Tube

The selected ion flow tube (SIFT) technique circumvents the major issues found with the FA by separating the ion creation region from the ion reaction region by a second quadrupole mass spectrometer.

Adams and Smith at the University of Birmingham found that their FA could not accurately model the more complex reactions which occurred in some gas-phase regions of interest, such as the interstellar medium. [14] The interstellar medium is a term commonly coined for the large H1 dust clouds which lie between stellar environments and are postulated to be regions where new stars are born. [15,16] Radiofrequency spectroscopic studies showed that the dense interstellar clouds contained small but significant concentrations of diatomic and polyatomic cations, and therefore studies explaining their origins became very topical. [17,18] Some diatomic and polyatomic molecules of interest (such as NH_3^+ [17]) could not be easily observed in a flowing afterglow because secondary reactions of the ions formed in the ionisation region with the ionising gas led to unwanted ions which were thermodynamically more favourable. The SIFT technique allowed each ion of interest to be selectively injected into the flow tube and reactions of ions having a single m/z ratio substantially aided in the understanding of product ion branching ratios and rate coefficients.

However, the SIFT technique does have deficiencies of its own. [2] Efficient operation of a quadrupole mass filter occurs at pressures below 10^{-5} Torr, and therefore the quadrupole mass filter must be separated from the flow tube and the ion source region (both have pressures approaching 1 Torr) by pinhole electrostatic orifices. Ion signals are substantially decreased by each orifice, such that the overall observable ion intensity in a SIFT instrument is lower than that of an FA. Also, because the newly introduced quadrupole chamber in the ion source region is required to be at a lower pressure than the flow tube, ions must be injected into the flow tube against the pressure gradient.

To inject an ion against the pressure gradient, a Venturi effect was employed which entrains ions into a helium carrier gas stream. The Venturi orifice requires optimisation for two parameters which were found to offset one another: minimisation of the back-streaming of flow tube gases into the quadrupole chamber, and minimisation of ion fragmentation as ions are forced against the pressure gradient. For instance, the advantageous characteristics of the 'NOAA/York injector' [19] for the back-streaming parameter were offset by the increased fragmentation observed compared to the 'Birmingham injector'. [20] The optimisation of these

two parameters has been further researched by Fishman and Grabowski, [21] and Milligan *et al*. [22]

Following the first publications by Smith and Adams, laboratories which had previously used FA techniques switched to using SIFT. Other laboratories which had previously been involved in gas-phase chemistry from different perspectives, also took on the SIFT technique and adapted it to their particular facets of research. Viggiano at Hanscom Air Force Base (USA) [23] developed a variable temperature SIFT (VT-SIFT) for measuring the temperature dependence of termolecular processes; Depuy, Bierbaum and co-workers at the University of Colorado (USA) [24] concentrated on negative ions in elucidating organic reaction mechanisms; Castleman at Pennsylvania State (USA) [25] examined the reactions of noble gases to determine ion-molecule reaction mechanisms and Grabowski at the University of Pittsburgh (USA) researched radical anion reactions related to biology. [26]

The coupling of differing ion sources onto the front of SIFT instruments also allowed for the development of new fields for which SIFT became applicable.

- An inductively-coupled plasma (ICP) ion source was integrated by Bohme to study the reactions of contaminants often observed in commercial ICP-MS instruments. [27]

- The same research group, more recently, effectively integrated a commercial electrospray (ESI) ion source for the study of gas-phase biological reactions. [28]

- The McEwan group at the University of Canterbury developed an FA as an ion source which yielded an instrument known as an FA-SIFT. [11] This instrument will be discussed in detail in chapter 2.

However, even with the SIFT instrument being able to examine reactions in a range of fields, the SIFT technique was primarily only able to provide information regarding the ion-neutral reaction rate coefficient, and the product ion distributions. The technique was used for physical chemical investigations, and it was certainly not a technique that was used in analytical chemistry.

1.2.3 SIFT-MS: A simple evolution

Spanel and Smith, in 1996, published research where a Keele University based

selected ion flow tube instrument (previously in Birmingham) was used to measure the concentrations of a range of analytes in whole air samples. [1] The technique, known as SIFT-MS, reversed the process which had been in common use for the previous 30 years for determining rate coefficients. The authors proposed a relatively simple idea, that if a rate coefficient and product ion(s) were known for an ion-molecule reaction, the concentration of neutral analyte can be found. The authors deemed the technique to be applicable to breath research and the non-invasive diagnosis of illnesses. The theory behind SIFT-MS will be discussed in detail in section 1.3.

Determining the concentrations of analytes in whole air samples requires that the reagent (precursor) ions do not react with the major components of air. [1] For instance, He^+ cannot be used as a precursor ion, as its exothermic charge transfer reactions with N_2, O_2, CO, Ar and H_2O would deplete the He^+ ion signal. The precursor ions of choice therefore are the terminal ions which form by ionising a mixture of air and water. Ionisation is achieved through a microwave discharge acting on the air-water mixture at ~0.5 Torr which forms a glowing stationary plasma. Due to the many collisions between ions and neutrals which will occur in the plasma (the mean free path is ~ 50 μm) the charge is very rapidly passed to the thermodynamically most stable species present, [29] which are the terminal ions H_3O^+, NO^+, and $O_2^{\bullet+}$. None of the three precursor ions react with the major components of dry air due to the thermodynamic constraints, [30,31] and therefore are the ions chosen to react rapidly with analytes that are present in dry air samples. H_3O^+, NO^+ and $O_2^{\bullet+}$ are called the SIFT-MS precursor ions.

When humid air is introduced to the SIFT-MS flow tube, the water which is present clusters with the H_3O^+ precursor ion to form ions at *m/z* 37, 55 and 73, which correspond to the $H_3O^+.H_2O$, $H_3O^+.(H_2O)_2$ and $H_3O^+.(H_2O)_3$ ions respectively. Each of the cluster ions can then react with the analyte which is entering the flow tube and therefore the three water cluster ions become precursor ions themselves. These ions will be the subject of further discussion in chapter 3. NO^+ also slowly clusters with water to form the $NO^+.H_2O$ and $NO^+.(H_2O)_2$ ions, but these are much less pronounced in SIFT-MS spectra (compared with the equivalent H_3O^+ clusters) as the rate coefficients are very much slower. [32]

Where the chemical kinetic information for a SIFT-MS precursor reacting with a neutral analyte is known, by simply monitoring the intensity of the precursor and product ions, a concentration for the analyte can be determined. Therefore, the response of the instrument to a change in analyte concentration is only limited by how fast the downstream

(analysing) quadrupole mass filter can alternate between the precursor and product ions and this can be as fast as once every 90 ms, or approximately 10 measurements of concentration per second. As the number of ions required to be measured increases, for example in the case where multiple analytes are being quantitated, the quadrupole cycling time and therefore the response time decreases accordingly. [1]

The concentration range for which the SIFT-MS technique is applicable for the quantitation of gas-phase analytes assumes less than 15% reduction in the precursor ion signal as a consequence of reaction with the analyte. Because the total analyte concentration must be "*small enough to only slightly reduce the count rate of the primary* (precursor) *ions*", [1] raising or lowering the sample flow will alter the amount of analyte entering the flow tube, therefore altering the size of the perturbation to the precursor ion intensity. A relatively small capillary flow affords the lowest detection limits.

1.2.4 Expanding the technique

It was apparent from the early publications by Smith and Spanel, that there was a major obstacle to SIFT-MS becoming a useful and usable technique both academically and commercially. This obstacle was the limited number of reactions studied where SIFT-MS precursor ions were reacting with analytes which are commonly observed in whole air samples. [1] Therefore, over the ensuing ten years a substantial number of articles regarding the gas-phase ion-molecule reaction kinetics of specific molecular functionalities (alcohols, heterocycles, amines etc.) were published. Each paper contained the ion-molecule rate coefficients and product ion branching ratios for a set of particular volatile analytes with the three SIFT-MS precursors. Only a small selection of important references are given here. [33-38] A review article on SIFT and the SIFT-MS technique was published in 2005. This contains a more thorough evaluation of the literature in this area. [39]

Possible SIFT-MS applications have also been the target of considerable interest. Medical and breath research applications have been the focus of most attention, but environmental monitoring and workplace health and safety are also considered to be plausible applications.

1.2.5 Application: medical and breath research

Examining the volatile organic compounds (VOCs) in exhaled breath is an example of a non-invasive diagnostic technique. [1,39-41] The application of GC-MS (gas chromatography mass spectrometry) and SIFT-MS techniques, [42] along with considerable biological research [43] has determined the presence of several analytes of metabolic importance in breath: isoprene, ethanol, acetone and ammonia. The monitoring of these analytes in the breath of healthy and/or ailing patients has shown the ability of SIFT-MS to give an insight into the condition of a patient. As an example, isoprene and ammonia are known to be markers of end-stage renal failure. [44]

The concentrations of analytes in the headspace of blood or urine samples has also received some interest. By measuring the concentrations of analytes which arise from bacterial action upon the substrate, specific bacteria can be identified. [45-47] The rapid selective identification of bacteria in the blood stream of a human could lead to increased medical efficacy and more targeted antibiotic treatment. However, the current size of a SIFT-MS instrument is a restricting factor on the commercialisation of medical applications. An instrument which is capable of being easily moved 'bed-side' would be more applicable. Even though current instrumentation is reduced in size compared to previous SIFT-MS instruments (discussed in section 1.2.8), further miniaturisation of the technology is required and has been undertaken.

1.2.6 Application: air quality

Ambient air monitoring and indoor air quality monitoring involves detection of volatile compounds (usually of environmental relevance) directly from an air sample either by an online method, or by a passive sampling onto a Tenax™ (or similar) adsorbent tube. Environmental agencies are able to use data such as this for comparison with maximum accepted ambient concentrations; industrial businesses are also able to use SIFT-MS to monitor ambient analytes which may be of harm to humans. The emission of petrol and diesel vapours into the atmosphere has received particular attention in this field due to the many toxic organic compounds that are contained in automobile emissions which may effect the environment. [48,49]

1.2.7 Application: shipping and fumigation

As there is no international standard for fumigation of shipping containers, workers in the shipping freight and border protection industries can be exposed to high fumigant levels. Exposure to high concentrations of methyl bromide in the process of fumigation is known to affect cognitive ability. [50] This is an occupational safety and health issue, and is a potential health hazard that is receiving more and more attention.

1.2.8 Instrumentation development

Concurrently with the development of the SIFT-MS technique and surrounding applications was the development of instrumentation based on SIFT-MS methodology that could be used in the commercial environment. Between the first publication regarding SIFT-MS in 1996 and the year 2000, research into the development of the SIFT-MS technique was restricted to large instruments which were originally designed to model the conditions of the upper atmosphere. [5] These large scale instruments were completely non-portable, and not optimised for analytical research.

In 1999, the first commercialisation of SIFT-MS was undertaken by the commercial firm PDZ Europa under the advisement of Smith and Spanel, the authors of the original SIFT-MS publication. The commercialisation venture was later taken over by Trans Spectra (Newcastle-under-Lyme, UK). Trans Spectra developed a small scale T-SIFT-MS (transportable selected ion flow tube mass spectrometer) which weighs ~700 kg and is approximately 2 m long by 1 m high by 0.8m deep. This instrument was marketed specifically at the medical sector. The majority of the minimisation for the T-SIFT-MS occurred due to the inclusion of turbomolecular pumps and a smaller flow tube. A photograph of the T-SIFT-MS purchased by the University of Canterbury and commissioned in early 2003 is shown in figure 1.01.

In 2003, a second company Syft Technologies Ltd. based in Christchurch, New Zealand began also with a goal to commercialise SIFT-MS and create an instrument which would be smaller and more commercially viable than the T-SIFT-MS. Launched in 2004, the Voice100 SIFT-MS was the attainment of this goal. The Voice100 affords a substantially smaller footprint than the T-SIFT-MS which is made possible by a 180° bend in the flow tube. Details of the operation of the Voice100 have been published recently. [51] A fundamental

understanding of the Voice100 SIFT-MS will be given through chapters 2 and 3 of this thesis.

Figure 1.01. The Trans Spectra T-SIFT-MS.

1.3 Theory of SIFT-MS Operation

The following derivations and formulae are adapted from a collection of publications. The research of Ferguson *et al*,. [5] Bolden *et al.* [52] and Adams and Smith [2] provide further information regarding the FA and SIFT techniques (theoretically very similar) and the research of Spanel and Smith [29,39,53] and Freeman and McEwan [54] provide further information regarding the SIFT-MS analytical methodology.

1.3.1 SIFT

The classical mode of operation of a SIFT instrument is to determine the kinetic parameters of an ion-molecule reaction; that is, to determine a reaction rate coefficient and the product ion branching ratios. For the reaction $A^+ + B \rightarrow D^+ + E$, a rate law is defined as equation 1.01 where k is the bimolecular rate coefficient, t is the time and $[A^+]$ and $[B]$ are the respective concentrations of A^+ and B.

$$\frac{-d[A^+]}{dt} = -k[A^+][B] \qquad (1.01)$$

If *[B] >> [A⁺]*, as always occurs in this technique, then a pseudo-first order rate law can be applied. As the reaction time (*t*) is defined as the reaction length (*l*) divided by the velocity of the ions sampled (v_0), equation 1 can be integrated to become equation 1.02, where $[A_0^+]$ is the initial concentration of A^+.

$$[A^+]=[A_0^+]\exp\left(\frac{-k}{v_0}\int_0^l [B]\,dz\right) \tag{1.02}$$

Assuming that the neutral reagent B is evenly distributed radially throughout the flow tube and across the entire length of the reaction region, such that B is mixed efficiently with the carrier gas at the sample inlet, B can be approximated to equations 1.03 and 1.04, where Φ_B is the flow of the neutral analyte in molecules s^{-1}, *a* is the radius of the flow tube and *z* is some fraction of the entire reaction length *l*.

$$B=0 \qquad z<0 \tag{1.03}$$

$$[B]=\frac{\Phi_B}{\pi a^2 v_0} \qquad z\geq 0 \tag{1.04}$$

Now as all parameters are understood, equation 1.02 can be evaluated to determine the rate law for a bimolecular process where the psuedo-first order approximation has been applied.

$$[A^+]=[A_0^+]\exp\left(\frac{-\Phi_B k l}{\pi a^2 v_0^2}\right) \tag{1.05}$$

From equation 1.05 it is apparent that once the flow tube size and ion velocity (both constants) are known, the rate coefficient *k* can be evaluated from the flow of neutral analyte and the concentration of A^+. In the case of SIFT, the concentration of ions are determined from the ion intensity on the particle multiplier which allows equation 1.05 to be simplified and rearranged to equation 1.06, where the intensities of A^+ and A^+_0 are $I(A^+)$ and $I(A^+_0)$, and the end correction (discussed in section 3.2.2) is defined as *e*.

$$\ln\left(\frac{I_{A^+}}{I_{A_0^+}}\right)=\frac{-\Phi_B k(l+e)}{\pi a^2 v_0^2} \tag{1.06}$$

By plotting the semi logarithmic decay of the intensity of a reagent ion against the neutral gas flow, a rate coefficient can be determined. Because this only involves measuring the intensity of one specific *m/z* ratio, the mass dependent radial diffusion in the flow tube and

mass discrimination in the downstream quadrupole chamber can be ignored. This model is a simple model, and is the standard method for rate coefficient determination.

A pseudo-first order rate coefficient for a termolecular process can also be determined at a specific pressure as the carrier gas (usually helium or argon) acts as the third body removing the excess energy of the reaction. By measuring rate coefficients across a range of carrier gas pressures, a pseudo-second order rate coefficient can be determined, again assuming that $[B] >> [A^+]$. [55]

Coincidentally with the measurement of a rate coefficient, a 'branching ratio' (relative product ion distribution of the primary reaction being studied) can easily be determined. This is deduced by extrapolating the relative intensities of the measured product ions to zero neutral flow where the effects of secondary chemistry, between a product ion and a neutral species, are removed. To effectively determine a branching ratio, the mass discrimination of the flow tube, quadrupole and lenses must be first understood.

1.3.2 SIFT-MS

One of the main features of the SIFT-MS is its ability to simultaneously measure the concentrations of many analytes in a single sample without chromatographic separation. [39] It is therefore apparent that by using equation 1.06 it is not possible to quantitatively measure multiple analytes simultaneously. For example, if a mixture of acetone and methanol in the parts-per-million-by-volume (ppmv) concentration range were introduced into a SIFT-MS flow tube where H_3O^+ was the chosen precursor, each analyte would reduce the ion intensity of H_3O^+ by an amount corresponding to the concentration of the analyte and the total analyte concentration could be found. However, the specific concentrations of each analyte would not be discernible if applying equation 1.06. Therefore, to separate and quantitate individual analytes, the intensities of the product ions are required to be measured as well as the intensity of the precursor ion. Unfortunately, by introducing two separate masses into a single equation the differential diffusion of the product and precursor ions must now be included (assuming the mass discrimination of the downstream quadrupole chamber is known), and inclusion of this term requires equation 1.06 be approached from a different perspective.

If N_i and N_p are the number densities (ions cm^{-3}) of a specific precursor ion and product ion pair in a flow tube, the decrease of N_i and N_p down the length of the reaction region is

determined by equations 1.07 and 1.08, where D_i and D_p are the diffusion coefficients of the precursor and product ions respectively and Λ is the characteristic diffusion length. [20]

$$\frac{dN_i}{dt} = -N_i \frac{D_i}{\Lambda^2} - N_i k[B] \tag{1.07}$$

$$\frac{dN_p}{dt} = -N_p \frac{D_p}{\Lambda^2} - N_p k[B] \tag{1.08}$$

Individually integrating and evaluating equations 1.07 and 1.08 down the course of the reaction length leads to equations 1.09 and 1.10, where N_i^t and N_i^0 are the number densities of the precursor ion at time = t and time = 0 respectively (the same situation applies to the product ions).

$$N_i^t = N_i^0 \exp\left(-k[B]t - \frac{D_i}{\Lambda^2}t\right) \tag{1.09}$$

$$N_p^t = N_p^0 \exp\left(-k[B]t - \frac{D_p}{\Lambda^2}t\right) \tag{1.10}$$

To determine *[B]* in a SIFT-MS, both the number densities of the precursor and product ions at the end of the reaction region need to be known at any one point in time, because the intensities at the start of the reaction region are unknown. Smith and Spanel found an analytical solution to the simultaneous evaluation of equations 1.09 and 1.10, which is given in 1.11. [1]

$$\frac{N_p^t}{N_i^t} = k[B]t \frac{\exp\left(k[B]t + \frac{D_i - D_p}{\Lambda^2}t\right) - 1}{k[B]t + \frac{D_i - D_p}{\Lambda^2}t} \tag{1.11}$$

To solve equation 1.11 for *[B]* is a complex task, however in the case of SIFT-MS, where the perturbation to the precursor ion signal is kept small such that *[B]* is very close to zero, the assumption given in equation 1.12 can be applied.

$$\frac{N_p^t}{N_i^t} = \exp\left(\frac{N_p^t}{N_i^t}\right) + 1 \tag{1.12}$$

With this assumption in hand, equation 1.11 can be simplified to equation 1.13, with the parameter D_e being defined in equation 1.14.

$$\frac{N_p^t}{N_i^t} = k[B]tD_e \tag{1.13}$$

$$D_e = \frac{\exp\left(\frac{D_i - D_p}{\Lambda^2}t\right) - 1}{\frac{D_i - D_p}{\Lambda^2}t} \tag{1.14}$$

For the general case of a standard SIFT-MS measurement, the number densities of the precursor and product ion are replaced by the intensities of two ions measured on the particle multiplier.

From equation 1.13 it is apparent that the concentration of an analyte is proportional to the intensity of the product ions which form. It is this proportionality that allows SIFT-MS to be a 'real-time' technique for the analysis of volatile organic compounds. Furthermore, the technique does not require calibration to a known standard if all the other flow and kinetic parameters are known. Because SIFT-MS exploits the chemical kinetics occurring in a well defined flow tube, the quantitation of an analyte relies on the understood knowledge of the rate coefficient for accuracy. Where this rate coefficient is very well understood, the uncertainty upon the measurement decreases. In contrast, GC-MS (gas chromatography – mass spectrometry) [56] and other chromatographic separation techniques require constant calibration and re-calibration to known standards for quantitation to be possible.

The system given in equation 1.13 becomes more complicated in a reaction with multiple product ion channels, and even further complicated in systems where multiple precursors give the same product ions. For instance, the reaction system for H_3O^+ and its sequential water clusters reacting with acetone is shown in reactions 1.15 – 1.17. This reaction system has four precursor ions and two product ions.

			Rate Coefficient	
$H_3O^+ + (CH_3)_2CO$	$\rightarrow$	$(CH_3)_2COH^+ + H_2O$	k_{A1}	(1.15)
$H_3O^+.H_2O + (CH_3)_2CO$	$\rightarrow$	$(CH_3)_2COH^+ + 2H_2O$	k_{A2}	(1.16)
$H_3O^+.(H_2O)_2 + (CH_3)_2CO$	$\rightarrow$	$(CH_3)_2COH.H_2O^+ + 2H_2O$	k_{A3}	(1.17)
$H_3O^+.(H_2O)_3 + (CH_3)_2CO$	$\rightarrow$	$(CH_3)_2COH.H_2O^+ + 3H_2O$	k_{A4}	(1.18)

To determine the concentration of acetone from this system requires a summation of the product ion densities across all product ions and a summation of the precursor ion

densities across all precursor ions multiplied by the respective rate coefficients. These types of situations are very common in SIFT-MS measurements, and the general SIFT-MS concentration formula (equation 1.13) must be amended to cater for such a system. The amended multiple product and precursor ion SIFT-MS concentration equation is given as equation 1.19, where $N^t_{P,i}$ is the number density of a product ion i, $N^t_{I,j}$ is the number density of the precursor ion j, and k_j is the rate coefficient for the reaction of the precursor j with B. As above, number densities of ions are determined from the number of ion counts per second on the particle multiplier.

$$[B]=\frac{1}{t}\frac{\sum_{i=1}^{n} N^t_{P,i}}{\sum_{j=1}^{n} N^t_{I,j}k_j} \tag{1.19}$$

The rate coefficient, k_j, in equation 1.19 is in units of cm^3 $molecule^{-1}$ s^{-1} and the number density of an analyte *[B]* is in units of molecules cm^{-3}. However, the number density of analyte in the flow tube is of little interest when using the SIFT-MS technique for analytical purposes, and the units of parts-per-million-by-volume (ppmv), parts-per-billion-by-volume (ppbv), and parts-per-trillion-by-volume (pptv) are much more ubiquitous. Determining the concentration in this way is a three step procedure. Initially the partial pressure of analyte in the flow tube must be determined by using an ideal gas relationship as shown in equation 1.20, where R is the gas constant, T is the temperature and N_A is Avogadro's number. Obviously, as R and N_A are constants, equation 1.20 will reduce to equation 1.21 which yields the analyte partial pressure in torr when *[B]* is in the standard units of molecules cm^{-3}.

$$P_{Analyte}=\frac{10^6[B]RT}{N_A} \tag{1.20}$$

$$P_{Analyte}(Torr)=1.035x10^{-19}[B]T \tag{1.21}$$

The flow of the analyte is then found from the total flow of gas through the flow tube, including the capillary flow as shown in equation 1.22, where Φ_{car} and Φ_{cap} are the flows of the carrier gas and capillary respectively and P_{FT} is the total pressure in the flow tube.

$$\Phi_{Analyte}=\left(\Phi_{car}+\Phi_{cap}\right)\frac{P_{Analyte}}{P_{FT}} \tag{1.22}$$

The concentration is finally found by a ratio of the analyte flow to the capillary flow, and then multiplying by the required factor, which is 10^6 for ppmv, 10^9 for ppbv and 10^{12} for

pptv. The example for ppbv is given as equation 1.23.

$$ppbv_{Analyte} = \frac{\Phi_{Analyte}}{\Phi_{cap}} 10^9 \tag{1.23}$$

By then combining equations 1.21, 1.22 and 1.23 for the ppbv case, a general expression for determining the concentration of the analyte in ppbv from the number density is found. This expression is given as equation 1.24.

$$ppbv_{Analyte} = \frac{1.035 \times 10^{-10} [B] T}{P_{FT}} \left(\frac{\Phi_{car}}{\Phi_{cap}} + 1 \right) \tag{1.24}$$

1.3.3 Limit of detection

Due to the recent development of the SIFT-MS technique, and the paradigm shifting nature of the technology, classical methods (such as those used by GC-MS) for determining the limit of detection (LOD) and limit of quantitation (LOQ) [57] do not strictly apply. However, the underlying theory is in principle the same. Recently, Milligan *et al*. [58] published a method for the determination of the LOD and LOQ directly from the background intensity of the ion signal at the product ion masses of interest, and the sensitivity (in counts s^{-1} $ppbv^{-1}$) of a measurement.

The LOD is widely accepted to be the minimum concentration or 'weight of analyte' that can be detected at a known confidence level. [59] This limit depends on the background signal and the statistical fluctuations of that signal. The LOD does not depend on the amount of signal arising from the analyte and therefore all ion intensities discussed in relation to the LOD are background ion intensities. Long and Winefordner [60] define a recommended confidence interval as three standard deviations above background, and therefore the minimum signal distinguishable above the background noise (B_m) is defined as equation 1.25, where B_μ is the average background signal and B_σ is the standard deviation of the background signal. All values of B are total accumulated product ion counts over a time t_c.

$$B_m = B_\mu + 3B_\sigma \tag{1.25}$$

The limit of detection is then defined as equation 1.26, where t_c is the time in seconds spent counting product ions and s is the sensitivity of the measurement, which is the number of counts per unit time of product ions per unit concentration (usually counts s^{-1} $(ppbv)^{-1}$). The

sensitivity s is then defined as equation 1.27 where $ppbv_{[B]}$ is the concentration of the analyte B in parts-per-billion-by-volume.

$$LOD = \frac{(B_m - B_\mu)}{s\ t_c} \tag{1.26}$$

$$s = \frac{N_P^t}{ppbv_{[B]}} \tag{1.27}$$

By solving equation 1.24 for *[B]* and then replacing the solved expression into equation 1.13, an equation for *s* can be found based purely on the flow tube parameters, precursor ion signal, diffusion correction and rate coefficient. This is given as equation 1.28.

$$s = \frac{k\ N_I^t\ t\ D_e\ P_{FT}}{1.035\text{x}10^{-10}\left(\frac{\Phi_{car}}{\Phi_{cap}} + 1\right)T} \tag{1.28}$$

Even though a concentration found using the SIFT-MS method is dependent on the sample flow rate into the flow tube, the flow tube pressure and temperature, and the precursor and product ion intensities, [1] experience has shown that at the LOD the only significant noise contribution in the measurement is from the variation in product ion intensity. Furthermore, Milligan *et al.* [58] observed that at concentrations less than 10 ppmv, the product ion signal obeys the Poisson distribution, and therefore the mean of the background ion signal (which always equates to substantially less than 10 ppmv) is equal to the standard deviation (equation 1.29).

$$B_\sigma = \sqrt{B_\mu} \tag{1.29}$$

The total accumulated product ion counts *B* are then related to the count rates *b* (in counts s^{-1}, the value usually determined from a particle multiplier) by equation 1.30.

$$b_\sigma t_c = B_\sigma \ \text{ and } \ b_\mu t_c = B_\mu \tag{1.30}$$

By substituting equation 1.25 into 1.26 we arrive at equation 1.31.

$$LOD_{ppbv} = \frac{3\text{B}_\sigma}{s\ t_c} \tag{1.31}$$

Thus by substituting equations 1.29 and 1.30 into 1.31 a simple expression for the limit of detection has been derived which is based on the mean background ion intensity. This is given as equation 1.32

$$LOD_{ppbv} = \frac{3\sqrt{b_\mu t_c}}{s\ t_c} \tag{1.32}$$

Therefore it is apparent, that if a background product ion intensity is known for a reaction with well understood kinetic parameters, a value for the LOD for a specific product ion sampling period can be found. Because equation 1.32 is a simple relationship, SIFT-MS does not require calibration curves for the calculation of an LOD, whereas the GC-MS technique does require such curves. [57]

1.3.4 Limit of quantitation

The limit of quantitation (LOQ) is commonly defined as a signal with a precision that satisfies an expected value. [57] If an acceptable precision is defined to be a measurement which has a relative standard deviation of ± 20%, then the LOQ will be reached when equation 1.33 is satisfied, where q_μ is the mean signal count rate (in counts s^{-1}) due to the sample, but not due to the background. Therefore the numerator is equal to the standard deviation of the total measured signal, and the denominator is the total of the accumulated counts from the sample.

$$\frac{\sqrt{(q_\mu + b_\mu)t_c}}{q_\mu\ t_c} = 0.2 \tag{1.33}$$

Because q_μ is known to be the concentration of an analyte (in ppbv) multiplied by its sensitivity (in counts s^{-1} $ppbv^{-1}$), equation 1.32 can be solved for t_c (remembering that t is the reaction time and t_c is the time spent counting the product ion signal) giving equation 1.34.

$$t_c = 25\frac{ppbv_{[B]}\ s + b_\mu}{\left(ppbv_{[B]}\ s\right)^2} \tag{1.34}$$

Therefore, when a specific limit of quantitation is required (for example 0.1 ppbv), the product ion sample time required to gain the LOQ can be determined. Solving equation 1.34 for $ppbv_{[B]}$ provides the LOQ for a given measurement time. It must be noted that only one root of the solved quadratic equation is positive.

$$LOQ_{ppbv} = \frac{25 + 5\sqrt{25 + 4\ b_\mu\ t_c}}{2\ s\ t_c} \tag{1.35}$$

1.4 Gas-Phase Ionic Reactions

At the core of the SIFT-MS technique is its ability to exploit the well understood kinetics of chemical reactions which occur in the gas phase. The reaction rate coefficient for a particular process is the key parameter which affords the success of SIFT-MS. However, even though the kinetics of a reaction are crucial to the SIFT-MS technique, the thermodynamics of a reaction cannot be discounted. If a process is thermodynamically unfavourable, it is unlikely to occur in the gas phase.

Gas phase ion-neutral reactions often proceed rapidly which is due to the potential energy surface being devoid of an activation energy barrier. Often, these reactions proceed so rapidly that every single ion-neutral collision will yield a product ion, such that the reaction rate coefficient will be equal to the collision limiting rate coefficient.

Each of the precursor ions will often react via different pathways due to the thermodynamic constraints of the reactions. The common reactive pathways often observed in SIFT-MS are discussed below.

1.4.1 Proton transfer

An example of a proton transfer reaction is given as reaction 1.36, where H_3O^+ transfers a proton to acetone. [34]

$$H_3O^+ + (CH_3)_2CO \rightarrow (CH_3)_2COH^+ + H_2O + 121 \text{ kJ mol}^{-1} \quad (1.36)$$

The process of proton transfer requires that the reagent ion has an available proton to donate, and that the proton affinity of the analyte (in this case acetone) is greater than the proton affinity of the conjugate base of the reagent ion (in this case H_2O). The proton affinity of a neutral species is the negative enthalpy of formation of an ion as defined in equation 1.37, which is the negative of the enthalpy of reaction for the hypothetical protonation reaction 1.38.

$$\Delta_f H°(MH^+) = \Delta_f H°(M) + \Delta_f H°(H^+) - PA \quad (1.37)$$

$$M + H^+ \rightarrow MH^+ \qquad \Delta H_r = -PA \quad (1.38)$$

When proton transfer reaction is known to be exothermic, experience has shown that the process will always occur with unit efficiency demonstrating that the process will occur at

the collision limiting rate coefficient, which is often in the order of 10^{-9} cm^3 $molecule^{-1}$ s^{-1}. [61] Conversely, where proton transfer is known to be endothermic, the pathway will not be observed. However, in the intermediate case where the proton affinities of the analyte and the conjugate base of the reagent ion are approximately equal, a gas-phase equilibrium is established. When the rate coefficients for the forward and reverse process are known, an equilibrium coefficient K can be determined where $K = k_{forward} / k_{reverse}$. As $\Delta G° = -RT \ln K$ and $\Delta G° = \Delta H° - T\Delta S°$, the contribution of the entropy to the reaction can be determined from the equilibrium coefficient when the temperature of a measurement is well defined. [62]

The gas basicity (GB) of a proton transfer reaction is the Gibbs free energy equivalent of reaction 1.37, manifested as $\Delta G_r = -GB$. For example, the gas basicity of acetone is 782.1 kJ mol^{-1}, and the gas basicity of water is 660 kJ mol^{-1}. [31] Therefore, the Gibbs free energy of proton transfer from H_3O^+ to acetone is -122.1 kJ mol^{-1}, as compared to the enthalpy of proton transfer (equation 1.15) of -121 kJ mol^{-1} (because the PA (H_2O) = 691 kJ mol^{-1}, PA (acetone) = 812 kJ mol^{-1}). [31] The difference of 1.1 kJ mol^{-1} is deemed to be an entropic effect, [16,63] revealing that the transfer of proton from H_3O^+ to acetone is entropically favoured. A change in entropy across the reaction coordinate of a proton transfer reaction has been proposed to be due to conformational changes and an alteration in the rotational degrees of freedom. [64]

Proton transfer processes occur from H_3O^+ and the sequential water clusters of H_3O^+. The $NO^+.H_2O$ ion has also been observed to transfer a proton to a neutral analyte, where the conjugate base of $NO^+.H_2O$ is proposed to be HNO_2, nitrous acid. [65] No other SIFT-MS precursor ions in the current study have a free proton to donate, and therefore will not undergo proton transfer.

1.4.2 Electron transfer

An electron transfer (often called charge transfer) pathway occurs for cation-neutral reactions when an electron is donated from a neutral species to a cation. An example of cationic electron transfer between $O_2^{\bullet+}$ and benzene is given as reaction 1.39, where benzene donates an electron to $O_2^{\bullet+}$. [30]

$$O_2^{\bullet+} + C_6H_6 \rightarrow C_6H_6^+ + O_2 + 2.8\ eV \quad (1.39)$$

The process of electron transfer will only occur when the ionisation energy (IE) of the neutral analyte (benzene in the above example) is greater than the electron affinity (EA) of the

precursor ion ($O_2^{\bullet+}$ from reaction 1.39). The thermodynamic quantities electron affinity and ionisation potential are defined in equations 1.40 and 1.41. [62]

$$\Delta_f H°(M) + IE = \Delta_f H°(M^+) \quad (1.40)$$

$$M \rightarrow M^+ + e^- \qquad \Delta H_r = IE = -EA \quad (1.41)$$

Electron transfer processes are often dissociative, such that the molecular ion which is formed as a result of the transfer of an electron, breaks into smaller fragments. The appearance energy (AE) of a fragment ion denotes the amount of energy required to observe a specific fragment ion, as shown in the hypothetical reaction 1.42. An example of a dissociative electron transfer reaction is then given as reaction 1.43 for the reaction of $O_2^{\bullet+}$ with n-butane, [35] where the appearance energy of $C_3H_7^+$ arising from n-butane is known to be 11.15 eV (and the ionisation potential of O_2 is 12.07 eV). [30]

$$AB \rightarrow A^+ + B + e^- \qquad \Delta H_r = AE \quad (1.42)$$

$$O_2^{\bullet+} + n\text{-}C_4H_{10} \rightarrow C_3H_7^+ + O_2 + CH_3 + 0.9 \text{ eV} \quad (1.43)$$

The SIFT-MS precursor ions $O_2^{\bullet+}$ and NO^+ will undergo the process of electron transfer when the ionisation potential of the analyte is less than 12.07 eV and 9.26 eV respectively. The $NO^+.H_2O$ ion has also been observed to undergo a dissociative electron transfer process, where the water molecule dissociates after it has gained an electron. [65] An example of this type of reaction is given as reaction 1.44 for aniline (IE = 7.72 eV), however the thermodynamics of the overall reaction are unknown.

$$NO^+.H_2O + C_6H_5NH_2 \rightarrow C_6H_5NH_2^+ + NO + H_2O \quad (1.44)$$

1.4.3 Hydride abstraction

The effective abstraction of a hydride by NO^+ or $O_2^{\bullet+}$ is a commonly observed process in a SIFT flow tube leading to an $[M - H]^+$ cation. An example of the abstraction of a hydride by NO^+ from acetaldehyde is shown as reaction 1.45. [34]

$$NO^+ + CH_3CHO \rightarrow CH_3CO^+ + NOH + 52.9 \text{ kJ mol}^{-1} \quad (1.45)$$

The parameter hydride affinity (HA) is coined to the hypothetical reaction given as reaction 1.46, however few cations have experimental values of HA. Where the hydride affinity of the precursor ion is greater than that of the conjugate base of the analyte, the

reaction will proceed as an exothermic pathway.

$$M^+ + H^- \rightarrow MH \qquad \Delta H_r = HA \qquad (1.46)$$

The hydride abstraction pathway will often occur with unit collision efficiency, but is also known to occur very slowly with a collision efficiency of less than 10^{-3}. For example the abstraction of a hydride from n-butane by NO^+ has a measurable but slow reaction rate coefficient as shown in reaction 1.47. [66]

$$NO^+ + n\text{-}C_4H_{10} \rightarrow C_4H_9^+ + NOH + 48 \text{ kJ mol}^{-1}$$

$$k = 2.5 \times 10^{-12} \text{ cm}^3 \text{ molecule}^{-1} \text{ s}^{-1} \qquad (1.47)$$

$O_2^{\bullet+}$ is often proposed to abstract a hydride from neutral analytes when an $[M - H]^+$ ion is observed. [67] However, due to the large ionisation energy of O_2, differentiating an electron transfer pathway (leading to O_2 + H as neutral species) from hydride abstraction (which gives the neutral species O_2H) is difficult using SIFT-MS.

1.4.4 Association

Association can occur by two different pathways, radiative association and termolecular association. An example of each is given in equations 1.48 and 1.49 for the radiative [67] and termolecular [32] pathways respectively.

$$NO^+ + c\text{-}C_6H_5CN \rightarrow NO.\ C_6H_5CN^+ + h\nu \qquad (1.48)$$

$$NO^+ + CH_3OH + He \rightarrow NO.\ CH_3OH^+ + He \qquad (1.49)$$

Radiative association pathways are generally assumed not to occur in the case of SIFT flow tubes (and the SIFT-MS technique) because the radiative lifetime of a collision complex is substantially longer than the mean free path of an ion in the flow tube (~50 μm). Bates and Herbst [68] define the upper pressure limit where radiative association occurs as 10^{12} molecules cm^{-3}, that is four orders of magnitude lower than the pressure regime of a SIFT flow tube. Therefore an ion will not have enough time to emit a photon before colliding with many different carrier gas atoms. The result of this assumption is that all association processes occurring in a SIFT-MS flow tube are via the process of termolecular association.

In termolecular association, a third body, such as a carrier gas atom, must collide with the collision complex and remove the excess vibrational and rotational energy. [68] The third

body allows for stabilisation of the collision complex at an energy less than the energy required to dissociate the complex. The energy that is removed by the third body is known as the binding energy which is defined in equation 1.50.

$$A^+ + M \rightarrow AM^+ \qquad \Delta H_r = -Binding\ Energy \qquad (1.50)$$

Where the binding energy is substantially greater than the thermal energy ($k_B.T$) the complex formed will not back-dissociate. It is therefore the magnitude of the exothermicity of the binding energy that will control the magnitude of the observed bimolecular reaction rate coefficient.[69,70]

Association processes occur commonly for the H_3O^+ and NO^+ precursor ions, and their respective water clusters. Because the observed pseudo-bimolecular reaction rate coefficient that is commonly measured on a SIFT-MS, is pressure dependent, care must be taken when transporting rate coefficients for association reactions between SIFT-MS instruments.

1.4.5 Ligand switching

A ligand-switching or metathesis reaction is one where a charged ligand bound to a stable analyte is transferred to another neutral analyte. Reactions of this nature are very common for the hydronium ion water clusters $H_3O^+.(H_2O)_n$ (n = 1, 2, 3). An example of a ligand-switching reaction is given as reaction 1.51 and 1.52 for diethyl ether reacting with the n = 1 and 2 case. [71]

$$H_3O^+.H_2O + CH_3OCH_3 \rightarrow CH_3OCH_3.H_3O^+ + H_2O \qquad (1.51)$$

$$H_3O^+.(H_2O)_2 + CH_3OCH_3 \rightarrow CH_3OCH_3.H_3O^+ + 2H_2O \qquad (1.52)$$

For the case of reaction 1.52, the ligand-switching reaction becomes more exergonic due to the apparent increase in entropy across the reaction coordinate. However, these pathways are often difficult to assign, and ambiguity between a ligand-switching and an association pathway often occurs. [71]

Ligand-switching reactions have also been previously observed for the $NO^+.H_2O$ precursor ion, leading to an $[M + NO]^+$ ion and expelling H_2O. [65]

1.5 Introduction to the Current Research

The ensuing seven chapters and appendices discuss the results of both experimental and theoretical investigations which have been performed between September 2004 and October 2007. Each chapter also contains the implications of the research in both academic and commercial fields. The underlying goal of the research presented here is to expand the current capabilities of the SIFT-MS technique both from an instrumentation and application point-of-view.

Chapter 2 outlines the experimental procedure and instrumentation that is used throughout the course of this thesis. A new instrument, the Voice100, which has been designed specifically for the SIFT-MS technique is introduced, along with a range of peripheral instrumentation.

Chapter 3 discusses three important concepts regarding the kinetic verification and development of the Voice100; the mixing of carrier gases, diffusion in mixed carrier gases and water cluster reactions in humid environments. A derivation and discussion of the fundamental aspects of each of these concepts will be given.

The details on the reactions of nine acyclic saturated hydrocarbons with O_2^+ and H_3O^+, and also the reactions of 21 hydrocarbon ions with H_2O are then given in Chapter 4. A knowledge of the kinetic parameters of these 39 reactions allows for the development of a SIFT-MS application for the quantitative analysis of hydrocarbons in the headspace of soil and water samples.

The reactions of 17 alkyl esters with six common SIFT-MS precursor ions are reported in Chapter 5. Pathways for many of the reactions studied are found to give a large degree of rearrangement, and two of these rearrangement pathways are studied using computational methods. An example of SIFT-MS detection of four isobaric alkyl esters is also provided.

Chapter six describes a number of reactions of common SIFT-MS precursor ions with the precursors and surrogates of chemical warfare agents. Furthermore, a qualitative study on the detection of the chemical warfare agents sarin, ethyl sarin and sulphur mustard is also discussed.

Chapter seven presents data on the reactions of 17 analytes that are classified as hazardous air pollutants by the US-EPA† with six common SIFT-MS precursor ions. A SIFT-MS method is then developed that can constantly monitor the concentration of a range

† The US-EPA is an acronym for the United States Environmental Protection Agency

of these toxic analytes.

A summary of the current research and suggestions for future directions which the research may take are then presented in Chapter 8.

Finally, References and Appendix A and B identify the sources of information discussed herein and derive some important equations encountered during this thesis.

CHAPTER 2

EXPERIMENTAL

Due to the evolutionary nature of the SIFT-MS instruments as discussed in chapter 1, a range of different SIFT-MS instruments are currently available and have been encountered during the course of this research. Each instrument used is aesthetically vastly different from another, with instruments ranging in size from less than a 1 m^3 for the smallest, up to the largest requiring two separate rooms to house all the required components; however, all instruments share the same concept and schematically are very similar. Two separate selected ion flow tube instruments that are of relevance to the research presented here will be discussed in this chapter. One, that is based at the University of Canterbury, is the flowing afterglow – selected ion flow tube mass spectrometer, and the other, based at Syft Technologies, is a Voice100 selected ion flow tube mass spectrometer. Following this discussion regarding instrumentation will be information pertaining to the ancillary systems and software used with the Voice100, physical methods of measuring rate coefficients and product ion branching ratios and a final short discussion of quantum chemical calculations that aid in SIFT-MS research.

2.1 The Flowing Afterglow – Selected Ion Flow Tube Mass Spectrometer

The University of Canterbury selected ion flow tube mass spectrometer was first designed and built between 1982 and 1985 and was discussed in some detail by Knight. [72] Dr. Knight details the original instrument that used a low pressure electron ionisation source resulting in a significant degree of ion fragmentation. The range of molecular and fragment ions were then individually mass selected by the first quadrupole mass filter, and injected into a fast flow of helium against the pressure gradient through a Venturi orifice. Ions reaching the far end of the flow tube were sampled through a pinhole orifice, mass selected on a second quadrupole mass filter and finally, the ions were detected using a particle multiplier. [11]

Modifications to this original design have been undertaken over the ensuing 15 years to expand the research capabilities and the instrument's overall ion signal. Petrie [73] altered the ion source from a co-linear to an off-axis system, and developed a new high pressure

electron impact ion source. Wilson [37] upgraded the particle multiplier assembly, and installed upstream facing ring inlets for introduction of neutral analytes into the flow tube with effective rapid mixing. Scott [74] and Fairley [75] both discuss the installation of a drift tube assembly, and the required electronics into the SIFT so as to be able to measure ion-mobility parameters. Then, as described by Fairley [75] and in more detail Milligan, [76] between 1996 and 1997, the University of Canterbury SIFT was relocated within the Chemistry Department, and rebuilt with some important modifications. A new flowing afterglow ion source was added enabling a wider range of ions to be injected into the flow tube, a dual annulus Venturi for splitting carrier gas flows, and greatly improved pumping was also added to enable better entrainment of ions into the carrier gas and lower absolute pressures in both the upstream and downstream chambers.

The instrument is currently in a very similar state to that detailed by Milligan [76] and shall only be discussed briefly for pertinence.

The FA-SIFT instrument (using the convention defined by Fairley [75]) is shown in a schematic diagram as figure 2.01 and shall be discussed in three sections: the ion creation region; the ion reaction region; and the ion detection region.

2.1.1 Ion creation region

The flowing afterglow source on the University of Canterbury FA-SIFT is similar in design to those previously used by Smith and Adam's group [77] and Bohme's group, [19] but most similar in design to the Bierbaum group [78] instrument, that is still in use today. Many sections of the FA source borrow from the schematics loaned from Professor Bierbaum, and the University of Canterbury SIFT research group is forever in her debt.

In the current research the only method of ion formation used has been a microwave discharge. The microwave discharge involves a ~2.5 GHz EMS Microtron 200 power supply, a type 5 microwave cavity (as per the definitions of Fehsenfeld *et al.* [79]) and a pyrex glass Wood's horn; a photograph of the assembly is given as figure 2.02. The Wood's horn is designed to extract ions and metastable atoms from the microwave discharge while not allowing photons into the flowing afterglow reaction region.

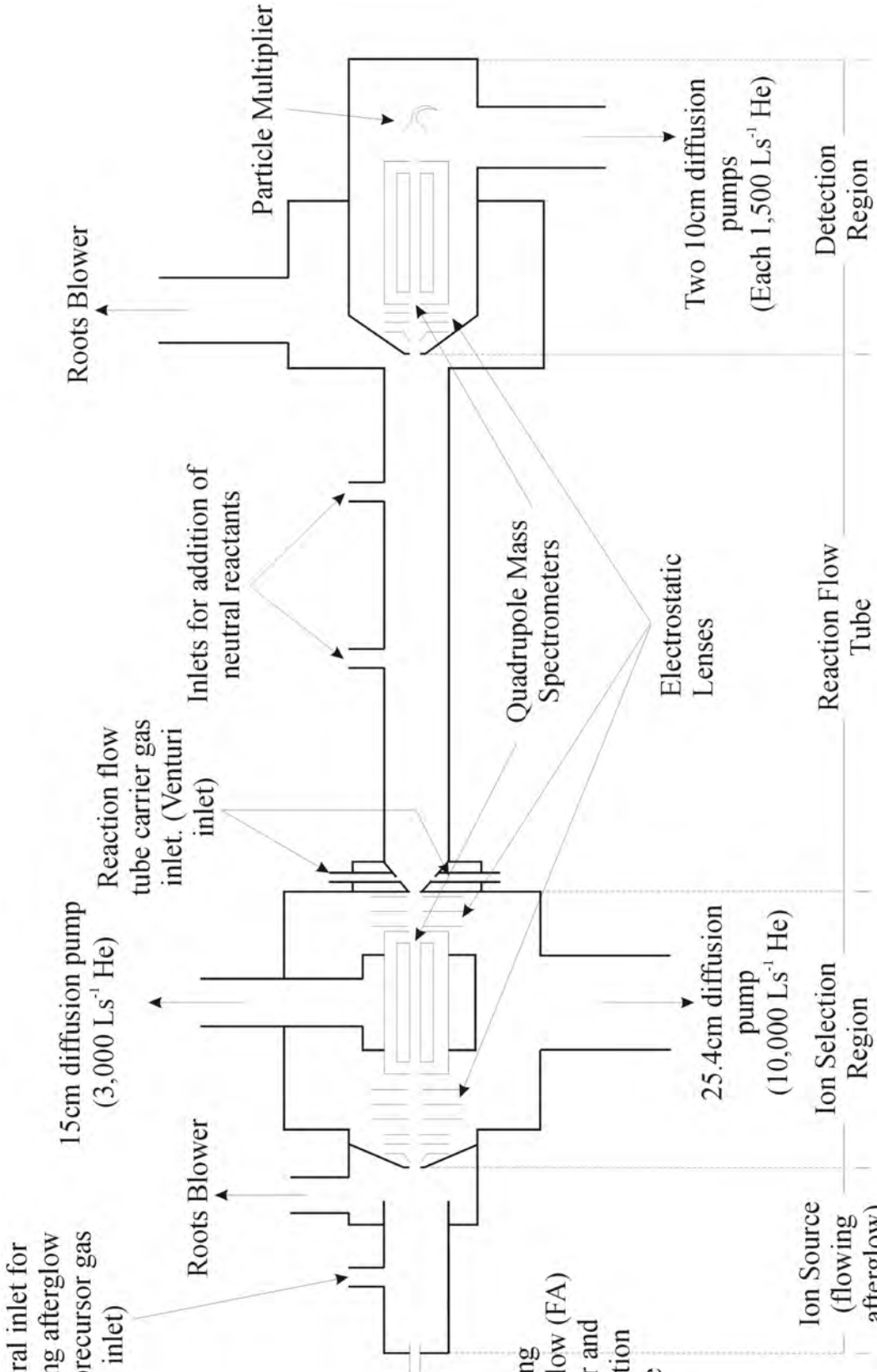

Figure 2.01 Schematic Diagram of the University of Canterbury flowing afterglow – selected ion flow tube mass spectrometer (FA-SIFT)

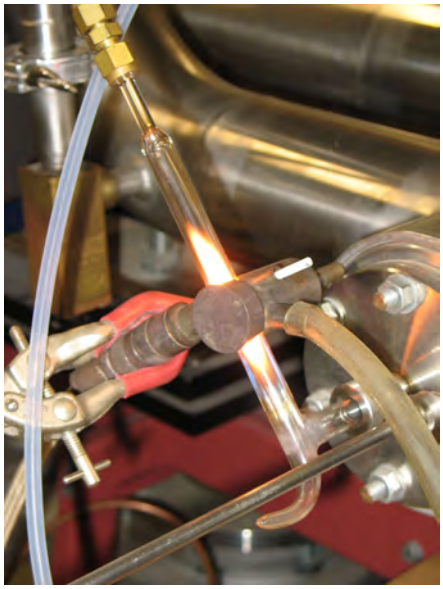

Figure 2.02 FA-SIFT: Helium being ionised in a microwave discharge cavity.

Removal of photons is achieved by positioning the type 5 microwave cavity orthogonal to the entrance aperture of the flowing afterglow reaction tube, and trapping all photons in the 'horn' section of the Wood's horn. A simple bend in the pyrex glass tube allows photons to be reflected into the flowing afterglow reaction region causing undesirable photo-ionisation effects. A rapid flow of helium (~60 Torr L s^{-1}) is passed through the microwave discharge where helium metastable atoms and helium ions are born. Because helium metastable atoms and helium ions have high electronic energies (the ionisation energy of helium is 24.6 eV [30]) the presence of any impurity will drastically alter the discharge, therefore all helium is first passed through a large tube containing molecular sieve at -196 K to remove all water and other impurities commonly found in helium. The excited helium plasma (a mixture of He^+ and He* and electrons) enter the flowing afterglow reaction region where two separate inlets, one finger inlet and one ring inlet allow the introduction of neutral analyte. By using the two inlets sequentially in a titration mode; softer ionisation, and therefore less fragmentation can be achieved. For instance, to examine the molecular ion of a hydrocarbon, direct ionisation by He* may not form the parent ion, but a number of fragment ions instead due to the large exothermicity of the reaction. However, by introducing an analyte with an intermediate ionisation energy such as oxygen (IE = 12.1 eV [30]) at the upstream ring inlet, the reaction between He^+ and He* produces O_2^+ that is then reacted with the hydrocarbon analyte. Less energetic ionisation of the hydrocarbon analyte added at the downstream finger inlet allows a more intense signal of the parent hydrocarbon ion..

Ions are sampled at the end of the flowing afterglow reaction region through a 2 mm

orifice in a molybdenum disk, that is positioned in the centre of a stainless steel nose cone, into the upstream high vacuum chamber. The entire flowing afterglow is pumped by an Edwards EH 1200 roots blower, that is backed by an Edwards E2M 80 backing pump enabling a pumping efficiency of 3024 L s^{-1} of air at 0.3 mbar.

The upstream chamber houses the upstream ion selection assembly. As is seen in figure 2.01, the quadrupole mass filter is sandwiched between 2 sets of lenses, with the quadrupole mass filter itself isolated for differential pumping. Ions are extracted from the flowing afterglow by electrostatic lenses and are focused into the quadrupole by two Einzel clusters of three electrostatic lenses each. The Einzel electrostatic lens arrangement focuses an ion beam by capturing the beam using the first lens, slowing the ions down and therefore condensing the beam with the second lens, and finally accelerating the condensed beam out using the third lens. By effectively collimating the ion beam prior to entering the quadrupole mass filter, greater transmission through the quadrupole is achieved. To gain the pressure required in the upstream chamber for effective ion transmission, two diffusion pumps are used independently to pump separate areas of the upstream chamber. A Varian VHS-400 25.4 cm oil diffusion pump (pumping speed 8000 L s^{-1} of helium) backed by a Leybold-Heraeus Trivac® D65B backing pump (pumping speed 65 L s^{-1} of helium) pumps the entire upstream chamber, while a Varian VHS-6 15 cm oil diffusion pump (pumping speed 2400 L s^{-1} of helium) backed by a Leybold-Heraeus Trivac® D30A backing pump (pumping speed 8 L s^{-1} of helium) is used to differentially pump the quadrupole region of the chamber.

2.1.2 Flow tube reaction region

The flow tube reaction region on the University of Canterbury FA-SIFT contains two major components: the Venturi orifice and the flow tube itself. Features essential for the optimum operation of a Venturi in a fast flow system have been published elsewhere, [21,22,80,81] and therefore only a short description of the relevant issues will be given.

The Venturi orifice contains two concentric annular slits for the introduction of carrier gas into the flow tube. The inner annulus is 0.025 mm wide and is 4.35 mm outside the ion aperture, and the outer annulus is 0.4 mm wide at a radial distance of 37.1 mm from the ion aperture, where carrier gas flows through each annulus are controlled independently. Helium is passed through the inner annular slit at 32 Torr L s^{-1} to create the Venturi effect, so that the ions may be injected into the flow tube against the pressure gradient. Helium is used for effective thermalisation of ions entering the flow tube from the upstream chamber due to the

very large ionisation potential of the strongly non-polarisable atoms. [14] It is common practice to split the flow of carrier gas such that only a fraction of the total carrier flow is through the annulus which creates the Venturi effect. [21] However, it is not common practice to inject multiple carrier gases into the flow tube, which is the case here as argon is passed through the outer annular slit at 46 Torr L s^{-1}. Argon is added to the flow tube to decrease the rate of radial diffusion of ions in the reaction region, and therefore increase the overall ion intensity. [75] The addition of argon to the SIFT flow tube, and the effects of mixing carrier gases will be discussed in depth in chapter 3 of this thesis. Needless to say, the design of the Venturi orifice is unchanged from the design reported by Fairley [75] and Milligan, [76] only the carrier gas composition differs from the previous publications.

The flow tube reaction region is effectively unchanged from the design reported in Petrie's thesis. [73] The flow tube has three ring inlets (as modified by Wilson [37]) for the introduction of neutral analyte to the flow tube. One inlet is specifically dedicated for trace gas analysis, while the remaining two are for the introduction of neutral analyte from the glass gas handling lines. The neutral inlet closest to the downstream end is used for determining reaction rate coefficients and has a reaction length of 50.4 cm which includes the 'end correction' for the ring inlet at the flow tube pressure of 0.35 Torr as discussed by Upshulte *et al*. [81]

2.1.3 Ion detection region

Ions are sampled into the downstream high vacuum chamber through a 0.46 mm hole in a molybdenum disk that is positioned in the centre of a nose cone similar in design to the ion extraction nose cone at the end of the flowing afterglow. On entering the downstream chamber, ions are focused into the downstream quadrupole mass filter by an Einzel cluster of electrostatic lenses. After mass separation in the quadrupole mass filter, ions are collected on a DeTech model 203 particle multiplier. Count pulses arising from the particle multiplier are passed to an Advanced Research Instruments Company F-100T preamplifier/discriminator that outputs 30 ns wide TTL pulses. This is connected to a lab card (PCL-812PG) and a home-built counter/ratemeter. The data acquisition has been previously described by Scott [74] and Fairley. [75]

The entire downstream chamber is pumped by two Varian VHS-4 oil diffusion pumps (pumping speed 1500 Ls^{-1} of helium) in parallel, each backed by a Welsh Scientific Company Duo-Seal 1397 two-stage mechanical pump.

2.1.4 Use of FA-SIFT in the current research

Even though the FA-SIFT has an neutral inlet dedicated to trace gas analysis, it is not specifically designed for that application, and has severe shortfalls when doing trace gas analysis work such as a very long start-up time (>3 hours), low overall ion intensity and a cumbersome software interface. Therefore the use of the FA-SIFT in this thesis is limited to the applications where its strengths lie, which are verification and proof of concept in the development of the Voice100 (section 2.2 and chapter 3), and the quantitative understanding of secondary chemistry (chapter 4).

2.2 The Voice100 Selected Ion Flow Tube Mass Spectrometer

2.2.1 An introduction to the Voice100 SIFT-MS

In early 2004, Syft Technologies Ltd. commissioned a new selected ion flow tube mass spectrometer specifically designed for the analysis of trace volatile organic compounds (VOCs). Because the instrument must compete in the commercial market place, the Voice100 was designed to be small and transportable so as to be easily integrated into a standard analytical laboratory environment, sensitive enough to quantitatively measure VOCs at concentrations required by specific target applications (as discussed in chapter 1), and finally be inexpensive such that laboratories might find it competitively priced. By November 2004 the Voice100 was released to the commercial market.

A photograph of the Syft Technologies Voice100 SIFT-MS (here after known as the Voice100) is given as figure 2.03. The instrument weighs approximately 490 kg, and is 1050 mm high by 730 mm wide by 1000 mm deep; the narrow width of the instrument ensures that it can fit through most doorways. The instrument is easily transportable as it sits on heavy duty integrated castor wheels, with lockable screw-down feet to ensure the Voice100 is stable while in operation. Integration into a laboratory environment requires only a pressurised helium and argon supply, and a 240 volt - 50 Hz power supply that is limited to a 15 A fuse.

Figure 2.03. Photograph of the Voice100 SIFT-MS.

A schematic diagram of the Voice100 SIFT-MS is shown as figure 2.04. When directly compared to the FA-SIFT shown in figure 2.01, the major difference is obvious. By bending the reaction flow tube through an 180º arc, the ion detection region is stacked on top of the ion selection region. However there are many more improvements from the FA-SIFT and T-SIFT [39] (Instrument Science Ltd., Cheshire, United Kingdom; discussed in chapter 1) that have enabled the Voice100 to be drastically condensed in size and made substantially more sensitive than either of the previous iterations of SIFT-MS instrument mentioned in this publication.

The Voice100 is modular in design; each section can be easily removed and replaced with minimal effort, ensuring short instrument downtimes. Due to the modular nature of the instrument, the detailed description of the Voice100 will be undertaken in sections closely related to those modules.

A T-SIFT (transportable selected ion flow tube; mentioned above) has been used for some initial and parallel investigations during the course of this research, as a single T-SIFT unit is owned by Syft Technologies. However, no kinetic studies nor instrumental validation studies have been undertaken on the T-SIFT that are reported here. This instrument has not undergone the critical kinetic validation that the Voice100 has (discussed in chapter 3).

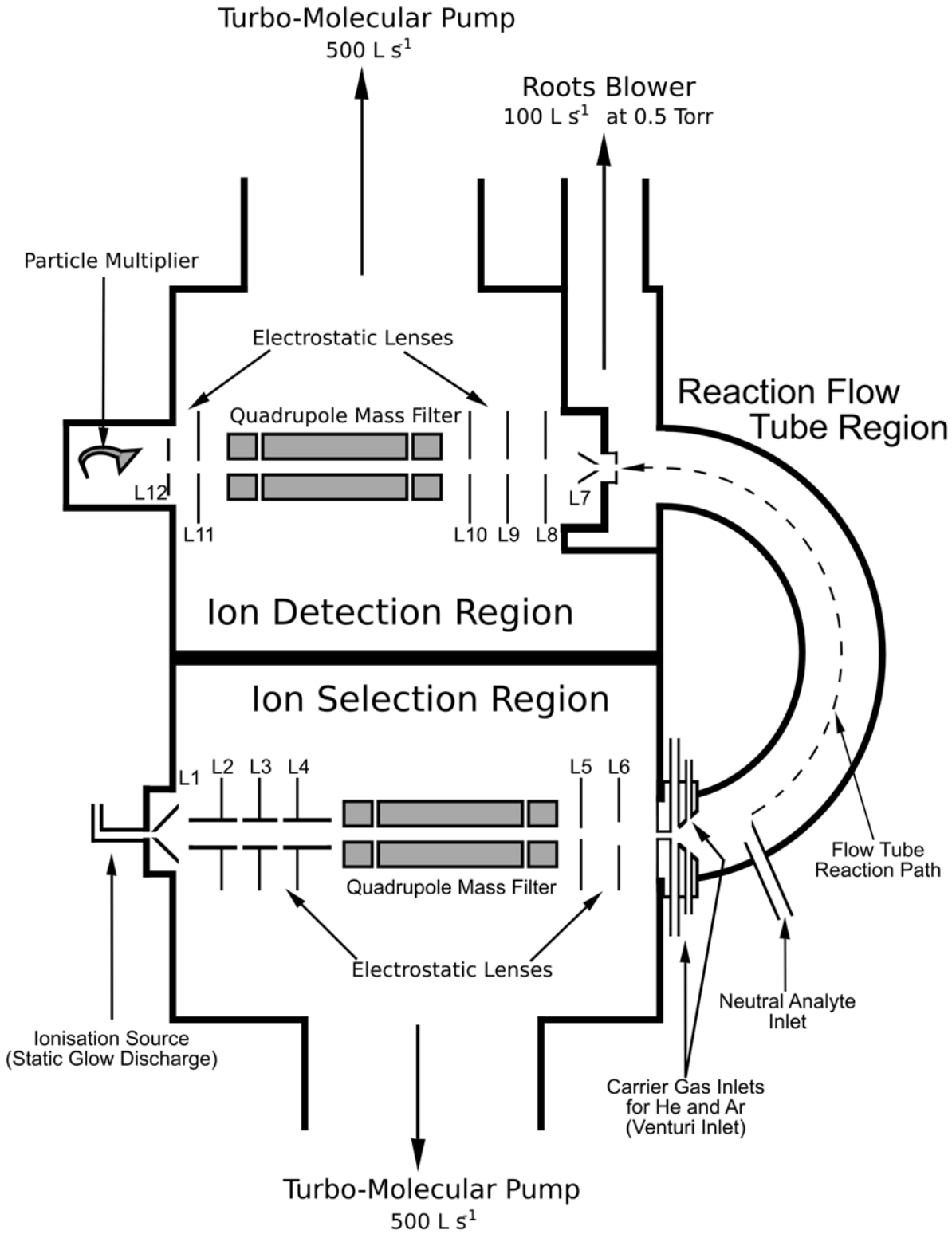

Figure 2.04. Schematic diagram of the Voice100 SIFT-MS.

2.2.2 Microwave ionisation and the static glow discharge source

In a very similar nature to the discussion given by Milligan [76] and mentioned in section 2.1.1, microwave energy is used to create ions in a glow discharge plasma source. [82,83] In the Voice100, a microwave power supply (hand-built by Roberto Zech, Brauna, Germany; http://www.dgOve.de) operating at 2450 MHz and at 50 watts is directly coupled to an Opthos Instruments type 5 (using the definitions of Fehsenfeld *et al.* [79]) microwave discharge cavity (Rockville, MD, USA) that is positioned around a 13 mm outer diameter quartz glass tube which is approximately 80 mm long. The microwave discharge is "lit" by an electrical sparking apparatus, similar to an automotive spark plug and the discharge has been found to light most effectively when the tuning stub is screwed completely down, and the coupling slider is pulled out as far a possible. A photograph of the static glow discharge ion source is shown as figure 2.05.

When tuning a microwave cavity, the reflected power from the cavity (type 5 in this case) is minimised by altering the focus of the microwave energy when the discharge is lit. However, the optimum tuning to light the cavity is different from the optimum tuning for a constant stable microwave discharge in a vacuum system. [84] In principle, the application of microwave power is sufficient for self ignition. However, the cavity is tuned to match the capacitance of the lit plasma that is a different tuning situation to the unlit plasma. Therefore an electrical spark is used to provide electrons that initiate the lighting of the microwave plasma.

The requirement to light the microwave cavity as discussed herein is in contrast to microwave discharge designs used on the T-SIFT of Smith, Spanel and co-workers, which lights automatically due to the positioning of the magnetron, and/or unstable microwave frequencies. [83]

The ionisation source is a static glow discharge. A slow leak of moist air from an air/water reservoir is allowed into the quartz glass tube such that the pressure in the region is approximately 0.3 Torr, as measured on a BOC-Edwards Pirani gauge. The water reservoir is isolated from the quartz tube by a section of bellows tubing, a solenoid valve, and a Swagelock needle valve controlled by an electronically actuated Mdrive stepper motor (John Brooks Ltd., Christchurch, NZ). The air/water reservoir is kept cool by a Peltier heat exchanger, and the tubing, solenoids and needle valve are kept warm with silicon rubber heater wire to avoid the formation of ice crystals in the transfer tubing. A photograph of the ion source assembly and air/water source reservoir is given as figure 2.06.

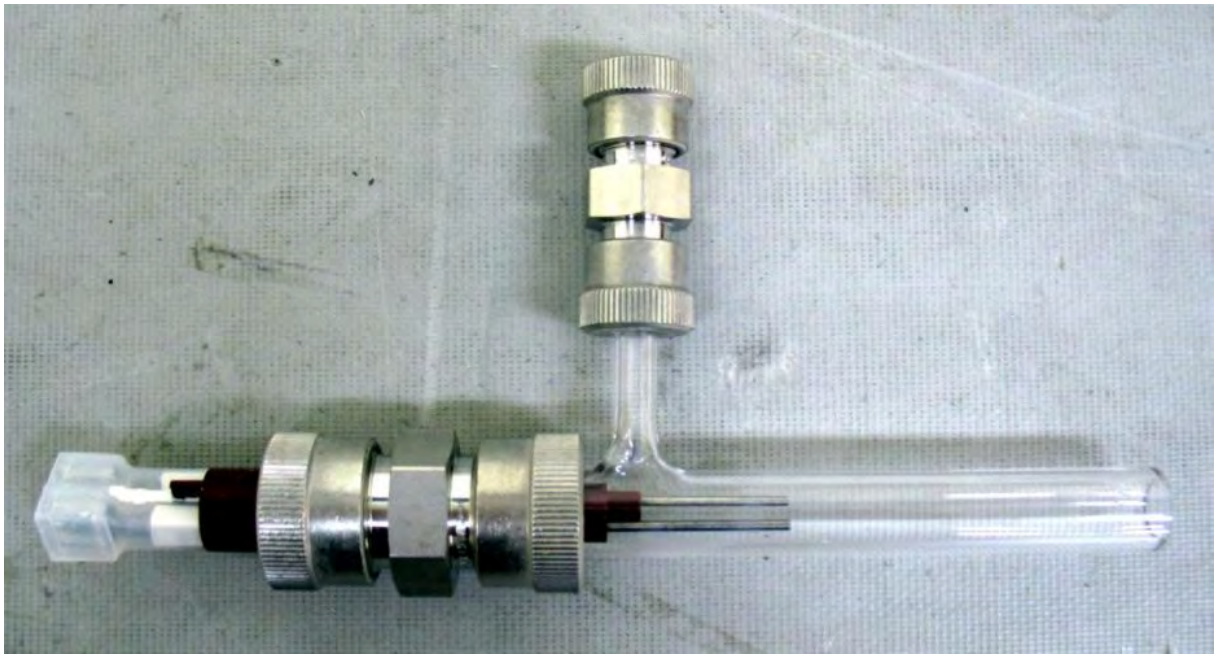

Figure 2.05. Microwave discharge quartz glass tube and igniter.

As the static glow discharge is not a flowing system, ions must be extracted from the plasma using electrostatic potentials and this is achieved by using two lenses in very close proximity. The first lens (L1 – figure 2.04) is the ion extraction lens, that typically is floated to 60 - 70 volts above ground. L1 is 30 mm in diameter, with a 0.8 mm orifice in the centre. Extraction of positive ions through the orifice is accomplished by placing a lens (L2) directly behind, but not touching L1 at a very negative potential (typically -120 volts). This strong negative potential breaks the plasma sheath, and pulls positive ions out of the static plasma. Further discussion of the ion optics will be given in section 2.2.4.

A quartz glass tube containing the microwave discharge is butted directly against the ion extraction lens (lens 1), and held in place by an O-ring and a compression fitting. A Wood's horn glass tube (as discussed in section 2.1.1) cannot be utilised on the Voice100 as the static glow discharge is required to be as close as possible to L1. This is because the motion of the ions in the static plasma is diffusion limited, ion-electron recombination is very fast (in the order of 10^{-6} - 10^{-7} cm^3 $molecule^{-1}$ s^{-1} [12]), and the presence of electrons in the plasma yields ambipolar diffusion. [13] Therefore, the ion intensity will be at its highest at the point where the ions are born and the extractable ion intensity must drop away substantially as the microwave cavity is moved away from the extraction orifice. Because of this decay in ion density with distance from the discharge, the microwave cavity is placed as close to L1 as possible to maximise the ion signal.

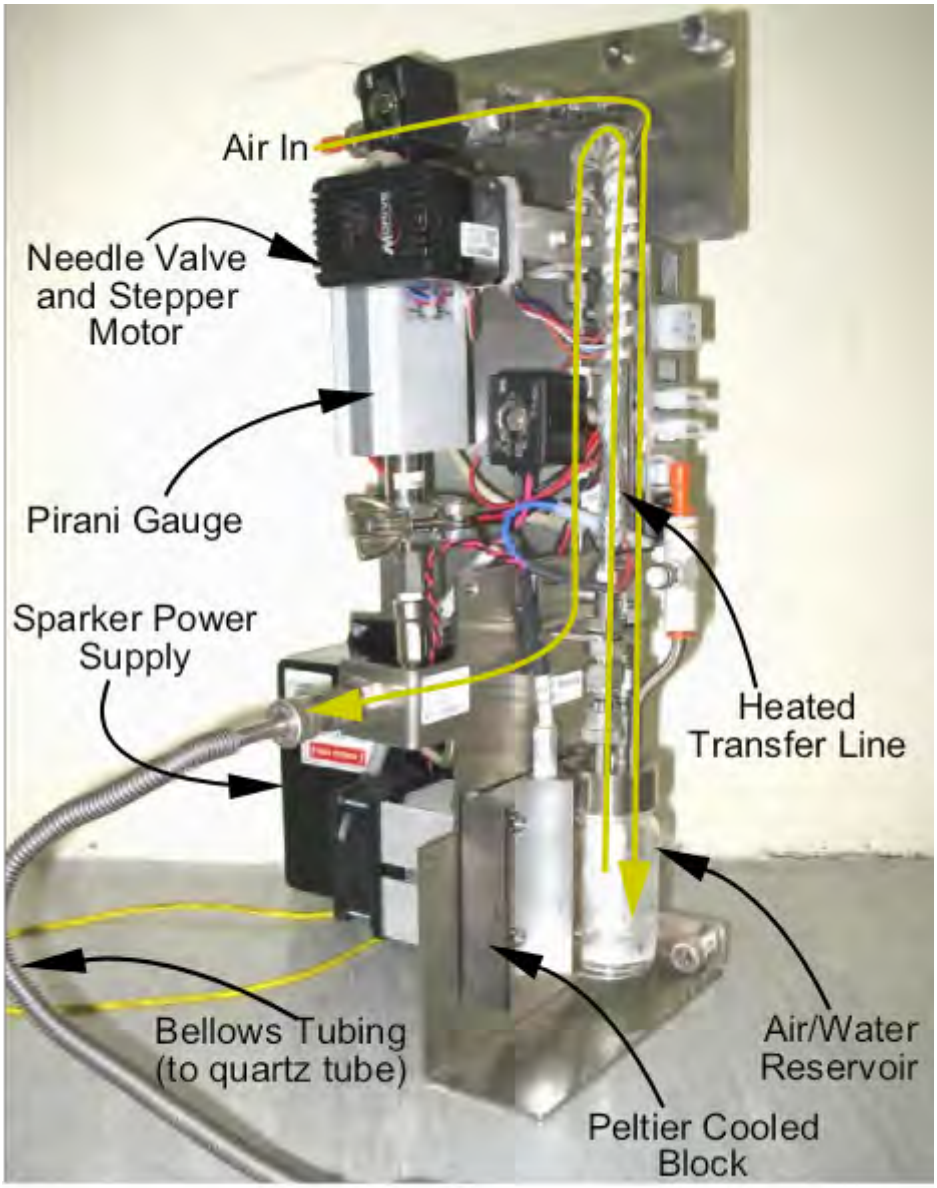

Figure 2.06. Air/water source inlet system.

The entire microwave discharge region is covered by an aluminium shield to minimise any electrical interference that may arise due to microwave radiation.

2.2.3 High vacuum chambers

As already noted, to minimise the footprint of the Voice100, the two high vacuum chambers are stacked vertically with the ion detection (upstream) chamber on top of the ion selection (downstream) chamber. This design feature is obvious from figure 2.04. The entire chamber block is milled from a single piece of aluminium that has overall dimensions of 290

mm x 410 mm x 380 mm, with a wall thickness of approximately 25 mm. The chambers are split by a wall of aluminium (wall thickness of ~25 mm) which separates the chambers into two approximately equal volumes.

Each chamber is individually pumped by a Pfeiffer TMH/U 521 turbo-molecular pump (one per chamber; pumping speed of 500 L s^{-1}), that are both backed by a single BOC-Edwards RV12 roughing pump. BOC Edwards fore-line traps containing activated charcoal have been installed between the turbo pumps and the backing pump to ensure minimal contamination of oil vapour in the detection chamber. Mist filters are placed on the outlet side of the backing pump so that oil vapour is not emitted from the instruments exhaust system. Having said that, the outlet of the instrument is always exhausted to the outside air (or a fume hood) as mist filters are designed for the removal of oil vapour and not toxic organic vapours, that may be emitted from the exhaust of the Voice100.

2.2.4 Ion optics and quadrupole ion filters

The ion optics and quadrupole ion filters for each chamber are housed on cartridge systems. Both high vacuum chambers have a cartridge that is easily removed and interchangeable between different Voice100 instruments. Each cartridge is screwed to the front of the high vacuum chambers by a 12 point flange containing a captured O-ring and both cartridges have two vacuum feed-throughs each, one for the quadrupole power supply, and one for the lens power supplies. As the ion optics on the upstream selection cartridge are slightly different from those on the downstream detection cartridge, an discussion of each individual cartridge is necessary. Specific components of the cartridge assembly are discussed in the next few paragraphs and are shown as figure 2.07.

Ions from the microwave plasma are drawn into the upstream selection chamber by the electrostatic potential difference between lens 1 and lens 2 (L1 and L2) where L1 is the extraction lens with an orifice size (Ø) of 0.8 mm as noted previously. L2, L3 and L4 (Ø = 16 mm) are tube lenses that have potentials applied to them such that they operate as an Einzel cluster (Einzel clusters have been discussed in section 2.1.1). Tube lenses have been installed as the first set of focusing lenses in the Voice100 due to the large fraction of ions entering the upstream chamber from the microwave discharge on divergent trajectories. By increasing the lens area with the use of tube lenses, a more effective set of potentials is applied to the ions, and therefore more effective focusing into the upstream quadrupole ion filter is achieved. However, the use of tube lenses leads to less effective pumping near the ion extraction orifice,

and slightly higher chamber pressures.

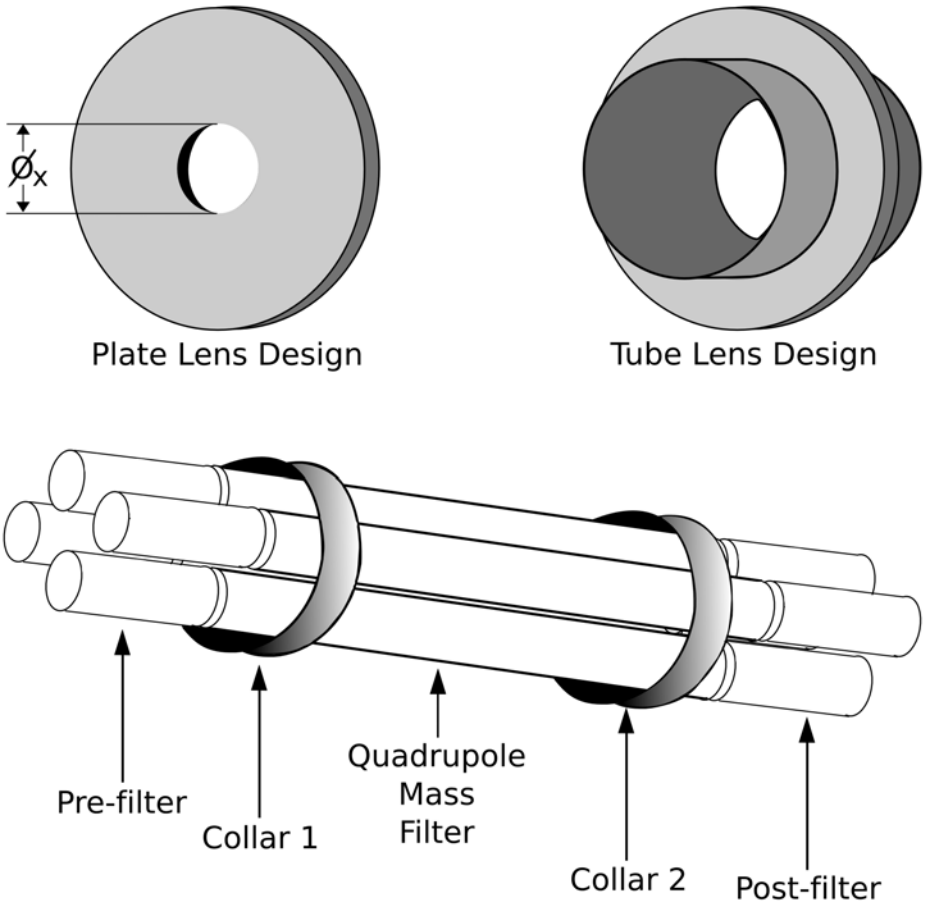

Figure 2.07. Lenses and quadrupole designs.

The upstream quadrupole ion filter (Hiden Analytical Ltd., Warrington, U.K.) used in the Voice100 is 260 mm long and is segmented into three sections: a pre-filter (25 mm long); the actual quadrupole ion filter itself (210 mm); and a post-filter (25 mm). The three segments together shall be referred to as the quadrupole assembly, and the central segment referred to as the quadrupole mass filter. Each of the rods are 12 mm in diameter with a 4 mm rod separation distance. Pre-filters and post-filters flank the quadrupole mass filter to place slightly divergent ions onto stable trajectories as they traverse the RF and DC potentials of the quadrupole mass filter and to allow ions to pass though the quadrupole mass filter's fringing fields with a greater transmission efficiency. [85-87] RF and DC potentials are applied to the 210 mm central segment by a purpose built quadrupole power supply for which the RF is operating at a frequency of 3 MHz giving a mass range of 10 – 70 amu. [88]

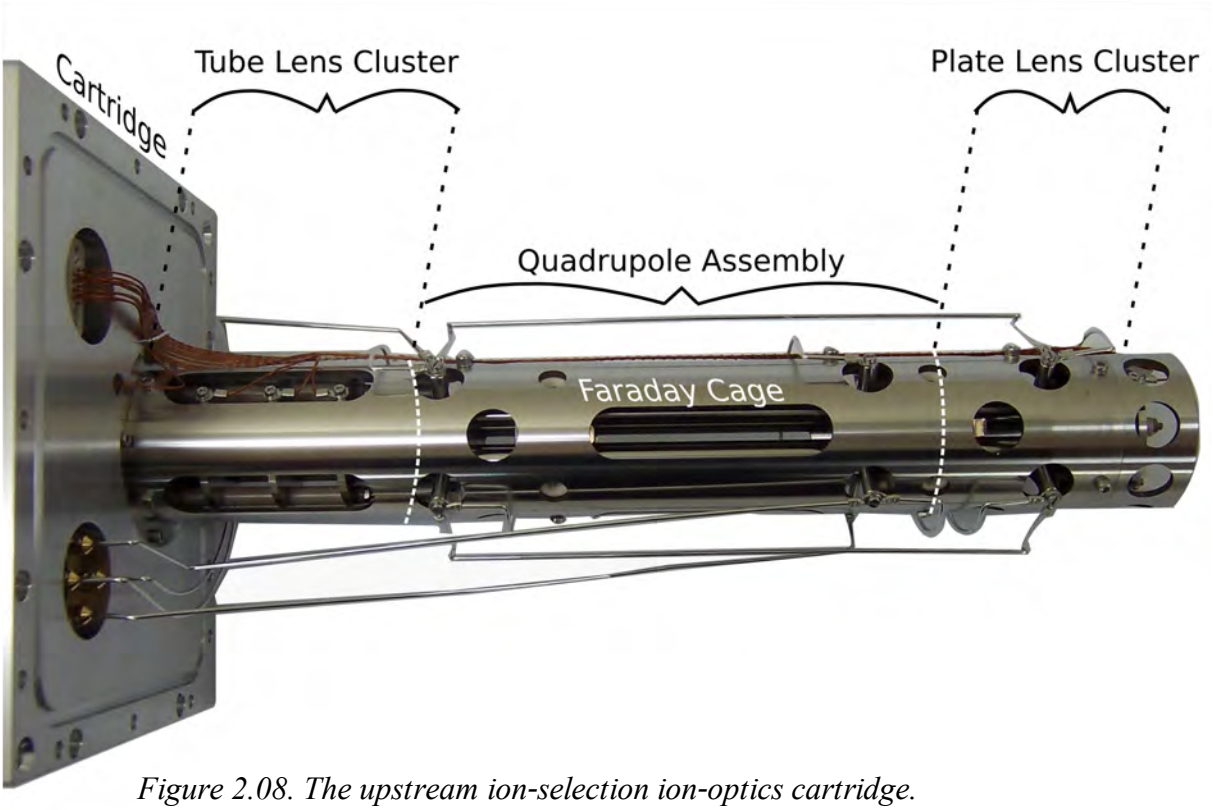

Figure 2.08. The upstream ion-selection ion-optics cartridge.

Only DC bias potentials are directly applied to the pre-filter and post-filter, with an RF potential only reaching each of the outer segments (pre-filter and post-filter) by capacitative coupling from the central segment. A collar at each end of the quadrupole assembly (as can be seen in figure 2.07) secures the assembly to a stainless steel enclosure (acting as a Faraday cage) that is directly bolted to the cartridge wall. An annotated photograph of the upstream ion selection ion optics cartridge is shown as figure 2.08.

Ions exiting the upstream quadrupole assembly are focused through a set of plate lenses (L4, L5 and L6; Ø = 4 mm, 8mm and 8mm respectively) operating in an Einzel configuration, and injected into the flow tube through the Venturi orifice (Ø = 0.8 mm) (discussed in section 2.2.5). Ions that are not focused through the Venturi orifice collide with the orifice plate and a representative ion intensity is measured on this plate in nano-Amperes.

The ion optics of the downstream ion detection cartridge are very similar in nature to those of the upstream ion selection cartridge, with a few subtle differences. Ion sampled from the flow tube through the 'bucket' (see section 2.2.5) are extracted into the ion selection chamber by the potential difference between the extraction orifice and L7 (a truncated cone shaped lens). L8, L9 and L10 are plate lenses (Ø = 8 mm) that are operating as an Einzel cluster and these lenses focus ions into the downstream ion detection quadrupole assembly.

The downstream ion detection quadrupole assembly is identical to the upstream ion selection quadrupole assembly, except the RF frequency is operating at 2 MHz to enable the mass range to be extended to 240 amu. [88]

Ions which exit the post-filter are finally focused by two plate lenses (L11 and L12; Ø = 8 mm) into an DeTech 2401C off axis continuous dynode particle multiplier that is biased between 1.8 and 4 kV below ground by an Applied Kilovolts (West Sussex, UK) high voltage power supply. A purpose-built pulse counter/discriminator converts and amplifies the ECL pulses from the particle multiplier into TTL pulses that are counted by a second purpose-built module.

2.2.5 Reaction flow tube region

The novel aspect of the Voice100 is its bent reaction flow tube. The flow tube is machined as a single stainless steel tube, that has an internal diameter of 48 mm; each end is connected to the chamber block by rotatable Conflat™ flanges. The outer edge of the tube has an arc radius of 120 mm, and is bent in a half circle as can be seen in figure 2.04.

Ions enter the flow tube through a Venturi orifice similar in design to that discussed in section 2.1.2, with a few minor modifications. Helium is introduced on an annular slit inlet, that is 2 mm outside the ion orifice, commonly at a flow of 15 Torr L s^{-1} to create the Venturi effect. An annular slot has been used as it gives less dissociation of ions upon injection when compared to a hole type injector. [22] Argon is added to the flow tube commonly at 25 Torr L s^{-1} through an inlet ~20 mm outside the ion orifice which is not an annular slit, but a series of holes drilled in a circle on the Venturi plate that surround the inner annulus. A hole type inlet was found by Fishman and Grabowski [21] to be almost as effective as an annulus, but obviously substantially easier to construct. The block upon which the Venturi plates are mounted is machined from polyethyl ether ketone (PEEK), and the Venturi plates are machined from stainless steel.

The only neutral analyte inlet into the flow tube is positioned 60 mm downstream of the Venturi orifice and 258 mm from the downstream sampling orifice, and is a simple upstream-facing finger inlet. Gases are removed from the flow tube by a BOC-Edwards EH 500 roots blower (pumping speed 140 L s^{-1} at 0.5 Torr of air) that is backed on by an E2M 28 backing pump (pumping speed 94 L s^{-1}). A quarter swing butterfly valve (Valvcon, Millford, NH, USA) separates the roots blower from the flow tube. These pumping speeds and the afore mentioned flows of helium and argon lead to a measured flow tube pressure of approximately

0.5 Torr, a Knudsen number of less than 10^{-9}, and using the simple method outlined by Ferguson *et al.*, [5] the Reynolds number is found to be ~135 for both helium and argon buffer gases. These parameters determine that the carrier gases in the Voice100 flow tube can be modelled by fluid dynamics, and the velocity profile leads to laminar flow (a parabolic velocity profile). [89]

Ferguson *et al.* [5] also published the distance required for a buffer gas to fully develop a laminar velocity profile, that is based on the Reynolds number and the radius of the flow tube. For the Voice100 this distance is found to be 80 cm, which is approximately 2.5 times longer than the entire flow tube. Therefore it must be concluded that during the reaction length of the flow tube, a laminar velocity profile is never fully developed. However, the Voice100 is not a turbulent flow tube (TFT) of the nature developed by Molina and co-workers [90,91] as the Reynolds number of the Voice100 flow tube is substantially lower than that reported for the TFT (R ~2000).

Also, as the Voice100 flow tube has a mixture of two carrier gases, there must be an effective mixing distance from the Venturi where the two carrier gases are evenly mixed. Due to the complexity of the system, no method of determining the length for effective mixing of helium and argon could be found in the literature, but it must be assumed that eddies, shock cells and mixing effects may differ between instruments and Venturi designs, and therefore direct measurement of the end correction becomes a very important parameter. For most kinetic measurements undertaken in this thesis, the end correction was found to be -28 mm (a decrease in reaction length) and therefore the actual reaction length was found to be 230 mm. When combined with the undeveloped laminar velocity profile, the Voice100 flow tube is found to be a very complex difficult system. A more in-depth review of the Voice100 flow tube will be given in chapter 3, including discussion of ion flight times, and ionic diffusion in mixed carrier gases.

Due to the difficulty in machining a 'nose cone', which is the preferred design used in the FA-SIFT, the Voice100 has a simple 'bucket' design from which ions are sampled on exiting the flow tube. On the leading flat surface of the bucket the ion extraction orifice is mounted and samples ions into the downstream ion detection chamber. Ions that are not sampled through the orifice collide with the disk (outer diameter 20 mm) and are collected as an ion current using a pico-ammeter.

2.2.6 Sample inlet system

As the primary task of the Voice100 is the detection of gas phase analytes in whole air

samples, the efficiency of introduction of neutral species into the instrument is of critical importance. By ensuring that the analytes are transported effectively from the sample (tedlar bag, headspace vial etc.) to the flow tube at an appreciable flow rate, with minimal absorption to the tubing walls, better limits of detection can be achieved.

The sample inlet system used across the course of this thesis is a Voice100 sample inlet module slightly modified for kinetics measurements and minimisation of dead space; a schematic drawing of the sample inlet system is given as figure 2.09.

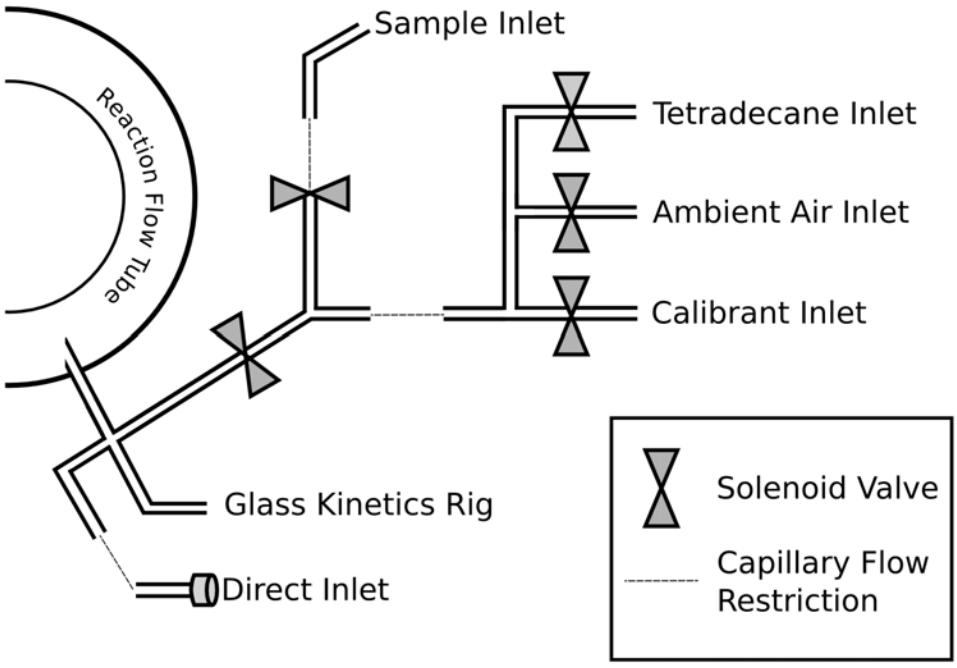

Figure 2.09. Modified Voice100 sample inlet system.

Four inlets are available on a standard commercial Voice100 instrument that are the sample inlet, the tetradecane inlet, the ambient air inlet and the calibrant inlet. The standard Voice100 sample inlet system has multiple inlets to allow the instrument to perform automated sequential tasks without any intervention by the user. In addition to the four standard inlets, two additional "short path" inlets (glass kinetics rig inlet and direct inlet) have been added to the Voice100 that was used for the majority of the research presented here. A short description of the uses and operational characteristics of each inlet shall now be given.

- **The sample inlet** is positioned on the front of the instrument above the LCD display (see figure 2.03) and is used for the addition of all standard samples to the flow tube. These standard samples include, but are not limited to, tedlar bags, headspace vials, direct breath samples, ambient air samples, third party thermal desorbers and

permeation ovens. The flow through the sample inlet is governed by its own capillary that has a flow rate of approximately 150 ml min^{-1}.

- **The tetradecane inlet** is designed to allow a flow of tetradecane vapour, that is stored in a removable reservoir on the instrument, into the reaction flow tube for calibration of the downstream ion selection quadrupole mass scan line. Both the solenoid and tetradecane reservoir are mounted on the inlet manifold. The flow is restricted by a capillary common to the tetradecane inlet, the ambient air inlet and the calibrant inlet that has flow rate of approximately 150 ml min^{-1}.
- **The ambient air inlet** allows room air, collected at the back of the instrument, into the flow tube for the measurement of an ambient air background. Ambient air backgrounds are important for removing the effects of an instrument's mass dependent chemical background i.e. the number of counts per second detectable at a specific mass when no analyte is being added to the flow tube.
- **The calibrant inlet** allows for the addition of a specific calibrant gas to the Voice100 flow tube. This calibrant gas is commonly a mix of benzene, toluene and xylene isomers at known concentrations that verify the instrument's ability to accurately quantify gas phase analytes. The calibrant inlet is mounted on the rear of the instrument.
- **The glass kinetics rig inlet** is a short path inlet with no flow restriction that is connected directly to glass gas handling line that will be discussed in section 2.5.1 - ancillary systems.
- **The direct inlet** is a short path inlet which has less than 1 ml of dead space between the sample inlet and the flow tube. The direct inlet has no solenoid valve, only a stainless steel Swagelock® cap, and is therefore only opened when the roots blower is pumping the flow tube. A capillary or high accuracy needle valve has been used on the direct inlet to restrict the flow of analyte entering the flow tube. The direct inlet is commonly used when very low detection limits are required and memory effects must be minimised, as the amount of analyte absorption to the walls of the short path inlet is very small.

All inlets are heated by silicon rubber heater wire powered by a purposed-built power supply and thermostat, and are normally held between 80 °C and 160 °C. All heater wire is covered by fibre glass insulation and sealed using fibre glass tape.

2.3 Data Acquisition and Analysis

The software packaged with the Voice100 is commercial software written by the software team at Syft Technologies. As this is a commercial product, only a very short overview of the important sections of the software pertaining to the current research will be given. However, a more detailed description of the kinetic data acquisition software written by Dr. Barry Prince and myself using the LabVIEW™ package will then be given.

2.3.1 Syft Technologies Voice100 control application and firmware

The commercial software packaged with a Voice100 operates in two stages, the firmware that is stored in flash memory on the instrument, and the control application that is stored on a PC. The instrument is connected to the PC running the control application by an ethernet cable that is either running in cross-over mode, or through a network. Control voltages are fed from the control application to the firmware which directly operates the hardware in the instrument.

The control application is the main interface for most users, that controls the operation of the instrument. From a completely "off" state (with the instrument plugged in to mains power) the control application takes the Voice100 to a state where mass spectra are run, then runs the specific mass spectra, and finally, acquires and outputs the data. Any ion optic parameter such as the lens voltages and quadrupole mass filter mass-dependent control voltages are altered from within the control application, and ion signal feedbacks (electrometer currents, detector counts per second) are read from within the control application. The control software can measure mass spectra in two ways, as a mass scan which is a plot of the ion signal versus m/z ratio, or as a selected ion monitoring scan (SIM scan). In SIM mode, only the ions of interest are scanned to give a plot of the selected ion intensity versus time. When both the reagent ions and the expected product ions of a specific well understood reaction are monitored in SIM mode, the output can be given as a concentration in parts-per-billion-by-volume (ppbv).

2.3.2 Kinetic data acquisition software and hardware

Using the LabVIEW™ (National Instruments, Austin TX, USA) visual programming package, specific software has been written to measure mass spectra and kinetic decay rates by controlling the downstream quadrupole mass filter, and monitoring the detector counts per

second through an external DAQ board. The external DAQ board also reads in an analogue input for the 2 Torr differential Baratron.

Mass scans are measured by controlling only the downstream quadrupole control voltages (that are fed into the quadrupole power supply) and measuring the signal returned from the counter/discriminator. Quadrupole scan line parameters (RF and DC mass dependent control voltage slopes and intercepts) are variable so that peak resolution, and mass position can be easily altered. All other remaining instrument parameters are controlled from the Syft control application.

Kinetic decay rates and therefore the measurement of rate coefficients is attained by running a SIM type scan (as mentioned in section 2.3.1) while monitoring the differential Baratron for a specific flow. The SIM scan is run by controlling the downstream ion detection quadrupole from the LabVIEW software, and the remaining parameters from the Syft control software. The display screen of the computer running LabVIEW is divided into two columns each with two sections: the left column contains the raw data acquisition panels, the SIM scan panel and the differential Baratron flow determination panel; while the flow tube parameter panel and finally the kinetic decay panel are on the right. Every point that is measured and deemed to be acceptable can be moved from the left column into the kinetic decay plot. Through an understanding of the reaction time (calculated from the flow tube parameters panel) and the slope of the kinetic decay plot, the software gives a rate coefficient based on all data collected for a specific reaction.

The screen capture of the LabVIEW kinetic acquisition software is given in figure 2.10, where each of the four sections are colour coded: the raw data is given in yellow, the average analyte flow in green, the flow tube parameters in blue, and the rate coefficient in red.

An output of the raw data, which is given in a comma separated values file, must be read into a spreadsheet package (such as Microsoft Excel) to be able to attain the product ion branching ratios and uncertainties due to scatter in the kinetic decay plots.

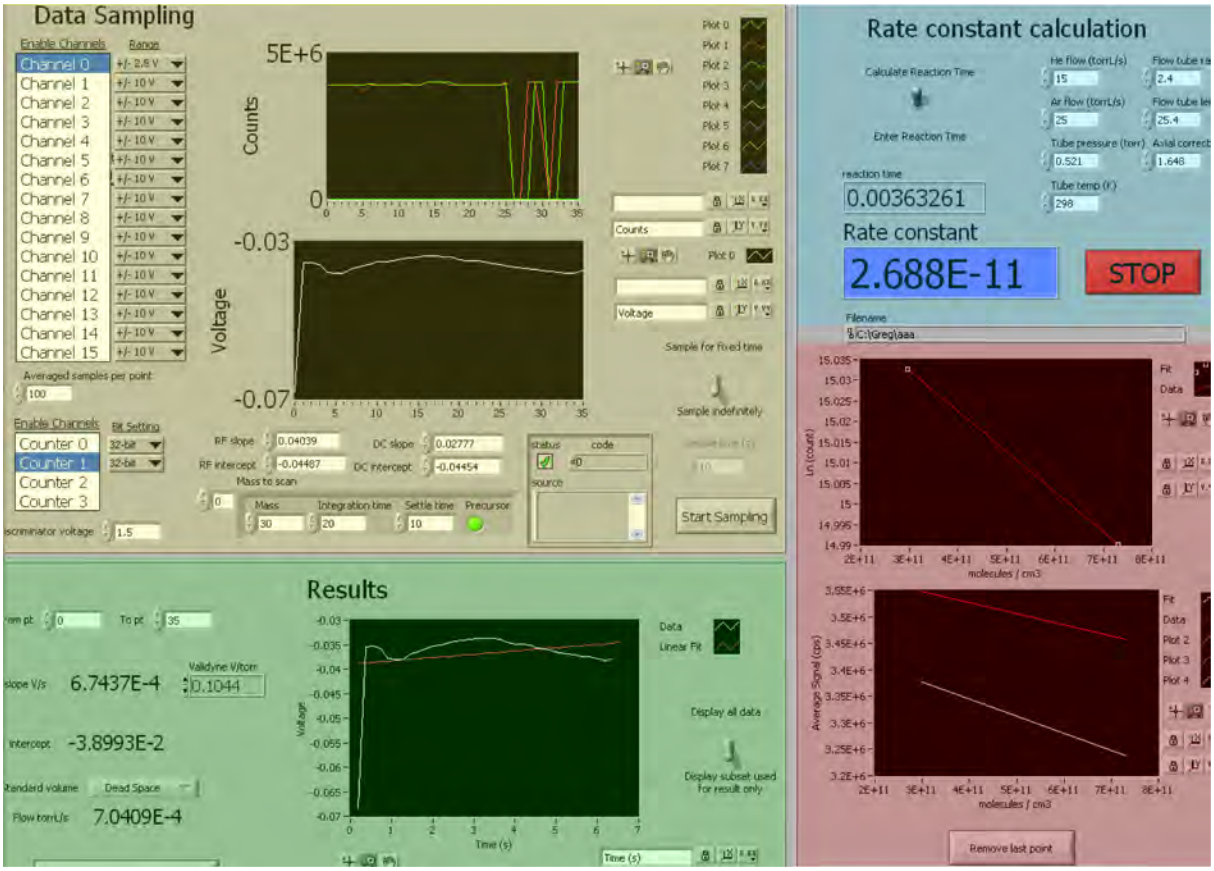

Figure 2.10. A colour coded screen capture of the LabVIEW kinetic acquisition software. Colour codes are discussed in the text.

2.4 Voice100 Standard Operating Conditions and Currents

2.4.1 Operating pressures

Given below in table 2.01 are a series of pressures usually found in the Voice100 instrument used in the majority of this research. These pressures are given with and without the carrier gases flowing, and are based on readings from active inverted magnetron (AIM) gauges (BOC-Edwards) in the two high vacuum chambers, a Pirani gauge (BOC-Edwards) in the microwave discharge region and a 2 Torr absolute Baratron (MKS Instruments) in the flow tube. All pressures are measured after allowing the instrument a sufficient 'pump-down' period (~ 30 minutes). The pump-down period allows the turbo-molecular pumps to reach full speed, and to remove solvents that may be absorbed to metal surfaces inside the instrument. The pump-down period of a Voice100 is substantially shorter than the 2-4 hours required for the FA-SIFT.

Table 2.01. Common operating pressures in the Voice100

Region	Without He or Ar flowing	With He and Ar flowing
Microwave Discharge	*0.3 Torr*	*0.3 Torr*
Ion Selection Chamber	*2×10^{-5} Torr*	*3×10^{-5} Torr*
Reaction Flow Tube	*$< 1 \times 10^{-3}$ Torr*	*0.5 Torr*
Ion Detection Chamber	*5×10^{-7} Torr*	*2×10^{-5} Torr*

2.4.2 Ion currents and detector signals

Ion currents and detector ion signals for each precsursor ion (H_3O^+, NO^+ and O_2^+) when no analyte is entering the flow tube are given in table 2.02. Ion currents that are measured at the sample inlet are collected on a circular disk (10 mm diameter) connected to a probe that is inserted into the flow tube through the sample inlet port. The probe is electrically isolated from the flow tube. The collection of ion currents on the Venturi orifice and sampling orifice are discussed in sections 2.2.4 and 2.2.5. The detector ion signals are measured when the downstream ion selection quadrupole resolution has a full width at half height of 0.7 amu.

Table 2.02. Ion currents and detector ion signals for the Voice100 at standard operating conditions.

Precursor Ion	Venturi Orifice	Sample Inlet	Sampling Orifice	Detector
H_3O^+	*12 nA*	*1.5 nA*	*45 pA*	*500,000 cps*
NO^+	*20 nA*	*2 nA*	*50 pA*	*800,000 cps*
O_2^+	*13 nA*	*1.5 nA*	*45 pA*	*600,000 cps*

2.5 Ancillary Systems

2.5.1 Glass gas handling line

The glass gas handling line or “kinetics rig” is a miniaturised semi-portable gas handling line similar to one of the three inlet manifolds shown in Dr. Milligan's thesis. [76] This glass gas handling line is designed to allow a controlled measurable *absolute* flow of analyte into the Voice100, as opposed to the other five sample inlets where analyte mixtures, and air samples are introduced. The system is evacuated by a BOC-Edwards RV12 backing

pump that is in series with a liquid nitrogen trap ensuring that no corrosive vapours enter the pump, and lowering the absolute pressure of the gas handling line by cryo-pumping.

Two types of gas taps are used in the gas handling line, these are Youngs (Acton, England) or BSG (Australia) taps. Youngs taps are teflon seated and therefore absorb far less vapour than the rubber O-ring seated BSG taps, however the BSG taps are much easier to source at much lower cost. A schematic representation of the gas handling line is shown in figure 2.11

Only one gas storage bulb can be connected to the line at any one time via the B14 fitting directly above the liquid nitrogen trap. Absolute pressures in the line are measured by a 10 Torr absolute Baratron with a home-built power supply. A similar supply is used to power the 2 Torr differential Baratron used for measuring the flow rates of analytes into the flow tube.

Often, an analyte held in the glass handling line is required to be accurately diluted in dry nitrogen or helium such that lower number densities of analyte can be easily introduced into the flow tube. Because the glass gas handling line only has one B14 fitting, dry nitrogen or helium is usually stored in the 10 litre calibrated volume. NO is stored in the 5 litre calibrated volume for measuring the reaction of $O_2^{\bullet+}$ + NO, that is discussed below.

As the line is semi-portable, it was moved to the University of Canterbury and connected to the FA-SIFT to verify that rate coefficients measured on the glass gas handling line correlated with values measured using the standard gas handling apparatus. [76] Rate coefficients measured on the semi-portable glass gas handling line for the well understood Ar^+ + O_2 reaction [55] were found be within the accepted uncertainty (± 15%) of the measurement undertaken using the standard FA-SIFT gas handling apparatus (4.6 x 10^{-11} cm^3 $molecule^{-1}$ s^{-1}). Both measured rates fell well inside the literature value for this reaction. [55]

The measurement of the rate coefficients of the water cluster ions is enabled by flowing water vapour into the flow tube through a tee that is upstream of the 'glass kinetics rig inlet' (figure 2.09). The water vapour is generated in a glass bubbler, and controlled by a 5 cm^3 min^{-1} at 0 ºC (a parameter commonly referred to as SCCM) MKS mass flow controller. A more in-depth discussion of water cluster rate coefficient measurement will be given in chapter 3.

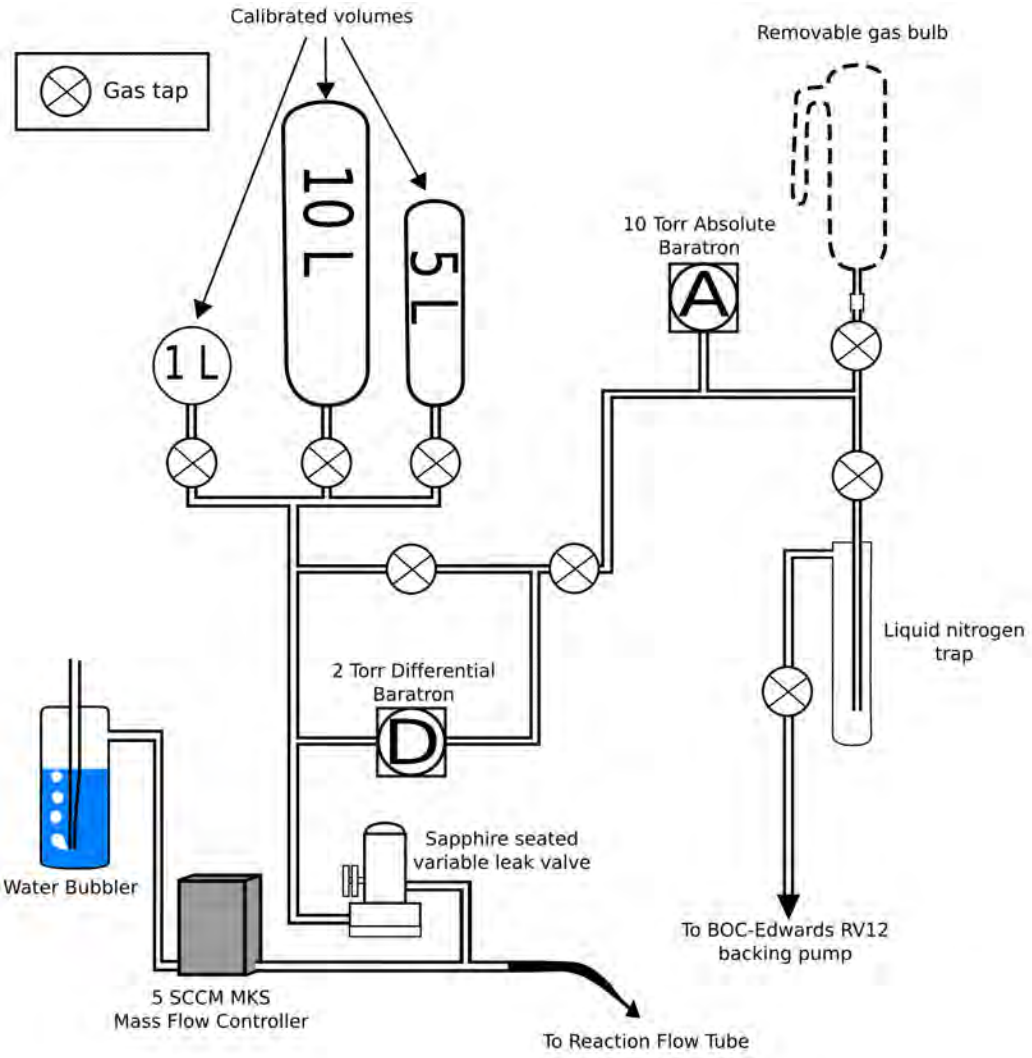

Figure 2.11. A schematic diagram of the semi-portable glass gas handling line.

2.5.2 Permeation apparatus

As SIFT-MS is an inherently quantitative technique, it is beneficial to create accurate dynamic dilutions in the low parts-per-million-by-volume range and for this a permeation apparatus is generally used. This apparatus consists of a highly accurate temperature controlled oven (VICI Metronics, Poulsbo, WA, USA) and a permeation tube which contains the analyte of interest. A permeation tube is a length of Teflon™ pipe sealed at each each end and filled with liquid analyte. By measuring the drop in mass of the tube over a several week period, a permeation rate at a specific temperature in ng min^{-1} is determined. [92] Then by placing the permeation tube in the high accuracy oven and flowing a measured flow of nitrogen over the tube, a gas phase equilibrium is established, and a constant stable gas phase

concentration is created. The equation for calculating a concentration from a permeation apparatus is given as equation 2.01 where C is the concentration in ppmv, M_W is the molecular mass in g mol^{-1}, F_C is the gas flow in cm^3 min^{-1} at 298 K and 25.5 is the molar volume at reference conditions. [93,94]

$$C = P\frac{\left(25.5 / M_W\right)}{F_C} \tag{2.01}$$

2.6 Methods of Measuring Rate Coefficients

During chapter 1, a discussion of the theory regarding the measurement of rate coefficients and product ion branching ratios was given. This section will discuss the physical aspects of measuring rate coefficients on the Voice100, although the methods given in this section are applicable to all selected ion flow tube instrumentation. All methods used for the measurement of rate coefficients and product ion branching ratios in this research are flow based methods (as opposed to the reaction length based methods used by Grabowski and co-workers in Pittsburgh [21,95]) and only the measurement or dilution of the flow varies between methods. Such that for the hypothetical reaction $A^+ + B \rightarrow C^+ + D$, the variation of the flow tube number density of B is required.

2.6.1 Absolute rate coefficient measurement

As the name suggests, absolute rate coefficients require the measurement of the absolute flow of analyte entering the flow tube in units of molecules cm^{-3}. This type of method has classically been the method of choice used on the University of Canterbury selected ion flow tube instruments. Using the apparatus given in figure 2.10, an absolute flow of reactant molecules is measured by first setting the sapphire-seated variable leak valve to a specific flow, and measuring a pressure drop across the differential Baratron for a known volume. Neutral analyte flows are determined in Torr L s^{-1}, that are converted to molecules cm^{-3} by the relationship shown as equation 2.02, where *[A]* is the concentration of analyte in the flow tube (molecules cm^{-3}), Φ_A and Φ_C are the flows of the neutral analyte and flow tube carrier gas respectively in Torr L s^{-1}, p_g is the pressure in the flow tube in Torr, k_B is Boltzmann's constant, T is temperature (K) and 1.33x10^{-4} Torr cm^3 Pa^{-1} m^{-3} is the unit conversion factor.

$$[A]=\frac{\Phi_A}{\Phi_A+\Phi_C}\frac{p_g}{k_B T}1.33\text{x}10^{-4} \qquad (2.02)$$

The kinetics of the reaction between H_3O^+ + CH_3OH was used to verify the flow tube kinetics of the Voice100 and is given as figure 2.12. A further discussion of the verification of the flow tube is given in chapter 3.

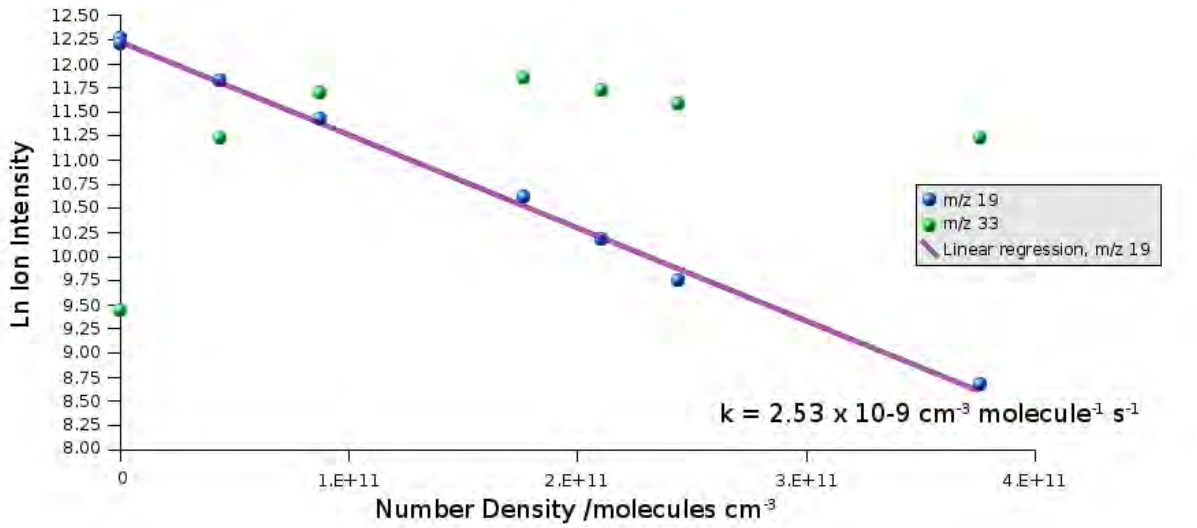

Figure 2.12. An example of an H_3O^+ + CH_3OH kinetic decay measured on a Voice100 by varying the absolute analyte flow.

2.6.2 Relative rate coefficient measurement

Where proton transfer is known to be exothermic, the reaction will always be found to occur with unit efficiency. [61] Therefore, an excellent estimation of the empirical rate coefficient for a exothermic proton transfer reaction can be made by calculating a collision rate coefficient (methods for determining an H_3O^+ collision rate coefficient will be discussed in section 2.8). Other rate coefficients for non-proton transfer processes (such as association or electron transfer) can then be determined by measuring that reaction simultaneously with a proton transfer reaction.

In this research, some NO^+ and O_2^+ rate coefficients have been measured simultaneously with an H_3O^+ proton transfer reaction. The method of 'relative rates' involves placing a neat sample of the reactant analyte in a Tedlar™ bag filled with nitrogen and flowing the headspace of the sample into the Voice100 instrument where the reactions of

H_3O^+, NO^+ and O_2^+ are monitored simultaneously by rapidly switching the upstream ion selection quadrupole mass filter. Serial dilutions of the sample in the Tedlar™ bag are then measured to ensure linearity, and from a plot of the relative dilution against $ln[A^+]$ a set of relative rate coefficients are determined. The use of this method does not require the measurement of an absolute flow, that is useful when the volatility of an analyte is very low (less than 2 Torr partial vapour pressure).

2.6.3 Permeation apparatus rate coefficient measurement

As a permeation apparatus (discussed in section 2.5.2) creates a dynamic dilution at an accurate concentration (normally quoted to be ± 10%), the number density of analyte in the flow tube can be easily determined from equation 2.02. However the drop in precursor ion intensity will often be very small due to the low analyte concentration entering the flow tube and this results in less removal of the reactant ion, and therefore more difficulty in solving equation 1.06 (first discussed by Spanel and Smith [1]) for *k*, the rate coefficient. As the permeation oven requires a long equilibration time and offers little advantage over either of the above two methods, the permeation apparatus has been only used for rate coefficient determination where it was absolutely necessary. The method also requires knowledge of an instruments mass discrimination factor, and this parameter will be addressed in chapter 3.

2.7 Carrier Gases and Reagents

Both helium and argon carrier gases have been sourced from Southern Gas Limited. Each has a stated purity of 99.9995% and were the carrier gases for all experiments in this work and were used without purification. Reagents that were used in a particular experimental section are discussed in the appropriate chapter of this thesis.

2.8 Ab Initio and Density Functional Theory Calculations

To complement the experimental research described herein, a number of ab initio and density functional theory calculations have been performed on specific systems for two reasons: to attempt to understand the mechanism of the reaction and to accurately determine the dipole moment and polarisability of a neutral analyte. For mechanistic understanding, a range of accurate energy methods have been used to examine the geometries and energetics of both ions and neutrals across a potential energy surface, such as the complete basis set (CBS)

methods of Petersson and co-workers [96-98] and the Gaussian compound methods. [99-106] Further details regarding mechanistic investigations are given in the appropriate chapter.

The methods of determining collision limiting rate coefficients used in the current research [107,108] require the knowledge of dipole moments and polarisabilities. Where literature values of these are unknown they have been calculated to the B3LYP density functional level of theory normally using the 6-311+G(d,p) basis set. Specific details of theory and basis set for each neutral analyte are given in the relevant chapter.

All calculations have been made using the Gaussian 03W quantum chemical package [109] using a 2.80 GHz Pentium 4 with 2 GB of RAM.

CHAPTER 3

INSTRUMENTAL VERIFICATION

The obvious major differences between the Voice100 and the previous versions of the selected ion flow tube (SIFT) instruments used by the University of Canterbury research group are the size, the bending of the flow tube through an 180 degree arc and the addition of argon to carrier gas. The large university based research instruments, have been reduced to a substantially smaller size through advances in engineering and pumping technology (as discussed in chapters 1 and 2). The Voice100 has a bent flow tube, however, this instrument is not the first selected ion flow tube instrument to have a bend in the flow tube. Although not shown in figure 2.01, the UoC FA-SIFT's (University of Canterbury flowing afterglow – selected ion flow tube) flow tube has two opposing 45° bends just after the Venturi orifice to enable two co-linear ion sources to be connected to the flow tube at the same time. [73] Due to the length of the UoC FA-SIFT tube, these bends are substantially far enough removed from the reaction region that they will cause little effect and will not alter the laminar velocity profile. In comparison, the Voice100 is the first SIFT instrument in the literature that has a bend in the reaction region. Also, argon has been added to the flow tube along with the helium. This addition has been made to minimise the effect of radial diffusion upon the ions that are transiting through the flow tube.

The instrumentation associated with the SIFT technique has undergone very little technological evolution since the first papers were published in the mid 1970's by Smith and Adams. [10,14] Furthermore, the size and carrier gases used in the flow tube of a SIFT instrument are very similar to those of the flow afterglow technique, that was first published in 1966. [6] Since these initial publications, few article have been published containing research into the performance of the SIFT flow tube. And those papers that have been published mainly focus on the performance of the SIFT venturi orifice. [22,81] It is therefore apparent that as the Voice100 contains substantial alterations to both the size and shape of the flow tube, and the carrier gases used in the flow tube, a verification of the performance must be undertaken.

As the SIFT-MS technique relies on a deep fundamental understanding of the ion-molecule chemistry occurring in the flow tube, the hydrodynamics of the flow tube must

first be very well characterised. [5] Therefore, with the changes to the flow tube reaction region design and carrier gas composition, a characterisation of the Voice100 flow tube hydrodynamics must first be undertaken. This chapter will first outline three important points regarding the verification of the Voice100. These are, the advantageous characteristics of adding argon to a flow tube, performance characteristics of the Voice100 flow tube's laminar velocity profile and a new method for measuring a mass dependent radial diffusion enhancement factor. Then finally, this chapter will discuss methods for resolving rate coefficients from reactions involving hydronium ion water clusters and neutral molecules in an excess of water vapour.

3.1 Mixing Carrier Gases – Addition of Argon

In the majority of selected ion flow tubes in use today, helium is the flow tube carrier gas of choice because it will not react with with any ionised species present due to its very high ionisation potential (24.1 eV [30]) and because helium atoms are strongly non-polarisable. A result of these characteristics is that interactions with energetic species near the Venturi orifice do not often lead to fragmentation or ionisation of the carrier gas. Because helium is a common carrier gas for measuring reaction rate coefficients, the majority of research into flow tube laminar velocity profiles and diffusion characteristics have also been based around helium flow tubes. [110] Helium is a useful carrier gas for academic research, but has two severe drawbacks: it is expensive and it allows for a large degree of radial diffusion. [75]

The SIFT technique requires a Venturi orifice to allow the flow tube to operate at a higher pressure than the upstream ion selection chamber. Because of the Venturi effect, ions that have been selected by the upstream quadrupole assembly (discussed in chapter 2) can be injected against the pressure gradient into the flow tube. However, ions that are entering the flow tube must do so at the lowest possible energy to ensure that fragmentation does not occur on injection.

Radial diffusion (discussed further in section 3.3) is defined as the diffusive motion of ions from the tube axis towards the walls of a flow tube. [111] As only ions from the centre of the flow tube (on-axis) are sampled into the downstream ion selection chamber, it is obvious that when there is a large degree of radial diffusion, fewer ions are available on axis for sampling. Also, when ions collide with the walls of the flow tube they are neutralised. The

radial diffusion of an ion through a carrier gas is known to be inversely proportional to the average collision cross section of the ion-carrier gas pair, [111] therefore by using a carrier gas that has a larger Van der Waal's radius than helium, the radial diffusion of an ion should decrease.

However, in a selected ion flow tube instrument, ions that enter the flow tube from the upstream ion selection chamber are often internally excited and collisions of these “hot” ions with larger more polarisable particles such as N_2 or Ar leads to greater ion fragmentation on injection when compared to helium. The observed excitation occurs either by acceleration of the ions through the upstream chamber (which can be minimised through a judicious choice of ion optic settings) or internal excitation occurring when the ions are borne in the microwave plasma.

The initial collisions in the flow tube between an ion and a carrier gas atom are thermalising collisions, and the carrier gas involved in these collisions is the thermalisation gas. In the Voice100 the carrier gas can be introduced through either of two inlets on the Venturi plate and a diagram of this plate is shown as figure 3.01. It is crucial to still employ helium as the gas that is first encountered by an ion entering the flow tube (the thermalisation gas) to ensure that minimal fragmentation occurs when ions are injected into the flow tube. This is supported by three spectra shown as figure 3.02, where a single carrier gas is flowing through both the carrier inlets on the Venturi plate. By using a helium carrier gas, little ion fragmentation is observed compared to argon or nitrogen that leads to substantial ion fragmentation on injection. The fragmentation that is observed is due to the excited ions colliding with the Ar or N_2 carrier gases and undergoing charge transfer, or dissociation processes. However, the apparent drawback of using helium as a carrier gas is the low overall ion intensity observable in the instrument due to the loss of ions in the flow tube by diffusive forces. All spectra shown in figure 3.02 are normalised to the upstream ion currents shown in table 2.02.

Even though argon or nitrogen cannot be used as a thermalisation gas that creates the Venturi effect, the advantageous nature of the larger particles can be employed by addition of these gases to the flow tube after the thermalisation region. These gases enter the flow tube through the outer hole inlet for the addition of secondary carrier gases as was discussed in chapter 2. Both argon and nitrogen are effective in decreasing the radial diffusion when added to the flow tube on the hole inlet, and yield very little fragmentation of the precursor ions that are entering the flow tube through the Venturi orifice as these ions still encounter helium

atoms first. Mass spectra of the mixed carrier gas flow tubes are given as figure 3.03.

Argon has been chosen as the secondary carrier due the higher overall ion signal that is measurable, higher ionisation potential, [30] and the slightly lower fragmentation compared to nitrogen. Also the proton bound dimer of N_2 (referred to as $(N_2)_2H^+$ - *m/z* 57) observed in figure 3.03 B is found at a mass over charge ratio that is critical in SIFT-MS analyses for the detection of acrolein and butanol as both yield major product ions with H_3O^+ at *m/z* 57, [33,34] and N_2H^+ will also proton transfer to each of these analytes (the proton affinity of N_2 is 493.8 kJ mol^{-1} [31]) making quantitation by the SIFT-MS technique difficult.

The N_2H^+, $(N_2)_2H^+$, ArH^+ and Ar_2H^+ ions are formed from excited H_3O^+ ions that are not effectively thermalised by the Helium carrier gas. The excited H_3O^+ ions are in electronic configurations that lead to exothermic proton transfer with either N_2 or Ar, and this process will occur with unit collision efficiency. Therefore, the amount of N_2H^+, $(N_2)_2H^+$, ArH^+ and Ar_2H^+ ions present compared to the parent H_3O^+ and $H_3O^+.H_2O$ gives an indication of the efficiency of the thermalisation region.

A small amount of Ar_2H^+ (*m/z* 81) is also observed in the mass spectrum when H_3O^+ is injected into a helium and argon mixed flow tube (not observable on the mass scale shown in figure 3.03 A), however this ion is at an intensity often less than 1000 counts s^{-1}, and an *m/z* value that does not interfere with important analytes.

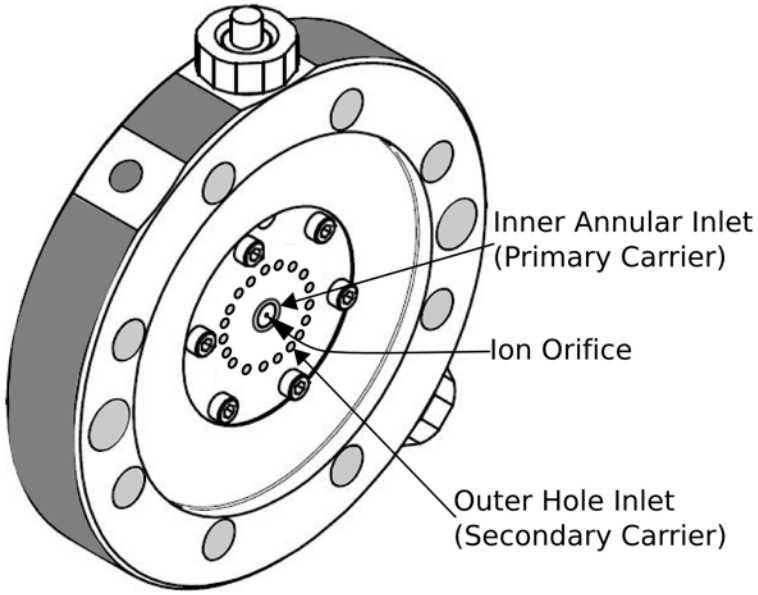

Figure 3.01. Venturi orifice design showing the primary and secondary carrier inlets.

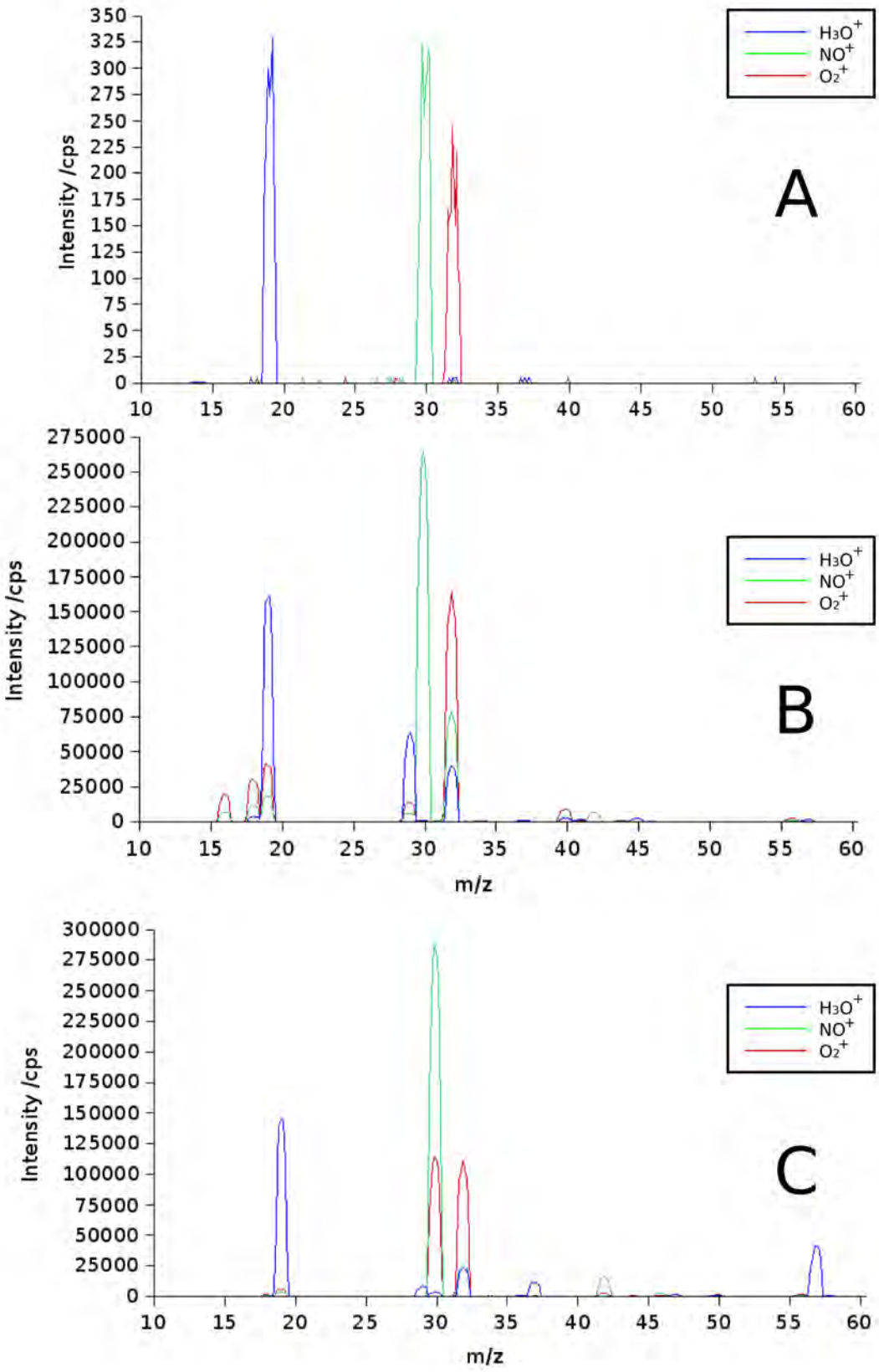

Figure 3.02. Mass spectra of each precursor ion in a specific carrier gas that is flowing through both the inner and outer Venturi ports (in a 3:5 ratio). Flow tube pressure is 0.5 Torr and total flow is 40 Torr L s^{-1}. Sample inlet is closed. A) He, B) Ar and C) N_2 .

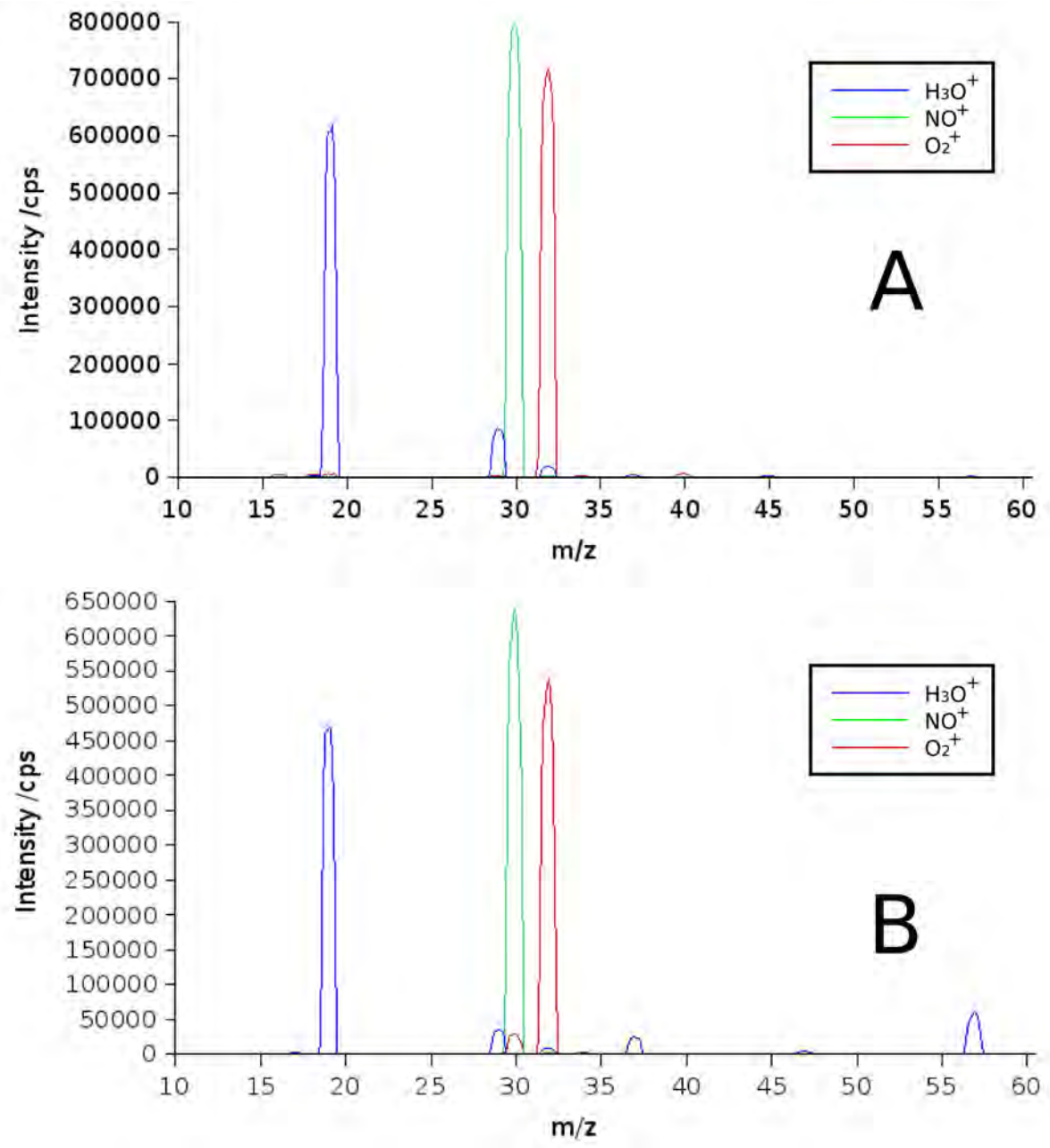

Figure 3.03. Mass spectra of each precursor ion in a mixed carrier gas where helium is flowing through the inner annulus at 15 Torr L s^{-1} and either A) Ar or B) N_2 is flowing through the outer hole inlet at 25 Torr L $^{-1}$. Flow tube pressure is 0.5 Torr, and the sample inlet is closed.

A large portion of the remainder of this chapter will focus on the effects of the addition of argon to a flow tube, and methods for correcting calculations which are simple in single carrier gases but that are made quite complex by the introduction of mixed carrier gases.

3.2 Flow Tube Performance

The fundamental region in a SIFT or flowing afterglow instrument is the flow tube. Here the ion-molecule reactions occur for a specific reaction time before being sampled into the downstream ion selection chamber where the reaction is halted. The first question that must therefore arise is 'what is the reaction time in a Voice100 flow tube?'

Using the methods outlined by Ferguson *et al.*, [5] Bolden *et al.* [52] and Adams *et al.* [10] and ignoring diffusion, ions are known to only move along the axis of a flow tube at the velocity of the carrier gas that the ions are in. When the flow tube is truly laminar the radially dependent form of the velocity profile can be expressed as

$$V(r)=2V_0\frac{[1-(r/a)^2+2s/a]}{1+4s/a} \tag{3.01}$$

where a is the radius of the flow tube, s is the pressure dependent wall slip coefficient and V_0 is the average (bulk) carrier gas velocity that can be easily determined from the total carrier gas flow (Φ_C), the flow tube pressure (P) and the temperature (T) as shown in equation 3.02.

$$V_0=\frac{\Phi_C}{\pi a^2 P}\frac{T}{273.15} \tag{3.02}$$

To clarify the situation, a diagram of the velocity profile is shown in figure 3.04

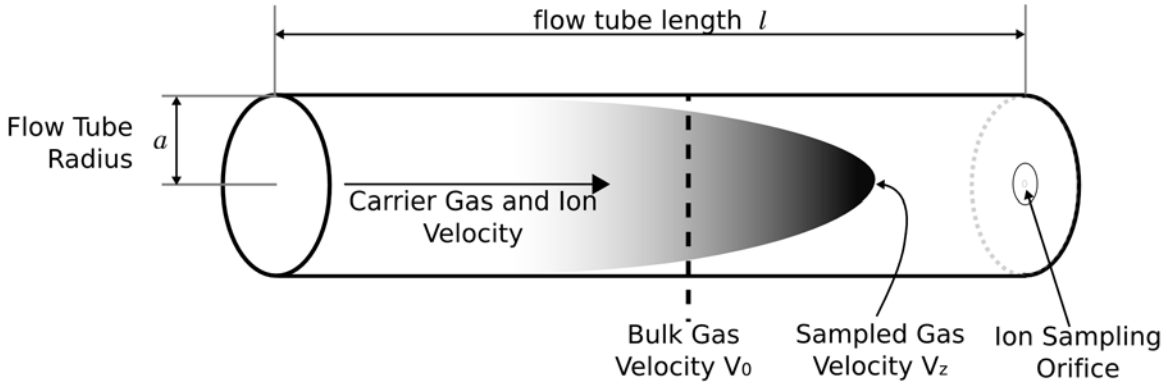

Figure 3.04. Laminar velocity profile of a cylindrical straight flow tube.

It is apparent from equation 3.01 that the centre of a laminar velocity profile (where $r = a$) should be at a velocity twice that of the bulk carrier when there is no wall slip, and that the value of V_z / V_0 (where V_z is the gas velocity at the centre of the flow tube) will drop to one as s approaches infinity. The literature mostly supports these assumptions. The UoC FA-SIFT has an empirical V_z / V_0 ratio of 1.49 [73], Smith and Spanel commonly apply a ratio of 1.5 to all of their experiments [39] and Upschlute *et al.* [81] have reported a range of V_z / V_0 values from 1.68 to 0.755.†

When equation 3.01 is solved for s, using the previously measured V_z/V_0 ratio, [73] the pressure dependent wall slip coefficient for the UoC FA-SIFT is found to be ~0.72 cm at 0.35 Torr. Therefore the value of the pressure independent wall slip coefficient s' (where $s' = s \,.\, P$) is 0.25 Torr cm. [10]. As the gases and tube material of the UoC FA-SIFT and Voice100 are similar, the value of s' for the Voice100 is assumed to also be ~ 0.25 Torr cm, which is not an unreasonable assumption because wall slip is based on the tube material and carrier gases. [112]

Because the determination of an ion transit time by computational methods requires the assumptions above, it is of importance to measure directly the ion time-of-flight which is an empirical measure of V_z. This will hopefully lead to further insight into the hydrodynamics of the Voice100 flow tube. As was mentioned in chapter 2, even though the Knudsen number and Reynolds number of the Voice100 flow tube are sufficiently small, the laminar velocity profile has not fully developed by the end of the flow tube. Since s' has now been estimated, by measuring an empirical V_z / V_0 ratio, we are in effect measuring the deviation of the Voice100 flow tubes velocity profile from laminar, where the laminar value is calculated by equation 3.01. However, any data obtained is only indicative for determining trends, and optimum conditions for the operation of the flow tube. The calculations here also ignore the axial drift velocity, which may alter the the value of V_z, although the effect should be minimal in altering the average time of flight.

3.2.1 Flow dependent deviation from laminar conditions

By pulsing ions down the flow tube in a similar manner to do that of an ion mobility spectrometer, an ion arrival time distribution can be collected. [113] The average of the ion arrival time distribution is an experimental measure of V_z. The ions are pulsed by inserting an

† Values reported that were less than 1 were deemed to be due to shock cells and end effects.

electrical probe, insulated from the flow tube, through the sample inlet. The electrical probe is a 10 mm diameter disk welded to the end of a short piece of wire and it is inserted into the flow tube 60 mm downstream from the Venturi inlet. It is electrically isolated from the flow tube such that the probe can be floated to a voltage independent of the flow tube. A judicious choice of voltages allows the ions to be "gated-off", such that few ions may pass. Then, by rapidly pulsing the voltage on the probe to ground for a short period of time (< 100 μs) ions are allowed to pass and an arrival time spectrum can be collected. Ion-arrival time spectra are collected using a LabVIEW program written specifically for this experiment. The LabVIEW software controls the voltages applied to the probe, the collection of ion signals on the detector, and also iterates the process to allow for the collection of statistically significant data. An example of an ion arrival time spectrum is shown as figure 3.05 where the average time of flight has been determined from the point where the area under the curve is equal on both sides. The curve is deemed to be any area that is greater than three standard deviations above the background signal. A range of ion times of flight with varying pressures and carrier gas compositions have been collected for a single Voice100 instrument. The times-of-flight and their corresponding ion velocities are given in table 3.01.

Ion arrival times, and therefore empirical ion velocities have an absolute error of ± 10% based on repetition of measurements. Calculated ion velocities have an unknown absolute error, but a very small relative error. V_0 has a small error (< 10%) based on uncertainties in the measurement of pressure and flow.

By examining the pressures observed in the upstream ion selection chamber and comparing the relevant pressures in the flow tube, it is found that the Venturi effect is sufficient for operation of the quadrupole mass filter. Pedder [86] recommends that quadrupole mass filters should be operated below 6×10^{-5} Torr. Even at the highest flow tube pressures given in table 3.01 that are near 1 Torr, the upstream chamber pressure is still found to be less than 3×10^{-5} Torr. Back-flow of flow tube gases into the upstream chamber was observed where the helium flow was 5 Torr L s^{-1} or less (not shown in table 3.01), as the flow of helium is too low to effectively establish the Venturi effect. Also, the maximum ion currents on the downstream disk were observed to be generated where the flow of argon was ≥ 20 Torr L s^{-1}.

The interesting data lies in the deviation of the experimental ion velocities from the calculated expected ion velocities determined from equation 3.01.

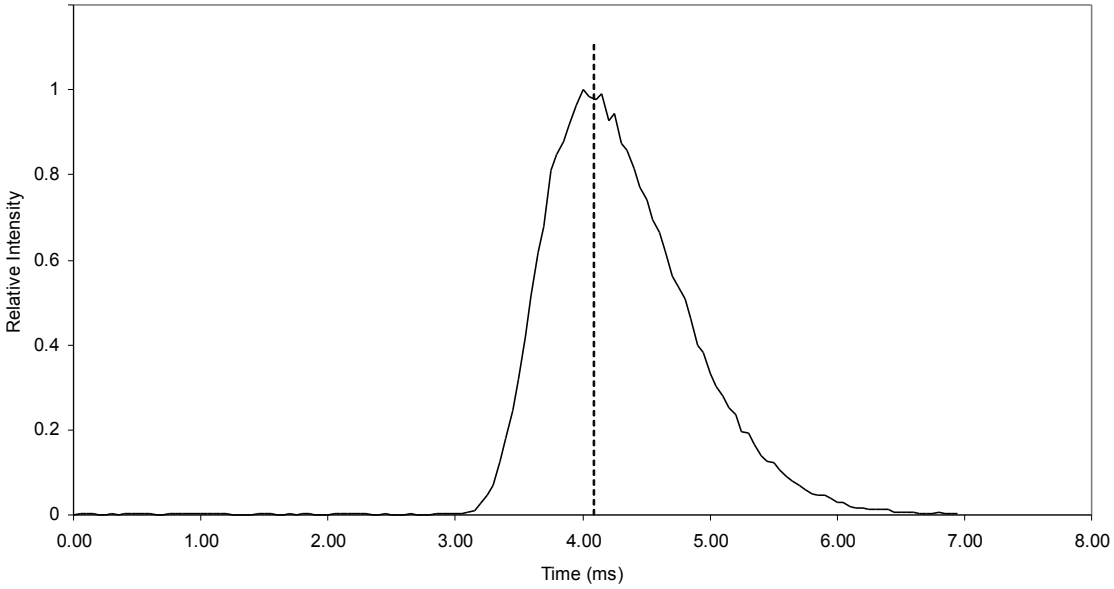

Figure 3.05. An example of an ion arrival time spectrum where the average time-of-flight is indicated by the dashed line.

Table 3.01. Ion times-of-flight across a range of flow conditions and pressures.

Flows /Torr L s^{-1}		***Pressures /Torr***		***Ion Velocities /m s^{-1}***			***V_Z / V_0 Ratio***	
Helium	*Argon*	*FT*[a]	*U/S*[b] */10^{-5}*	*V_0*	*Calculated*[c] *V_z*	*Experimental*[d] *$\langle V_z \rangle$*	*Calculated*	*Empirical*
10	10	0.25	1.47	48.2	65.6	71.2	1.36	1.49
	20	0.40	1.56	45.2	66.4	70.6	1.47	1.52
	25	0.46	1.61	45.9	69.3	70.6	1.51	1.52
	30	0.52	1.66	46.3	71.3	71.5	1.54	1.53
	35	0.59	1.70	46.0	72.2	71.5	1.57	1.52
	40	0.65	1.75	46.4	73.8	68.9	1.59	1.46
15	10	0.34	1.60	44.3	63.4	65.6	1.43	1.48
	20	0.47	1.68	44.9	67.8	71.1	1.51	1.55
	25	0.53	1.72	45.5	70.1	70.2	1.54	1.52
	30	0.59	1.76	46.0	72.2	70.1	1.57	1.51
	35	0.66	1.80	45.7	72.7	69.5	1.59	1.49
	40	0.72	1.85	46.1	74.7	66.6	1.62	1.42
20	10	0.38	1.72	47.6	69.5	69.9	1.46	1.47
	20	0.47	1.80	51.3	77.5	64.3	1.51	1.24
	30	0.55	1.88	54.8	84.9	64.5	1.55	1.18
	40	0.65	1.97	55.7	88.6	60.3	1.59	1.07
30	10	0.52	1.92	46.4	71.5	70.5	1.54	1.51
	20	0.61	1.98	49.4	78.1	64.9	1.58	1.31
	30	0.70	2.06	51.7	83.2	59.6	1.61	1.16
	40	0.79	2.14	53.4	87.6	57.3	1.64	1.07
40	10	0.66	2.12	45.7	72.7	70.8	1.59	1.55
	20	0.76	2.20	47.6	77.6	64.8	1.63	1.36
	30	0.85	2.27	49.7	82.0	58.8	1.65	1.19
	40	0.94	2.39	51.3	86.2	56.5	1.68	1.10

a) FT is the pressure in the flow tube in Torr
b) U/S is the pressure in the upstream ion selection chamber in Torr
c) calculated using equation 3.01 where $a = 0$ cm, and $s = 0.25 / P$ as discussed in the text
d) measured from time-of-flight experiments as discussed in the text

The $<V_z> / V_z$ ratio is an indicator of the deviation from laminar flow in the reaction region. Where the $<V_z> / V_z$ ratio is approximately unity, a laminar velocity profile is present between the sample inlet and the sampling orifice. This measurement does not infer any information regarding the velocity profile upstream of the sample inlet.

For the majority of data where the flow tube pressure is found to be ≤ 0.55 Torr, the calculated ion velocity V_Z is found to be approximately equal to the empirical ion velocity $<V_Z>$. This finding gives strong support to the estimation of the pressure independent wall slip coefficient from the UoC FA-SIFT data (s' = 0.25 Torr cm) as a large proportion of empirical data is found to agree with the calculated parameters. A comparison of the calculated versus measured ion velocity shows that as the pressure in the flow tube is increased, the difference between the two ion velocities becomes larger. Figure 3.06 shows a graphical representation of this deviation from expected values. The region where the measured ion velocity is within ± 10% of the expected value, the flow is defined as laminar, which is required for correct operation of a SIFT instrument. Outside of the ± 10% region is an unacceptable velocity profile. It must be noted here that the balance of the carrier gas leading to the rise in flow tube pressure shown in figure 3.06 is from argon.

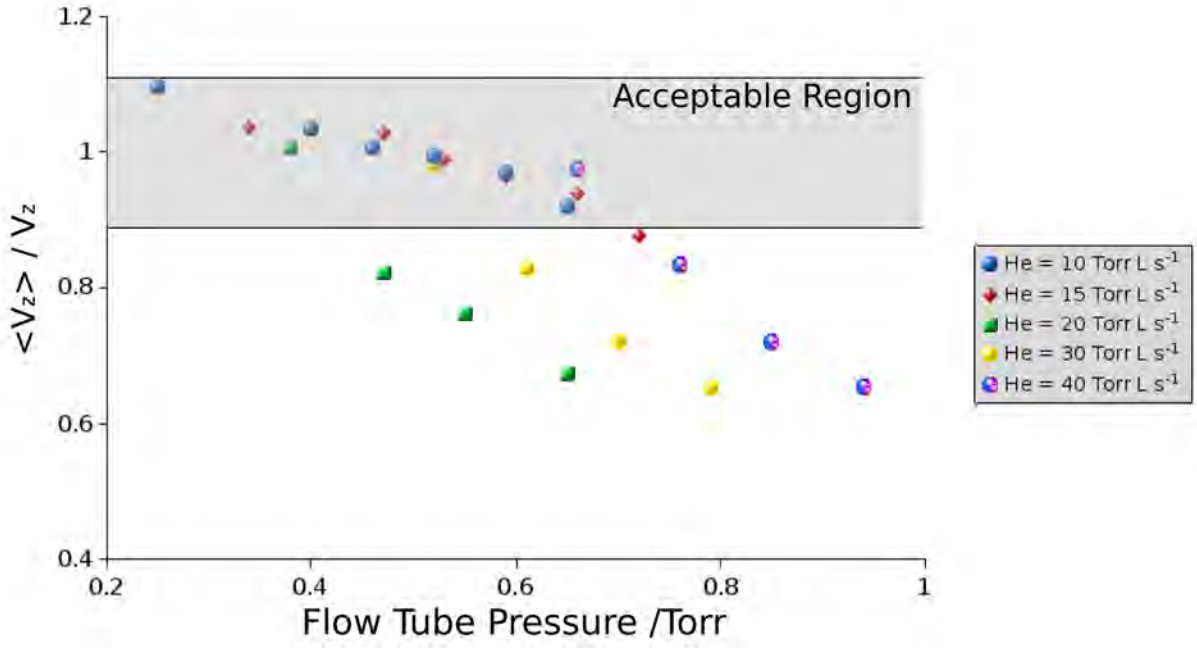

Figure 3.06. Deviation of the measured ion velocity $<V_Z>$ from the calculated ion velocity V_Z where the acceptable region is defined as ±0.1 from unity.

As many of the $<V_z>$ values correlate with their calculated counterparts it must be concluded that the calculation employed by Ferguson *et al.* [5] to determine the length to

reach an equilibrium laminar velocity profile must be an upper limit for a flow tube, as many values here have reached what seems to be an approximate laminar velocity profile.

Higher pressures generally perturb the laminar velocity profile and move $<V_z>$ back toward the bulk gas velocity. An explanation for this finding may be that the 'shock cells' that are near the Venturi orifice are stabilised for longer distances down the flow tube by the higher pressures in the flow tube. A shock cell is an flow region where the pressure is greater or less than the equilibrium pressure expected from the flow of the gas. [114] It is apparent that the further down the flow tube the shock cells are stabilised for, then the longer it must take for the laminar velocity profile to develop.

Where low flows of helium are used through the inner annulus (10-15 Torr L s^{-1}) the $<V_z> / V_z$ ratio is found to be approximately unity for all argon flows, however, as the inner annulus helium flow is increased to 20 Torr L s^{-1} or greater, an increasing argon flow is found to substantially perturb the ion velocity ratio and therefore deviate the flow away from laminar. This observation may be due to the ineffective pumping by the roots blower at these higher pressures. Since the minimum argon flow required to maintain a substantial ion current is 20 Torr L s^{-1}, the helium flow must be kept at 10-15 Torr L s^{-1}.

Therefore, the optimal flows chosen for the Voice100 instrument studied here are 15 Torr L s^{-1} of helium, and 25 Torr L s^{-1} of argon which gives the most effective thermalisation of ions when injected into the flow tube, and the closest $<V_z> / V_z$ ratio to unity. Also by having an argon flow of 25 Torr L s^{-1} the largest possible ion signal measurable on the Voice100 can be found using these carrier gases. These carrier gas flows will be used in all casesstan in this thesis unless otherwise noted.

3.2.2 End Correction

The end correction is a correction factor for the mixing effects of an analyte entering the flow tube from the neutral inlet. [81] However, because the analyte mixing effects are difficult to separate from the inaccuracies of all other factors involved in a SIFT measurement, the end correction becomes an empirical correction factor that ensures rates measured on any particular SIFT instrument will correlate with literature data. End corrections for a range of different flows have been determined by measuring the rate coefficient for $O_2^{\bullet+}$ + NO with a known ion velocity $<V_z>$ and comparing the observed rate coefficient with the literature rate coefficient. The reaction of $O_2^{\bullet+}$ + NO is a well understood

electron transfer reaction giving a single product with a rate coefficient of 4.4×10^{-10} cm^3 $molecule^{-1}$ s^{-1} ± 30%. [55] By measuring this with varying carrier gas composition, further insight into the laminar velocity profile can be found.

The ion time-of-flight for a specific set of carrier gas parameters can be converted to a velocity when the distance travelled through the reaction region is known. By then adjusting the distance travelled by adding an end correction in centimetres, an effective reaction length is found. Where the end correction is negative, the effective reaction length is shorter than the distance from the sample inlet to the sampling orifice. Conversely, when the end correction is positive, the effective reaction length is longer than the sample inlet to the sampling orifice.

Table 3.02. Flow-based end corrections where the ion time-of-flight $<V_z>$ is known. A positive end correction is an increase in reaction length.

Flow /*Torr L* s^{-1}		***Rate Coefficient k /***	***End Correction /***
Helium	*Argon*	10^{-10} cm^3 $molecule^{-1}$ s^{-1}	*cm*
10	20	4.67	+ 1.5
	25	4.53	+ 0.8
	30	5.14	+ 3.7
	35	5.28	+ 4.3
	40	5.63	+ 5.6
15	20	3.61	- 5.7
	25	3.97	- 2.8
	30	4.09	- 1.9
	35	4.83	+ 2.3

Table 3.02 shows an increasing argon flow, with a static helium flow, yields an increasing reaction length. This is consistent with having increased turbulence at higher argon flows as the shortest possible reaction length is at laminar flow. Positive end corrections have been measured for some flows, which may be attributed to the neutral inlet being very close to the Venturi plate (6 cm apart). Shock cells extending from the helium and argon carrier inlets may allow for mixing of the analyte to occur upstream of the neutral inlet. Although when the helium and argon flows are 10 and 40 Torr L^{-1} s^{-1} respectively, the end correction gives an increase in reaction length of 5.6 cm, which is physically unlikely. It is concluded then that the absolute values given in table 3.02 are correction factors that do not only adjust for the mixing effects of the analyte, but also correct for the error that has compounded in the measurement of the reaction time. However, all values reported in table 3.02 are found to lie within the reported uncertainty of the literature rate coefficient for the reaction of $O_2^{\bullet+}$ and NO. [55] The end correction factor for optimal carrier gas flows (15 Torr L s^{-1} of helium and

25 Torr L s^{-1} of argon) is -2.8 cm, not an unreasonably large correction (~10% of the physical distance between the sample inlet and the sampling orifice).

By the addition of an end correction factor, reaction rate coefficients which are measured on a Voice100 are effectively calibrated to instruments which have previously a rate coefficient for the $O_2^{\bullet+}$ + NO reaction. Conversely, reaction rate coefficients measured on other SIFT instruments should now be applicable to the Voice100 assuming no mass discrimination.

3.3 Ionic Diffusion in Carrier Gas Mixtures

3.3.1 Introduction

Consider the hypothetical reaction $A^+ + B \rightarrow D^+ + E$ that occurs with a unit collision efficiency. To determine a concentration using the methods discussed in chapter 1, it is important to ensure that the conversion of A^+ to D^+ is also counted with unit efficiency, such that the addition of analyte to the flow tube does not perturb the total number of ions being counted by the detector. Even though the ratio of A^+:D^+ may change, the total ion intensity ($A^+ + D^+ \equiv A^+_0$) must remain the same for equation 1.13 to hold. Any perturbation to the total ion intensity is known as mass discrimination, and the mass discrimination factor F_{MD} is defined as equation 3.03.

$$A^+ + F_{MD}D^+ = A^+_0 \tag{3.03}$$

In turn the concentration calculation (equation 1.13) may be altered for mass discrimination (equation 3.04) where in this case N_p and N_i are the intensities in counts s^{-1} of D^+ and A^+ respectively and *[B]* is the number density of the analyte B in the flow tube. The "diffusion coefficient" shown in equation 1.13 has been removed here and replaced by F_{MD}. The diffusion coefficient discussed by Spanel and Smith [1] only takes into account ionic diffusion in the flow tube, and not the mass discrimination resulting from electrostatic interactions.

$$\frac{F_{MD}N_p}{N_i} = k[B]t \tag{3.04}$$

As equation 3.04 relies on the value of F_{MD} for an accurate determination of *[A]*, it is critical to be able to rapidly and accurately measure F_{MD} or an equivalent parameter.

In a selected ion flow tube instrument, mass discrimination has been previously

postulated to arise from a linear combination of two regions, the flow tube reaction region, and the downstream ion detection chamber. [115] Mass discrimination arising from the ion optics (quadrupoles and lenses) has been previously studied in depth, [116,117] where higher mass ions were found to be discriminated against when compared to low mass ions (Voice100 mass range is 10 – 300 amu). This parameter is defined as M_R. The discrimination of ions through the downstream ion detection chamber requires an empirical measurement that has previously been outlined by Spanel and Smith [115] involving a determination of the mass-dependent ratio of ions on the sampling orifice disk to the detector.

The mass discrimination arising from the flow tube occurs because only those ions that are in the centre of the flow tube are sampled into the downstream ion detection chamber, and therefore any ion that diffuses off axis will not be sampled; a phenomenon known as radial diffusion. [5] This parameter has been found to be much more difficult to determine experimentally, and the current literature methods [115] have not accurately been able to determine this parameter for a Voice100. In the remainder of this section, both a theoretical and experimental approach to determining radial diffusion in a flow tube will be given.

3.3.2 Diffusion theories

The diffusive motion of an ion in a carrier (buffer) gas has been a point of investigation for more than 100 years. Between 1888 and 1905 Nernst, Townsend and Einstein [111,118] all independently published similar equations that relate the weak field mobility of an ion to the diffusion coefficient. This relationship is shown as equation 3.05 where the K is the weak field ionic mobility, e is the ionic charge, D is the diffusion coefficient, k_B is Boltzmann's constant and T is the temperature.

$$K = \frac{eD}{k_B T} \tag{3.05}$$

K relates the directional diffusive velocity to any weak field being applied, and D relates the ionic flux (number of ions per second per cm^2 along the direction of flow) to the number density. K is usually evaluated for standard conditions of 1 atmosphere and 0 °C that is called the reduced ion mobility K_0. Both the weak field ion mobility and diffusion coefficients are scalar proportionality constants that can give insight into the motion of an ion moving through a carrier gas, and are therefore of interest to SIFT-MS. Ellis and co-workers

[119] proposed a theory in 1975 that determines the ionic mobility of an ion in a single carrier gas based on the collision cross section of the ion-neutral pair. Assuming the theory of Ellis and co-workers, [119] the ionic mobility of an ion moving through a carrier gas under the influence of a weak field can be determined by equation 3.06, where N is the number density of carrier gas atoms (molecules cm^{-3}), m_i and m_c are the masses of the ion and carrier molecules respectively (kg), and $\Omega'(T_{eff})$ is a collision integral that is obtained from tabulated values of $\Omega(T_{eff})$ [120] where the relationship between $\Omega'(T_{eff})$ and $\Omega(T_{eff})$ is defined in equation 3.07. The evaluation of $\Omega'(T_{eff})$ requires knowledge of the potential well for the ion-carrier gas interaction, as r_m is the minimum energy distance of interaction (the value of r where the potential energy is at a minimum).

$$K = \frac{3e}{16N}\left(\frac{2\pi}{k_B T}\right)^{1/2}\left(\frac{m_i + m_c}{m_i m_c}\right)^{1/2}\frac{1}{\Omega'(T_{eff})} \tag{3.06}$$

$$\Omega'(T_{eff}) = \frac{\Omega(T_{eff})}{\pi r_m^{\,2}} \tag{3.07}$$

Simply then, if the minimum well distance is known for an ion-carrier gas interaction, the value of K can be evaluated. However, determining the value of r_m is a non-trivial calculation. A simple (12, 4) hard-sphere interaction potential has been employed for this type of calculation, such that the potential energy $V(r)$ as an ion approaches an atom is given by equations 3.08 – 3.10 where r is the ion-neutral distance. A (12,6,4) potential [120] has also been applied to this type of calculation both in the current study and previously. [121] This potential is found to give values of K_0 which are very similar to the much simpler (12,4) potential and therefore the (12,6,4) potential was given no further investigation. However, only molecules with relatively small polarisablities (<fr 20 $Å^3$) have been studied here. If this study was to be expanded to larger molecules, a (12,6,4) potential may be required to accurately model the collision cross section.

$$V(r) = \frac{B}{r^{12}} - \frac{C_4}{r^4} \tag{3.08}$$

$$B = \left(\frac{\sigma_{hs}}{\pi}\right)^4\left[C_4 + \frac{3}{2}kT\left(\frac{\sigma_{hs}}{\pi}\right)^2\right] \tag{3.09}$$

$$C_4 = \frac{1}{2}\frac{e^2\alpha}{4\pi\varepsilon_0} \tag{3.10}$$

Here, ε_0 is the permittivity of free space, α is the polarisability of the neutral carrier gas atom (m^3), and σ_{hs} is the hard sphere cross section for the ion-neutral interaction (m^2). The values of polarisability for all carrier gas atoms or molecules of interest have be sourced from the CRC Handbook of Chemistry and Physics. [122] Dryahina and Spanel [121] have developed the method of de Gouw *et al.* [123] to enable estimates of hard sphere collision cross sections for an ion-carrier gas interaction. They first calculate the lowest energy geometry using a quantum chemical calculation, then using purpose built software, they iterate collisions of the ion-carrier pair to determine an average cross section. Finally, the collision cross section is converted to an ionic mobility using a parameterised function. The values of ionic mobility determined by Dryahina and Spanel [121] for a helium carrier gas seem to give excellent agreement with measured literature values. However, this agreement is via a parameterised function, and since the Voice100 uses argon as well as helium, the same parameterisation cannot be assumed.

For the Voice100, Blanc's law (equation 3.11) can easily determine the ionic mobility of an ion in a carrier gas mixture where χ_j is the molar fraction of carrier gas, $Kj(0)$ is the reduced ionic mobility of an ion in a single gas, and $K_{mix}(0)$ is the reduced ionic mobility in the carrier gas mixture. [111]

$$\frac{1}{K_{mix}(0)} = \sum_j \left(\frac{\chi_j}{K_j(0)} \right) \tag{3.11}$$

For the standard operating flows determined in section 3.2, $1/Kmix$ will be approximately $0.95/K_{Ar} + 0.05/K_{He}$, and therefore the majority of all ion-carrier collisions will be with an argon atom. Obviously K_{mix} assumes that the carrier gases are completely mixed.

The percentage of collisions with a specific carrier gas in a mixture can be determined from the Van der Waal's radius of the carrier atom. The Van der Waal's radius of argon (1.8 ≈) is only 1.5 times larger than that of helium (1.2 ≈) [122] however, when the collision cross sections of an ion-helium and ion-argon collision are compared using the 12,4 potential shown above, the attractive area under the curve of the potential well for an ion-argon interaction is ~5.5 times greater than the same measurement for an ion-helium interaction. The multiplication of these two factors leads to approximately 8 times more likelihood of an ion-argon interaction than an ion-helium interaction. This factor is supported by the polarisability ratio of helium to argon, where argon (1.64 $\approx^3$) is 8 times greater than that of helium (0.21 $\approx^3$). [122]

Blanc's law can also be applied to diffusion in a mixture of carrier gases at low fields (the case of the Voice100 SIFT-MS instrument), such that $K_{mix}(0)$ can be easily related to $D_{mix}(0)$ by the Nernst-Townsend-Einstein relationship given as equation 3.05. At the higher fields commonly used in drift tubes and ion mobility spectrometers, the Nernst-Townsend-Einstein relationship does not hold for mixtures of carrier gases, and a much more complex derivation is required. [124] These equations have been solved to ensure that the weak field encountered by ions as they approach the ion sampling orifice does not affect the overall diffusion to any extent. The equations are given as 3.12 – 3.17, where 3.13 is the reduced form in the case of the Voice100 SIFT-MS. A in-depth derivation of the following equations is given in appendix A.

$$\frac{<T_{R,A}>_{mix}}{<D_{R,A}>_{mix}}(1+0.5\gamma_{R,A})=\sum_j \chi_j \frac{(T_{R,A})_j}{(D_{R,A})_j}\frac{<v_j>_{mix}}{v_j}(1+0.5\gamma_{R,A}) \tag{3.12}$$

$$\frac{<T_{R,A}>_{mix}}{<D_{R,A}>_{mix}}=\left(0.95\frac{(T_{R,A})_{Ar}}{(D_{R,A})_{Ar}}+0.05\frac{(T_{R,A})_{He}}{(D_{R,A})_{He}}\right)(1+0.5\gamma_{R,A}) \tag{3.13}$$

$$<T_{R,A}>_{mix}=T+\frac{<\zeta_{R,A}>_{mix}<m_c>_{mix}<v>^2_{mix}\left(1+0.5<\beta_{R,A}>_{mix}\right)}{k_B} \tag{3.14}$$

$$<\zeta_R>_{mix}=\frac{0.85(m_i+<m_c>_{mix})}{4m_i+3(0.85)<m_c>_{mix}} \tag{3.15}$$

$$<\zeta_A>_{mix}=\frac{4m_i-0.85(2m_i-<m_c>_{mix})}{4m_i+3(0.85)<m_c>_{mix}} \tag{3.16}$$

$$<\beta_R>_{mix}\approx 0 \qquad <\beta_A>_{mix}\approx\frac{m_i}{m_i+<m_c>_{mix}}+\frac{m_i<m_c>_{mix}}{(m_i+<m_c>_{mix})^2} \tag{3.17}$$

For the above equations the subscripts R and A are the radial and axial directions respectively and each must be solved independently, any parameter occurring in $<x>_{mix}$ notation is an ensemble averages of the carrier gas mixture. For example $(T_{R,A})_{Ar}$ is the temperature of an ion diffusing through argon in either the axial or radial direction, and $<T_{R,A}>_{mix}$ are the same two parameters in a carrier gas mixture. D is the diffusion coefficient, γ_R is 0, γ_A is 1, v_j and $<v_j>_{mix}$ are the ion velocities (from the time of flight measurements) in the single carrier gas and the carrier gas mixture respectively, and $<m_c>_{mix}$ is the molar weighted averaged of the carrier gas mixtures. [111] Assuming the measured ion velocities from section 3.2 are averaged velocities for the entire reaction length, the diffusion coefficient can be evaluated. These values have been calculated for a range of ions where the radial

temperature is only found to exceed the axial temperature by < 5% and therefore $<D_{R,A}>_{mix}$ is found to equal Blanc's law within an acceptable uncertainty. Equation 3.13 reduces to an equation similar to Blanc's law when the ionic temperature of an ion diffusing through helium and argon are equal. For the radial case, if $<T_R>_{mix} = (T_R)_{Ar} = (T_R)_{He}$, equation 3.13 reverts to Blancs law (equation 3.11) which has been solved for diffusion using the Nersnt-Townsend-Einstein relationship (equation 3.05).

Once a diffusion coefficient D for a specific ion moving through a carrier gas at a known temperature and pressure has been determined, the factor of relative discrimination or enhancement compared to the precursor ion, $d_{p,i}$, can be determined from equation 3.18, where D_i and D_p are the diffusion coefficients for the precursor and product ion respectively (cm^2 s^{-1}), t is the total reaction time (from the reaction length, empirical ion velocity and end correction) and Λ is the characteristic diffusion length for a cylindrical flow tube, which is determined from equation 3.19. [111]

$$d_{p,i} = \frac{\left(\exp\frac{D_i - D_p}{\Lambda^2}t - 1\right)}{\frac{D_i - D_p}{\Lambda^2}t} \tag{3.18}$$

$$\frac{1}{\Lambda_{11}^2} = \left(\frac{2.405}{r_0}\right)^2 + \left(\frac{\pi}{l}\right)^2 \tag{3.19}$$

The value of Λ determined here ignores the higher order modes of diffusion (which can be determined from a Bessel function) and focuses only on the fundamental mode, as higher modes have been deemed to have little effect of the overall evaluation of $d_{p,i}$. [115] For the Voice100 flow tube (r_0 = 2.4 cm, l = 25.84 cm), Λ is found to be 1 cm. The UoC FA-SIFT is known to have a value of Λ = 1.5 cm, and Spanel and Smith report 0.83 cm for their r_0 = 2.05 cm tube. [115] Due to the changes in flow tube design on the Voice100, the cylindrical approximation of Mason and McDaniel [111] may not hold as equation 3.19 assumes a straight cylindrical cavity with no variations in the azimuthal angle. However, with no other options for the calculation of Λ, a cylindrical cavity approximation must be used. Mixing of carrier gases will not influence the value of the diffusion length, as it is a boundary condition defining where the ion intensity drops to zero as ions collide with the flow tube wall.

3.3.3 Results of theoretical diffusion calculations

The methods presented in the preceding section have been calculated by first determining the lowest energy conformer(s) of 31 specific ions that are of interest to SIFT-MS studies using the Gaussian 03W package (see section 2.8). Precursor ions, and their respective water clusters have been calculated to the MP4 level of theory with the aug-cc-pVDZ basis set, while the remainder of ions have been calculated using the B3LYP density functional with the 6-311+G(d,p) basis set. For each molecule, the Hessian matrix was evaluated to ensure that the conformer was an energy minima and had no negative vibrational frequencies. All collision cross sections for ion-helium and ion-argon collisions were evaluated using the software written by Kseniya Dryahina† that iterates a simulated ion-carrier collision across a range of angles.

Table 3.03. Ions that have been studied by theoretical means. Ions generated from the stated analyte and arising from the named precursor ion.

Analyte	***Ions studied arising from precursor ion shown***			***References***
	H_3O^+	NO^+	O_2^+	
Acetone	$C_3H_6OH^+$ $C_3H_6OH^+.H_2O$ $(C_3H_6O)_2.H^+$		$C_3H_6O^+$ CH_3CO^+	[34]
Ethanol	$C_2H_5OH_2^+$	$C_2H_5O^+$	$C_2H_5O^+$	[33]
Benzene	$C_6H_7^+$	$C_6H_6^+$	$C_6H_6^+$	[125]
Toluene	$C_7H_9^+$	$C_7H_8^+$	$C_7H_9^+$	[126]
o-Xylene	o-$C_8H_{11}^+$	o-$C_8H_{10}^+$	o-$C_8H_{10}^+$	[35]
m-Xylene	m-$C_8H_{11}^+$	m-$C_8H_{10}^+$	m-$C_8H_{10}^+$	[35]
p-Xylene	p-$C_8H_{11}^+$	p-$C_8H_{10}^+$	p-$C_8H_{10}^+$	[35]
Chloropicrin	CCl_3^+			
HCN[a]	$HCNH^+$		HCN^+	[127]
DMS[b]	$C_2H_6SH^+$	$C_2H_6S^+$		[128]
DMDS[c]	$C_2H_6S_2H^+$	$C_2H_6S_2^+$		[129]
Water	$H_3O^+.H_2O$ $H_3O^+.(H_2O)_2$ $H_3O^+.(H_2O)_3$	$NO^+.H_2O$		[130]

a) Hydrogen cyanide

b) Dimethyl sulphide

c) Dimethyl disulphide

Table 3.03 gives the neutral species chosen for this study, their reactions with the common SIFT-MS precursors to give 37 explicit product ions, and the references to the specific reactions from the literature. Table 3.04 gives the theoretical values of ionic mobility

† http://www.jh-inst.cas.cz/~dryahina/

and diffusion for a helium carrier gas using both the methods of Viehland *et al.* [120] and Dryahina and Spanel, [121] and table 3.05 the same calculations for an argon carrier gas. Table 3.06 then lists the values of ionic mobility and diffusion for carrier gas mixtures using the method of Blanc's law (equation 3.11). Table 3.07 finally lists the values of $d_{p,i}$ for each of the methods. On a general inspection of tables 3.04 to 3.07, it is apparent that

- The use of argon as a carrier gas drastically reduces the ionic mobility and diffusion when compared to the helium carrier gas
- The methods of Viehland and Dryahina yield very similar results for the helium carrier gas, but markedly different results for the argon carrier gas
- The use of Blanc's Law yields a value of D_{mix} that is very similar to the the diffusion coefficient found for the same ions moving through a pure argon carrier gas.
- The values of $d_{p,i}$ for each A^+/D^+ pair in a carrier gas mixture are almost identical to the same values in the argon carrier gas.

A comparison of the $D_{Voice100}$ values in tables 3.04 and 3.05 shows that the addition of argon to the flow tube will drastically reduce the diffusion coefficient of a particular ion. For instance, H_3O^+ diffusing through helium has a $D_{Voice100}$ value using the Viehland method of 873 $cm^2\ V^{-1}\ s^{-1}$.The diffusion coefficient for the same ion diffusing through argon is a factor of five less. Therefore, H_3O^+ ions will migrate away from the central flow tube axis (where the ions are sampled) five times slower in argon than in helium.

Looking only at the data in table 3.04, the Viehland and Dryahina methods seem to correlate very well, with the Dryahina method reporting $D_{Voice100}$ values approximately 10% higher than the Viehland method. However, when comparing the same data in table 3.05 for ions migrating through argon, the two methods are found not to correlate. This is attributed to the parameterised nature of the Dryahina method catering only for a helium carrier gas.

When the values of $D_{Voice100}$ using the Viehland method from tables 3.04 and 3.05 are compared with the D_{mix} values in table 3.06, the D_{mix} values are found to be very similar to an ion migrating through pure argon. This finding is not surprising, as Blanc's Law is not a linear function, but is weighted toward the carrier gas atom of greater mass.

Finally, looking at the diffusion enhancement coefficients table 3.07 (refer to equation 3.18), for any given precursor ion/product ion pair, the argon only system is found to very accurately reproduced the helium/argon mixture. In fact, the helium/argon mixture is found to be slightly less than the argon only system. This observation is attributed to the uncertainty in the calculation and is not expected to be true of a real system.

Table 3.04. Calculation of diffusion coefficients for specific ions in a Voice100 flow tube when using helium as a carrier gas where σ_{hs} is the hard sphere collision cross section, K_0 is the reduced ionic mobility, D_0 is the diffusion coefficient at 1 Torr and 298 K and $D_{Voice100}$ is the diffusion coefficient at Voice100 conditions.

HELIUM CARRIER GAS			***Viehland Method[a]***			***Dryahina Method[b]***		
Ion	***m/z***	σ_{hs} / 10^{-16} cm^2	K_0 / $cm^2\ V^{-1}\ s^{-1}$	D_0 / $cm^2\ s^{-1}$	$D_{voice100}$[c] / $/cm^2\ s^{-1}$	K_0 / $cm^2\ V^{-1}\ s^{-1}$	D_0 / $cm^2\ s^{-1}$	$D_{voice100}$[c] / $cm^2\ s^{-1}$
H_3O^+	19	28.2	20.2	397	873	21.8	429	942
$H_3O^+.H_2O$	37	37.9	14.7	289	636	16.3	320	702
$H_3O^+.(H_2O)_2$	55	48.3	11.4	224	491	12.7	250	548
$H_3O^+.(H_2O)_3$	73	60.8	9.2	181	396	10.1	198	435
NO^+	30	28.4	19.2	376	827	21.0	411	905
$NO^+.H_2O$	48	37.4	14.5	284	624	16.2	319	699
O_2^+	32	28.3	19.0	375	823	20.9	412	903
$C_3H_6OH^+$	59	47.5	11.7	229	503	12.9	253	555
$C_3H_6O^+$	58	47.0	11.6	228	501	13.0	256	561
CH_3CO^+	43	40.6	13.7	269	590	15.1	296	651
$C_3H_6OH^+.H_2O$	77	56.2	9.8	193	423	10.9	214	469
$(C_3H_6O)_2.H^+$	117	72.6	7.6	217	475	8.4	235	517
$C_2H_5OH_2^+$	47	44.3	12.7	249	546	13.9	272	598
$C_2H_5O^+$	45	41.1	13.7	270	592	14.9	293	642
$C_6H_7^+$	79	59.1	9.5	186	408	10.3	203	446
$C_6H_6^+$	78	58.5	9.6	188	412	10.4	205	451
$C_7H_9^+$	93	60.2	9.2	181	398	10.1	199	436
$C_7H_8^+$	92	65.5	8.7	171	375	9.3	183	402
o-$C_8H_{11}^+$	107	64.7	8.4	165	361	9.4	185	406
o-$C_8H_{10}^+$	106	71.0	7.9	155	340	8.6	169	370
m-$C_8H_{11}^+$	107	65.7	8.4	166	364	9.3	182	400
m-$C_8H_{10}^+$	106	72.5	7.8	152	335	8.4	165	363
p-$C_8H_{11}^+$	107	65.0	8.4	165	363	9.4	185	407
p-$C_8H_{10}^+$	106	67.8	8.1	160	351	9.0	177	388
$C^{35}Cl_3^+$	117	50.4	11.0	217	476	12.0	235	517
$HCNH^+$	28	32.5	17.1	335	736	19.3	230	834
HCN^+	27	31.5	17.3	341	748	18.9	371	815
$C_2H_6SH^+$	63	49.1	11.7	229	503	12.8	252	554
$C_2H_6S^+$	62	47.6	11.2	221	485	12.4	245	537
$C_2H_6S_2H^+$	95	57.9	9.6	189	416	10.8	212	465
$C_2H_6S_2^+$	94	56.4	9.5	186	409	10.5	207	453

a) Ref [120]

b) Ref [121]

c) Voice100 parameters are assumed to be 0.5 Torr and 300 K.

Table 3.05. Calculation of diffusion coefficients for specific ions in a Voice100 flow tube when using argon as a carrier gas where σ_{hs} is the hard sphere collision cross section, K_0 is the reduced ionic mobility, D_0 is the diffusion coefficient at 1 Torr and 298 K and $D_{Voice100}$ is the diffusion coefficient at Voice100 conditions.

ARGON CARRIER GAS			***Viehland Method[a]***			***Dryahina Method[b]***		
Ion	***m/z***	σ_{hs} / 10^{-16} cm^2	K_0 / $cm^2\ V^{-1}\ s^{-1}$	D_0 / $cm^2\ s^{-1}$	$D_{voice100}$[c] / $/cm^2\ s^{-1}$	K_0 / $cm^2\ V^{-1}\ s^{-1}$	D_0 / $cm^2\ s^{-1}$	$D_{voice100}$[c] / $cm^2\ s^{-1}$
H_3O^+	19	42.5	4.45	87.5	192	7.70	152	332
$H_3O^+.H_2O$	37	54.5	3.45	67.8	149	4.98	98.0	215
$H_3O^+.(H_2O)_2$	55	67.6	3.07	60.4	133	3.67	72.3	158
$H_3O^+.(H_2O)_3$	73	83.0	2.41	47.4	104	2.84	55.8	123
NO^+	30	42.8	4.06	79.8	175	6.64	131	287
$NO^+.H_2O$	48	54.0	3.39	66.6	146	4.72	92.8	204
O_2^+	32	42.7	3.98	78.1	172	6.53	128	282
$C_3H_6OH^+$	59	66.0	3.04	59.8	131	3.71	72.9	160
$C_3H_6O^+$	58	65.5	3.00	58.9	129	3.75	73.8	162
CH_3CO^+	43	57.9	3.49	68.5	150	4.52	88.9	195
$C_3H_6OH^+.H_2O$	77	76.7	2.60	51.1	112	3.04	59.9	131
$(C_3H_6O)_2.H^+$	117	96.2	2.62	39.0	86	2.28	44.9	98.4
$C_2H_5OH_2^+$	47	62.3	3.44	67.5	148	4.12	81.0	178
$C_2H_5O^+$	45	58.5	3.46	67.9	149	4.43	87.1	191
$C_6H_7^+$	79	79.7	2.48	48.7	107	2.91	57.3	126
$C_6H_6^+$	78	79.0	2.53	49.7	109	2.95	58.0	127
$C_7H_9^+$	93	81.3	2.37	46.5	102	2.79	54.8	120
$C_7H_8^+$	92	87.3	2.32	45.7	100	2.60	51.2	112
o-$C_8H_{11}^+$	107	86.4	2.16	42.4	93	2.57	50.6	111
o-$C_8H_{10}^+$	106	93.5	2.13	41.9	92	2.38	46.8	103
m-$C_8H_{11}^+$	107	87.6	2.14	42.1	92	2.54	49.9	110
m-$C_8H_{10}^+$	106	95.5	2.01	39.8	87	2.33	45.8	101
p-$C_8H_{11}^+$	107	86.8	2.19	43.1	95	2.68	52.7	116
p-$C_8H_{10}^+$	106	90.4	2.19	43.1	95	2.46	48.4	106
$C\,^{35}Cl_3^+$	117	69.5	2.62	51.4	113	3.15	62.0	136
$HCNH^+$	28	46.7	4.04	79.4	174	6.24	123	269
HCN^+	27	47.8	4.19	82.4	181	6.16	121	266
$C_2H_6SH^+$	63	66.1	3.06	60.2	132	3.65	71.9	158
$C_2H_6S^+$	62	68.0	3.01	59.1	130	3.56	70.1	154
$C_2H_6S_2H^+$	95	78.8	2.47	49.5	106	2.87	56.4	124
$C_2H_6S_2^+$	94	77.0	2.52	48.5	109	2.94	57.8	127

a) Ref [120]

b) Ref [121]

c) Voice100 parameters are assumed to be 0.5 Torr and 300 K.

Table 3.06. Calculation of diffusion coefficients for specific ions in a Voice100 flow tube by Blanc's law when using a completely mixed composition of 15 Torr L s^{-1} of helium and 25 Torr L s^{-1} argon as carrier gases.

Ion	***m/z***	***D_{Mix}*** */cm^2 s^{-1}*	***Ion***	***m/z***	***D_{Mix}*** */cm^2 s^{-1}*	***Ion***	***m/z***	***D_{Mix}*** */cm^2 s^{-1}*
H_3O^+	19	202	$(C_3H_6O)_2.H^+$	117	89.5	p-$C_8H_{11}^+$	107	99.0
$H_3O^+.H_2O$	37	156	$C_2H_5OH_2^+$	47	155	p-$C_8H_{10}^+$	106	99.0
$H_3O^+.(H_2O)_2$	55	139	$C_2H_5O^+$	45	156	$C^{35}Cl_3^+$	117	118
$H_3O^+.(H_2O)_3$	73	109	$C_6H_7^+$	79	112	$HCNH^+$	28	183
NO^+	30	184	$C_6H_6^+$	78	114	HCN^+	27	190
$NO^+.H_2O$	48	153	$C_7H_9^+$	93	107	$C_2H_6SH^+$	63	138
O_2^+	32	180	$C_7H_8^+$	92	105	$C_2H_6S^+$	62	136
$C_3H_6OH^+$	59	137	o-$C_8H_{11}^+$	107	97.4	$C_2H_6S_2H^+$	95	111
$C_3H_6O^+$	58	135	o-$C_8H_{10}^+$	106	96.3	$C_2H_6S_2^+$	94	114
CH_3CO^+	43	158	m-$C_8H_{11}^+$	107	96.7			
$C_3H_6OH^+.H_2O$	77	117	m-$C_8H_{10}^+$	106	91.4			

Table 3.07. Diffusion enhancement coefficients based on a precursor ion/product ion pair. Values of helium, argon and mix are evaluated from tables 3.04, 3.05 and 3.06 respectively.

Precursor	***Product***		***$d_{p,i}$***		***Precursor***	***Product***		***$d_{p,i}$***	
Ion	***Ion***	***He***	***Ar***	***Mix***	***Ion***	***Ion***	***He***	***Ar***	***Mix***
H_3O^+	$H_3O^+.H_2O$	1.90	1.13	1.12	NO^+	$NO^+.H_2O$	1.72	1.08	1.08
	$H_3O^+.(H_2O)_2$	2.97	1.18	1.17		$C_2H_5O^+$	1.89	1.07	1.07
	$H_3O^+.(H_2O)_3$	4.06	1.28	1.27		$C_6H_6^+$	3.31	1.2	1.19
	$C_3H_6OH^+$	2.86	1.18	1.18		$C_7H_8^+$	3.73	1.23	1.22
	$C_3H_6OH^+.H_2O$	3.71	1.25	1.24		o-$C_8H_{10}^+$	4.21	1.26	1.25
	$(C_3H_6O)_2.H^+$	5.17	1.35	1.34		m-$C_8H_{10}^+$	4.28	1.28	1.27
	$C_2H_5OH_2^+$	2.49	1.13	1.13		p-$C_8H_{10}^+$	4.06	1.25	1.24
	$C_6H_7^+$	3.90	1.27	1.26	O_2^+	$C_3H_6O^+$	2.46	1.12	1.12
	$C_7H_9^+$	4.03	1.29	1.29		CH_3CO^+	1.88	1.06	1.06
	o-$C_8H_{11}^+$	4.57	1.32	1.31		$C_6H_6^+$	3.26	1.19	1.18
	m-$C_8H_{11}^+$	4.53	1.33	1.31		$C_7H_8^+$	3.69	1.22	1.21
	p-$C_8H_{11}^+$	4.56	1.32	1.30		o-$C_8H_{10}^+$	4.15	1.25	1.24
	$C^{35}Cl_3^+$	3.12	1.25	1.24		m-$C_8H_{10}^+$	4.23	1.27	1.26
	$HCNH^+$	1.43	1.05	1.06		p-$C_8H_{10}^+$	4.01	1.24	1.23
	$C_2H_6SH^+$	3.03	1.19	1.18		HCN^+	1.21	0.98	0.98
	$C_2H_6S_2H^+$	3.90	1.27	1.26		$C_2H_6S^+$	2.45	1.11	1.11
						$C_2H_6S_2^+$	3.23	1.19	1.18

All values of $d_{p,i}$ determined in table 3.07 can be normalised to the H_3O^+ value of $d_{p,i}$ (defined as unity) by determining the diffusion enhancement factor for the $H_3O^+ \rightarrow NO^+$ and $H_3O^+ \rightarrow O_2^+$ pairs, and multiplying the $NO^+/O_2^+ \rightarrow D^+$ value of $d_{p,i}$ by that factor. For example $H_3O^+ \rightarrow NO^+$ in helium yields $d_{NO^+,H_3O^+}(He) = 1.08$, and therefore all values of d_{p,NO^+} must be multiplied through by 1.08. The normalised values of the diffusion enhancement coefficient d_{p,H_3O^+} dependent on their carrier gas are shown graphically as figure 3.07.

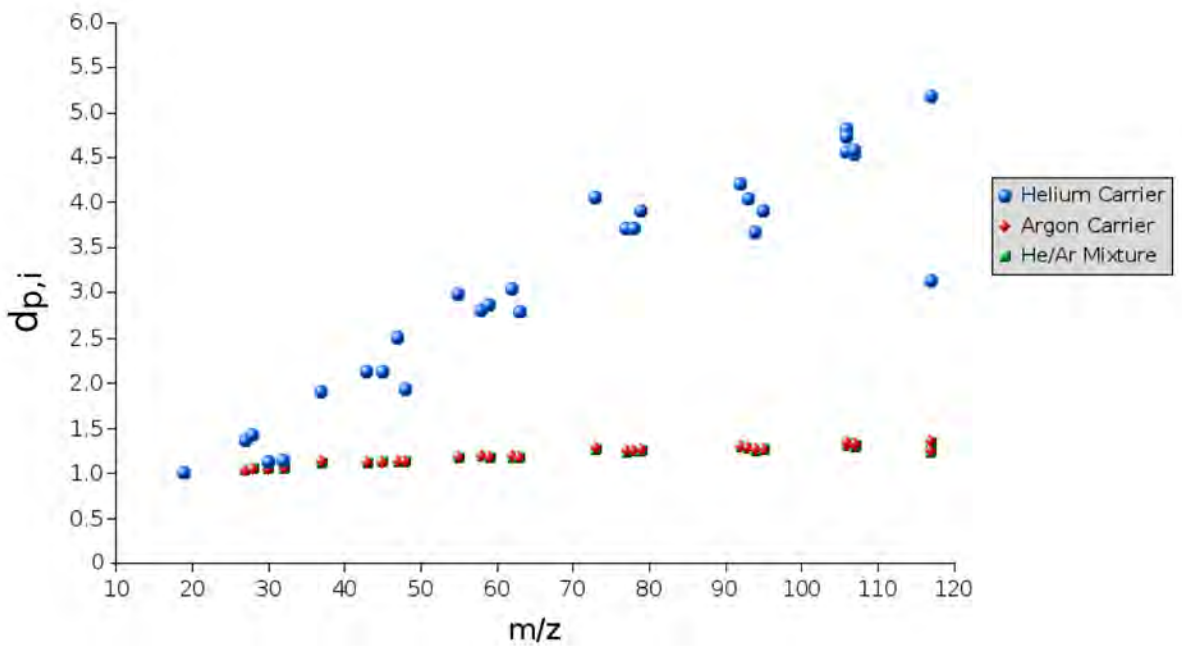

Figure 3.07. Values of $d_{p,i}$ normalised to the H_3O^+ value of $d_{p,i}$ in specific carrier gases where 'He/Ar mixture' is the optimum conditions for a Voice100 flow tube given in section 3.3. Values of 'He/Ar Mixture' are obscured behind the 'Argon Carrier' values. Outlier point in the 'Helium Carrier' values discussed in text.

It may be then concluded that even though 37.5% by flow of the carrier gas in the flow tube is helium, it is mainly argon that affects the diffusion of an ion in the Voice100 flow tube. Also, the effect of diffusion enhancement in the ion signal of larger ions apparent in a helium carrier is substantially minimised when using argon as a carrier gas. This however does not mean that the overall ion intensity that reaches the far end of the flow tube is reduced. Rather it is the lower mass ions that exhibit less radial diffusion loss in argon carrier gas, and their number density is enhanced. Therefore it is not discrimination of high mass ions, but enhancement of low mass ions in argon that causes the increase in overall ion intensity.

The outlier of the 'Helium Carrier' series in figure 3.07 at *m/z* 117 is the C $^{35}Cl_3^+$ ion that has a much smaller cross section to mass ratio than its isobaric relation $(C_3H_6O)_2H^+$ (*m/z* 117 – the acetone proton-bound dimer). The small cross section of the C $^{35}Cl_3^+$ ion outlines that the above calculations are largely dependent on collision cross section, and that a simple mass dependent parameterisation will not accurately determine values of $d_{p,i}$.

As $d_{p,i}$ is a diffusion enhancement function, F_{MD} (equations 3.03 and 3.04) must be inversely proportional to $d_{p,i}$, and because the dimensionless mass discrimination factor from the downstream chamber ion optics (M_R) is a well understood parameter where higher mass ions are discriminated against, [116] [117] we can now define F_{MD} in equation 3.20 which is similar to that defined by Spanel and Smith. [115]

$$F_{MD}=\frac{M_R}{d_{p,i}} \tag{3.20}$$

3.3.4 Measurement of empirical diffusion coefficients

It is common practice in a selected ion flow drift tube or ion mobility spectrometer to measure a diffusion coefficient in a specific field (in Townsend's) in order to determine the reduced ion mobility K_0. [75] However to determine these values in the field free environment of the Voice100 flow tube is a much more difficult task. Ions cannot be controlled or focused by optics in the flow tube, and more importantly, only three ions of limited mass range can currently be selectively injected into the flow tube from the upstream chamber through the Venturi orifice.

A previous approach to determining diffusion coefficients empirically in a field free flow tube is less than satisfactory by its very nature. Spanel and Smith [115] published an empirical method for determining both the diffusion enhancement of large ions in the flow tube region, and mass discrimination of heavy ions by the ion optics of the downstream ion detection chamber in one step. This method entailed flowing a substantial flow of an analyte into the flow tube through the sample inlet such that all precursor ions are immediately converted to product ions very near to the neutral inlet port. By using a judicious choice of analytes (substituted benzenes and ketones) that form terminal ions rapidly with H_3O^+, the ratio of the ion current on the downstream sampling orifice to the ion signal on the particle multiple can be evaluated to determine differences in mass discrimination between precursor ions (where no analyte is flowing) and product ions (with analyte flowing). Equation 3.21 and 3.22 outline this point in more detail for the reaction of $A^+ + B \rightarrow D^+ + E$, where $I_{D/S}$ is the ion

current on the downstream orifice (pA), and I_{Det} is the ion signal detected on the particle multiplier.

$$d_{p,i} = \frac{I_{D/S}(D^+)}{I_{D/S}(A^+)} \tag{3.21}$$

$$M_R = \frac{I_{det}(D^+) I_{D/S}(A^+)}{I_{D/S}(D^+) I_{det}(A^+)} \tag{3.23}$$

The values of M_R are determined from the ratio of the downstream electrometer to the detector and a measurement in this manner leads to a knowledge of the mass discrimination of the ion optics assuming that the extraction efficiency of the ion sampling orifice is independent of mass, such that the ratio of the number of ions entering the downstream chamber compared to the disk current must not vary across the applicable *m/z* range. If this assumption holds, the measurement of M_R should accurately represent the mass discrimination of the downstream chamber ion optics. However, the determination of $d_{p,i}$ using this method has a severe flaw. By adding a sufficient flow of analyte to a flow tube to achieve complete conversion to the terminal product ion in the vicinity of the sample inlet (typically a number density of ~ 2 x 10^{14} molecules cm^{-3} of analyte is necessary), the diffusion characteristics of the flow tube are substantially perturbed. For instance, when adding 0.5 Torr L s^{-1} of pure benzene vapour to a helium flow tube (40 Torr L s^{-1} of carrier gas), Blanc's law is altered to the form given in equation 3.24, which requires knowledge of a benzene ion moving through benzene vapour.

$$\frac{1}{K_{mix}} = \frac{0.2}{K_{benzene}} + \frac{0.8}{K_{He}} \tag{3.24}$$

Also, if 20% of all $C_6H_7^+$ collisions in the flow tube are with neutral benzene species, resonant proton transfer will drastically affect the motion of the protonated benzene ions through the helium carrier gas. Both of these effects are substantially reduced in the helium/ argon environment of the Voice100 flow tube, where the molar fraction of benzene required by Blanc's law drops to 0.035 as opposed to 0.2 in the helium only flow tube shown above. However even at this reduced collision fraction, resonant proton transfer may alter the observable diffusion characteristics. The resonant proton transfer of protonated benzene is the reaction of Benzene.H^+ + Benzene, which does not yield a separated product.

Clearly from the above arguments, the addition of large flows of neutral analyte to the flow tube introduces difficulties when measuring the diffusion coefficients of specific ions. Therefore, a new method has been designed where low concentrations of analyte that are

diluted in a carrier gas (usually argon) are introduced into the flow tube through the sample inlet. The new method does not determine $d_{p,i}$ directly. Instead it is obtained from solving the simple equation 3.20 for the diffusion enhancement factor having first determined the values of M_R and F_{MD}. The mass dependent function of M_R is found using the method of Spanel and Smith [115] by employing a range of analytes that cover the mass range 17 – 173 amu. These analytes are benzene, toluene, and xylene, which all form the $[M + H]^+$ ion when reacted with H_3O^+ and acetone, methyl ethyl ketone and 3-pentanone which yield proton bound dimers as terminal ions when reacted with H_3O^+. The value of M_R for O_2^+ (*m/z* 32) is then determined from the reactions of O_2^+ with benzene and toluene, by assuming that the product ions formed have the same absolute value of M_R to the $[M + H]^+$ ions formed from the H_3O^+ reactions. Table 3.08 gives the mass dependent values of M_R determined for the mass discrimination resulting from the downstream detection chamber ion optics. The data has then been fitted to a linear step wise function.

Table 3.08. Downstream ion detection chamber mass discrimination values (M_R) on a standard Voice100 instrument. All values are relative to H_3O^+.

Ion	***m/z***	***M_R***
H_3O^+	19	1.00
$C_6H_7^+$	79	1.38
$C_7H_9^+$	93	1.64
$C_8H_{11}^+$	107	2.58
$(C_3H_6O)_2.H^+$	117	4.30
$(C_4H_8O)_2.H^+$	145	17.7
$(C_5H_{10}O)_2.H^+$	173	117.
O_2^+	32	0.79

F_{MD} is determined by flowing a known concentration of analyte in the ppmv range into the flow tube, and solving equation 3.04. Low concentrations of a range of analytes are created by using a permeation apparatus as discussed in chapter 2, where the diluent gas is always the same gas that is the majority component of the flow tube (argon in the case of the Voice100 in its standard operating environment). Due to the availability of compounds in permeation tubes, only compounds that yield product ions across a small mass range (28 – 108 amu) have been used. Table 3.09 lists the permeation tubes used, their quoted permeation rate and uncertainty, and the values of F_{MD} determined for each precursor ion/product ion pair using the same ion optic parameters as were used in table 3.08. Reactions of analytes with NO^+ and $O_2^{\bullet+}$ have been enabled again by assuming the product ions formed from the reactions of both benzene and toluene with H_3O^+, NO^+ and $O_2^{\bullet+}$ yield product ions that have

the same values of F_{MD}.

Table 3.09. Values of the instrument mass discrimination function F_{MD} determined using a permeation oven all normalised to H_3O^+ = 1.00, where $F_{MD}(NO^+)$ = 0.91, and $F_{MD}(O_2^+)$ = 0.73.

Analyte	***Perm. Rate @ T (±)***	***Ions***		***m/z***	***k (±)***	***[Ref]***	***F_{MD}***
	/ng min^{-1}	*Precursor*	*Product*		*/10^{-9} cm^3 molecule^{-1} s^{-1}*		
Hydrogen cyanide	592 @ 30°C (2%)	H_3O^+	$HCNH^+$	28	3.80 (15%)	[127]	0.63
Hydrogen sulphide	2725 @ 50°C (2%)	H_3O^+	H_3S^+	35	1.65 (15%)	[129]	0.58
Acetaldehyde[a]	1544 @ 50°C (- %)	H_3O^+	$C_2H_4OH^+$	45	4.20 (20%)	[34]	0.55
Dimethyl amine	1836 @ 50°C (2%)	H_3O^+	$C_2H_6NH_2^+$	46	2.10 (15%)	[129]	0.45
		NO^+	$C_2H_6NH^+$	45	1.60 (15%)	[129]	0.40
		O_2^+	$C_2H_6N(H)^+$	44.5[b]	1.60 (15%)	[129]	0.37
Ethanol	996 @ 50°C (2%)	H_3O^+	$C_2H_6OH^+$	47	2.70 (20%)	[33]	0.59
		O_2^+	$C_2H_5O(H)^+$	45.5[b]	2.30 (15%)	[33]	0.66
Acetone	2337 @ 50°C (2%)	H_3O^+	$C_3H_6OH^+$	59	3.90 (20%)	[34]	0.43
		NO^+	$C_3H_6O.NO^+$	88	1.20 (20%)	[342]	0.37
Dimethyl sulphide	5450 @ 50°C (2%)	H_3O^+	$C_2H_6SH^+$	63	2.50 (25%)	[128]	0.65
		O_2^+	$C_2H_6S^+$	62[c]	1.32 (15%)	[128]	0.54
Benzene	3256 @ 50°C (2%)	H_3O^+	$C_6H_7^+$	79	2.00 (20%)	[131]	0.47
Toluene	2705 @ 50°C (2%)	H_3O^+	$C_7H_9^+$	93	2.30 (20%)	[126]	0.47
Dimethyl disulphide	988 @ 50°C (2%)	H_3O^+	$C_2H_6S_2H^+$	95	2.60 (15%)	[129]	0.46
		O_2^+	$C_2H_6S_2^+$	94[d]	1.84 (15%)	[129]	0.38
Methyl bromide	1856 @ 30°C (2%)	O_2^+	CH_3Br^+	96	2.20 (20%)	[132]	0.56
Dibromoethane	3794 @ 70°C (2%)	O_2^+	$C_2H_4Br^+$	108[e]	3.00 (20%)	[132]	0.68

a) The acetaldehyde tube is uncertified
b) See text for *m/z* weighting
c) *m/z* 62 is formed as a 60 % channel
d) *m/z* 94 is formed as an 80 % channel
e) Average of the two bromine isotopes

The reactions of O_2^+ with dimethyl sulphide and dimethyl disulphide yield molecular ions in 60% and 80% channels respectively. [128,129] The values of F_{MD} for each of the molecular ions has been determined by using estimated F_{MD} values for the fragment ions that are formed in smaller product ion branching ratios. These reactions, their product ion branching ratios, and the estimated F_{MD} values for the fragment ions are given in equations 3.25 and 3.26.

			BR	F_{MD}	
$O_2^+ + (CH_3)_2S$	→	$C_2H_6S^+ + O_2$	60%		(3.25)
		$CH_3S^+ + O_2 + CH_3$	25%	0.47	
		$CH_2S^+ + O_2 + CH_4$	15%	0.46	
$O_2^+ + (CH_3)_2S_2$	→	$C_2H_6S_2^+ + O_2$	80%		(3.26)
		$CH_3SCH_2^+ + O_2 + HS$	10%	0.42	
		$CH_3S_2^+ + O_2 + CH_3$	5%	0.47	

$CH_2S_2^+ + O_2 + CH_4$	5%	0.47

Both the reactions of dimethylamine and ethanol with O_2^+ yield two product ions, the molecular ion $[M]^+$ and the $[M - H]^+$ ion. The overall mass discrimination factors of these two product ions are assumed to be the same, and therefore the values are reported at the average of *m/z* 44.5 and *m/z* 45.5 respectively.

A plot of the values in table 3.09 shows that across the measured mass range there is a drop in the values of F_{MD}, such that the product ions are not being discriminated against, but instead enhanced. This plot is shown as figure 3.08.

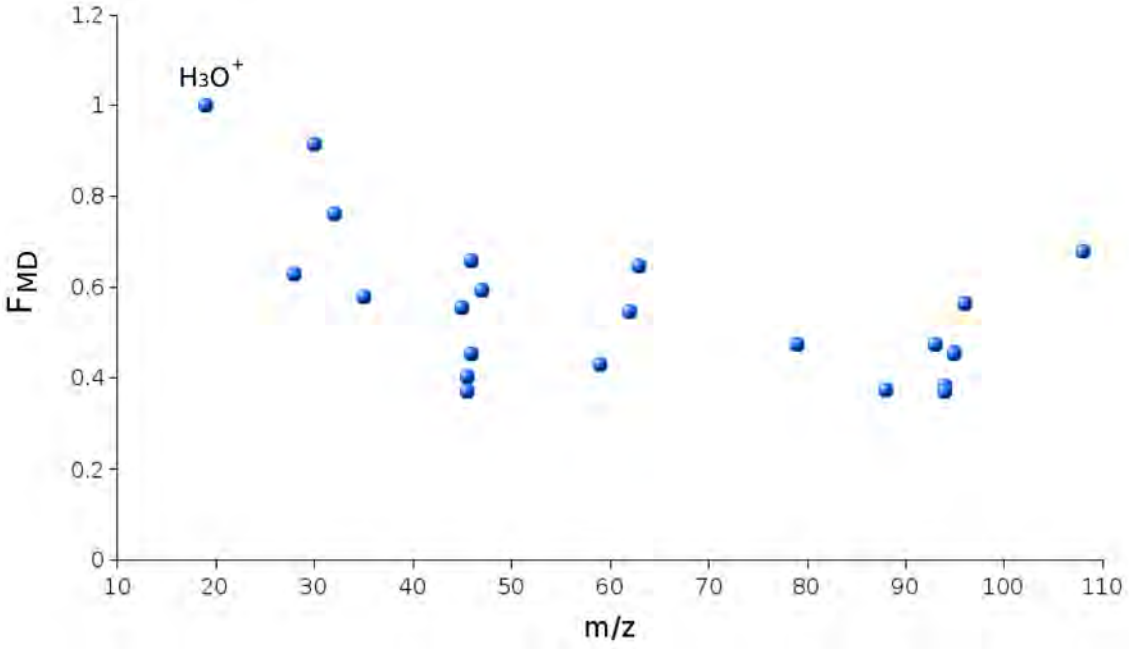

Figure 3.08. Values of the overall mass discrimination factor F_{MD} measured on a Voice100.

The above values are now easily translated into diffusion enhancement parameters by multiplying the reciprocal of the F_{MD} values by the equivalent value for M_R, i.e. solving equation 3.20 for $d_{p,i}$. The empirical mass dependent values of $d_{p,i}$ are given in table 3.10, which have been determined from a linear stepwise function of the M_R values in table 3.08. As an adjunct, the empirical diffusion enhancement parameters of three different ions diffusing through a 'helium-only' flow tube (Voice100 with 40 Torr L s^{-1} of helium flowing split through the inner and outer carrier inlets at a ratio of 3:5 yielding a flow tube pressure of 0.5 Torr) have been measured. The measured parameters, F_{MD} and $d_{p,i}$ of three neutral analytes, ethanol, acetone and dimethyl disulphide are shown in table 3.11.

Table 3.10. Empirical values of the diffusion enhancement factor $d_{p,i}$ determined on a Voice100 by the subtractive method defined in the text.

Ion	$d_{p,i}$	***Ion***	$d_{p,i}$	***Ion***	$d_{p,i}$
$HCNH^+$	1.28	$C_2H_6OH^+$	1.64	$C_6H_7^+$	2.92
H_3S^+	1.40	$C_2H_5O(H)^+$	1.46	$C_7H_9^+$	3.47
$C_2H_4OH^+$	1.70	$C_3H_6OH^+$	2.73	$C_2H_6S_2H^+$	3.78
$C_2H_6NH_2^+$	2.10	$C_3H_6O.NO^+$	4.10	$C_2H_6S_2^+$	4.74
$C_2H_6NH^+$	2.49	$C_2H_6SH^+$	1.90	CH_3Br^+	3.13
$C_2H_6N(H)^+$	2.56	$C_2H_6S^+$	2.34	$C_2H_4Br^+$	3.99

Table 3.11. Overall instrument mass discrimination and diffusion enhancement parameters of specific ions in a 'helium-only' flow tube. 40 Torr L s^{-1} of helium, P = 0.5 Torr.

Analyte	***Ion***		F_{MD}***(He)***	$d_{p,i}$***(He)***	$d_{p,i}$***(He) / $d_{p,i}$(He/Ar)***
	Precursor	*Product*			
Ethanol	H_3O^+	$C_2H_5OH_2^+$	0.131	7.44	4.54
Acetone	H_3O^+	$C_3H_6OH^+$	0.0822	13.7	5.03
Dimethyl disulphide	H_3O^+	$C_2H_6S_2H^+$	0.0436	38.5	10.2

The final column in table 3.11 gives the ratio of the $d_{p,i}$ values determined in helium, over the value for the same ion measured in the standard Voice100 flow tube conditions (15 Torr L s^{-1} of He, 25 Torr L s^{-1} of Ar). The three $d_{p,i}$ values given in table 3.11 give an acceptable mass dependent R^2 linear correlation of greater than 0.96.

The uncertainty of measurement for the determination of the empirical $d_{p,i}$ data is found to be solely based on the uncertainties on the rate coefficients shown in table 3.09. Any uncertainty arising from the permeation rate (for the certified tubes) is minimal in comparison, as this is always ± 2%.

3.3.5 Comparison of empirical and calculated diffusion enhancement parameters

A plot of the calculated and measured values $d_{p,i}$ for ions diffusing through the 'helium-only' flow tube is given as figure 3.09, where the empirical data is found to lie substantially above the calculated parameters. The same trend is observed in figure 3.10 which is a similar plot but for ions diffusing through a standard Voice100 flow tube that contains the helium/argon mixture discussed in section 3.1. It is apparent then that the experimental method and theory have a large discrepancy. Dryahina and Spanel [121] compare the values calculated for the reduced ionic mobility K_0 to a range of literature K_0 values, and find a very good correlation, such that all calculated parameters fell within the

experimental error of measurement. As all values of K_0 determined by either the Viehland or Dryahina methods which are reported in table 3.04 are very similar to the experimental K_0 values, [120,121] it must be concluded that the calculation of K_0 by either the Viehland method or the Dryahina parameterisation holds for a helium only carrier gas.

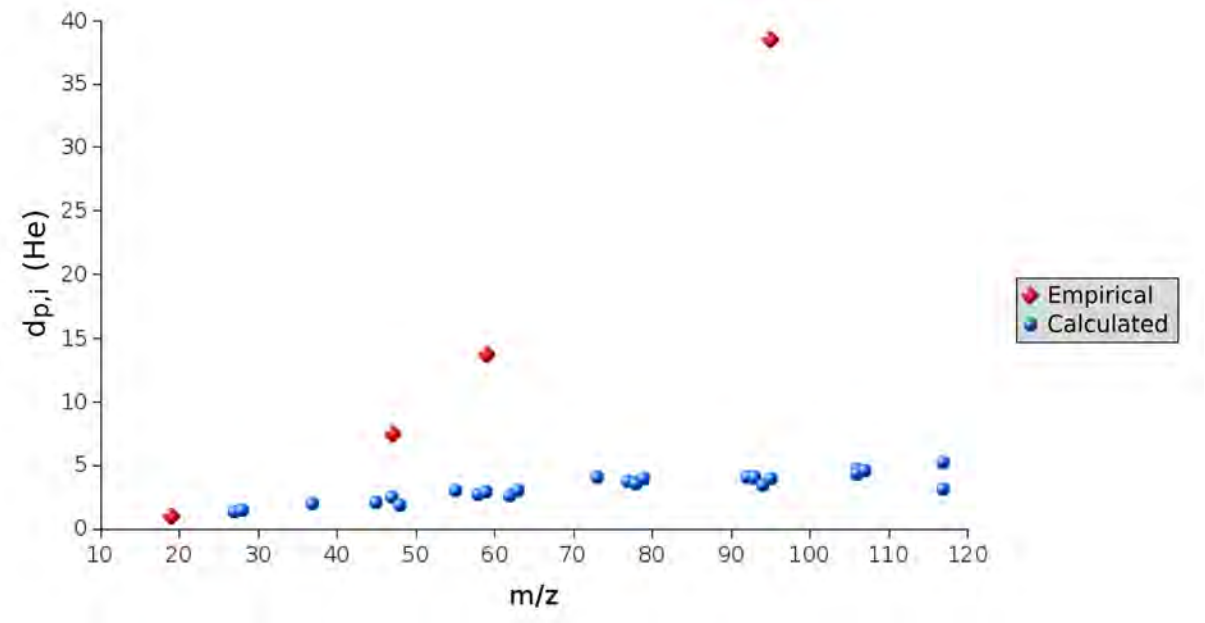

Figure 3.09. The empirical and calculated diffusion enhancement parameters of a range of ions diffusing through a Voice100 flow tube containing only helium (40 Torr L s^{-1} split in a 3:5 ratio between the inner and outer orifices) at 0.5 Torr.

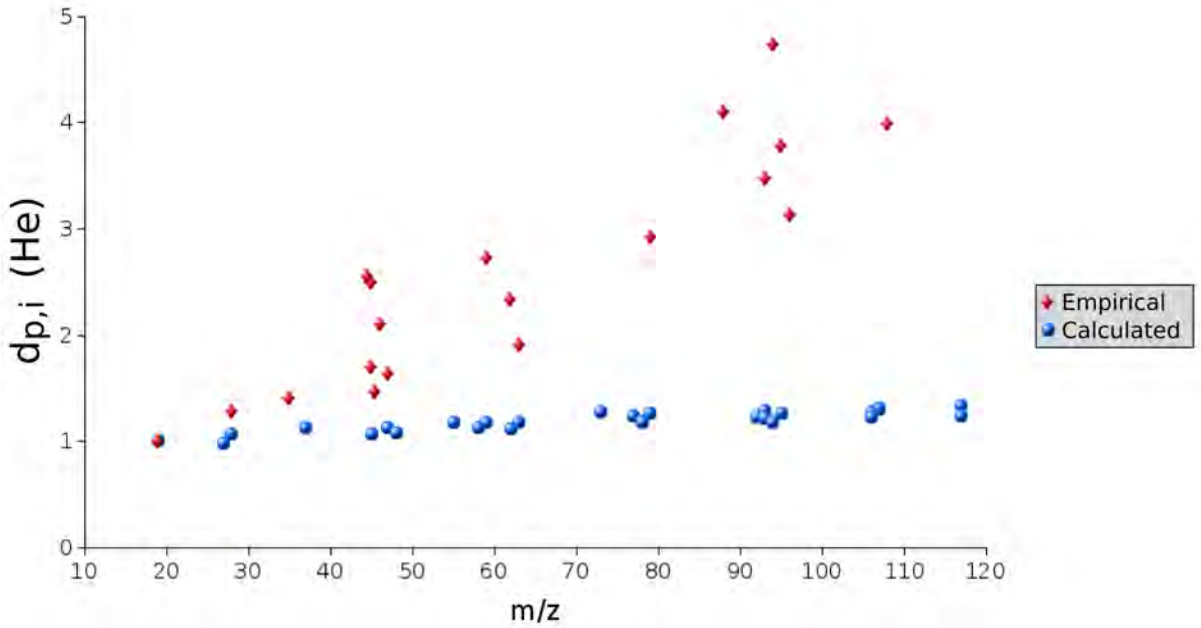

Figure 3.10. The empirical and calculated diffusion enhancement coefficients of a range of ions diffusing through a Voice100 flow tube containing a helium/argon mixture (15 Torr L s^{-1} He inner annulus; 25 Torr L s^{-1} Ar outer hole inlet) at 0.5 Torr.

If we assumed that collisions in the Voice100 flow tube are essentially between argon atoms and ions, literature values of K_0 for an ion diffusing through argon at a low field can be compared directly with the empirical data gathered here. H_3O^+ in Ar has been reported to have an experimental K_0 of 3.13 ± 0.15 $cm^2\ V^{-1}\ s^{-1}$ in a field of 40 Td. [133] When compared to the calculated values shown in table 3.05, the Viehland method gives an approximate value that is 30% greater than the experimental value (and the Dryahina parameterisation has already been discounted as a useful measure for ions in argon in section 3.3.3). Since the calculations of K_0 reproduce experimental results to an acceptable level of uncertainty, the deviations shown in figures 3.09 and 3.10 must arise from another source.

The discussion regarding equation 3.23 alludes to the proposed source of the large difference between the experimental and theoretical $d_{p,i}$ values. If the ion extraction efficiency has no mass dependence, M_R can be determined from the ratio of the detector signal to the ion extraction disk current. However for the Voice100, and all standard SIFT-MS instruments that extract ions through an orifice in a disk, this is not the case.

The ion sampling disk at the end of the Voice100 flow tube commonly has an applied potential of ~ -8 V, and therefore the field energy is known to be negligible for the majority of the reaction length when compared to the thermal energy as shown in equation 3.27. Here e is the elementary charge, E is the field (in V cm^{-1}), λ is the mean free path which is $1 / N\sigma$, and m_i and m_c are the ion and carrier gas masses respectively. [111]

$$\left(\frac{m_c}{m_i}+\frac{m_i}{m_c}\right) e E \lambda \ll k_B T \tag{3.27}$$

Assuming the collision cross sections calculated in table 3.05 for an ion-argon collision and a field of 0.32 V cm^{-1} at a distance of 4 cm,† equation 3.27 evaluates as 0.148 $k_B\ T$ for an H_3O^+ ion, and 0.083 $k_B\ T$ for the proton bound dimer of acetone (m/z 117). But as an ion approaches the sampling orifice the effective value of E increases, such that when an ion is 1 cm away from the extraction orifice, the left term of equation 3.27 is now greater than $k_B\ T$ for H_3O^+. The value for the proton bound dimer of acetone however is still less than $k_B\ T$, and therefore is less affected by the field than H_3O^+. The above argument also ignores the large field that penetrates into the flow tube from L1 which is directly behind the ion sampling orifice at a very negative potential (often as large as -100 V). The mass relationship shown in

† It is noted that this is large assumption if the only lens is the ion orifice, because the field is known to drop proportional to the square of the distance.

equation 3.27 outlines the point that lower mass ions will be affected more greatly by a field than high mass ions and it is therefore the differing momentum of ions approaching the disk that leads to the discrepancy observed in figures 3.08 and 3.09.

As the potential applied to the ion sampling orifice is negative, cations are by nature attracted to the lens, and as the above argument states, ions with less momentum (lighter ions) are more greatly affected by the field. Using a descriptive argument, a light ion that is on the centre axis of the flow tube approaching the orifice may get moved off axis by the potential field and collide with the disk creating a current observable on the downstream electrometer. Compare this situation to a heavier ion, also on the centre axis of the flow tube, that has greater momentum and will be influenced less by the field. There is therefore less probability for it to move off axis than the lighter ion and consequently greater probability for it to enter the downstream chamber through the orifice. In effect therefore, higher mass ions should give a greater $I_{det} / I_{D/S}$ ratio than low mass ions and lead to reverse mass discrimination.

However, as this phenomenon is both coupled to the downstream chamber ion optics mass discrimination and the differential diffusion resulting from the flow tube it cannot be determined empirically using a standard Voice100 apparatus. The value of E (the field strength) cannot be easily determined for a Voice100 tube as in reality both the electrometer and L1 emit fields into the flow tube. But, if we assume that the calculated values of K_0 using the method of Viehland *et al.* [120] are correct for all measured ion-carrier collisions, the parameter can be resolved by a subtractive method as shown in equation 3.28, where the empirical $d_{p,i}$ is resolved into two parameters, the calculated $d_{p,i}$ the diffusion enhancement term, and M_p the momentum based mass discrimination parameter. The values of M_p are also linked to the carrier gas due to momentum relying on the reduced mass relationship (which will alter between He, Ar and He/Ar mixtures) and therefore this parameter is completely empirical. A selection of M_p values for both the helium and helium/argon carrier gas are then given in table 3.12.

$$d_{p,i}(Empirical) = d_{p,i}(Calculated) \; x \; M_p \tag{3.28}$$

Because the calculated values of $d_{p,i}$ for the helium and argon carrier gas mixture are found to be near unity across the measured mass range, the M_p parameter is responsible for the majority of the enhancement of higher mass ions observed on a Voice100. This is in direct

contrast to the helium only flow tube where both the M_p and flow tube diffusion enhancement parameters lead to the observed enhancement of higher mass ions.

Table 3.12. Empirical values of the M_p enhancement parameter, where Mp (He/Ar) is for a standard Voice100 flow tube comprising both helium and argon in a 3:5 ratio and at a pressure of 0.5 Torr.

Ion	***m/z***	***$D_{p,i}$ (He)***	***M_p (He)***	***$D_{p,i}$ (He/Ar)***	***M_p (He/Ar)***
$HCNH^+$	28			1.28	1.21
$C_2H_4OH^+$	45			2.10	1.59
$C_2H_6OH^+$	47	7.44	2.99	1.64	1.45
$C_2H_5O(H)^+$	45.5			1.46	1.36
$C_3H_6OH^+$	59	13.7	4.80	2.73	2.31
$C_2H_6SH^+$	63			1.90	1.61
$C_2H_6S^+$	62			2.34	2.11
$C_7H_9^+$	93			3.47	2.87
$C_2H_6S_2H^+$	95	38.5	9.87	3.78	3.00
$C_2H_6S_2^+$	94			4.74	4.02

3.3.6 Conclusions

The overall measurement of the mass discrimination function F_{MD} is now known to consist of three non-separable parts, the mass discrimination due to the ion optics of the downstream chamber, the flow tube diffusion enhancement, and the momentum based diffusion enhancement parameter that arises near the ion sampling orifice. This new third parameter cannot be determined theoretically due to the requirement that the field strength E must be known accurately over the short region in which it is important. This is not possible in current flow tube designs.

The previous method of measuring mass discrimination used on the FA-SIFT at the University of Canterbury applies a similar method to that discussed by Spanel and Smith. [115] However, a thorough understanding of mass discrimination is less important on the FA-SIFT, as it's primary use is the measurement of ion-molecule rate coefficients that requires only the measurement of one ion at a specific mass. Although, measurement of product ion branching ratios would benefit from an accurate understanding of mass discrimination and therefore it is recommended that the new method discussed here is implemented on the FA-SIFT.

3.4 Determining Rate Coefficients for Hydronium Ion Water Cluster Reactions

3.4.1 Introduction

Of the three precursor ions used on the Voice100 (H_3O^+, NO^+ and O_2^+), H_3O^+ tends to be of general use due to its ability to very softly ionise neutral species through the process of proton transfer. The product ion from proton transfer $[M + H]^+$ is one mass unit higher than the neutral analyte. [61] However, in the SIFT-MS method, H_3O^+ suffers from a series of secondary reactions due to its reasonably rapid reactions with neutral water species forming the hydronium ion water clusters $H_3O^+.(H_2O)_n$ (n = 1, 2, 3). [71] Water is present in any gaseous samples. These water clustering reactions have been studied quite rigorously during the 1960's and 1970's due to their importance to the chemistry of the earth's upper atmosphere, [9,130,134-136] which is similar to the conditions in a Voice100 flow tube (pressure ~1 Torr, ion density ~10^7 ions cm^{-3}). The sequential termolecular clustering reactions of the hydronium ions with H_2O are given as reactions 3.29 – 3.31, where, in the case of the Voice100, M = He or Ar.

$$H_3O^+ + H_2O + M \rightarrow H_3O^+.H_2O + M \quad (3.29)$$

$$H_3O^+.H_2O + H_2O + M \rightarrow H_3O^+.(H_2O)_2 + M \quad (3.30)$$

$$H_3O^+.(H_2O)_2 + H_2O + M \rightarrow H_3O^+.(H_2O)_3 + M \quad (3.31)$$

When the Voice100 is operating at the conditions given in section 2.2, with a capillary flow of ~150 ml $atmosphere^{-1}$ min^{-1}, a range of relative $H_3O^+.(H_2O)_n$ (n = 0, 1, 2, 3) intensities are observable based on the moisture content of the sample entering the flow tube. For instance, a sample of 'dry nitrogen' will yield mostly H_3O^+ (*m/z* 19), with approximately 10 % conversion to $H_3O^+.H_2O$ (*m/z* 37). A breath sample (6% water at ~35 ºC) yields predominantly $H_3O^+.(H_2O)_2$ and $H_3O^+.(H_2O)_3$.

If each of the hydronium ion water clusters were to react in an identical fashion with an analyte, the formation of these higher mass clusters would be of little importance. However, as the hydronium ion grows in cluster size the proton affinity increases by approximately 90 kJ mol^{-1} per cluster and therefore the reactivity towards proton transfer processes decreases with increasing cluster size. The proton affinities of each of the cluster

ions are given in table 3.13, which are sourced from the NIST webbook database. [31]

Table 3.13. Proton affinities of the hydronium ion water clusters based on the proton affinity of H_3O^+ and the sequential enthalpy of binding. [31]

	Proton Affinity */kJ mol^{-1}*
H_3O^+	*691*
$H_3O^+.H_2O$	*827*
$H_3O^+.(H_2O)_2$	*911*
$H_3O^+.(H_2O)_3$	*984*

It is well understood that when a proton transfer reaction is known to be exothermic, it will always occur with unit efficiency, such that the reaction rate coefficient k of the hypothetical reaction $AH^+ + B \rightarrow BH^+ + A$ can be predicted with some accuracy by calculation of the collision rate coefficient k_c. [61] Since a large majority of the analytes (B) commonly studied by SIFT-MS have a proton affinity greater than 691 kJ mol^{-1} (the proton affinity of H_2O), reaction rate coefficients for the specific analyte reacting with H_3O^+ can be easily calculated (see section 2.8). However, the same analyte B will usually have a proton affinity less than 984 kJ mol^{-1}, and will therefore not react with $H_3O^+.(H_2O)_3$ by the process of proton transfer at the collision limiting rate coefficient. The reaction of $H_3O^+.(H_2O)_3 + B$ may instead yield products such as $B.H_3O^+.(H_2O)_n$ where n can be 0 – 3. This "switching reaction" can have any value of k/k_c (the reaction efficiency) and it is therefore of great importance to be able to accurately measure the reactions of the hydronium ion water clusters with specific analytes. A more accurate understanding of the water cluster chemistry of a particular analyte leads to a more accurate measurement of a concentration. Also, due to the nature of the commercial environment, it is of interest to be able to rapidly increase the database of compounds available to SIFT-MS users, and therefore a simple rapid method to measure rate coefficients of the hydronium ion water clusters is very useful.

Firstly, using the instrument mass discrimination data from section 3.3 to normalise the count values, the rate coefficients for the sequential reactions shown in reactions 3.29 – 3.31 where determined for a Voice100 by altering the moisture content entering the flow tube through the sample inlet, and fitting rate coefficients to that data. Accurate mixtures of nitrogen and water vapour were generated using knowledge of the vapour pressure of water at a room temperature. Bierbaum *et al.* [130] have measured these termolecular rate coefficients

at a similar flow tube number density of helium. The rate coefficient for the formation of *m/z* 73 from *m/z* 55 was found in the present study to be much faster than that predicted by Bierbaum *et al*. that may be attributed to the presence of argon. However Young *et al.* [134] have previously measured the sequential clustering reactions of the hydronium ion in an argon environment, and found the formation of *m/z* 73 to be slower than that of Bierbaum and co-workers. No explanation is known for this anomaly. The pseudo-bimolecular rate coefficients for the sequential reactions of the hydronium ion water clusters fitted to Voice100 data are given as reactions 3.32 – 3.34, where each has a sequential uncertainty of ± 25%. These rate coefficients apply to a flow tube pressure of 0.5 Torr, which is equivalent to a number density of ~1.6 x 10^{16} molecules cm^{-3}. The rate coefficients for the reverse processes to those shown in reactions 3.32 – 3.34 are known to be very slow, and therefore will not affect the overall measured rate coefficient. [130] M is defined as the third body in a termolecular process, in this case argon.

$$H_3O^+ + H_2O \xrightarrow{M} H_3O^+.H_2O \qquad k = 1.1 \times 10^{-11}\ cm^3\ molecule^{-1}\ s^{-1} \quad (3.32)$$

$$H_3O^+.H_2O + H_2O \xrightarrow{M} H_3O^+.(H_2O)_2 \qquad k = 2.4 \times 10^{-11}\ cm^3\ molecule^{-1}\ s^{-1} \quad (3.33)$$

$$H_3O^+.(H_2O)_2 + H_2O \xrightarrow{M} H_3O^+.(H_2O)_3 \qquad k = 4.0 \times 10^{-11}\ cm^3\ molecule^{-1}\ s^{-1} \quad (3.34)$$

The reactions of the water clusters of the hydronium ion with an analyte have been previously measured using the variable temperature flowing afterglow technique (VT-FA) by Viggiano and co-workers. [137] By varying the temperature and pressure in the inlet lines and flowing afterglow reaction region, reasonable selectivity of a specific $H_3O^+.(H_2O)_n$ ion was gained. This type of measurement is difficult to undertake, and is not an efficient method for rapidly measuring the reactions of hydronium ion water clusters with analytes.

An initial approach to measure the water clustering rates involved attempting to selectively inject a range of $H_3O^+.(H_2O)_n$ ions into the flow tube through the Venturi orifice using the upstream quadrupole mass filter. This approach was abandoned because any *m/z* 37 ions injected into the flow tube were found to de-cluster back to *m/z* 19 irrespective of the ion injection energy, and no $H_3O^+.2H_2O$ (*m/z* 55) nor $H_3O^+.3H_2O$ (*m/z* 73) ions were measurable on the Venturi plate electrometer. It is concluded that water cluster ions cannot be directly injected into the Voice100 flow tube from the upstream ion selection chamber.

A second and much more successful approach involves solving the rate law

expressions for all reactions occurring in the flow tube simultaneously, and this topic shall be the main focus of the remainder of this chapter.

3.4.2 Solutions to the $H_3O^+.(H_2O)_x$ integrated rate law

For the sequential reactions of $H_3O^+.(H_2O)_{n-1} + H_2O + M \rightarrow H_3O^+.(H_2O)_n + M$ where n = 1, 2, or 3, a rate law for each step can be written as equations 3.35 – 3.38, where $\upsilon(X^+)$ is the observed rate of reaction for X^+, k_n is the reaction rate coefficient for the reaction of $H_3O^+.(H_2O)_{n-1} + H_2O$, k_{Bn} is the reaction rate coefficient for the reaction of $H_3O^+.(H_2O)_{n-1} + B$, and $[Y]$ is the concentration of Y whether it is an ion or neutral.

$$\nu(H_3O^+) = -k_1.[H_3O^+][H_2O] - k_{B1}.[H_3O^+][B] \tag{3.35}$$

$$\nu(H_3O^+.H_2O) = -k_2.[H_3O^+][H_2O] - k_{B2}.[H_3O^+.H_2O][B] + k_1.[H_3O^+][H_2O] \tag{3.36}$$

$$\nu(H_3O^+.2H_2O) = -k_3.[H_3O^+][H_2O] - k_{B3}.[H_3O^+.2H_2O][B] + k_2.[H_3O^+.H_2O][H_2O] \tag{3.37}$$

$$\nu(H_3O^+.3H_2O) = -k_{B4}.[H_3O^+.2H_2O][H_2O] + k_3.[H_3O^+.2H_2O][B] \tag{3.38}$$

Where the observed rates and values of k_n are known, and the value of k_{B1} has been determined by standard methods, the values of k_{B2}, k_{B3} and k_{B4} can be obtained from solving the equations using analytical methods. This has been achieved using the Mathematica package and the very complex solutions to the integrated rate laws are given in appendix B.

Because equations 3.35 – 3.38 are rate laws such that $\upsilon(X^+) = d[X^+]/dt$, each equation will hold true for all values of t, and each term of one equation will take into account contributions from the other terms. To simplify the scenario, as $t \rightarrow 0$, each term will affect other terms less, and therefore where t is very close to zero the contributions between terms of one equation may be discounted. Practically, this assumption means that each term of each equation can be integrated independently of the others as long as the time length t is a fraction of the entire reaction time. By then iterating the calculation over each time fraction used the values of k_{Bn} can be obtained by solution of the equations. The four integrated rate expressions where each term has been independently integrated are given as equations 3.39 – 3.42, where I_0^{Y+} and I_t^{Y+} (where Y^+ is any ion) are the intensities of the ion measured on the particle multiplier.

$$I_t^{H_3O^+} = -\left(I_0^{H_3O^+}\exp\left(-k_1[H_2O]t\right)\right)+\left(I_0^{H_3O^+}-I_0^{H_3O^+}\exp\left(-k_{B1}[B]t\right)\right) \quad (3.39)$$

$$I_t^{H_3O^+.H_2O} = -\left(I_0^{H_3O^+.H_2O}\exp\left(-k_2[H_2O]t\right)\right)+\left(I_0^{H_3O^+.H_2O}-I_0^{H_3O^+.H_2O}\exp\left(-k_{B2}[B]t\right)\right)$$
$$+\left(I_0^{H_3O^+}-I_0^{H_3O^+}\exp\left(-k_1[H_2O]t\right)\right) \quad (3.40)$$

$$I_t^{H_3O^+.2H_2O} = -\left(I_0^{H_3O^+.2H_2O}\exp\left(-k_3[H_2O]t\right)\right)+\left(I_0^{H_3O^+.2H_2O}-I_0^{H_3O^+.2H_2O}\exp\left(-k_{B3}[B]t\right)\right)$$
$$+\left(I_0^{H_3O^+.H_2O}-I_0^{H_3O^+.H_2O}\exp\left(-k_2[H_2O]t\right)\right) \quad (3.41)$$

$$I_t^{H_3O^+.3H_2O} = \left(I_0^{H_3O^+.3H_2O}-I_0^{H_3O^+.3H_2O}\exp\left(-k_{B4}[B]t\right)\right)$$
$$+\left(I_0^{H_3O^+.2H_2O}-I_0^{H_3O^+.2H_2O}\exp\left(-k_3[H_2O]t\right)\right) \quad (3.42)$$

3.4.3 Experimental process

The first requirement is a complete understanding of the reaction of the unclustered H_3O^+ ion with the analyte of interest that is gained by the methods discussed in section 2.6.1. An accurate measurement of the reaction rate coefficient is required because each of the hydronium ion water cluster rate coefficients are measured relative to the H_3O^+ rate coefficient. Once this understanding has been gained, a small leak of water vapour is passed into the flow tube from the water bubbler through a 5 SCCM flow controller shown in figure 2.10 (chapter 2) A suitable leak is established by increasing the water vapour flow rate until the signal of *m/z* 73 is greater than 2% of the *m/z* 19 signal. Then, by varying the flow of analyte from the glass gas handling line, reaction rate coefficients for the water cluster ions are measured in the standard way. A reasonable pressure is required in the glass gas handling line to avoid back-flushing of water vapour through the needle valve. Therefore many analytes with vapour pressures less than 3 Torr require a dilution by argon in order to effectively measure the neutral analyte flow. Back-flushing manifests as a measurable pressure increase on the flowing side of the differential Baratron used in the glass gas handling line (figure 2.10). An example of a hydronium ion water cluster rate measurement is shown in figure 3.11.

The slopes of each ion decaying with respect to the analyte flow divided by the reaction time gives the effective rate coefficient k_{eff}. Finally, using the model shown in 3.39 – 3.42 a guess is made for the initial H_3O^+ intensity at the start of the flow tube and the values of k_{Bn}. Then, the intensities of H_3O^+ and its three sequential water clusters are determined

along the course of the flow by iterating the results returned from equations 3.39 – 3.42 over a very short time period (1/1000th of the reaction time). The guessed values of k_{Bn} give an initial guess for k_{eff} where all values of k_n are known (from reactions 3.32 – 3.34) across a range of appropriate flows. Then by using a Newton-Raphson optimisation, k_{Bn} values are fitted to the empirical k_{eff} values. The situation is further simplified as k_{B1} is already known from a decay rate that has been measured in the absence of water vapour. The results of this type of analysis for using sec-butyl acetate as a test case are given in table 3.14 and the decay rates are shown in figure 3.11. In table 3.14, k_c is the collision limiting rate coefficient, which is the theoretical upper limit of a rate coefficient determined using the method prescribed by Su and Chesnavich. [107]

For the reaction of $H_3O^+.(H_2O)_2$ with sec-butyl acetate, the value of k_{Bn} is observed to be ~20% greater than k_c. This observed discrepancy is attributed to the uncertainty of the measurement and deconvolution which is discussed further in section 3.4.4.

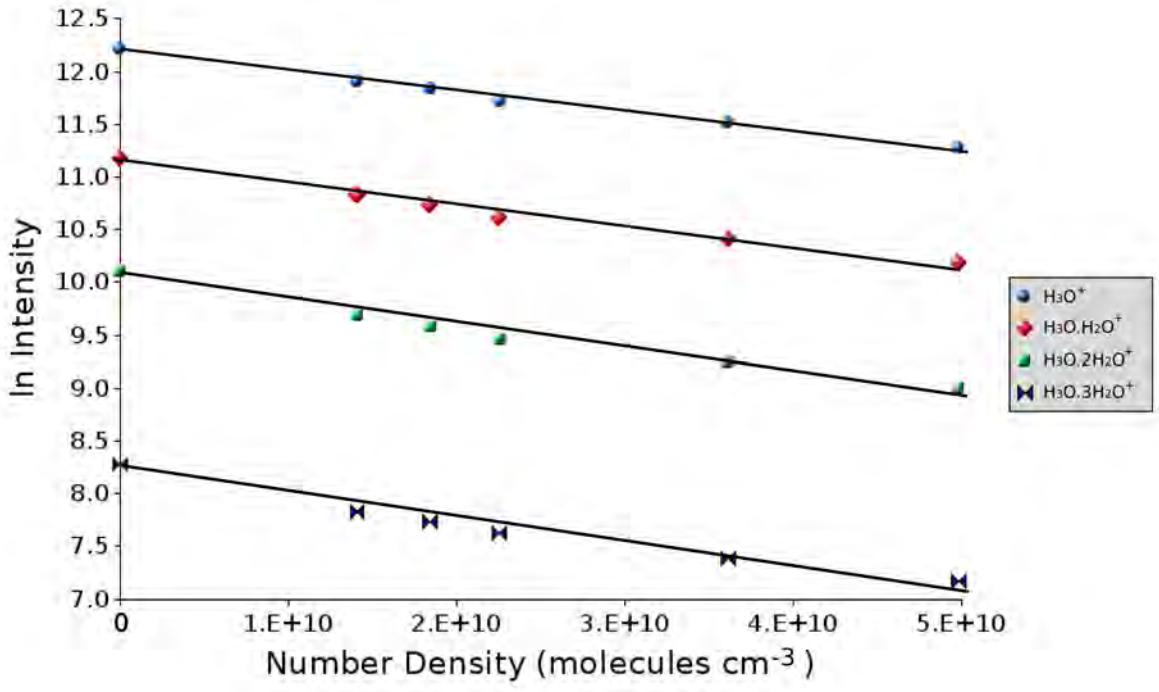

Figure 3.11. Example of a rate coefficient measurement using H_3O^+ and the three successive H_2O cluster ions reacting with sec-butyl acetate.

Table 3.14. Apparent rate coefficients, k_{eff} and deconvoluted rate coefficients k_{Bn} for the reactions H_3O^+ and the three sequential water clusters with sec-butyl acetate.

n	***Ion***	***k_{eff}/cm^{-3} molecule^{-1} s^{-1}***	***k_{Bn}/cm^{-3} molecule^{-1} s^{-1}***	***k_c/cm^{-3} molecule^{-1} s^{-1}***
1	H_3O^+	3.08 x 10^{-9}	3.1 x 10^{-9}	3.3 x 10^{-9}
2	$H_3O^+.H_2O$	2.90 x 10^{-9}	2.1 x 10^{-9}	2.5 x 10^{-9}
3	$H_3O^+.(H_2O)_2$	2.75 x 10^{-9}	2.6 x 10^{-9}	2.2 x 10^{-9}
4	$H_3O^+.(H_2O)_3$	2.60 x 10^{-9}	1.8 x 10^{-9}	2.0 x 10^{-9}

3.4.4 Uncertainties

The absolute uncertainty on the measurement of a rate coefficient using the Voice100 in the absence of water is ± 15%, which is the uncertainty on k_{B1}. This is similar to the value quoted by Scott [74] for the University of Canterbury FA-SIFT. When water vapour is added to the flow tube, the uncertainty on the value of k_{eff} is greater than for a standard measurement, and is deemed to be ± 20%, where the 5% increase is due to the slight curvature observed in the decay plot at higher flows. Each fitted value of k_n (the rate coefficients of the sequential water clustering reactions) is deemed to have a large absolute uncertainty of ± 25% determined from the difference between the expected and measured ion intensities of *m/z* 19, 37, 55 and 73 over a range of humidities and repeated measurements.

As values of k_B rely on the sequential addition of water molecules and the measurement of k_{eff}, the absolute uncertainty on the individual values of k_{Bn} is found to increase rapidly as *n*, the cluster size, increases. Therefore the absolute uncertainties on the rate coefficients for the reactions of the hydronium ion water clusters reacting with an analyte are given in table 3.15.

Table 3.15. The absolute uncertainties of measurement for a $H_3O^+.(H_2O)_n$ + Analyte rate coefficient.

n	***Ion***	***Uncertainty on***		
		k_{eff}	k_n	k_{Bn}
1	H_3O^+	± 15%		± 15%
2	$H_3O^+.H_2O$	± 20%	± 25%	± 45%
3	$H_3O^+.(H_2O)_2$	± 20%	± 50%	± 70%
4	$H_3O^+.(H_2O)_3$	± 20%	± 75%	± 95%

3.4.5 Validation of method

The analytical solutions to equations 3.35 – 3.38 (the solutions derived in appendix B) and the simplified iterative method have been compared with the empirical rate of hydronium ion water clusters reacting with acetone as measured by Yang *et al.* [138] and the rates of the same ions reacting with a acetone and methanol as measured by Viggiano *et al*. [137] in table 3.16. The values determined by the analytical solutions and the iterative method are found to be exactly the same within 0.1% and therefore only the iterative solutions are given. The differences in the $H_3O^+.(H_2O)_2$ and $H_3O^+.(H_2O)_3$ rate coefficients measured in this study compared to the literature rate coefficients is indicative of the large uncertainty. However, the two methods presented here are preferred due to the ease of measurement. From the comparisons shown in table 3.16, it is seen that the current methods give acceptable agreement with the literature values, albeit with increasing uncertainty for the *m/z* 55 and *m/z* 73 clusters. The $H_3O^+.(H_2O)_2$ rates measured here are found to be faster than the previously measured rates in both cases. This anomaly may be due to a k_n rate coefficient not accurately modelling the Voice100 flow tube.

Phosphine is a third test case for the above method where the results (which have recently been published in Analytical Chemistry [58]) accurately reflect the thermochemistry of the studied reactions. The proton affinity and gas basicity of phosphine are known to be 785 kJ mol^{-1} and 750 kJ mol^{-1} respectively. Therefore, with reference to table 3.13, H_3O^+ is expected to transfer a proton at the collision limiting rate (k_c). The cluster ions $H_3O^+.(H_2O)_2$ and $H_3O^+.(H_2O)_3$ may undergo ligand switching reactions but proton transfer will not occur.

Table 3.16. Comparison of literature $H_3O^+.(H_2O)_n$ + analyte rate coefficients to those determined using the method described in the text.

n	***Compound***	***k_{Bn} [kc] /10^{-9} cm^3 molecule^{-1} s^{-1}***				
		Acetone			*Methanol*	
		This study	*Ref [138]*	*Ref [137]*	*This Study*	*Ref [137]*
1	H_3O^+	3.9 [3.9]	3.8 [3.9]		2.7 [2.7]	2.7 [2.7]
2	$H_3O^+.H_2O$	2.7 [3.1]	3.2 [3.1]	2.3 [3.1]	2.3 [2.3]	1.9 [2.2]
3	$H_3O^+.(H_2O)_2$	3.7 [2.8]	2.8 [2.8]	2.2 [2.8]	3.3 [2.1]	1.8 [2.1]
4	$H_3O^+.(H_2O)_3$	2.3 [2.6]	2.4 [2.6]	2.1 [2.6]	0.8 [2.0]	1.7 [2.0]

The reaction of $H_3O^+.H_2O$ with PH_3 has been calculated by ab-initio methods and is found to be approximately thermo-neutral with the inclusion of an entropy term. The four

reactions of the hydronium ion water clusters with phosphine were measured and deconvoluted to obtain a value for k_{Bn} using the method described above and are given as equations 3.43 – 3.46. Each reaction was found to occur at or very near the collision limiting rate prior to deconvolution. The $PH_3.H_3O^+$ ions shown in equations 3.45 and 3.46 were observed in the mass spectra. However it is impossible to tell which precursor ion these product ions were formed from without the aid of isotopic labelling, which is outside of the scope of the current research.

			k_{Bn} (k_c) /10^{-9} cm^3 molecule^{-1} s^{-1}	
$H_3O^+ + PH_3$	→	$PH_4^+ + H_2O$	1.7 (1.7)	(3.43)
$H_3O^+.H_2O + PH_3$	→	$PH_4^+ + 2H_2O$	1.5 (1.5)	(3.44)
$H_3O^+.(H_2O)_2 + H_2O$	→	$PH_3.H_3O^+ + 2H_2O$	0.6 (1.3)	(3.45)
$H_3O^+.(H_2O)_3 + H_2O$	→	$PH_3.H_3O^+ + 3H_2O$	0.6 (1.1)	(3.46)

The product ion channels shown in reactions 3.44 and 3.45 are ligand switching reactions that are only postulated, because the secondary association reaction of the PH_4^+ ion with water also forms the *m/z* 54 ($PH_4.H_2O^+$) ion that cannot be discounted. The observation that the measured rate coefficients of these two reactions are slower than k_c (although very close to k_c with uncertainty) gives support to the thermodynamic predictions above.

3.5 Conclusions

The Voice100 SIFT-MS, due to its decreased size and other engineering constraints, has much more complex flow tube dynamics than previous SIFT instruments. Through a range of experiments described in this chapter the performance and diffusion characteristics of the Voice100's flow tube has been analysed to such an extent that the measurement of ion-neutral reaction rate coefficients is possible. Also, a much more in-depth understanding of the mass discrimination of SIFT-MS instruments has now been gained. The ability to accurately measure the mass discrimination on the Voice100 allows for a more exact determination of ion-molecule product ion branching ratios.

Furthermore, a reduced method for the measurement and deconvolution of rate coefficients for the water cluster ions reacting with analytes has been presented that now enables the SIFT-MS compound database to be rapidly expanded such that new and interesting applications can be added and analytical measurements can take place in the presence of water vapour.

CHAPTER 4

GeoVOC: GEOCHEMICAL VOLATILE ORGANIC COMPOUNDS

4.1 An Introduction to Oil and Gas Exploration

The oldest and simplest method used in oil and gas exploration is the detection of oil macro-seeps, where a black tar-like substance is seen to come out of the ground through sedimentary rocks. Thousands of these macro-seeps can be found around the world, however the most important of all is at the site of the 'inception of the modern petroleum industry' at Oil Creek, near Titusville in Pennsylvania, USA in August of 1859. [139] This aptly named site is disputed to be the first major commercial venture into the extraction of high quality petroleum oil in the world that increased the yearly petroleum oil production of the USA from less than 2000 barrels† in 1858, to well over 2.5 million barrels seven years later. By drilling a 69 ½ ft well near to an observed macro-seep where oil was seen to be bubbling through a river, Edwin L. Drake found that the oil extracted was a lighter more volatile substance than the thick tar that exuded from the river bed. [139] This finding was common among the early 'wildcat' drillers, who would drill a well near a known macro-seep or previous oil well, in an attempt to exploit the regions oil supply. [140] These early findings, however, were based upon a random chance of finding a large, easily observable macro-seep and science played little part in the exploration for new drilling sites.

In 1861, T. Sterry Hunt proposed the 'anticlinal theory', one of the first geochemical theories to be published that was based on scientific findings. The theory was based on observations in Canada, where he discovered that the majority of oil was found along the rises of anticlinal folds, and with this observation was able to successfully predict other sites of oil accumulation. [139] An anticlinal fold is a ridge where the oldest strata is in the middle of the fold, and the younger strata falls either side creating a cap. If the strata above the anticline is non-porous, volatile hydrocarbon matter such as oil and gas may get trapped at the top of the anticline by the action of flowing water (the hydrodynamic effect) leading to accumulation. [141]

† 1 Oil Barrel (blue) = 42 US Gallons = 159 L

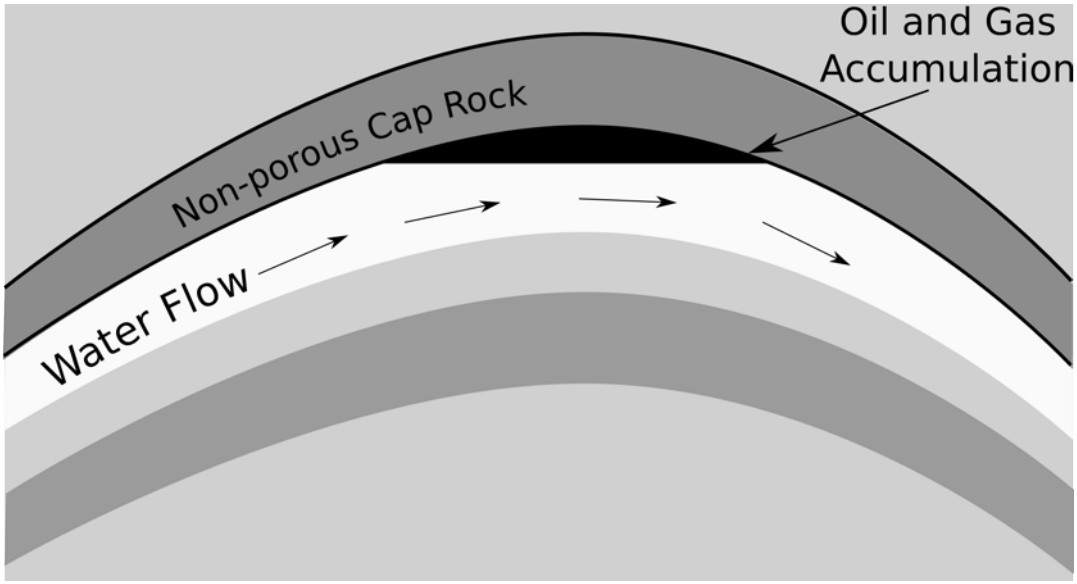

Figure 4.01. Oil and gas accumulation at the top of an anticline.

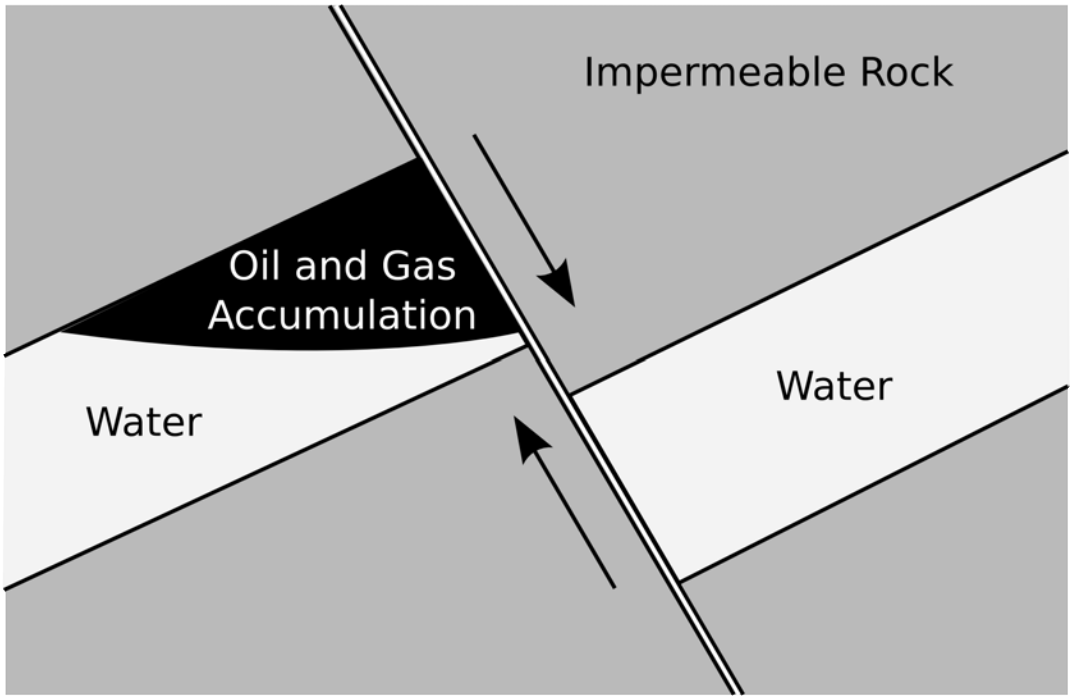

Figure 4.02. A fault based oil and gas accumulation where the motion of the fault line has trapped hydrocarbon matter.

Figure 4.01 shows an anticlinal cap and an accumulation of oil underneath the cap. Faults are also known to accumulate hydrocarbons, which are similar to anticlinal folds except instead of a cap shape, a fracture in the crust rock leads to two tectonic regions slipping past one another. [140] Figure 4.02 shows a fault and the accumulation of oil at the fault.

If there is a crack in the cap rock or fault line, oil may seep out and rise to the surface causing the observation of a macro-seep. However, if the crack in the cap rock is very minor, or the cap rock is very mildly porous a 'micro-seep' can be observed.

A micro-seep is defined as a region where low molecular weight hydrocarbons (C_1 – C_5) are not actively seeping toward the surface (i.e. not being forced by pressure or water currents), but instead passive seepage occurs such as diffusion. [142] These seep zones usually contain low molecular weight hydrocarbons which can be observed at the surface to be above the normal background levels of the strata. Also the patterns of hydrocarbon density commonly occur in a halo, crescent, apical or linear shapes that are aligned to the source of the hydrocarbon accumulation below. [142] Therefore near-surface or surface detection of hydrocarbons should be an effective method for a preliminary detection of a hydrocarbon reservoir. [143] However, the use of near-surface hydrocarbon detection has not been rapidly taken up by the large majority of petro-chemical exploration companies because both the mechanisms of seepage and migration are still very poorly understood. [144] Often, a point of seepage may be tens to hundreds of kilometres away from a reservoir because of a long migration pathway that may result from sediments, tectonics or fluid flows where all of these mechanisms are referred to as horizontal migration. [145] Therefore because near-surface hydrocarbon analysis does not necessarily accurately reflect the make-up of the strata below, the technique has not been commercially well received. But by collaborative use of near-surface detection technologies and sub-surface imaging techniques, a more definitive knowledge of oil and gas reservoirs may be obtained. Figure 4.03, adapted from Schumacher [146] outlines the link between these two techniques, and four possible mechanisms of micro-seepage. Vertical and horizontal migration are both known to be aided by regions of high salt content (figure 4.03b and c), and physical barriers may in certain situations lead to physical fractionation of deeper wells from more shallow wells (figure 4.03d).

The origins of oil in the earth has been long debated, however it is now widely accepted that the majority of methane and larger paraffinic molecules (propane, butane etc.) that are below the surface of the earth, arise from biogenic sources. [140] Plankton and other small organisms are believed to have accumulated in clays and other sediments on the ocean floor. These accumulations are very slowly over time lithified into black marine shale that becomes the major strata where oil is created. Shallow fresh water environments are also known to bear large amounts of 'microbial gas', so dubbed as the methane found in these areas is known to be generated from bacterial action. The origins of oil and gas deposits are usually

determined by carbon isotope ratio mass spectrometry. [147,148]

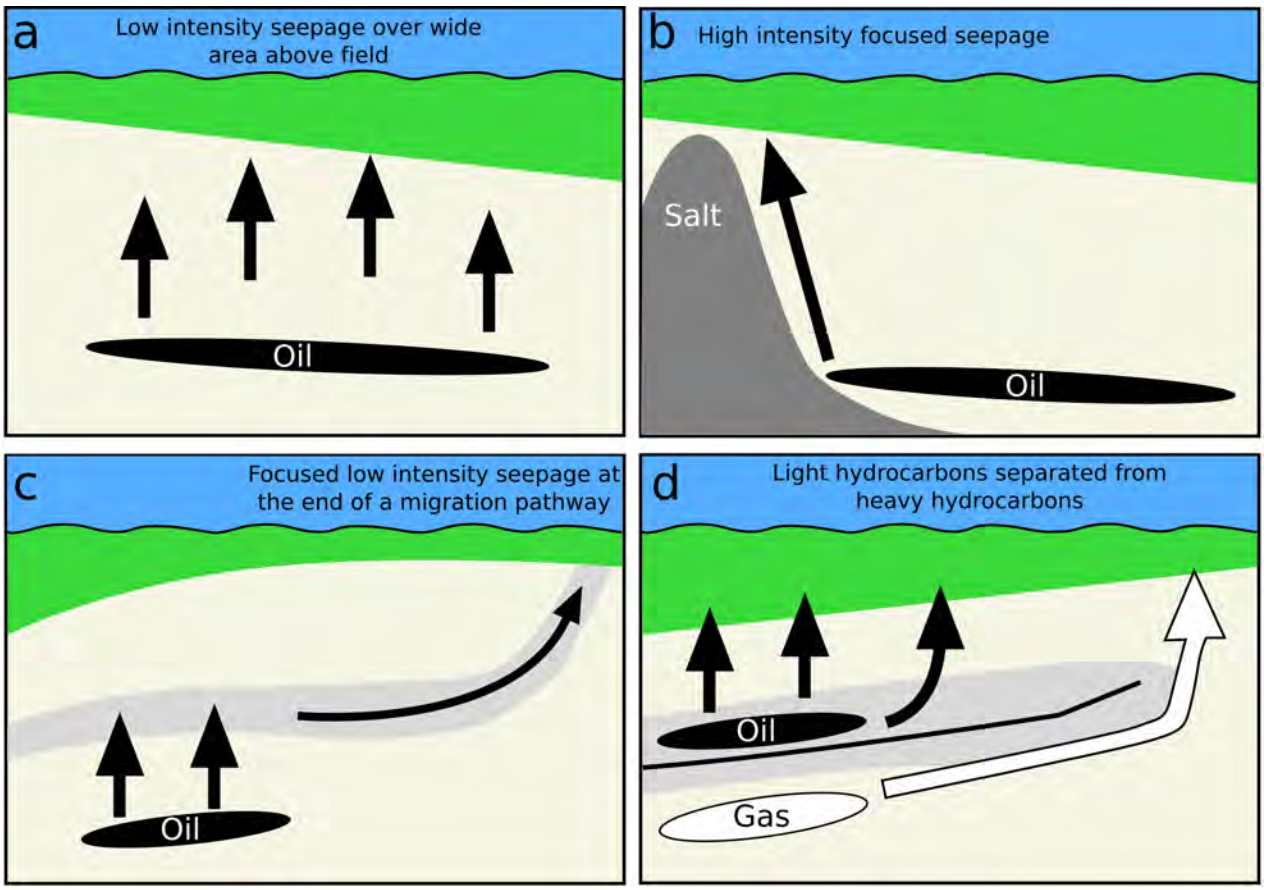

Figure 4.03. Four proposed mechanisms of micro-seepage. Figure adapted from Thrasher et al. [145] and Schumacher. [146]

Two major sub-surface imaging techniques are commonly used in the process of oil exploration today. Seismic imaging exploration involves creating acoustic waves and measuring the radiation and propagation of these waves through the earth, either as a land based investigation by the use of explosives, or an offshore investigation where compressed air is commonly used. [140] The other technique is satellite imaging that uses a range of spectroscopic techniques to measure the reflected light from the surface of the earth where, through a range of deconvolution techniques, can give information regarding the sub-surface. [149] Five “Landsat” satellites were launched by NASA in 1972 for this application.

The detection of oil and gas micro-seeps has been an evolving process for the past 70 years. Originally Laubmeyer and Sokolov independently developed techniques for the near-surface detection of hydrocarbons using chemical assays on soils to detect methane concentrations, [150] but these techniques were superseded by the evolution of the gas chromatography - flame ionisation detector (GC-FID) technique. Using a judicious choice of

column substrate, the GC-FID technique can determine the concentrations of a range of hydrocarbons from soil headspace, or from a liquid sample by comparing the FID signal for a sample and calibrated standard at a specific column retention time. [59] An excellent example of the exploitation of the GC-FID technique was by Richers *et al.*, who in 1983 [151] corroborated evidence between satellite imaging of the folding and faulting of a specific region in the Wyoming desert (using the Landsat satellites) and the near-surface detection of light hydrocarbons. By simply measuring the concentrations of the $C_1 - C_4$ branched and linear hydrocarbons, a map of the hydrocarbon density was produced that resembled the satellite image of the geological features. Further to this investigation, Jones and Drozd [152] have measured the ratios of near-surface light hydrocarbons and found simple, easily discernible ratios for determining whether the well below is gas, gas condensate (a mixture of gas and oil) or oil.

Once a well has been discovered, similar analysis techniques can also be applied to measuring the concentrations of hydrocarbon analytes that are present in the gas, gas condensate or oil samples arising from the well. Thompson, [153,154] using GC-FID, developed a method for the classification of a well based on the relative compositions of linear, branched and cyclic hydrocarbon compounds arising from the well. Both of the papers published determine parameters of aromaticity, paraffinicity and normality based on ratios of specific hydrocarbons. For example one of the nine parameters published in the 1987 paper takes a ratio of toluene to n-heptane in an attempt to determine the relative aromaticity of the oil in the well. When compared with other ratios, such as paraffinicity, important conclusions can be drawn regarding the age and potential ability of a well to produce oil or gas.

GC-FID is known to be an accurate method for the quantitative measurement of hydrocarbon samples, [59] however analysis times are generally slow, on the order of 5-20 minutes, and quantitation is only enabled through a direct calibration to a standard. Also the GC-FID technique when compared over a range of laboratory range instruments has shown the uncertainties to be large (often ± 30%) for many important volatile hydrocarbon compounds. [155,156] It must then be of beneficial nature to the application to be able to either decrease the sample time or decrease the uncertainty or both.

SIFT-MS was proposed as a technique for the analysis of geochemically formed hydrocarbons that could potentially overcome the drawbacks of GC-FID. The strong points of SIFT-MS lie in its ability to rapidly and quantitatively analyse samples with no sample preparation. The uncertainty of a SIFT-MS measurement is based mostly on the uncertainty in

the rate coefficient measurement, and therefore an accurate measurement of kinetic parameters leads to a substantially decreased uncertainty. Because the SIFT-MS method entails analysis of geochemically formed volatile organic compounds, the method has been coined “GeoVOC”.

This chapter will outline the approach taken to enable a SIFT-MS instrument to analyse samples containing volatile hydrocarbons that are of interest in oil and gas exploration. The reaction rate coefficients and product ion branching ratios of precursor ions reacting with hydrocarbons, and the ensuing secondary reactions with H_2O are fully investigated and referenced to previous investigations of a similar nature. Through an understanding of these processes new SIFT-MS based applications have been developed that can aid the oil exploration industry in the discovery of oil and gas reservoirs. A selection of the important data that is presented in this chapter has also been published elsewhere. [157]

4.2 Measurement of Kinetic Parameters

4.2.1 Introduction and previous investigations

Because of the ubiquitous nature of small hydrocarbon compounds, a large amount of research into their ion-molecule chemistry has been undertaken over the past 50 years. Ferguson, co-workers and other researchers made an in-depth investigation into the $O_2^{\bullet+}$ + CH_4 reaction that was known to be slightly endothermic toward electron transfer. [158-162] Where $O_2^{\bullet+}$ was found to be in a vibrational and electronic ground state, the studied reaction yielded a product ion proposed to be CH_2OOH^+. It was also discovered during the course of these investigations that the reaction of the excited O_2^{+}* ion was found to react with CH_4 to give exothermic product ion channels at m/z 31, 16 and 15 corresponding to the CH_3O^+, CH_4^+ and CH_3^+ ions. Reaction kinetic studies of larger hydrocarbons have been also been measured, but not to such an in-depth extent. Wilson et al. [163] and Spanel and Smith [35] have undertaken independent investigations into the light hydrocarbons reacting with ions of interest to SIFT-MS studies. Both found very slow reaction rates with respect to the H_3O^+ and NO^+ precursor ions, and rapid reactions with a large degree of fragmentation toward the $O_2^{\bullet+}$ ion. These observations are due to

- The higher proton affinity of H_3O^+ when compared with acyclic light

hydrocarbons (methane, ethane and propane have known proton affinities of 543.5, 596.3 and 625.7 kJ mol^{-1} respectively) [31]. Proton transfer is an ineffective process and will not occur at an appreciable rate, although some association is observed

- The ionisation energies of all linear hydrocarbons C_9 or lighter are known to be greater than NO^+, and therefore the electron transfer process to NO^+ will not occur. [30]

Because of the thermodynamic constraints, $O_2^{\bullet+}$ is the precursor ion of choice used for light linear hydrocarbons. The reactions of the light linear hydrocarbons (C_1 - C_9) with $O_2^{\bullet+}$ have been studied, where the reaction rate coefficients and product ion branching ratios of $O_2^{\bullet+}$ + n-heptane and $O_2^{\bullet+}$ + n-nonane are currently not known in the literature. The reactions of the C_1 – C_4 hydrocarbons are repeated for prudence to ensure that the differing carrier gases used in the current study lead to similar results when compared to previous investigations.

The reactions of H_3O^+ with C_1 – C_8 linear hydrocarbons have also been measured in the mixed carrier gas environment to establish the association ratios in the mixed He/Ar carrier gas of the Voice100 instrument.

Finally, the reactions of a range of product ions (formed from the reaction of $O_2^{\bullet+}$ reacting with a linear hydrocarbon) with water have been studied. Because samples introduced into the SIFT-MS instruments are generally whole air samples, or the headspace above substrates containing volatile compounds, water is generally the major reactive analyte present that is commonly found in a concentration range of 0.5 – 6% by volume. When the concentration of water is this high in the flow tube, the secondary reactions of product ions with water vapour may become a hindrance to SIFT-MS analyses if the reaction rate coefficients are appreciably fast. These secondary reactions with water vapour will completely alter the concentration profile of an analyte in the flow tube if the reaction proceeds with unit efficiency through proton transfer to form H_3O^+ such as is shown in the hypothetical reaction 4.01.

$$C_xH_y^+ + H_2O \rightarrow H_3O^+ + C_xH_{y-1} \quad (4.01)$$

Measurement of the rate coefficients and product ion branching ratios for the relevant $C_xH_y^+$ ions reacting with water gives some insight into the behaviour of the primary reactions in the presence of water vapour. To this end the reactions of 21 $C_xH_y^+$ ions with water have also been measured.

4.2.2 Experimental conditions

The University of Canterbury FA-SIFT (as discussed in chapter 2) has been used for all the kinetic measurements in this chapter, where the helium and argon flows are 32 and 46 Torr L s^{-1} respectively. This yields a flow tube pressure of ~0.25 Torr and an ion velocity on the sampled axis of the flow tube of 120 m s^{-1}. Collision limiting rate coefficients are calculated by either the Langevin method or by the method of Su [108] as discussed in the experimental chapter.

4.2.3 Chemicals

Both the helium and argon carrier gases were sourced from BOC Gases and have a quoted purity of 99.9995%. The helium was further purified through the molecular sieve trap at -196 K. Methane used was an alpha standard from BOC Gases. Ethane, propane, butane and pentane were sourced from Sigma Aldrich in lecture bottles at a purity >99.5%. C_6 and larger linear hydrocarbons were sourced from Sigma Aldrich as analytical grade reagents that have purities in excess of 99%.

4.2.4 Results

The reactions that have been investigated in this work are summarized in table 4.01 ($O_2^{\bullet+}$ + n-C_xH_y), table 4.02 (H_3O^+ + n-C_xH_y) and table 4.03 ($C_xH_y^+$ + H_2O).

The previous investigation by Wilson *et al.* [163] on the same instrument as the data presented here had difficulty generating $O_2^{\bullet+}$ completely free of the O_2^+* species. Formation of the excited ion was postulated to be via Penning ionisation from the metastable helium atoms in the flowing afterglow to give O_2^+ ($a^4\Pi_u$). This ion will exist in the flow tube when using a helium carrier gas, because collisional quenching via helium is known to be an ineffective process. [164] In the previous studies by Ferguson and co-workers, [160-162] the process of Penning ionisation was observed to occur by studying the reaction of $O_2^{\bullet+}$ with methane and detecting products ions other than CH_2OOH (m/z 47). However, in the study presented here, no product ions other than m/z 47 were observed for the $O_2^{\bullet+}$ + CH_4 reaction and therefore if the Penning ionised O_2^+ ($a^4\Pi_u$) was forming, the ion was short lived. The lack of O_2^+ ($a^4\Pi_u$) is attributed to the addition of argon to the flow tube. Argon is in excess compared to the

standard carrier gas helium (the carrier gas used by Wilson et al. [163]), that will facilitate effective relaxation of the excited O_2^+ ($a^4\Pi_u$) to the ground state O_2^+ ($x^4\Pi_u$) as collisional quenching of O_2^+ ($a^4\Pi_u$) by argon is an efficient process. [164]. Therefore, in the Voice100, that also has an excess of argon in the flow tube, any O_2^+ ($a^4\Pi_u$) formed in the microwave discharge region and injected into the flow tube will also be quickly relaxed to O_2^+ ($x^4\Pi_u$) by collision with argon atoms and will not affect the chemistry observed here.

For all the reactions measured here, the calculation of the enthalpies of reaction assume that the barrier for the isomerisation of an ion will always be less than the product ion's internal energy, and therefore an ion will exist in its lowest energy conformational structure. For example, $C_4H_9^+$ (m/z 57) is assumed to always exist as the tertiary butyl cation. However, due to the nature of SIFT-MS and the majority of mass spectrometry techniques, neutral products cannot be characterised and therefore any neutral products that are postulated in any reaction are tentative. The enthalpy of formation of C_9H_{20} has been determined from a linear extrapolation of smaller linear hydrocarbons.

4.2.5 Reactions of $O_2^{\bullet+}$ + n-C_xH_y

Reactions of methane, ethane, propane and n-butane with $O_2^{\bullet+}$ in the FA-SIFT have been published by this group previously, [163] and as mentioned above, repetition of these reactions is only to illustrate the similarity between bimolecular reactions occurring in differing carrier gas environments. The differences between the current and previous measurements for all four reactions are found to be within experimental uncertainty (± 20%). Methane is found to react approximately 20% faster than all listed previous measurements except that of Smith *et al*. [159] The observed increase in the reaction rate coefficient compared to the majority of previous measurements is attributed to the presence of argon in the flow tube as the mechanism of the $O_2^{\bullet+}$ + methane reaction is known to be through a termolecular pathway and the increased polarisability of the third-body leads to easier removal of energy from the association complex. [5]

Table 4.01. Reactions of $O_2^{\bullet+}$ with the given hydrocarbon measured at 298 K, 0.25 Torr, with a carrier gas mixture of 40% helium, 60% argon.

Neutral Molecule	***Ie[a] / eV***	***Products***	***BR***	***k_{exp} [k_c][b] / 10^{-9} cm^3 molecule^{-1} s^{-1}***	***Previous Measurements***
CH_4	12.61	$CH_2OOH^+ + H$	1.00	0.006 [1.2]	0.005,[c,d] 0.0052,[e] 0.0063[f]
C_2H_6	11.52	$C_2H_6^+ + O_2$	0.30	0.97 [1.3]	1.1,[c] 1.2[g]
		$C_2H_5^+ + (O_2 + H)$	0.55		
		$C_2H_4^+ + O_2 + H_2$	0.15		
C_3H_8	10.94	$C_3H_8^+ + O_2$	0.15	1.2 [1.4]	1.4[c,g]
		$C_3H_7^+ + (O_2 + H)$	0.40		
		$C_3H_6^+ + O_2 + H_2$	0.05		
		$C_2H_5^+ + O_2 + CH_3$	0.05		
		$C_2H_4^+ + O_2 + CH_4$	0.35		
C_4H_{10}	10.57	$C_4H_{10}^+ + O_2$	0.25	1.4 [1.5]	1.4,[c] 2.0,[g] 1.5[h]
		$C_4H_9^+ + (O_2 + H)$	0.05		
		$C_3H_7^+ + O_2 + CH_3$	0.60		
		$C_3H_6^+ + O_2 + CH_4$	0.05		
		$C_2H_4^+ + O_2 + (C_2H_6)$	0.05		
C_5H_{12}	10.28	$C_5H_{12}^+ + O_2$	0.20		1.6,[h] 0.8[i]
		$C_4H_9^+ + O_2 + CH_3$	0.10		
		$C_3H_7^+ + O_2 + (C_2H_5)$	0.30		
		$C_3H_6^+ + O_2 + (C_2H_6)$	0.40		
C_6H_{14}	10.13	$C_6H_{14}^+ + O_2$	0.20	1.8 [1.7]	1.99,[g] 1.7[h]
		$C_5H_{11}^+ + O_2 + CH_3$	0.05		
		$C_4H_9^+ + O_2 + (C_2H_5)$	0.35		
		$C_4H_8^+ + O_2 + (C_2H_6)$	0.25		
		$C_3H_7^+ + O_2 + (C_3H_7)$	0.05		
		$C_3H_6^+ + O_2 + (C_3H_8)$	0.10		
C_7H_{16}	9.93	$C_7H_{16}^+ + O_2$	0.15	1.7 [1.8]	
		$C_5H_{11}^+ + O_2 + (C_2H_5)$	0.30		
		$C_5H_{10}^+ + O_2 + (C_2H_6)$	0.15		
		$C_4H_9^+ + O_2 + (C_3H_7)$	0.15		
		$C_4H_8^+ + O_2 + (C_3H_8)$	0.15		
		$C_3H_7^+ + O_2 + (C_4H_9)$	0.05		
		$C_3H_6^+ + O_2 + (C_4H_{10})$	0.05		
C_8H_{18}	9.80	$C_8H_{18}^+ + O_2$	0.15	1.9 [1.9]	1.8[j]
		$C_6H_{13}^+ + O_2 + (C_2H_5)$	0.30		
		$C_6H_{12}^+ + O_2 + (C_2H_6)$	0.10		
		$C_5H_{11}^+ + O_2 + (C_3H_7)$	0.15		
		$C_5H_{10}^+ + O_2 + (C_3H_8)$	0.10		
		$C_4H_9^+ + O_2 + (C_4H_9)$	0.10		
		$C_4H_8^+ + O_2 + (C_4H_{10})$	0.10		
C_9H_{20}	9.71	$C_9H_{20}^+ + O_2$	0.05	2.1 [2.0]	
		$C_7H_{15}^+ + O_2 + (C_2H_5)$	0.10		
		$C_7H_{14}^+ + O_2 + (C_2H_6)$	0.05		
		$C_6H_{13}^+ + O_2 + (C_3H_7)$	0.20		
		$C_6H_{12}^+ + O_2 + (C_3H_8)$	0.05		
		$C_5H_{11}^+ + O_2 + (C_4H_9)$	0.10		
		$C_5H_{10}^+ + O_2 + (C_4H_{10})$	0.10		
		$C_4H_9^+ + O_2 + (C_5H_{11})$	0.25		
		$C_4H_8^+ + O_2 + (C_5H_{12})$	0.10		

a) Ionisation energies are sourced from the NIST webbook database. [30]

b) The experimental (k_{exp})and calculated (k_c) collision rate coefficients are listed in units of 10^{-9} cm^{-3} molecule^{-1} s^{-1}.

c) Ref [163] d) Ref [161] e) Ref [162]

f) Ref [159] g) Ref [165] h) Ref [35]

i) Ref [29] j) Ref [66]

Table 4.02. Reactions of H_3O^+ with the given hydrocarbon measured at 298 K, 0.25 Torr, with a carrier gas mixture of 40% helium to 60% argon.

Neutral Molecule	***PA[a] / kJ mol^{-1}***	***Products***	***BR***	***k_{exp} [k_c][b] / 10^{-9} cm^3 molecule^{-1} s^{-1}***		***Previous Measurements***
CH_4	543.5	No Reaction				No reaction[c]
C_2H_6	596.3	No Reaction				No reaction[c]
C_3H_8	625.7	No Reaction				No reaction[c,d]
C_4H_{10}		No Reaction				0.003,[c,d] no reaction[e]
C_5H_{12}		Adduct	1.00	0.15	[1.9]	
C_6H_{14}		Adduct	1.00	0.19	[2.0]	<0.1,[e] 0.03[f]
C_7H_{16}		Adduct	1.00	0.40	[2.2]	0.26[f]
C_8H_{18}		Adduct	1.00	0.50	[2.3]	0.9,[e] 0.58[f]

a) Proton affinities are sourced from the NIST webbook database where available. [31]
b) The experimental and calculated collision rate coefficients are listed in units of 10^{-9} cm^{-3} molecule^{-1} s^{-1}.
c) Ref [163] d) Ref [29]
e) Ref [35] f) Ref [66]

Table 4.03. Reactions of the given ion with H_2O measured at 298 K, 0.25 Torr, with a carrier gas mixture of 40% helium, 60% argon.

Ion	***PA[a] conj. base / kJ mol^{-1}***	***Products***	***BR***	***k_{exp} [k_c][b] / 10^{-9} cm^3 molecule^{-1} s^{-1}***		***Previous Measurements***
CH_2OOH^+		Adduct	1.00	0.02	[2.5]	0.021[c]
$C_2H_4^+$	755.2	Adduct	1.00	0.025	[2.7]	No reaction[d]
$C_2H_5^+$	680.5	$H_3O^+ + C_2H_4$	1.00	2.5	[2.7]	1.86,[e] 6.0[f]
$C_2H_6^+$	616	$H_3O^+ + C_2H_5$	1.00	2.2	[2.7]	2.95,[f] 1.2[g]
$C_3H_6^+$	736	Adduct	1.00	0.05	[2.5]	
$C_3H_7^+$	751.6	Adduct	1.00	0.007	[2.5]	
$C_3H_8^+$	671.4	$H_3O^+ + C_3H_7$	1.00	2.3	[2.5]	1.4[h]
$C_4H_8^+$	785	No reaction				
$C_4H_9^+$	802	No reaction				
$C_4H_{10}^+$		Adduct	1.00	0.04	[2.4]	0.041-0.044[h]
$C_5H_{10}^+$		No reaction				
$C_5H_{11}^+$	(808)	No reaction				
$C_5H_{12}^+$		Adduct	1.00	0.05	[2.4]	
$C_6H_{12}^+$		Adduct	1.00	0.004	[2.3]	
$C_6H_{13}^+$	813.9	Adduct	1.00	0.004	[2.3]	
$C_6H_{14}^+$		Adduct	1.00	0.004	[2.3]	0.0015-0.0056[h]
$C_7H_{14}^+$		No reaction				
$C_7H_{16}^+$		No reaction				
$C_8H_{16}^+$		No reaction				
$C_8H_{17}^+$		No reaction				
$C_8H_{18}^+$		Adduct	1.00	0.002	[2.3]	

a) Proton affinities are sourced from the NIST webbook database where available. [31]
b) The experimental and calculated collision rate coefficients are listed in units of 10^{-9} cm^{-3} molecule^{-1} s^{-1}.
c) Ref [161] d) Ref [166]
e) Ref [55] f) Ref [167]
g) Ref [168] h) Ref [169]

New minor exothermic product ion channels have been observed for the reaction of $O_2^{\bullet+}$ with propane and n-butane, that are outlined in reactions 4.02 and 4.03, however due to the nature of the product ions observed, impurities in the neutral analytes cannot be discounted.

$$O_2^{\bullet+} + C_3H_8 \rightarrow C_3H_6^+ + O_2 + H_2 \quad 0.05 \quad -101 \text{ kJ mol}^{-1} \quad (4.02)$$

$$O_2^{\bullet+} + \text{n-}C_4H_{10} \rightarrow C_2H_4^+ + O_2 + (C_2H_6) \quad 0.05 \quad -56 \text{ kJ mol}^{-1} \quad (4.03)$$

The reactions of the larger hydrocarbons that have not been previously measured on the FA-SIFT are found to react at, or very near to, the calculated collision limiting rate with electron transfer and dissociative electron transfer being the predominant reaction pathways.

n-Pentane is found to react in a similar fashion to the previous study by Spanel and Smith. [35] A minor product ion channel was observed at m/z 44 corresponding to the $C_4H_8^+$ ion as shown in reaction 4.04, that was not reported by Spanel and Smith, however difficulty arose in determining whether this exothermic channel was primary, secondary or due to an impurity in the neutral analyte. The $C_4H_8^+$ ion is therefore not mentioned in table 4.01.

$$O_2^{\bullet+} + \text{n-}C_5H_{12} \rightarrow C_4H_8^+ + O_2 + (CH_4) \quad <0.05 \quad -225 \text{ kJ mol}^{-1} \quad (4.04)$$

Again for n-hexane similar results are obtained when compared to the previous investigation by Smith and Spanel. [35] However in this study, individual product ion branching ratios are included for each product ion. The rate coefficient for the $O_2^{\bullet+}$ + n-hexane reaction is observed to occur slightly faster than the calculated collision limiting rate, however the discrepancy is within the experimental uncertainty of the measurement.

Arnold *et al.* [170] have previously studied n-octane reacting with $O_2^{\bullet+}$ at 300 K and found a range of product ions. When comparing the product ion branching ratios to the current investigation, and ignoring product ion branching fractions less than 5%, the both investigations correlate very well.

Two previously unknown reaction rate coefficients for the reactions of $O_2^{\bullet+}$ with n-hexane and n-nonane have been measured here. Both of these reactions proceed as expected, with rate coefficients approximately equal to the collision limiting rate coefficient, and a wide range of fragmentation observed. The thermochemistry of each of the reaction pathways is given in reactions 4.05 and 4.06 where the enthalpy of formation of n-nonane is estimated to be -229 kJ mol^{-1} based on a linear extrapolation of the enthalpies of formation of n-pentane, n-hexane, n-heptane and n-octane. The enthalpy of formation of $C_7H_{15}^+$ is an

approximated value determined from a different isomer, also the enthalpy of formation of C_5H_{11} (the neo-pentyl radical) was not found in the NIST webbook database, and was sourced from experimental data listed in the Computational Chemistry Comparison and Benchmark Database (CCCBDB). [171]

$O_2^{\bullet+} + n\text{-}C_7H_{16}$	$\rightarrow$	$C_7H_{16}^+ + O_2$	0.15	-206 kJ mol^{-1}	(4.05)
		$C_5H_{11}^+ + O_2 + (C_2H_5)$	0.30	-91 kJ mol^{-1}	
		$C_5H_{10}^+ + O_2 + (C_2H_6)$	0.15	-263 kJ mol^{-1}	
		$C_4H_9^+ + O_2 + (C_3H_7)$	0.15	-176 kJ mol^{-1}	
		$C_4H_8^+ + O_2 + (C_3H_8)$	0.15	-214 kJ mol^{-1}	
		$C_3H_7^+ + O_2 + (C_4H_9)$	0.05	-128 kJ mol^{-1}	
		$C_3H_6^+ + O_2 + (C_4H_{10})$	0.05	-143 kJ mol^{-1}	
$O_2^{\bullet+} + n\text{-}C_9H_{20}$	$\rightarrow$	$C_9H_{20}^+ + O_2$	0.05	-228 kJ mol^{-1}	(4.06)
		$C_7H_{15}^+ + O_2 + (C_2H_5)$	0.10	(-50) kJ mol^{-1}	
		$C_7H_{14}^+ + O_2 + (C_2H_6)$	0.05	-243 kJ mol^{-1}	
		$C_6H_{13}^+ + O_2 + (C_3H_7)$	0.20	-82 kJ mol^{-1}	
		$C_6H_{12}^+ + O_2 + (C_3H_8)$	0.05	-313 kJ mol^{-1}	
		$C_5H_{11}^+ + O_2 + (C_4H_9)$	0.10	-227 kJ mol^{-1}	
		$C_5H_{10}^+ + O_2 + (C_4H_{10})$	0.10	-264 kJ mol^{-1}	
		$C_4H_9^+ + O_2 + (C_5H_{11})$	0.25	-197 kJ mol^{-1}	
		$C_4H_8^+ + O_2 + (C_5H_{12})$	0.15	-236 kJ mol^{-1}	

As is observed in table 4.01, a large proportion of ion products formed, when reacting $O_2^{\bullet+}$ with a linear hydrocarbon, are ions that are not specific to any particular neutral hydrocarbon. Common ions formed (often in sizeable product ion branching ratios) are at m/z 71, m/z 57 and m/z 43 corresponding to the relatively thermodynamically stable 2-methylbutyl ($C_5H_{11}^+$ $\Delta H_f°$ = 661 kJ mol^{-1}), tert-butyl ($C_4H_9^+$ $\Delta H_f°$ = 711 kJ mol^{-1}) and iso-propyl ($C_3H_7^+$ $\Delta H_f°$ = 801 kJ mol^{-1}) cations.

4.2.6 Reactions of H_3O^+ + n-C_xH_y

Table 4.02 displays the bimolecular rate coefficients for the association reactions of H_3O^+ with eight acyclic hydrocarbons at the given conditions. Even though the proton affinities of only methane, ethane and propane are known of the non-branched chain hydrocarbons, it is assumed that all acyclic hydrocarbons in table 4.02 have a proton affinity less than that of H_2O (PA = 691 kJ mol^{-1} [30]) as above this value, exothermic proton transfer is expected to be observed.

Pseudo-bimolecular rate coefficients were fast enough to be measurable for n-C_5H_{12}, n-C_6H_{14}, n-C_7H_{16} and n-C_8H_{18}. As the mass of the neutral analyte increases, the ratio of the experimental reaction rate (k_{exp}) over the collision limiting rate coefficient (k_c) increases. This observation is assumed to be due to the increase in the number of degrees of freedom in the molecule. As the number of degrees of freedom increase, the lifetime of the collision complex between H_3O^+ and the linear hydrocarbon will also increase, which leads to a higher chance of undergoing a stabilising collision with an argon atom, and therefore a greater k_{exp} / k_c ratio. The data is shown graphically as figure 4.04. A sigmoidal type plot is expected to be observed if the analytes shown in figure 4.04 were extended to a high enough mass, because the value of k_{exp} / k_c cannot surpass unity.

Sequential clustering of water molecules following the formation of the first water cluster [H_3O^+.M] was observed to occur, and these reactions were found to be very rapid, such that the formation of the first water cluster was the rate limiting step. However, due to the difficult in measuring these sequential water cluster reactions, rate coefficients for these processes were not obtained. The result obtained here is similar in nature to that observed by Spanel and Smith. [35]

4.2.7 Reactions of $C_xH_y^+$ + H_2O

Three reactions shown in table 4.03 are of acute importance to measuring hydrocarbons using the SIFT-MS method. These reactions are given below in equations 4.07, 4.08 and 4.09, where all three reactions are aided by the thermodynamically stable neutral species formed during the reaction and these provide exoergic pathways.

$C_2H_5^+ + H_2O$	→	$H_3O^+ + C_2H_4$	1.00	-11 kJ mol^{-1}	(4.07)
$C_2H_6^+ + H_2O$	→	$H_3O^+ + C_2H_5$	1.00	-75 kJ mol^{-1}	(4.08)
$C_3H_8^+ + H_2O$	→	$H_3O^+ + C_3H_7$	1.00	-20 kJ mol^{-1}	(4.09)

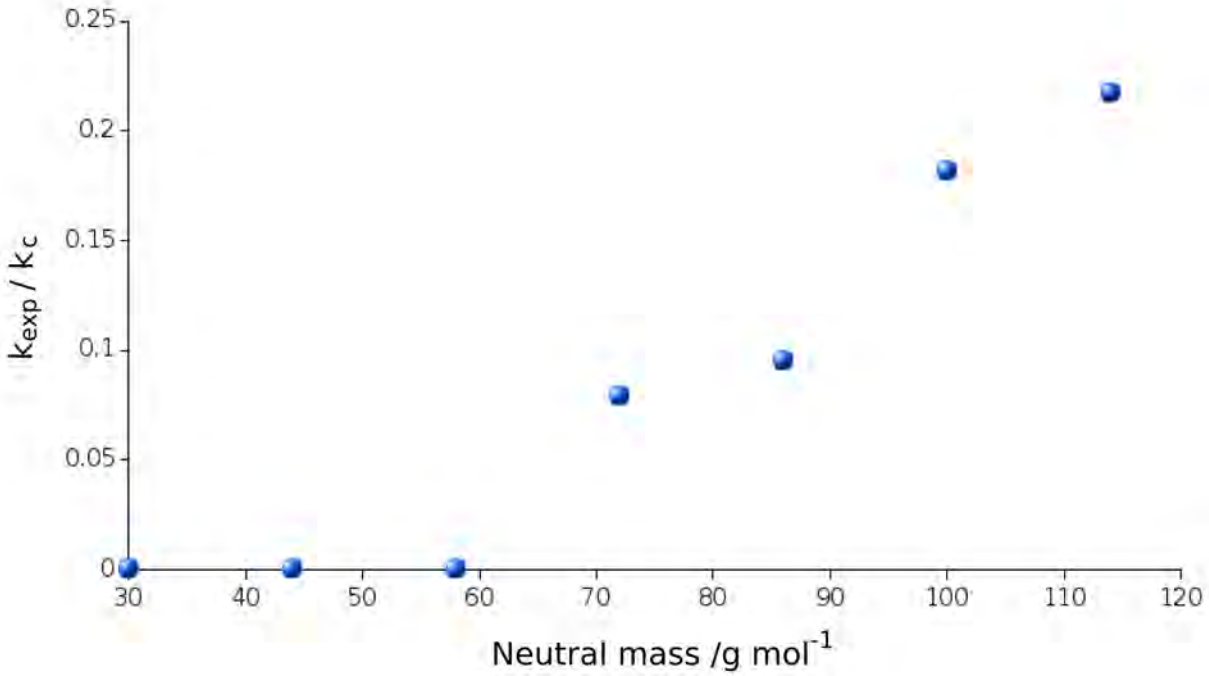

Figure 4.04. The reaction efficiency of the studied non-branched hydrocarbons reacting with H_3O^+.

Because the above reactions occur with unit reaction efficiency, the observable signals of m/z 29, m/z 30 and m/z 44 at the end of the flow tube can be drastically altered by the presence of water in the flow tube. For example, if $O_2^{\bullet+}$ is injected into the flow tube and a mixture of ethane and water is passed through the sample inlet, the intensities of each ion (O_2^+, $C_2H_6^+$ and H_3O^+) can be modelled down the length of the flow tube (assuming no diffusive losses) as is shown in figure 4.05 where the initial $O_2^{\bullet+}$ intensity is 800,000 counts s^{-1} and the ethane and water number densities are 9 x 10^{11} and 3 x 10^{13} molecules cm^{-3} respectively. It is immediately obvious from figure 4.05 that any $C_2H_6^+$ formed is immediately converted to H_3O^+ because of the large rate coefficient, and substantially greater number density of water molecules. Therefore it is crucial when attempting to quantify ethane and propane concentrations using the SIFT-MS technique to ensure that the water concentration entering the flow tube is as low as possible.

Hydrocarbon ions in table 4.03 that are found to form an adduct with H_2O will not affect the SIFT-MS method in such a substantial way as ions that proton transfer to H_2O, as adduct formation leads to an ion at a m/z ratio which is much more easily measured, e.g. $C_4H_{10}^+.H_2O$ at m/z = 76. Again, as with the $H_3O^+ + C_xH_y^+$ reactions, any adducts that are formed very rapidly cluster second and third water molecules such that the formation of the first cluster $[M^+.H_2O]$ is the rate-limiting step.

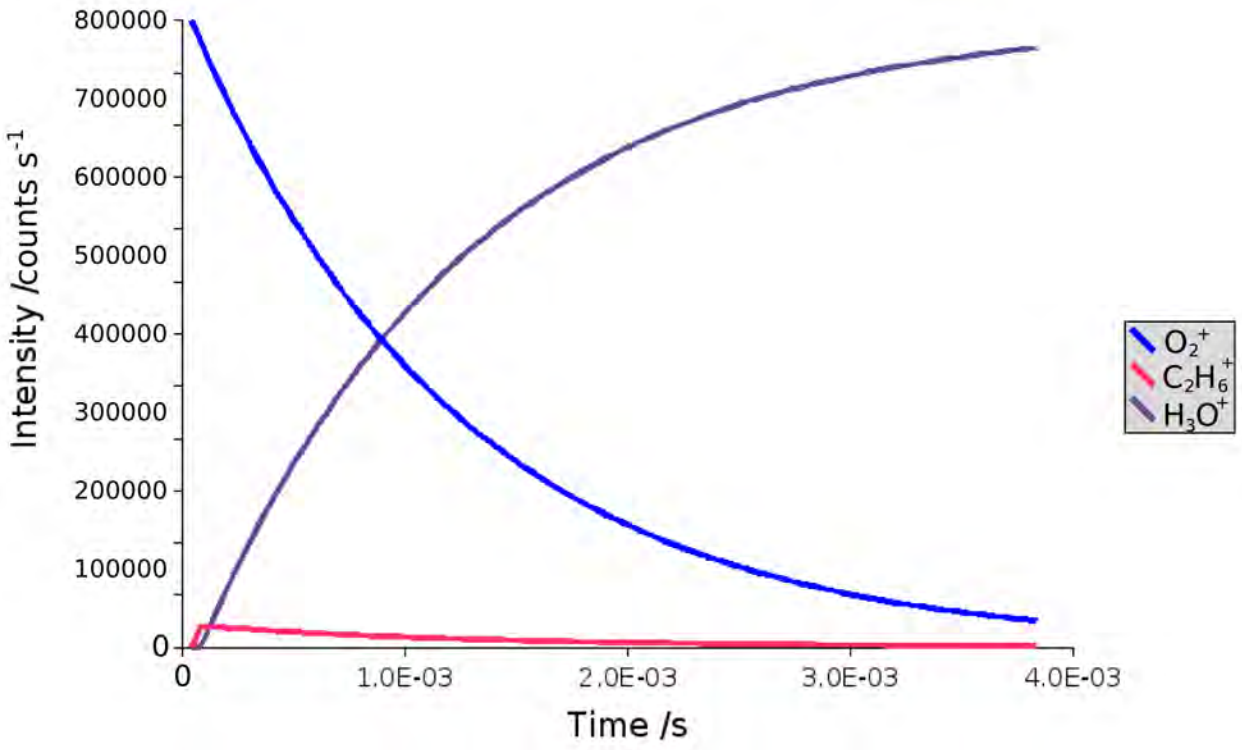

Figure 4.05. Formation of $C_2H_6^+$ and its immediate conversion to H_3O^+ during the reaction length. Ethane and water number densities are 9 x 10^{11} and 3 x 10^{13} molecules cm^{-3} respectively.

4.2.8 Other important secondary chemistry

Even though water is the major reactive analyte in most SIFT-MS analytical samples, secondary chemistry of other analytes may also play an important role in the determination of hydrocarbon concentrations in soil headspace. From the literature it is known that $C_2H_4^+$ will react rapidly with small hydrocarbons to produce $C_3H_7^+$. [172] This will skew the observed product ion branching ratio in favour of the $C_3H_7^+$ ion that is a common ion formed from many of the small hydrocarbons reacting with $O_2^{\bullet+}$. However, because the concentration of most hydrocarbon samples analysed using the SIFT-MS method are in the mid-to-low parts-per-million-by-volume (ppmv) concentration range, the number density of the analyte is substantially low enough not to alter the relative ratios of the product ions.

4.3 Analytical Method

4.3.1 From kinetic parameters to an analytical method

The measurement of kinetic parameters does not in itself make a suitable method for analytical quantitation because the SIFT-MS technique relies on being able to measure precursor and product ion intensities independent of interferences. Each analyte must give a product ion that is formed explicitly from that analyte and not from any other analyte because deconvolution of a single peak which contains ions resulting from more than one analyte is very difficult if not impossible. For instance, $C_3H_7^+$ is formed from the reaction of $O_2^{\bullet+}$ with propane, n-butane, n-pentane, n-hexane and n-heptane and therefore cannot be used for the detection or quantitation of any of those analytes. Also, any ion formed that is of interest to the SIFT-MS analytical method must have little or no interferences at its m/z ratio such as $C_2H_6^+$ (m/z 30), which is only formed from the reaction of $O_2^{\bullet+}$ with ethane, however m/z 30 overlaps with a signal for NO^+ that can be quite large† (often ~1000 counts s^{-1} when injecting O_2^+) and therefore $C_2H_6^+$ cannot be used for the measurement of ethane.

Once a judicious choice of product ions have been made, the method must be verified against a synthetic standard across a range of concentrations and humidities to ensure that no unforeseen interferences occur. Only after this verification can the method be applied to a particular application with confidence. Also obtained from the verification step are the limit of detection and limit of quantitation according to the procedure outlined in Milligan *et al.* [58]

4.3.2 Removal of water from samples

Section 4.2.7 outlines two important factors for the detection and quantitation of hydrocarbons by SIFT-MS: 1) detection will be very difficult when the humidity of the sample is high and 2) any variability in the humidity of the sample, even when the humidity is low, may drastically alter the observed relative ratios of the product ions and therefore the concentration. Each of these two points can be circumvented by first drying the samples prior to entering the flow tube.

---

† NO^+ is formed from excited $O_2^{\bullet+}$ entering the flow tube and colliding with the carrier gas to make O^+ which rapidly reacts with N_2 (from air) to form NO^+ as a terminal ion. [173]

GeoVOC samples are normally the air headspace above moist soil or water held in a can or bottle, such that drying the actual sample is not practical. Lowering the sample temperature below 0 °C is an option, however the observable concentrations of most of the measured hydrocarbons would be decreased because each has a substantially lowered vapour pressure at 0 °C when compared to room temperature. Also, decreasing the temperature to 0 °C requires a long incubation period which is not favourable as the advantages of the SIFT-MS technique is a lack of sample preparation. [39] Therefore an in-line unit that is part of the sample introduction system is preferred that can dessicate the headspace gas before entering the flow tube.

For this specific application a purpose built Nafion™ dryer unit has been used to selectively remove water from the headspace gas. Nafion™ is a semi-permeable co-polymer of tetrafluoroethylene (teflon) and perfluoro-3,6-dioxa-4-methyl-7-octenesulfonic acid that reactively diffuses polar compounds such as water across a concentration gradient, but is completely non-reactive toward non-polar compounds. [174,175] A length of Nafion™ tubing (Perma-pure Inc, Toms River, NJ USA) was placed inside a glass tube through which a rapid flow of dry nitrogen can be passed. Water is then selectively removed from the samples while leaving the linear, non-polar hydrocarbon compounds completely unaffected. Using a standard cylinder of dry nitrogen (Southern Gas <99.9995% pure) the water concentration of humidified air (~ 4% water vapour) is decreased with this arrangement by 60 fold to 0.07% as measured by SIFT-MS. This calculation assumes the rate coefficients for the sequential water clustering reactions as discussed in chapter 3. The design of the Nafion™ dryer is shown as figure 4.06, and the drying efficiency is shown in figure 4.07. The conditions shown in figure 4.07 require a three hour equilibration time to remove water molecules adsorbed to the surface of the Nafion™ tubing and the glass tube.

A commercial equivalent of the purpose-built dryer discussed here (Perma-pure Inc.) has been purchased that uses a stainless steel outer tube instead of glass making the apparatus more robust. The commercial dryer was also found to yield a slightly better drying efficiency and a more rapid equilibration time, however due to time constraints on the project only a selection of experiments in the current chapter used the commercial equivalent.

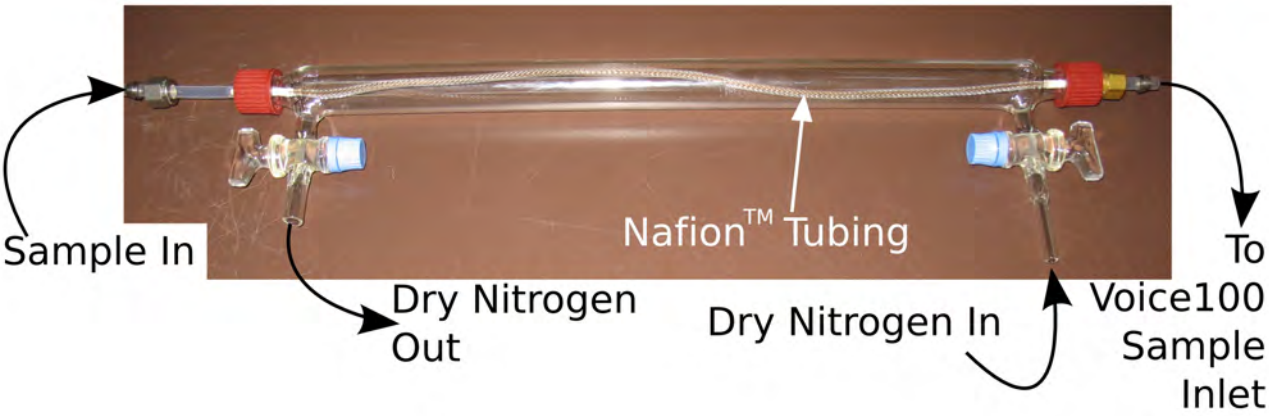

Figure 4.06. Purpose built Nafion™ dryer design, where dry nitrogen is flushed over the outer surface of the Nafion™ tubing.

4.3.3 The GeoVOC method

The analytes, their chosen explicit product ions, the effective rate coefficient (rate coefficient multiplied by the product ion branching ratio) and the method for determining the analyte concentration are given in table 4.04.

All analytes use the $O_2^{\bullet+}$ ion as a precursor, and these reactions are monitored as the main detection method for the linear hydrocarbons. Due to the slow reaction rate coefficients of H_3O^+ with the C_1 – C_6 linear hydrocarbons, only the reactions of H_3O^+ with n-heptane and n-octane are monitored, and the data obtained is only used in support of the concentration determined using the $O_2^{\bullet+}$ precursor ion.

For reactions of n-nonane, n-octane, n-heptane, n-hexane, n-pentane and n-butane with $O_2^{\bullet+}$, the molecular ion is preferred as the explicit ion. A molecular ion such as $C_4H_{10}^+$ can only be formed from C_4H_{10} and not from larger hydrocarbon species. For prudence it is important to measure the intensities of the secondary adducts of the molecular ions with water where the rate coefficient is appreciable. Because the concentration of the water entering the flow tube is very low, the intensity of the molecular ion of propane ($C_3H_8^+$) is not substantially perturbed by reactions with H_2O, and can also be used for quantitation.

Ethane concentrations are measured by monitoring the intensities of $O_2^{\bullet+}$ and $C_2H_4^+$ and allowing for the 35% channel to $C_2H_4^+$ from the $O_2^{\bullet+}$/propane reaction, and the 5% channel of the $O_2^{\bullet+}$/n-butane reaction. Methane is measured by monitoring the very slow reaction of $O_2^{\bullet+}$ and m/z 47 (CH_2OOH).

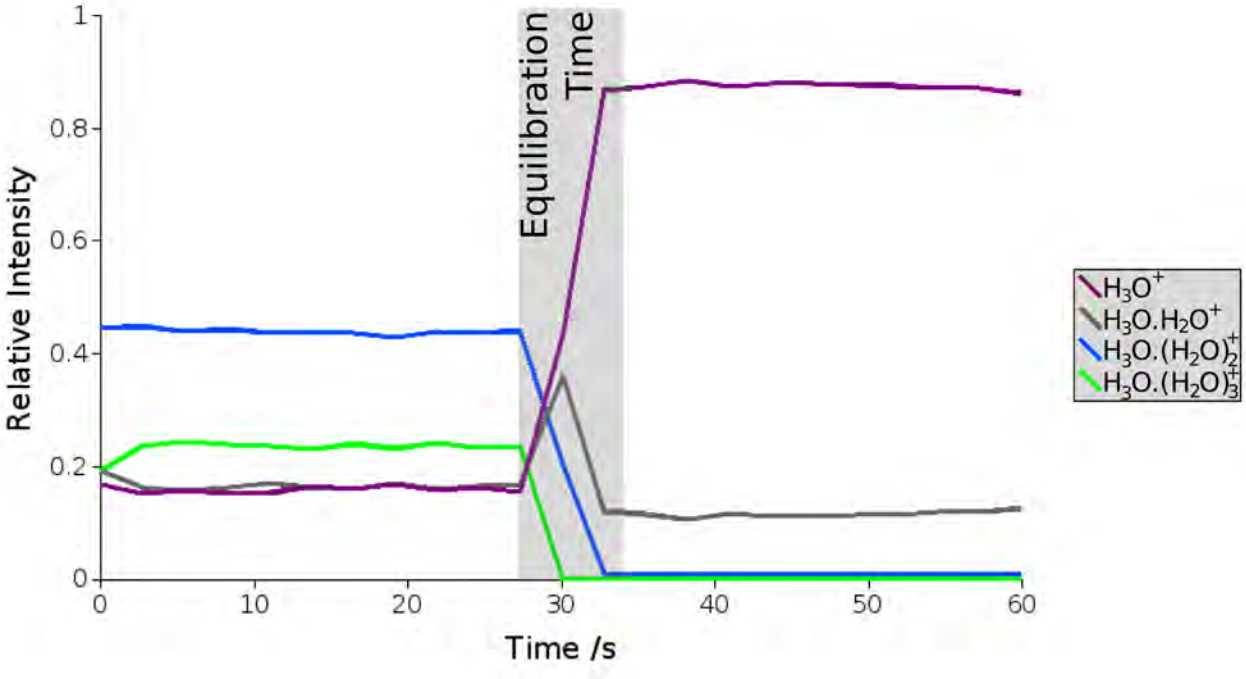

Figure 4.07. A plot of the hydronium ion water clusters observed when a humidified air sample is allowed directly into the flow tube (0 – 26 seconds) and when it is passed through the purpose-built Nafion™ Dryer (33 – 60 seconds).

Table 4.04. The parameters of the GeoVOC method.

Analyte	***Ions***			***Effective k[a] /***	***Post-processing requirements[b]***
	Precursor	*Product (m/z)*		*cm_3 molecule^{-1} s^{-1}*	
n-Nonane	$O_2^{\bullet+}$	$C_9H_{20}^+$	(128)	1.0×10^{-10}	Subtract isotope of m/z 127
n-Octane	H_3O^+	$C_8H_{18}^+.H_2O$	(132)	5.0×10^{-10}	
	$O_2^{\bullet+}$	$C_8H_{18}^+$	(114)	1.0×10^{-10}	Subtract isotope of m/z 113
n-Heptane	H_3O^+	$C_7H_{16}^+.H_2O$	(118)	4.0×10^{-10}	
	$O_2^{\bullet+}$	$C_7H_{16}^+$	(100)	2.6×10^{-10}	Subtract isotope of m/z 99
n-Hexane	$O_2^{\bullet+}$	$C_6H_{14}^+$	(86)	1.8×10^{-10}	Subtract isotope of m/z 85
n-Pentane	$O_2^{\bullet+}$	$C_5H_{12}^+$	(72)	6.0×10^{-10}	Subtract isotope of m/z 72
n-Butane	$O_2^{\bullet+}$	$C_4H_{10}^+$	(58)	7.0×10^{-11}	Subtract isotope of m/z 57
Propane	$O_2^{\bullet+}$	$C_3H_8^+$	(44)	4.2×10^{-10}	Subtract isotope of m/z 43
Ethane	$O_2^{\bullet+}$	$C_2H_4^+$	(28)	1.5×10^{-10}	Subtract contribution from C_3-C_4
Methane	$O_2^{\bullet+}$	CH_2OOH^+	(47)	6.0×10^{-12}	

a) An effective rate coefficient is the observed rate coefficient from tables 4.01 or 4.02 multiplied by the product ion branching ratio. Values of k are specific for the instruments discussed herein, and may vary for other SIFT instruments.
b) Post-processing steps are discussed in the text

Subtractions must also be made for isotopic overlap that occurs from commons ions. For example, the carbon 13 peak of $C_4H_9^+$ will occur at m/z 58 that overlaps with $C_4H_{10}^+$. Because the thermodynamically favourable ions such as $C_4H_9^+$ occur at a mass that is 1 amu lower than the molecular ions, these subtractions are often large. However, because the natural abundances of the carbon isotopes are very well understood, this type of subtraction is routine.

Branched hydrocarbons can also be added to the GeoVOC method because these reactions have been studied previously on other SIFT instruments. [35,66,168] By monitoring the NO^+ precursor ion and the hydride abstraction product ion for each branched hydrocarbon, a concentration can be directly measured because NO^+ is known not to react with linear hydrocarbons at an appreciable rate. [55] The reactions of iso-butane, iso-pentane and and iso-hexane with NO^+ are given as reactions 4.10 – 4.12.

				k /cm^3 molecule^{-1} s^{-1}		
$NO^+ + i\text{-}C_4H_{10}$	→	$C_4H_9^+ + NOH$	1.00	0.9×10^{-9}	-39 kJ mol^{-1}	(4.10)
$NO^+ + i\text{-}C_5H_{12}$	→	$C_5H_{11}^+ + NOH$	1.00	1.4×10^{-9}	-36 kJ mol^{-1}	(4.11)
$NO^+ + i\text{-}C_5H_{14}$	→	$C_6H_{13}^+ + NOH$	1.00	1.2×10^{-9}	-53 kJ mol^{-1}	(4.12)

However, each of the branched hydrocarbons also reacts with $O_2^{\bullet+}$($i\text{-}C_4H_{10}$ is the exception), and therefore the total product ion intensity resulting from the branched hydrocarbons reacting with $O_2^{\bullet+}$ must be subtracted to determine the concentration of the linear hydrocarbons. The literature rate coefficients and product ion branching ratios for the $O_2^{\bullet+}$ + iso-butane and iso-pentane are given below in reactions 4.13 and 4.14. Reaction 4.15 then lists the reaction of iso-hexane with $O_2^{\bullet+}$ that is not currently known in the literature, and the rate coefficient and product ion branching ratio given are estimates from a calibration to a known standard.

$O_2^{\bullet+} + i\text{-}C_4H_{10}$	→	$C_4H_{10}^+ + O_2$	No reaction		-134 kJ mol^{-1}	(4.13)
$O_2^{\bullet+} + i\text{-}C_5H_{12}$	→	$C_5H_{12}^+ + O_2$	0.10	1.6×10^{-9}	-169 kJ mol^{-1}	(4.14)
$O_2^{\bullet+} + i\text{-}C_6H_{14}$	→	$C_6H_{14}^+ + O_2$	0.15	1.8×10^{-9}	-196 kJ mol^{-1}	(4.15)

4.3.4 Sampling procedures

Three separate sample types can be presented to a SIFT-MS for GeoVOC analysis; these are soil samples, water samples, and well gas (or gas condensate) samples. A photograph

of each of the sampling vessels is shown in figure 4.08.

Figure 4.08. Sampling vessels for the three types of GeoVOC measurement.

The soil technique involves sampling 150-500 g of soil into a robust canister from at least 2 m below the surface (to ensure minimisation of aerobic microbial activity) and sealing the canister for transport to the laboratory. Upon their arrival at the laboratory, the samples are incubated at 20 °C overnight. The lid of each can is pierced with a punch and the headspace above the soil samples is introduced into the Voice100 for analysis via the Nafion™ dryer. By sampling the soil in a grid pattern, a profile of the hydrocarbon concentration can be determined for a specific area of interest. A similar process can also be applied to soil samples that have been taken from various depths during the drilling of well.

The water based technique involves sampling 100-600 ml of water that arises from drinking or irrigation wells that have been drilled to at least 50 m below the surface into disposable 750 ml mineral water bottles. The water that arises from these wells is commonly known as bore water. The bore water is sampled in a controlled fashion to ensure that no hydrocarbons escape prior to sampling that would dilute the observed concentration. As the Henry's law constant of small hydrocarbons in water lies substantially toward the hydrocarbons being in the gas phase (e.g. air/water partition coefficients of methane, ethane and propane are 67.4, 50.6 and 71.6 kPa m^3 mol^{-1} respectively) [122] all small hydrocarbons that have been dissolved in water at the elevated pressure and temperature below the surface

of the earth will move into the gas phase once the constraints of the aquifer have been removed. Therefore, all hydrocarbons trapped in the bore water will move into the gas phase once inside the sampling vessel. The headspace is then introduced to the Voice100 (via the Nafion™ dryer) simply by piercing the side of the bottle with a sampling needle. Because many farms and commercial ventures often have irrigation or drinking-water wells, this type of sampling can rapidly give information regarding the hydrocarbon concentrations well below the surface of the earth.

The final application discussed in this chapter is analysis of neat gas samples which are taken while drilling a gas, or gas condensate well. During the drilling of a new exploratory well, the headspace of the earth that is displaced by the auger, or more directly, the gas coming from the well is sampled into aluminium tubes called Isotubes™ for transport to a laboratory. Each Isotube™ has two valves, and the gas inside is at atmospheric pressure. Because of the nature of the samples that are placed inside Isotubes™, the concentrations of the hydrocarbons inside the tubes are often very high and can be outside the linear range of the Voice100 that commonly has a capillary flow of 150 SCCM. Therefore, either the capillary flow is required to be substantially reduced (usually to < 10 SCCM) or serial dilutions of the Isotube gas into nitrogen using tedlar bags can be measured.

A case study of a similar application will be given toward the end of this chapter.

4.3.5 Comparison to Standards

Five standard mixtures have been used for validating the GeoVOC method in both wet and dry environments. These are

- *"15 ppmv"* - a certified mixture of methane, ethane, propane, n-butane, n-pentane and n-hexane each at 15 ppmv with the balance being nitrogen. Supplied by Scott Specialty Gases (Plumsteadville, PA, USA) with a quoted uncertainty of ± 10% on each hydrocarbon.
- *"Iso standard"* - a certified mixture of iso-butane (15.6 ppmv), iso-pentanes (two isomers totalling 30.6 ppmv) and iso-hexanes (3 isomers totalling 45.4 ppmv) with a balance of nitrogen. Also supplied by Scott Specialty Gases with a quoted uncertainty of ± 10% on each hydrocarbon isomer.
- *"50 ppmv"* - a non-certified mixture of methane, ethane, propane and n-butane each at 50 ppmv. Supplied by BOC Gases (Auckland, New Zealand) with an unknown

uncertainty.

- *"High conc."* - a NIST traceable† certified standard of methane (70.45%), ethane (9%), propane (6%), n-butane (3%), iso-butane (3.02%), n-pentane (1.01%) and iso-pentane (1.01%) with a balance of CO_2, helium and nitrogen. Supplied by Scott Specialty Gases with a quoted uncertainty of ± 5% on each hydrocarbon isomer. This standard is outside the linear quantitation range of the Voice100, and has therefore been diluted 2000 fold.

As a first experiment, a sample of the 15 ppmv standard was placed in a tedlar bag with 1 ml of water, allowed to equilibrate for ~ 1 hour, and then measured with and without the Nafion™ dryer tube in-line with the sample inlet system to verify that the Nafion™ dryer is selectively removing water and not hydrocarbons from the sample headspace. This experiment is shown in figure 4.09. The addition of the Nafion™ dryer system to the sample inlet line of a Voice100 instrument gives much more accurate measurements of the hydrocarbons in the mixture. It can be concluded then that the Nafion™ dryer system is selectively removing water vapour from a gas phase mixture of hydrocarbons such that the hydrocarbon concentrations can be quantified by the GeoVOC method.

As proof of linearity with the Nafion dryer system, four serial dilutions of a methane alpha standard (BOC Gases) have been directly measured on the Voice100 using the GeoVOC method and Nafion dryer system. Linearity is found to be excellent, with an R^2 correlation value of greater than 0.99. A plot of the correlation is shown in figure 4.10.

Following these initial investigations, each of the standard hydrocarbon mixtures mentioned above plus the methane alpha standard appropriately diluted in nitrogen has been measured using the GeoVOC method *with* the Nafion dryer system. The standards were measured in dry and moist environments, where moist environments were generated by adding 1 ml of water to the tedlar bag containing the standard, and allowing the mixture to equilibrate for 1 hour at 20 °C. The data for all standards is presented in table 4.05.

The concentrations measured by the Voice100 using the GeoVOC method and the Nafion dryer system for all standards shown in table 4.05 lie within ± 30% of the concentration quoted by the suppliers. This error also includes the inherent inaccuracy of the quoted concentration (ranging between ± 5% and ± 20%).

† A standardised validation method http://ts.nist.gov/qualitysystem/

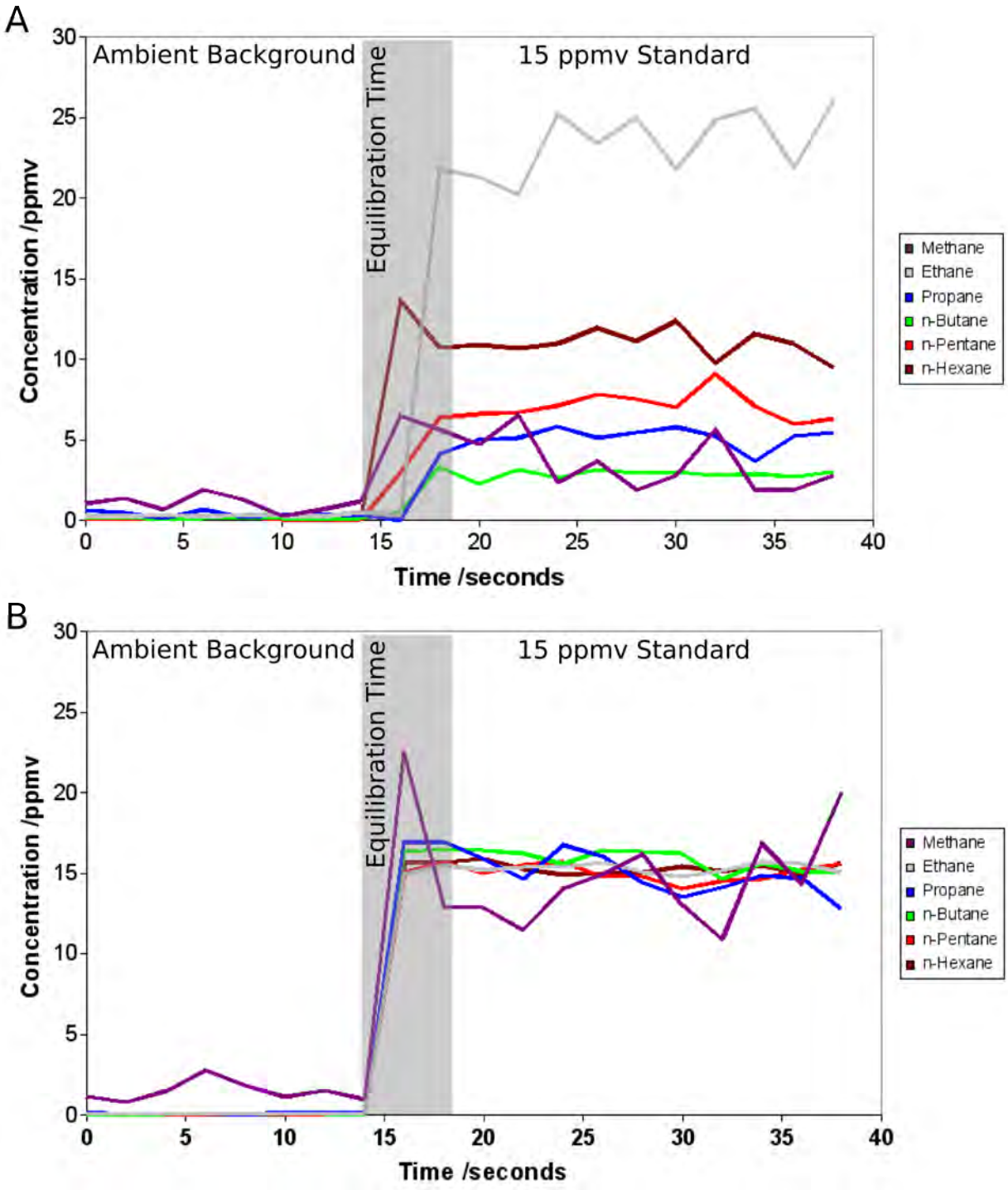

Figure 4.09. Example of Nafion™ drying efficiency using the GeoVOC method. Chart (A) shows the wet '15 ppmv' standard on a Voice100 without the Nafion dryer system; chart (B) shows the same wet '15 ppmv' standard with the Nafion dryer system. In both spectra ambient air is sampled for the first 15 seconds to determine a constant background.

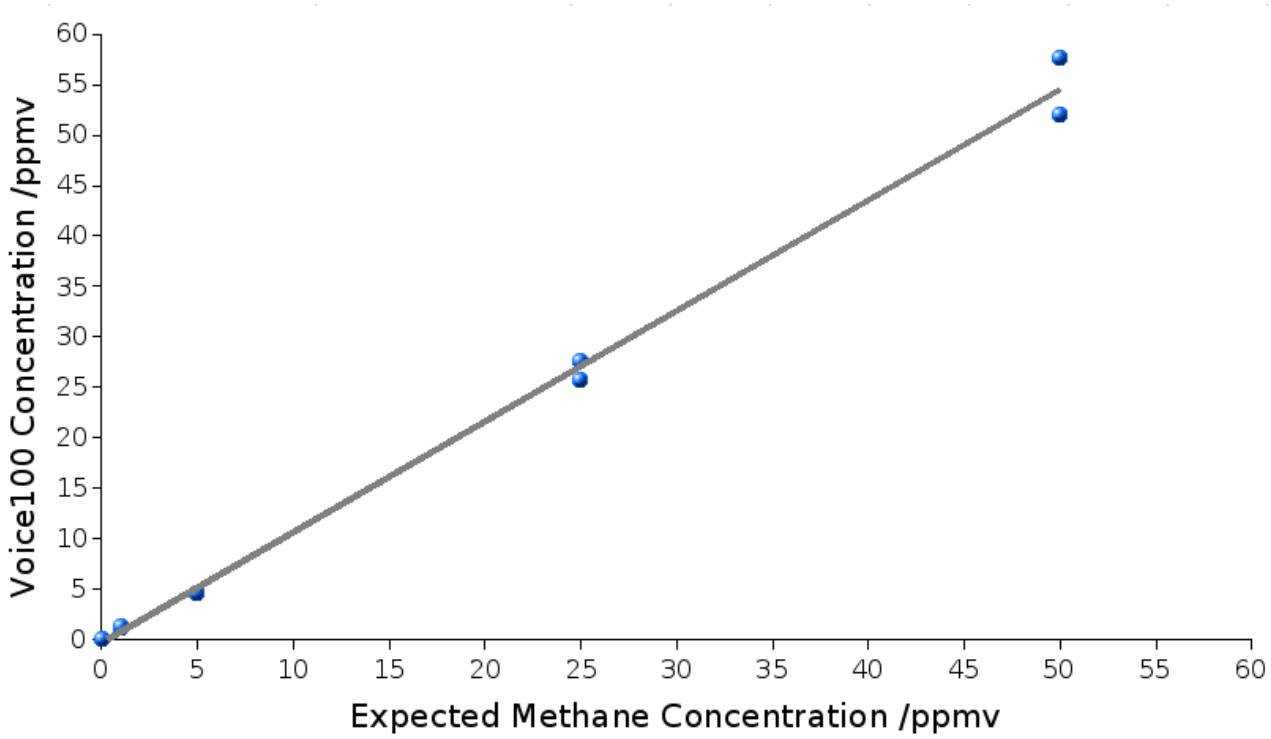

Figure 4.10. Linearity of measurement across a range of concentrations of methane using a Voice100. Methane concentrations were generated using serial dilutions of an alpha standard.

The largest deviations from the quoted uncertainty are found for methane and the branched hydrocarbons. Methane has a slow rate coefficient with $O_2^{\bullet+}$ giving a much greater uncertainty of measurement. A slow rate coefficient leads to fewer product ions per unit concentration that in turn increases the uncertainty. The concentrations of branched species are found to be slightly under-reported, which can be attributed to the Nafion co-polymer interacting with the slightly polar branched species and affecting the observed concentration.

The dry samples measured using the Nafion™ dryer system have a median error closer to zero than the wet samples. However, the upper quartiles and lower quartiles for both the wet and dry samples are similar. Therefore the median of the dry samples is skewed toward upper quartile, or conversely, the distribution is skewed toward lower errors. A statistical box plot that is shown in figure 4.11 outlines this skew, and also shows the spread of data to be greater for the dry data than the wet. The humidified (wet) samples show a normal distribution about the median.

Table 4.05. Verification of the GeoVOC method coupled with the Nafion dryer tube by comparison to known hydrocarbon standards.

Standard[a]	***Hydrocarbon***	***Quoted conc. / ppmv***	***Voice100 Dry***[b] ***/ ppmv***	***Error %***	***Voice100 Wet***[b] ***/ ppmv***	***Error %***
15 ppmv	Methane	15	15.3	+2.6	14.1	-6.2
	Ethane	15	15.8	+5.1	15.2	+1.4
	Propane	15	14.7	-1.9	14.3	-4.8
	n-Butane	15	14.9	-0.4	14.8	-1.2
	n-Pentane	15	15.6	+4.3	16.0	+6.5
	n-Hexane	15	15.3	+2.2	15.5	+3.2
Iso Standard[c]	iso-Butane	15.6	15.4	-1.1	16.5	+5.8
	iso-Pentane(s)	30.6	27.3	-10.9	29.5	-3.6
	iso-Hexane(s)	45.4	38.8	-14.5	41.2	-9.4
Mixture[d]	Methane	7.5	9.6	+28.6	8.0	+6.2
	Ethane	7.5	6.8	-9.3	6.2	-17.8
	Propane	7.5	9.2	+22.9	8.7	+16.4
	n-Butane	7.5	6.9	-7.7	6.3	-16.2
	n-Pentane	7.5	7.9	+5.3	6.9	-8.0
	n-Hexane	7.5	7.9	+4.9	7.2	-4.0
	iso-Butane	7.8	6.8	-12.7	6.5	-17.1
	iso-Pentane(s)	15.3	11.7	-23.5	11.2	-26.1
	iso-Hexane(s)	22.7	16.6	-26.7	16.1	-29.1
50 ppmv	Methane	50	41.8	-16.4	37.0	-26.0
	Ethane	50	52.8	+5.6	52.2	+4.4
	Propane	50	41.6	-16.8	41.6	-16.8
	n-Butane	50	55.1	+10.2	60.7	+21.4
High Conc.	Methane	352	363	+3.9	368	+5.2
	Ethane	45	37.3	-17.1	39.1	-13.2
	Propane	30	26.4	-12.0	27.0	-10.1
	n-Butane	15	15.7	+4.7	17.0	+13.0
	n-Pentane	5.05	3.8	-24.6	4.3	-13.4
	iso-Butane	15.1	13.9	-8.1	15.0	-0.5
	iso-Pentane	5.05	6.2	+24.1	6.1	+22.0
			RMS Error	2.7		4.1
			Upper Quartile	4.9		5.2
			Median	-1.1		-4.0
			Lower Quartile	-12.7		-13.4

a) Both the '15 ppmv' and the 'Iso Standard' (Scott Specialty Gases) have a quoted uncertainty of ± 10% on the quoted concentration for each isomer. The '50 ppmv' standard (BOC Gases) does not have a listed analytical uncertainty. The 'High Conc.' standard is NIST Traceable, and has a quoted uncertainty of ± 5% on each hydrocarbon isomer.

b) Voice100 dry and Voice100 wet refer to measurements made using dry or humidified standards respectively. Both wet and dry measurements were made using the Nafion drying tube.

c) The 'Iso Standard' contains mixtures of iso-pentanes and iso-hexanes that are are not currently able to be resolved by SIFT-MS.

d) 'Mixture' refers to a 1:1 mixture of the '15 ppmv' standard with the 'Iso standard', and therefore is expected to have an analytical error of at least ± 20%.

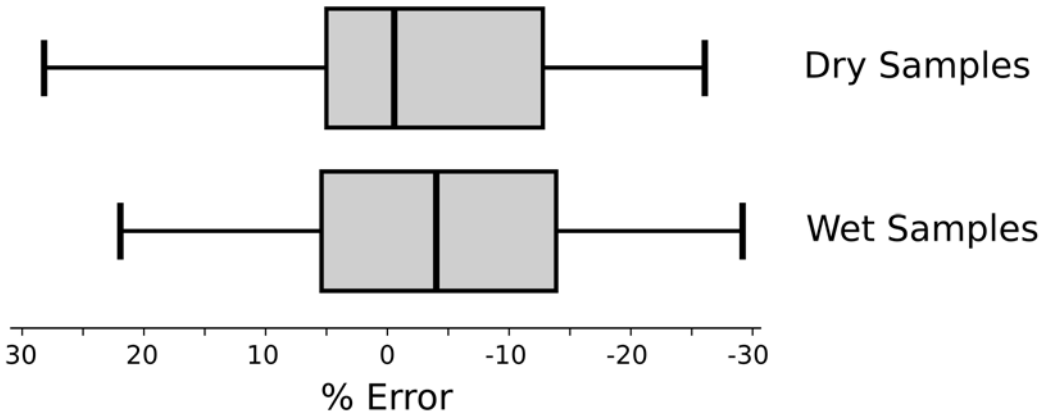

Figure 4.11. A 'box plot' of the percentage difference between the concentration measured on the Voice100 and the quoted concentration.

Limits of detection (LOD) and limits of quantitation (LOQ) for each of the hydrocarbons measured above (linear C_1 – C_6, and branched C_4 – C_6) have also been ascertained using the method prescribed by Milligan *et al.* [58] that was also discussed in the introduction chapter. Each of these parameters are given in table 4.06 for a total scan time of 70 seconds, where b_μ is the product ion intensity when measuring an ambient air chemical background and s is the sensitivity of the measurement in counts s^{-1} $ppbv^{-1}$ where the initial $O_2^{\bullet+}$ intensity is 800,000 counts s^{-1}. The LOD and LOQ for ethane are determined by the addition of the propane values to the LOD and LOQ determined for ethane using m/z 28 ($C_2H_4^+$), as the effect from n-butane is deemed to be minimal. Contributions to the LOD and LOQ of linear C_4 – C_6 hydrocarbons by their branched isomers is also deemed to be minimal.

The values obtained in table 4.06 show that detection and quantitation of the C_2 – C_6 linear and branched hydrocarbons can be achieved in the low ppbv range. In comparison to the recent publication by Milligan *et al.* [58] where a SIFT-MS LOD of 120 pptv (parts per trillion by volume) for phosphine has been achieved, the values in table 4.06 are not astounding. This is attributed to only using one product ion for each linear hydrocarbon, where the branching fraction for the product ion of interest is less than unity. Also the high chemical background found in a SIFT-MS instrument at the masses of interest contributes to the poor LODs. The chemical background in a Voice100 is postulated to be due to pump oil vapour, from either the roots blower or flow tube backing pump (E2M28), diffusing into the flow tube reaction region. The use of a fully fluoronated pump oil, such as fomblin, would reduced the chemical background at the studied masses if a reduced LOD were required.

Table 4.06. Limits of detection (LOD) and limits of quantitation (LOQ) for each of the compounds measured in table 4.05 using a total scan length of approximately 70 s (1.5 s total scan time per product ion). Values calculated by the method of Milligan et al. [58]

	***b*$_\mu$ /** *counts s^{-1}*	***sensitivity (s) /*** *counts s^{-1} ppbv^{-1}*	***LOD /*** *ppbv*	***LOQ /*** *ppbv*
Methane	37.3	0.0077	1900.	3100.
Ethane	48.2	0.98	17.	26.
Propane	23.0	0.20	58.	110.
n-Butane	74.2	0.60	35.	47.
n-Pentane	24.8	0.40	30.	54.
n-Hexane	44.4	0.48	34.	51.
iso-Butane	38.5	2.6	6.0	9.4
iso-Pentane(s)	23.3	1.6	7.4	14.
iso-Hexane(s)	141.	2.1	14.	17.

The very poor LOD associated with methane is not necessarily a hindrance to the GeoVOC method. As methane is usually the most common analyte in geochemical samples, and is often measured at concentrations 100 times greater than the next most concentrated analyte, [152] it is favourable to have a very low sensitivity so that high concentrations of methane can be measured alongside lower concentrations of the heavier hydrocarbons. The parameter *s* (sensitivity) is directly related to the rate coefficient by equation 4.16 which is a rearrangement of the standard SIFT-MS concentration equation, where N_p and N_i are the intensities of the product and precursor ions respectively, *k* is the rate coefficient, *t* the reaction time and 6 x 10^5 is the number of molecules cm^{-3} ppbv^{-1} for a Voice100 with a capillary flow of 150 ml min^{-1}.

$$\frac{N_p}{[B]} = \frac{s}{6x10^5} = kN_it \tag{4.16}$$

Therefore, when the value of *k* is found to be small, such as for the reaction of $O_2^{\bullet+}$ + methane, the sensitivity of the measurement will be low and the conversion of precursor ions to product ions will be inefficient. This minimal conversion becomes useful when evaluating equation 4.17, that is the assumption upon which equation 4.16 relies.

$$\frac{N_p}{N_i} = \ln\left(\frac{N_p}{N_i} + 1\right) \tag{4.17}$$

As more ions are converted to product ions, the assumption of equation 4.17 becomes less true, and SIFT-MS measurements are considered to be outside the linear range. If we define an acceptable deviation from the assumption in equation 4.17 as 15% (such that any greater deviation shall be defined as outside the linear range for quantitation), for a reaction of

800,000 counts s^{-1} of $O_2^{\bullet+}$ reacting with propane, the maximum concentration that can be quantified when propane is the only reactive analyte and the capillary flow is 150 SCCM is ~75 ppmv. For the same deviation of 15%, the maximum quantifiable concentration of methane is ~15000 ppmv. However, the situation becomes more complex because $O_2^{\bullet+}$ will often be reacting with more than one analyte for any one sample, and a linear combination of the sensitivity parameters for each analyte must be taken to determine the allowable maximum value of N_p / N_i during a measurement. Conversely, by measuring the initial precursor ion intensity before opening the sample inlet the value of $N_i(0)$ can be determined, which is the total ion intensity assuming an accurate knowledge of the instrument mass discrimination function. Now, equation 4.17 can be solved easily because $\Sigma N_p = N_i(0) - N_i$, where $N_i(0)$ is the precursor intensity in the absence of sample, N_i is the precursor ion intensity in the presence of sample and ΣN_p is the total of all product ions formed from i (the precursor) in the presence of sample as shown in equation 4.18.

$$\frac{N_i(0)}{N_i} - 1 = \ln\left(\frac{N_i(0)}{N_i}\right) \tag{4.18}$$

As defined above, if the maximum deviation from this assumption is 15%, when $N_i(0)$ is 800,000 count s^{-1}, N_i must be greater than 580,000 counts s^{-1} for the measurement of a concentration by the SIFT-MS technique to be accurate and precise when the capillary flow is 150 ml min^{-1}. This type of calculation is often very important in the GeoVOC method, as total hydrocarbon concentrations in GeoVOC soil, well and water samples often are in excess of 0.1% by volume total hydrocarbon which requires a lower capillary flow, or a serial dilution in nitrogen.

Based on the above verification, the GeoVOC method on a Voice100 combined with the Nafion dryer system is a robust technique for the analysis of hydrocarbons from oil and gas seeps across the range of humidities commonly found in soil and water samples. The total scan time for the measurement of the LOD and LOQ was approximately 70 seconds, that leads to a maximum sample throughput of 50 samples per hour (through the use of an auto-sampler or multiple sample inlets). By decreasing the total scan time, an increase in sample throughput can be achieved, however this is at the expense of the detection and quantitation limits, and therefore the specific requirements of the application must be well defined before deploying a method of this type into a commercial setting such as an oil rig, or exploration operation. Two cases studies shall now be discussed that outline the application of the GeoVOC method to the quantitative detection of linear and branched hydrocarbons.

4.4 Case Study: The Depth-dependent Composition of an Oil/Gas Well

4.4.1 Introduction

A large north American energy company that has expertise in deep water oil and gas exploration is interested in the use of SIFT-MS on drilling rigs for the 'real-time' detection and quantitation of light hydrocarbons as the well is being drilled. The technique is said to be real-time as the SIFT-MS at the site of drilling (on the oil rig) is required to be constantly reporting the concentrations of the light hydrocarbons of interest as the well is being drilled. With a SIFT-MS instrument on location there is no need for sample collection and subsequent analysis in a laboratory.

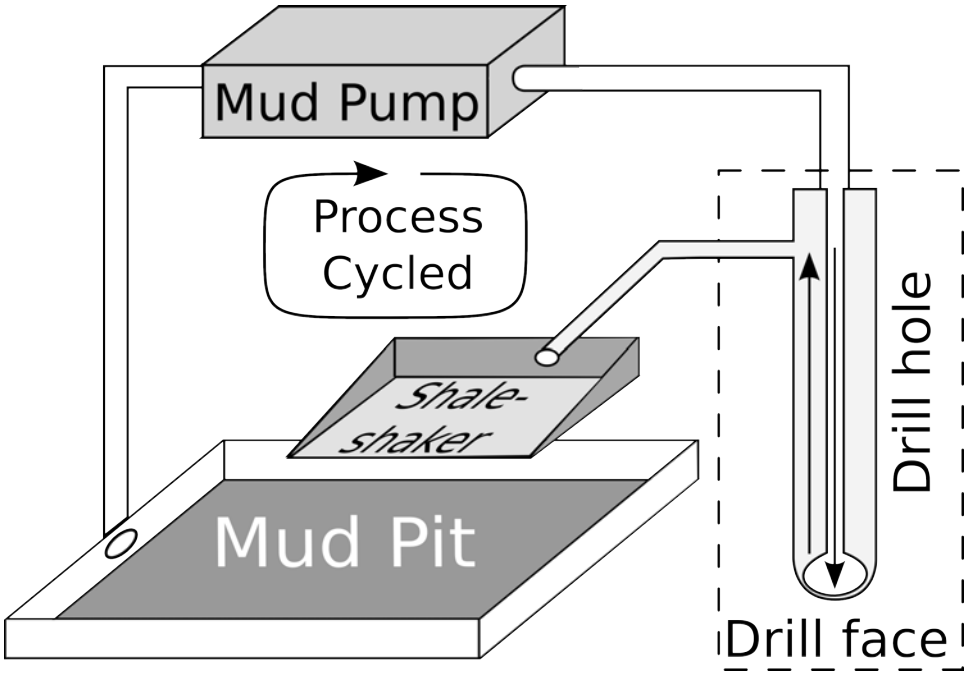

Figure 4.12. A stylised diagram of the mud circulation process. Figure adapted from Conway. [140]

To test that the Voice100 can accurately quantify the hydrocarbons in the GeoVOC method across a very wide concentration range, two sets of hydrocarbon samples (where each set was from a different drilling site) were sent to New Zealand for analysis. The samples were contained in Isotubes™ (see figure 4.08) and each gas sample was correlated to a drilling depth, where these ranged from 3000 to 4500 metres below sea level. The gas in the Isotubes™ was the headspace that has evolved from the earth displaced by the drilling process.

The drilling process, as alluded to in the introduction to this chapter, is a complex task that is driven by the pressure to minimise cost and maximise oil recovery. The drilling process involves forcing fluids past a rotating 'drill bit' such that the fluid keeps the bit cool, and removes the 'cuttings' (shards of rocks) away from the drill bit. The cuttings are then removed and the remaining fluid (commonly called mud) is re-cycled back down the pipe to the drill face. A diagram of this mud circulation system adapted from Conway [140] is shown in figure 4.12. Information on the composition of the strata is found by observing the appearance, acidity and consistency of the mud in the 'shale-shaker' and 'mud pit' regions. Headspace gas of the mud at these regions can also be sampled to determine the composition of the hydrocarbons in the well at the drill face. This composition determination has traditionally been achieved with GC-FID.

Some information regarding the strata where the samples are taken is also known such as the depth where oil shale is present. This information is not made available however, until after the sample has been analysed. An oil shale is a region of rock that is known to contain a large amount of organic matter known as kerogen, but not necessarily oil or gas, as the region may not have reached a high enough temperature for oil formation to occur. [176] Therefore regions containing oil shale are sites that are not targets for hydrocarbon extraction. In turn then, sites that do not contain oil shale, but are found to have high concentrations of hydrocarbons may be sites for oil extraction.

4.4.2 Results obtained

Plots of the depth dependence on hydrocarbon composition for each of the two drilling sites (site A and site B) are shown in figures 4.13 and 4.14, where the expected oil shale regions that are known for site A are indicated. Site B has no known geological features such as oil shale regions.

For site A, the highest concentrations of all hydrocarbons are found at lower depths (between 4390 and 4450 m) as are the three identified oil shale regions, however the peak of highest hydrocarbon concentration (4405 m) is found not to occur in an oil shale region. This non-oil shale, hydrocarbon rich depth could be a site where oil or gas can be efficiently extracted. The relative hydrocarbon abundance plot for site A indicates the region to be a gas or possibly gas condensate reservoir as methane is between 80 and 90% of the entire measurable hydrocarbon concentration. [152]

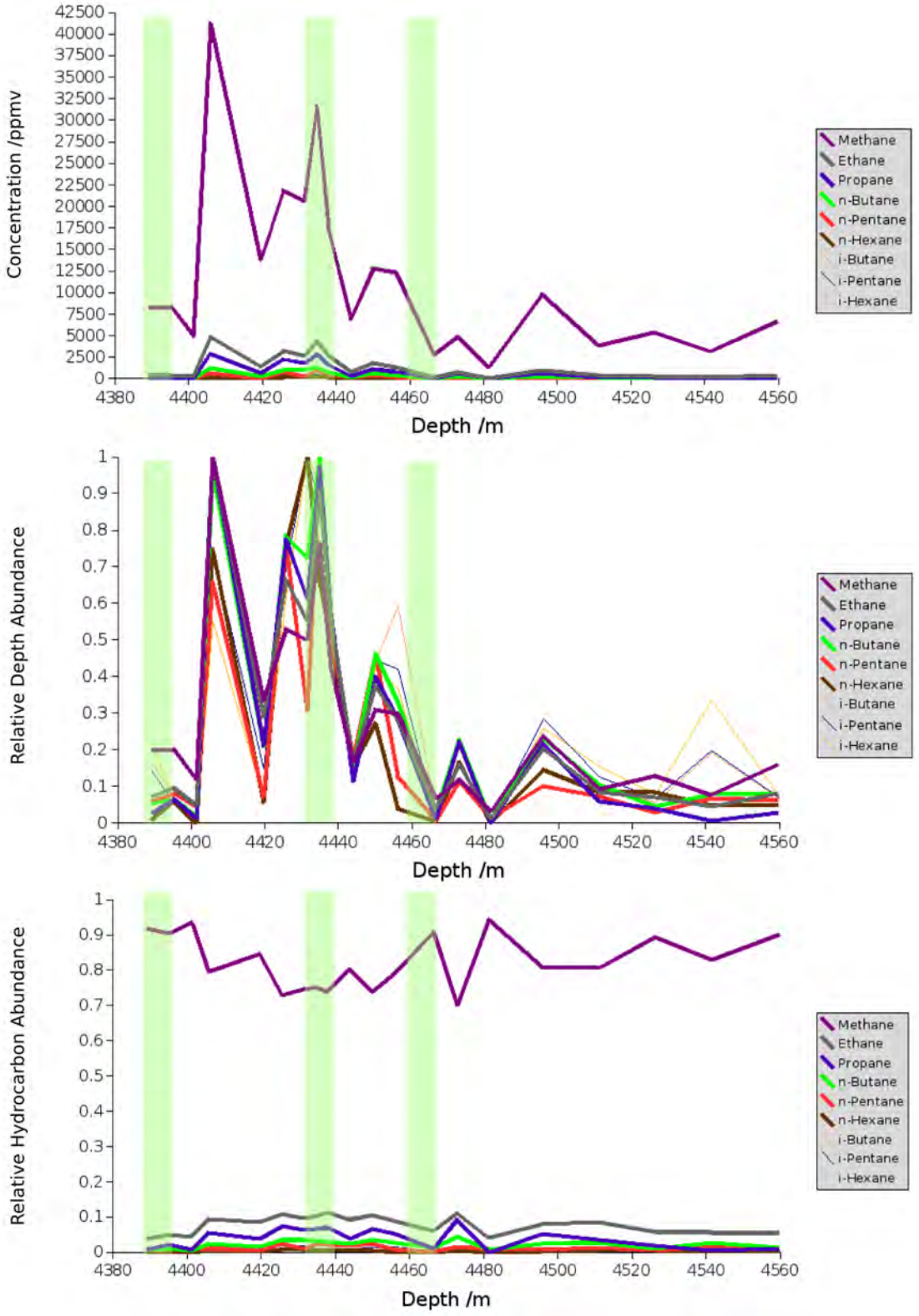

Figure 4.13. The depth dependence of the C_1 – C_6 hydrocarbons for site A. The "Relative Depth Abundance" plot shows the concentration of a hydrocarbon compared to the maximum concentration of that hydrocarbon for any depth. The "Relative Hydrocarbon Abundance" plot shows the concentration of a single hydrocarbon divided by the total concentration for one depth. Oil shale regions are shown by the semi-transparent green bars.

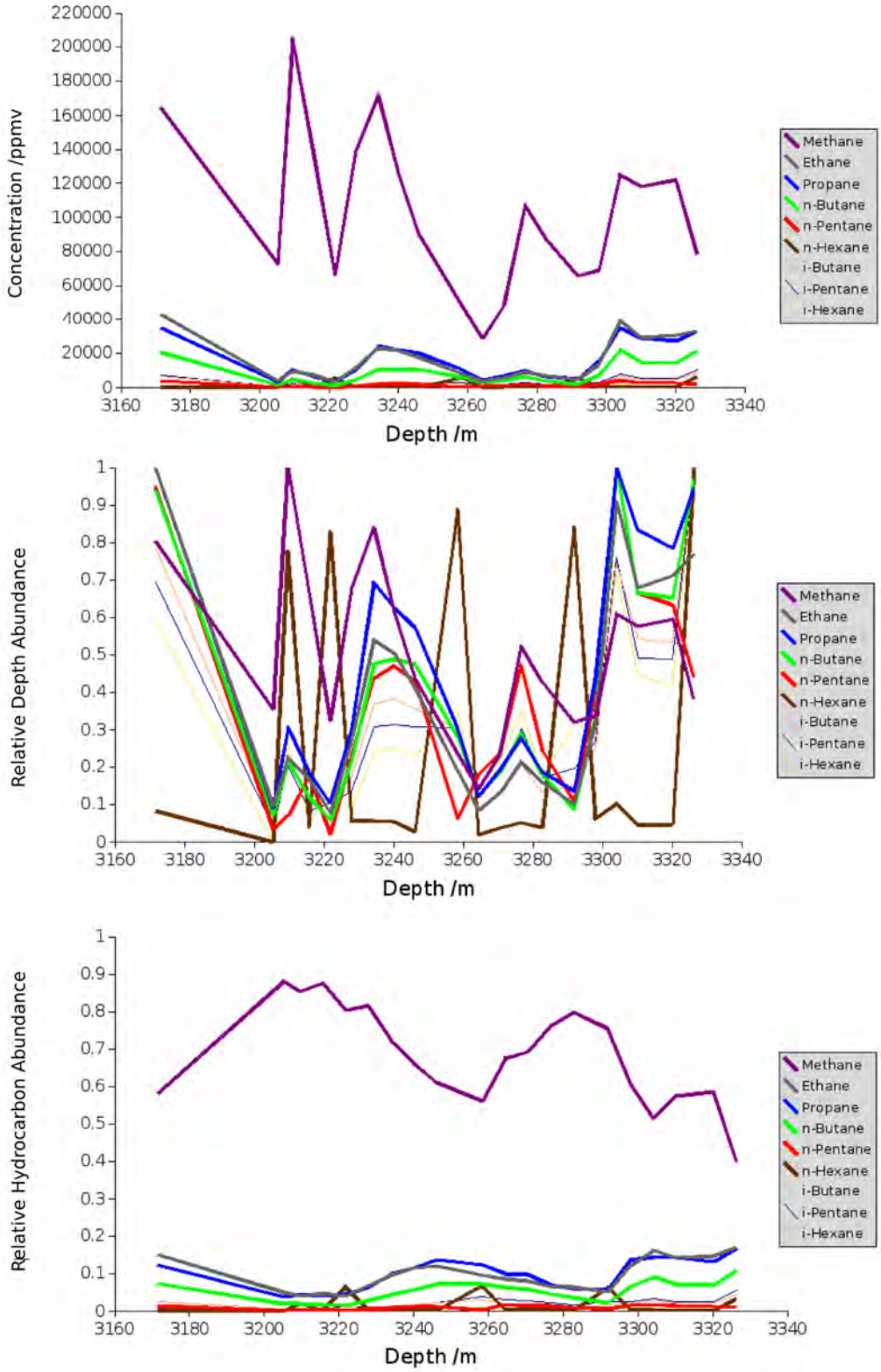

Figure 4.14. The depth dependence of the C_1 – C_6 hydrocarbons for site B. The "Relative Depth Abundance" plot shows the concentration of a hydrocarbon compared to the maximum concentration of that hydrocarbon for any depth. The "Relative Hydrocarbon Abundance" plot shows the concentration of a single hydrocarbon divided by the total concentration for one depth.

Site B is found to have very high concentrations of hydrocarbons in the Isotubes™ that were received from the drilling company. In fact the concentrations for methane (15%) are above the upper explosive limit† in some cases. In comparison, the concentrations found in site A were an order of magnitude lower. The reservoir at site B is likely to be a gas condensate or possibly an oil reservoir, although the concentration of methane is found to vary from 40% to almost 90% of the total hydrocarbon concentration.

At lower depths, the ratio of methane to other measured hydrocarbons decreases indicating that more gas is trapped at the top of the reservoir near the impermeable cap, and the heavier hydrocarbons are lower in the reservoir.

However, the relative depth abundance plot indicates that there is no specific depth at site B where drilling would yield high concentrations of all the hydrocarbons at once, although between 3300 and 3320 m is likely to be the target depth. No information regarding the geology of site B was made available.

4.4.3 Comparison to GC-FID measurements

To validate the GeoVOC method and the SIFT-MS technique for the interested North American energy company, three Isotubes™ were taken at random and measured on a Hewlett Packard 5890 GC-FID at the University of Canterbury with a 30 m x 0.321 m Agilent GS-Q column isothermal at 120 °C, an injector and detector temperature of 250 °C and a helium carrier flow of ~20 cm sec^{-1}. Initially, using 0.1 ml injections, serial dilutions of the "high conc." standard (as discussed in section 4.3.5) were measured to calibrate the GC-FID response for methane, ethane, propane, n-butane and iso-butane across the applicable concentration range. The linearity of methane is shown in figure 4.14, where the R^2 correlation was found to be >0.996. The response of the GS-Q column at 120 °C did not give reproducible peaks that could be integrated for the C_5 hydrocarbons (the "high conc." standard has no C_6 hydrocarbons). Temperature programming was also found to not yield acceptable peaks for either of these hydrocarbons, and therefore the C_5 hydrocarbons are not included in the analysis.

The entire chromatographic separation of the $C_1 - C_4$ hydrocarbons was found to take

† Highest concentration where explosion can occur, above this limit there is not enough oxygen to initiate a reaction.

460 seconds, following which a temperature program of 120 seconds was required to ensure no residual material was left on the column prior to beginning a new run. This leads to a sample throughput of approximately 6 samples per hour. Following the calibration step, 3 samples were chosen at random from the 40 Isotubes™, and measured on the GC-FID again using 0.1 ml injections.

The data obtained from the three tubes measured on the GC-FID has been directly compared against the concentrations measured on a Voice100 SIFT-MS instrument, as shown in figure 4.16. In figure 4.16-A, a concentration for iso-butane is not reported for the GC-FID measurement, because the peak area was found to be too small to allow for accurate integration at the specified conditions.

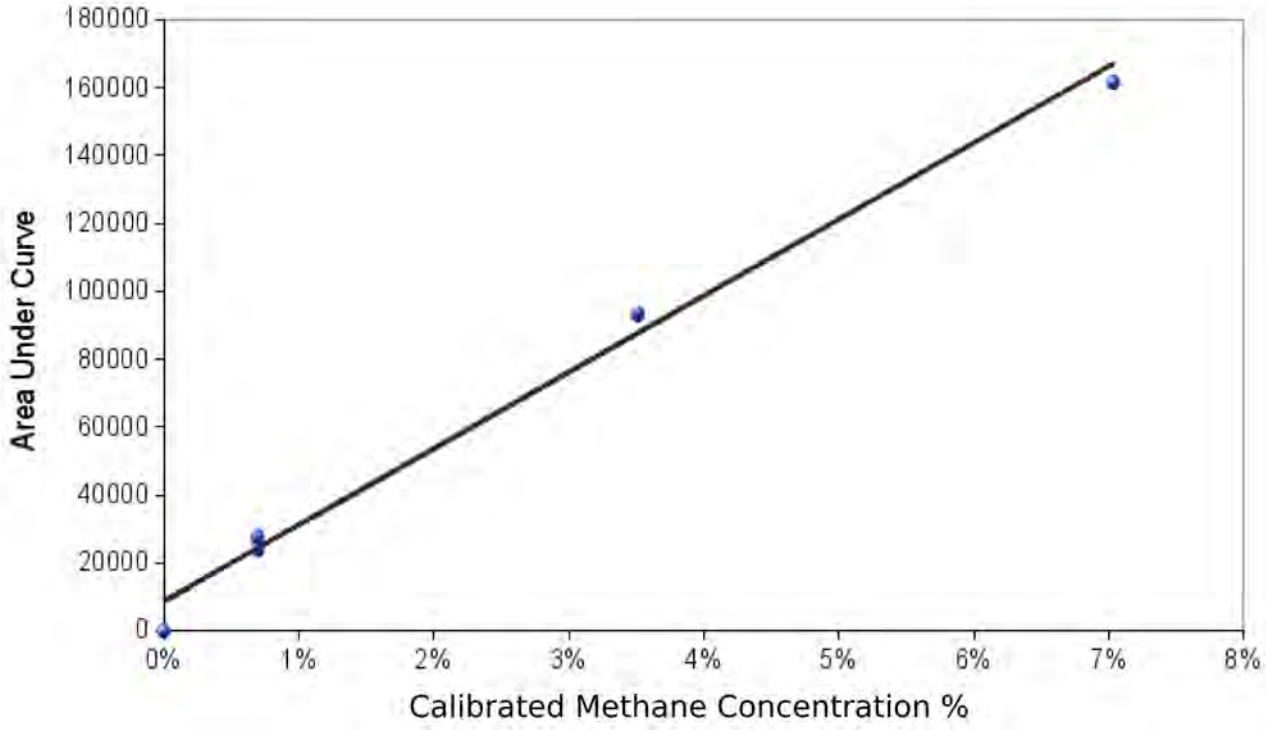

Figure 4.15. Linearity of methane calibration measurements on a Hewlett Packard 5890 GC-FID using a 30 x 0.321 mm GS-Q column isothermal at 120 °C, injector and detector temperatures were set at 250 °C, and the helium carrier velocity was ~ 20 cm /sec. Retention time for methane was found to be 137 seconds. Calibrated methane concentrations were determined using serial dilutions of the "high conc." standard.

In general the data shown in figure 4.16 gives good agreement between the two methods of concentration measurement. The samples at 'site A – 4390 m' and 'site B – 3275 m' are found to give excellent agreement between the Voice100 and the GC-FID data.

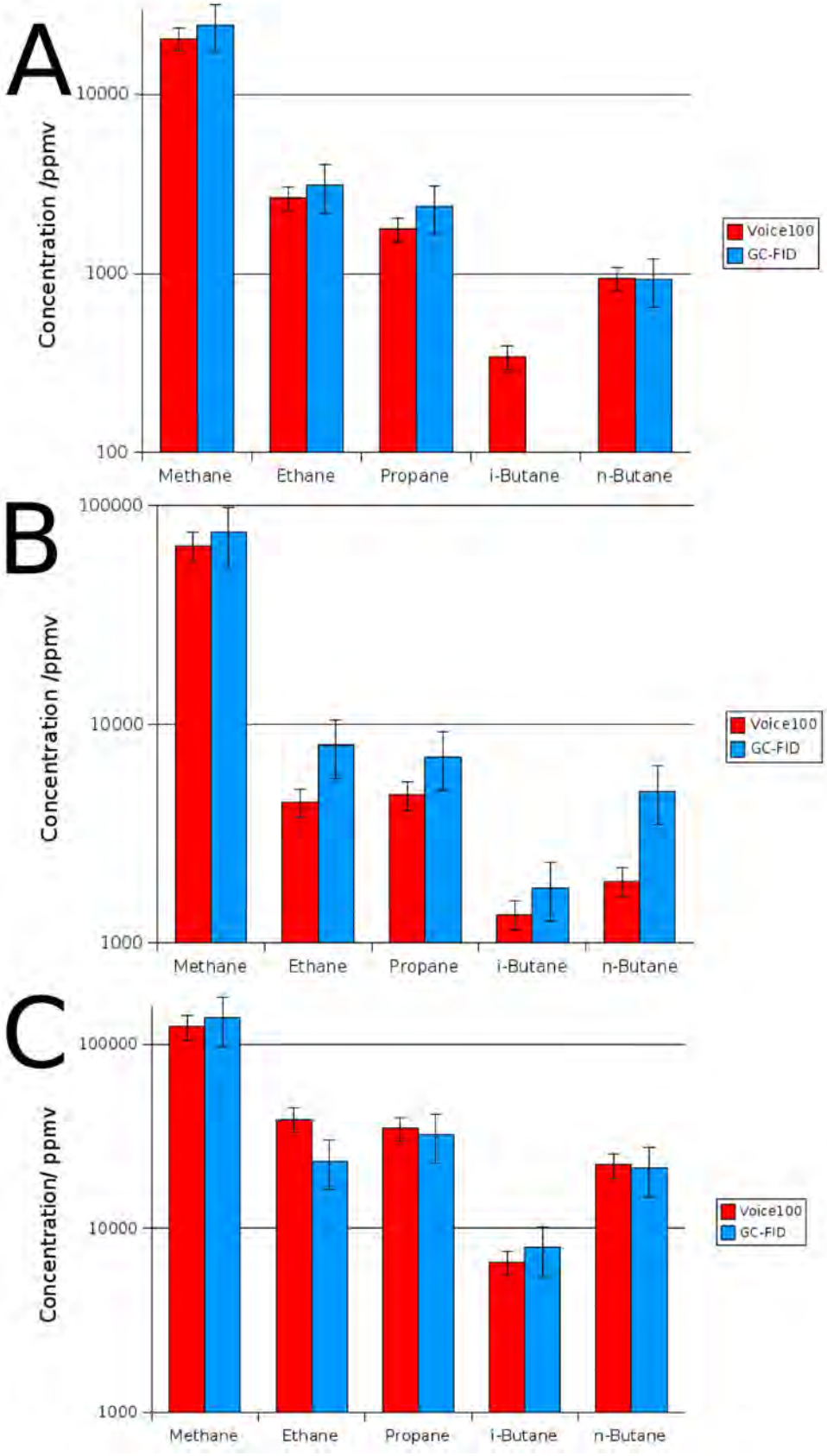

Figure 4.16. Comparison of measured concentrations for specific Isotubes™ on a GC-FID and a Voice100 on a logarithmic scale. A) Site A, 4390m. B) Site B, 3260 m. C) Site B, 3275 m. Error bars are ± 15% on Voice100 data and ± 30% on GC-FID data.

For both sites, all five hydrocarbon species are found to agree within the expected uncertainty on the experimental precision where the Voice100 uncertainty is ± 15% and the GC-FID uncertainty is ± 30%. The GC-FID and Voice100 data for 'Site B – 3260 m' is found to only agree for 3 of the 5 measured compounds, with ethane and n-butane not correlating to within the expected uncertainty. The variation observed for ethane may be attributed to an increased uncertainty on the ethane Voice100 measurement because of the required subtraction to m/z 28 from the $O_2^{\bullet+}$ + propane channel. Assuming these uncertainties are additive, the uncertainty on the ethane Voice100 precision may be as large as ± 30%. The discrepancy in the n-butane data is quite large, and seems to be for no apparent reason.

In most cases the Voice100 is found to under-measure the concentrations obtained by the GC-FID measurements, and this general trend may be indicative of a Voice100 scaling factor, such as the capillary flow, being incorrect.

4.5 Case Study: Hydrocarbon Micro-seep Detection Using Water Samples

4.5.1 Introduction

The western regions of the North Island of New Zealand have provided substantial reservoirs of oil and gas in the past and both offshore and onshore extraction processes have been common in this area. The area is made up of two basins, the Taranaki basin that has afforded many sites for extraction, [177] and the Wanganui basin that is still largely unexplored. [178] A New Zealand petrochemical exploration company is interested in the Wanganui basin, and surrounding lesser explored areas as possible sites for oil extraction. Four particular formations (formally named geological regions which have a specific rock stratum) are of interest, which are the Matemateaonga, Brunswick and Rapanui formations, and the Mount Stewart anticline. These regions are defined in figure 4.17, which also includes the site of the Whangaehu-1 exploration well. Whangaehu-1 was drilled in January 1996, and was found to be not a commercial feasible extraction site. As noted in the introduction section, when exploring for new possible sites for oil extractions, it is important to reference sites that were found to be successful or unsuccessful.

A previous study of the isotopic distribution of the hydrocarbons arising from micro-seepage in the Wanganui basin has shown the organic compounds to arise from biogenic sources.

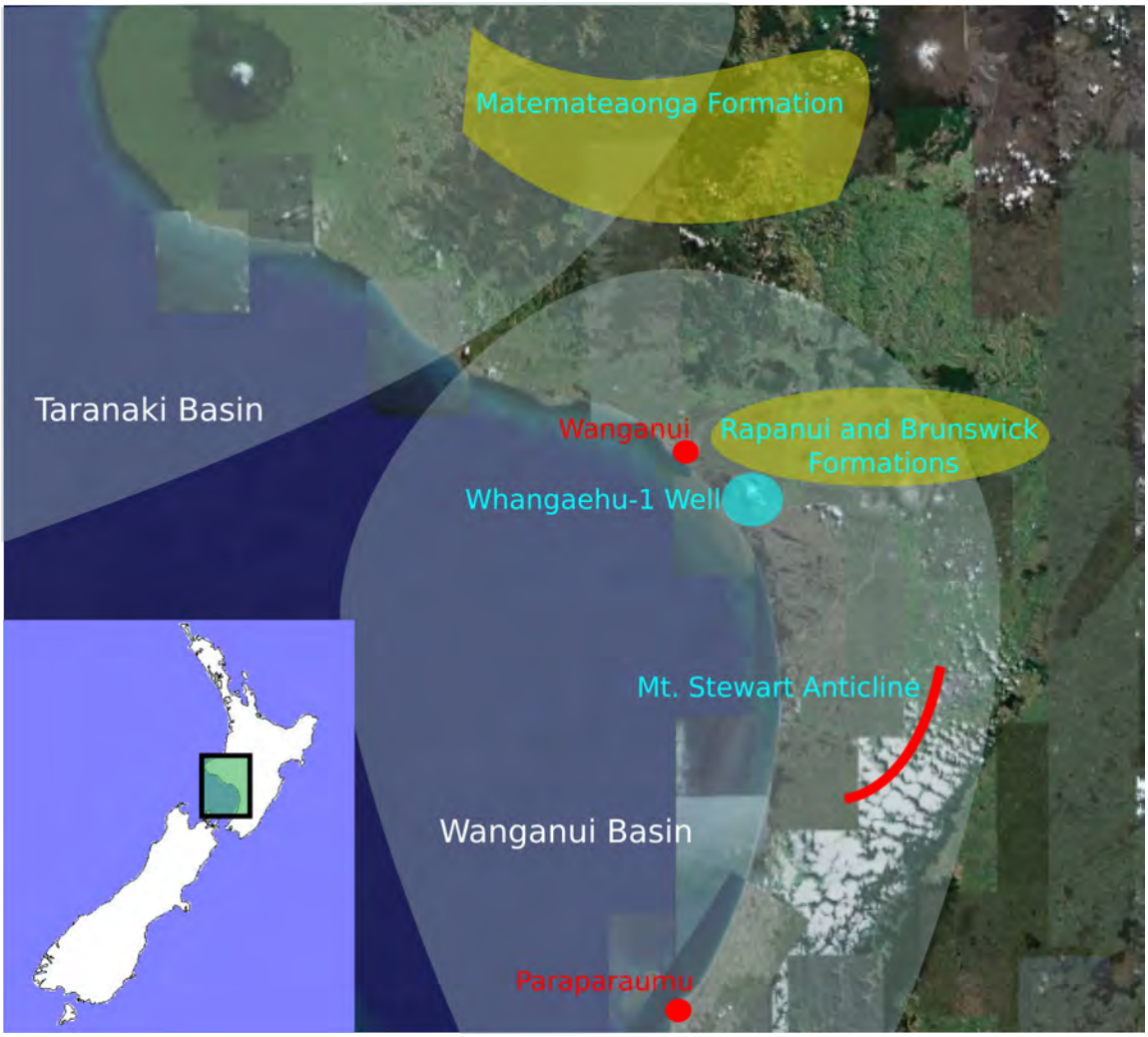

Figure 4.17. The Wanganui and south-eastern Taranaki basins in New Zealand with particular geological features highlighted.

Some seismic information on the region is also known.

- Coal, lignite and peat are common at various levels through the 4-5 km thick "Plio-Pleistocene succession" (a layer of strata that is approximately 2 million years old), but these are a very minor component of the strata.
- The majority of the geological depositing processes of the Wanganui basin have occurred while the region was under-water.
- Of the regions of interest, only the lower Matemateaonga has substantial deposits of organic matter that have occurred during non-marine periods. These have been deposited as thin layers of coal and carbon-rich mudstone.
- The Brunswick and Rapanui formations are known to contain thin layers of

lignite and carbon rich clays.

- The Mount Stewart anticline is very near to a thick layer of peat, that is an organic rich material.

From the knowledge of the strata, it has been proposed that organic rich regions of the Wanganui basin may contain light hydrocarbons (methane) that could be extracted for commercial purposes. The preliminary study has been undertaken, with an outlook toward a thorough study in the future.

4.5.2 SIFT-MS preliminary study

The SIFT-MS technique has been employed to study the concentrations of saturated acyclic hydrocarbons in four water samples. Each water sample was taken from a well in the Wanganui basin where the geology has indicated an increased organic component of the strata below the surface.

The four sites are listed as A – D, (with reference to figure 4.17) where site A is near Wanganui, site B is west of the Mount Stewart anticline, site C is approximately 50 km north of Paraparaumu and site D is in the township of Paraparaumu. At each site a 750 ml disposable mineral water was half filled with water arising from an artesian well, where care was taken to ensure the sampled water had not yet reached the surface. The four samples were then shipped to Christchurch, New Zealand for SIFT-MS analysis using a Voice100 with the GeoVOC method and the Nafion^{TM} dryer system.

4.5.3 Results and discussion

Table 4.07 lists the concentrations measured by the Voice100 for the C_1 – C_6 acyclic saturated hydrocarbons across the four sites of interest.

It is apparent from table 4.07 that the majority of gas rising through the water wells is methane. In the extreme case of site B, methane is found to be 6000 fold greater than the concentrations of all other measured hydrocarbons added together. As the distribution of hydrocarbons lies strongly toward methane, any reservoir that may lie below is a gas reservoir, and not a gas condensate or oil reservoir (when applying the method of Jones and Drozd). [152]

Table 4.07. Voice100 determined concentrations for the preliminary survey of four water wells in the Wanganui basin of New Zealand.

	***Concentration** /ppmv*			
	Site A	*Site B*	*Site C*	*Site D*
Methane	1220	22.6	35400	0.96
Ethane	0.33	0.30	2.49	0.01
Propane	0.19	0.23	0.44	0.10
n-Butane	0.39	0.38	2.18	0.16
n-Pentane	0.04	0.03	0.08	0.04
n-Hexane	0.06	0.03	0.22	0.02
iso-Butane	0.06	0.07	0.22	0.01
iso-Pentane(s)	0.01	0.04	0.05	0.01
iso-Hexane(s)	0.	0.05	0.15	0.01

Site C is found to contain the highest concentration of hydrocarbons, followed by sites A, B and D. Sites C and D are physically close to one another (approximately 50 km apart), yet their observed hydrocarbon concentrations are markedly different. This drastic difference in concentration may be due to differing sub-surface horizontal migration pathways for the two systems (refer to figure 4.03), sampling anomalies, differing water well depths where the samples were taken, or a genuine observation of a gas reservoir approximately 50 km north of Paraparaumu.

The very high concentration of methane observed for site C, and to certain extent site A is promising, and may indicate the presence of a gas reservoir in the Wanganui basin. The preliminary nature of the current investigation however, precludes any further conclusions being drawn.

4.6 Concluding Remarks

From a thorough investigation of the gas-phase ion molecule chemistry of a range of hydrocarbons analytes with two SIFT-MS precursors, and a quantitative study of the ensuing secondary reactions with water, the GeoVOC method has been implemented on a Voice100 SIFT-MS instrument. The quantitative analysis of some C_1-C_9 acyclic saturated hydrocarbons in moist samples has then been enabled through the incorporation of a Nafion™ drier system that selectively removes moisture and does not perturb the concentration of hydrocarbons

The accuracy of the GeoVOC method was then determined by comparing the results found on a Voice100 to a range of commercial gas standards. This comparison yielded an

RMS error of ± 2% for dry samples and ± 4% for humidified samples, however the humidified samples were found to slightly under-report the calibrated concentrations.

Two case studies were then given in support of SIFT-MS as a technique for the analysis of acyclic hydrocarbon compounds related the oil exploration industry. A depth dependent quantitative analysis of two oil wells during the drilling process and the use of bore water samples to determine information regarding a possible new gas reservoir in the North Island of New Zealand. Both of these case studies strongly support SIFT-MS as a valuable technique for aiding in the oil and gas exploration process.

CHAPTER 5

REACTIONS AND REARRANGEMENTS OF ALKYL ESTERS

5.1 Introduction

Ester compounds, that are formed by a dehydration reaction of an alcohol with a carboxylic acid, are known to most high school students to be compounds that have a fruit-like aroma. For instance, a commonly performed experiment in New Zealand high school chemistry laboratories is the reaction of butanoic acid with ethanol forming ethyl butanoate, a key component in the flavours of pineapple, banana and strawberry. [179] However, the fruity aromas of ester compounds are generally limited to the simpler esters, and the aroma strength is known to decrease with the volatility of the compound. [180] The small ester compounds, where small shall be defined to be less than 16 carbons, are considered to be the 'work horses' of the food and flavour industry. Over 200 ester compounds are permitted as flavour additives by the U.S. F.D.A. (United States of America Food and Drug Administration) for use in foods, [181] where the majority of this use is for the addition of fruit-like flavours. These esters tend to be saturated (alkyl esters), as the addition of double bonds and aromatic groups to the ester side chains substantially alters the aroma profile. [180] Small ester compounds are also known to naturally occur in fruits and vegetables, and a few pertinent examples of this are given below. [179,182,183]

- The majority of *banana* odour and flavour is due to s-butyl ethanoate, s-butyl butanoate and 3-methyl butanoate.
- *Apple* aroma is known to contain ethyl butanoate and ethyl hexanoate.
- The headspace of *nectarines* is known to contain ethyl ethanoate as a major component.
- The aroma of *Honeydew melon* is dominated by a range of small ethanoate esters such as methyl, ethyl, propyl and butyl ethanoates.
- *Citrus* aroma is strongly associated with small ethyl esters.

Because these small alkyl esters are all strongly volatile (e.g. vapour pressure of ethyl ethanoate is 90 Torr at 25 °C and butyl ethanoate is 11 Torr at 25 °C [184]) and have an

impact on the aroma and flavour of a food, they can be excellent targets for process control in the food and flavour industry. This industry is estimated to spend between 1.5 and 2% of their total sales revenue on process control and appraisal, and therefore an efficient methodology for this process control will lead to increase in profit. [185]

Process control, comes under the blanket of quality assurance, which is a set of activities that checks to see whether the characteristics or qualities of a product actually exist in the product. [186] For instance, if a product is claimed to have a banana aroma, this parameter must be quantitatively tested to ensure that the banana aroma exists in the product prior to sale. It is therefore apparent that a quantitative measure of the banana-related esters in the headspace above the product would be very useful.

Also, island nations such as New Zealand are often interested in protecting the native flora and fauna of their country by restricting the movement of plants, fruits and vegetables across their borders. [187] Therefore, the detection of volatile compounds that are related to fruits and vegetables in shipping containers and luggage is of interest to many border security organisations.

Ester compounds are also commonly used commercially as solvents in paints, glues and varnishes. The majority of s-butyl ethanoate that is commercially synthesised is used as a solvent in artificial cellulose, while only a small percentage is consumed in flavours and fragrances.

SIFT-MS is an ideal technique for the detection of esters in all of these applications due to its rapid screening ability, low limits of detection and its wide quantitation range which is parts-per-trillion-by-volume (pptv) up to parts-per-million-by-volume. [58] However, as has been mentioned previously in this thesis, proper utilisation of SIFT-MS as an analytical technique, at a level that will provide quantitation, relies on a fundamental understanding of the reactions that are occurring in the flow tube between the SIFT-MS precursor ions (NO^+, $O_2^{\bullet+}$ and $H_3O^+(H_2O)_n$ where n = 0, 1, 2, 3) and the analytes of interest. This chemistry is known as the primary chemistry. As well the primary chemistry, an understanding of the secondary reactions of product ions with H_2O is required for accurate quantitation in humid environments. However, in comparison to the data present in chapter 4, a qualitative approach is taken here such that the secondary rate coefficients are not measured, but only the sequential reaction pathways of the product ions are followed.

A selection of important data presented in this chapter has been published in the Journal of Physical Chemistry A. [51]

5.2 Measurement of Kinetic Parameters

5.2.1 Introduction and previous investigation

Spanel and Smith [36] have previously studied the reactions of the SIFT-MS precursors (excluding the hydronium ion water clusters) with methyl and ethyl methanoates, ethanoates, propanoates and butanoates† where they found that most reactions occurred at or near the collision limiting rate coefficient, and yielded no unexpected product ions. H_3O^+ was found to give simple predictable proton transfer and NO^+ was found to give association products. The $O_2^{\bullet+}$ precursor ion was found to react via dissociative electron transfer pathways often cleaving the ionised alkyl esters at the $R_1CO\text{-}OR_2$ bond forming R_1CO^+ and OR_2 fragments (where R_1 and R_2 are alkyl chains). This type of reaction shall be coined as an ester cleavage reaction and is shown in reaction 5.01.

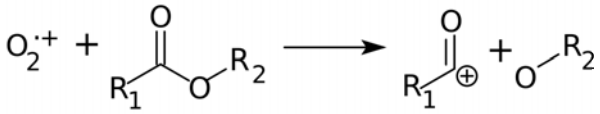

(5.01)

To expand the capabilities of SIFT-MS to be able to quantitate larger ester compounds, the reaction rate coefficients, and product ion branching ratios of 17 alkyl esters reacting with NO^+, $O_2^{\bullet+}$, and $H_3O^+(H_2O)_n$ where n = 0, 1, 2, 3 have been studied. In addition to these measurements, the secondary reactions of many of the product ions with water have been monitored to qualitatively observe how the product ion branching fractions alter with humidity.

5.2.2 Experimental Conditions

The instrument used for measurement of reaction rate coefficients and product ion branching ratios in this chapter is the Voice100 SIFT-MS as described in section 2.2 of this thesis. The glass gas handling line (section 2.5.1) has been used to introduce neutral analytes to the Voice100's flow tube which is operated with 15 Torr L s^{-1} of helium through the inner carrier annulus and 25 Torr L s^{-1} of argon through the outer hole inlet. The flow tube pressure is then found to be ~0.5 Torr. These are the optimised conditions for the Voice100 flow tube as discussed in chapter 3.

† IUPAC nomenclature will be used throughout the course of this chapter where formates, acetates, propionates and butyrates shall be referred to as methanoates, ethanoates, propanoates and butanoates respectively.

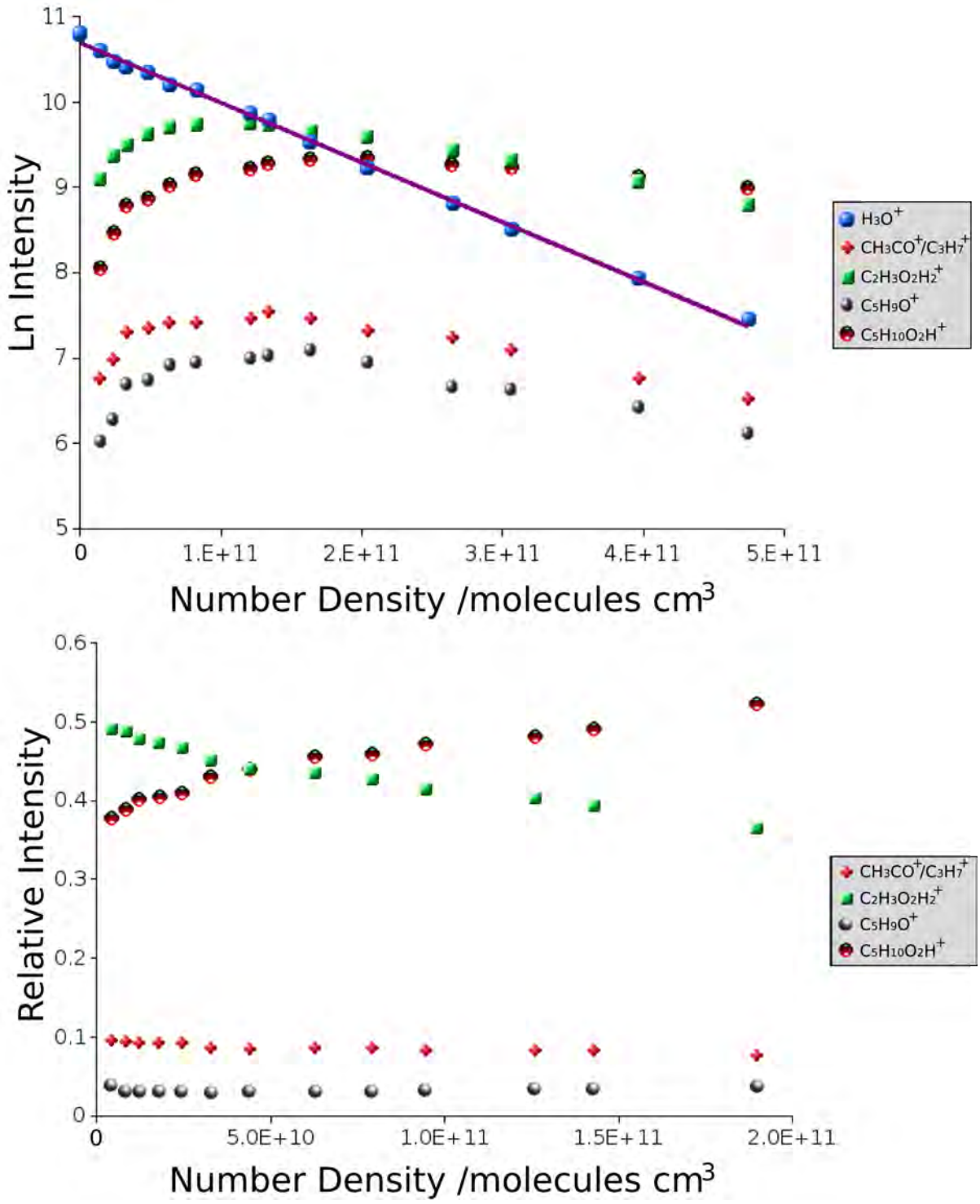

Figure 5.01. Example of an ion-molecule kinetics plot (top) and a branching ratio determination (bottom) for the reaction of H_3O^+ + n-propyl ethanoate (C_3H_7O-$COCH_3$).

Collision limiting rate coefficients have been calculated using the method of Su [108] where the required dipole moments and polarisabilities for each alkyl ester studied have been calculated using the Gaussian 03W suite of software employing B3LYP density functional theory using the 6-311G(d,p) basis set with added diffuse functions where necessary. The collision limiting rate coefficients are deemed to have an expected uncertainty of ± 20% based mostly on the uncertainty of the dipole moment. Small variations in the calculation of the polarisability have little effect on the calculated collision limiting rate coefficient.

An example of an ion molecule kinetics plot and a branching ratio plot are shown in figure 5.01.

5.2.3 Chemicals

Both the helium and argon carrier gases were sourced from Southern Gas Services (Christchurch, New Zealand) and have a quoted purity of 99.9995%. Neither gas was purified further. Ester compounds were sourced from Sigma Aldrich with stated purities of 98% or greater, except for n-butyl butanoate and iso-propyl propanoate from Alfa Aesar (Heysham, UK; purity 98%) and iso-propyl ethanoate that was sourced from Acros Organics (New Jersey, USA; purity 99+%). All alkyl ester compounds were further purified by freeze-pump-thaw cycling.

5.2.4 Results and general discussion

Experimental absolute rate coefficients and collision limiting rate coefficients for the reactions of 17 alkyl esters with H_3O^+, $H_3O^+.H_2O$, $H_3O^+.(H_2O)_2$, $H_3O^+.(H_2O)_3$, NO^+ and $O_2^{\bullet+}$ are given in table 5.01. Reaction rate coefficients for the hydronium ion water clusters are calculated by the method prescribed in chapter 3, using the iterative method. The uncertainty on the H_3O^+, NO^+ and $O_2^{\bullet+}$ rate coefficients is ± 15%, and the uncertainties on the $H_3O^+.H_2O$, $H_3O^+.(H_2O)_2$ and $H_3O^+.(H_2O)_3$ rate coefficients are ± 45%, ± 70% and ± 95% respectively. The calculated dipole moments and polarisabilities for each of the alkyl esters used for determining the collision limiting rate coefficients are given in table 5.02. Also included in table 5.02 are some thermodynamic parameters of interest. Where the values are available, proton affinities and ionisation energies have been sourced from the NIST database, [30,31] with uncertainties on the ionisation energies of ± 0.2 eV and proton affinities of ± 3 kJ mol^{-1}.

[188,189] Table 5.03 then lists the observed product ion masses, an estimation of the ionic structure and the observed product ion branching ratio.

Table 5.01. Rate coefficients of 17 alkyl esters reacting with the SIFT-MS precursor ions measured at 298 K and 0.5 Torr.

Compound	***k_{exp} [k_c] [a,b] /10^{-9} cm^3 $molecule^{-1}$ s^{-1}***					
	H_3O^+	*$H_3O^+.H_2O$*	*$H_3O^+.2H_2O$*	*$H_3O^+.3H_3O$*	*NO^+*	*$O_2^{\bullet+}$*
n-Butyl Methanoate	3.0 [3.5]	3.2 [2.8]	1.7 [2.7]	<0.01 [2.3]	1.3 [2.9]	2.2 [2.8]
n-Propyl Ethanoate	3.3 [3.3]	3.0 [2.4]	3.2 [2.1]	3.2 [2.0]	1.8 [2.7]	2.2 [2.6]
n-Butyl Ethanoate	2.9 [3.3]	3.4 [2.5]	4.6 [2.2]	1.8 [2.0]	2.0 [2.8]	2.3 [2.7]
i-Butyl Ethanoate	3.2 [3.3]	3.3 [2.5]	4.1 [2.2]	<0.01 [2.0]	2.2 [2.8]	2.3 [2.7]
s-Butyl Ethanoate	3.1 [3.3]	2.1 [2.5]	2.6 [2.2]	1.8 [2.0]	2.1 [2.8]	2.5 [2.7]
t-Butyl Ethanoate	3.2 [3.2]	2.2 [2.5]	2.9 [2.1]	1.8 [1.9]	1.8 [2.7]	2.0 [2.6]
Methyl Propanoate [c]	2.7 [3.1]	3.0 [2.4]	3.9 [2.1]	0.7 [1.9]	1.5 [2.6]	1.9 [2.5]
Ethyl Propanoate [c]	2.9 [2.9]	3.3 [2.2]	4.6 [1.9]	1.3 [1.8]	1.7 [2.4]	2.2 [2.3]
n-Propyl Propanoate	3.3 [3.0]	3.7 [2.3]	4.6 [2.0]	<0.01 [1.9]	2.2 [2.5]	2.2 [2.5]
i-Propyl Propanoate	3.1 [3.0]	2.8 [2.3]	3.1 [2.0]	<0.01 [1.9]	2.1 [2.5]	2.2 [2.5]
n-Butyl Propanoate	2.9 [3.1]	2.9 [2.4]	3.0 [2.1]	1.7 [1.9]	1.8 [2.6]	2.4 [2.5]
t-Butyl Propanoate	3.0 [3.1]	3.6 [2.4]	2.7 [2.1]	<0.01 [1.9]	1.8 [2.6]	2.3 [2.5]
Ethyl Butanoate	3.0 [3.2]	2.9 [2.2]	3.7 [2.1]	<0.01 [1.9]	2.4 [2.7]	2.5 [2.6]
n-Propyl Butanoate	3.2 [3.2]	2.8 [2.4]	3.6 [2.1]	<0.01 [1.9]	2.0 [2.6]	1.8 [2.6]
i-Propyl Butanoate	2.8 [3.2]	1.5 [2.4]	3.4 [2.1]	<0.01 [1.9]	2.2 [2.6]	2.7 [2.6]
n-Butyl Butanoate	3.1 [3.2]	3.6 [2.5]	2.4 [2.1]	1.1 [1.9]	2.2 [2.7]	2.9 [2.6]
i-Butyl Butanoate	2.9 [3.2]	3.2 [2.5]	1.9 [2.1]	1.3 [1.9]	2.0 [2.7]	2.0 [2.6]

a) Experimental rate coefficients (k_{exp}) for H_3O^+, NO^+ and O_2^+ are quoted with ±15% error, and collision limiting rates (k_c) with ±20%. The uncertainty on the hydronium ion water cluster rates is discussed in the text. Collision rates determined by the parameterised trajectory method of Su. [108]
b) Rate coefficients of $H_3O^+.nH_2O$ that appear anomalously large are discussed in the text.
c) Comparable with literature values for H_3O^+, NO^+ and O_2^+ reactions. [36]

The dipole moments determined in this study by quantum chemical methods are found to be approximately 20% higher than the literature values. However, all the literature values of dipole moment shown in table 5.02 were determined from liquid phase measurements, and these are known to have a large uncertainty based on association effects. [122] In the liquid phase, distortions from the lowest energy conformational geometry may be facilitated by interactions with surrounding molecules which would in turn alter the observable dipole moment of the molecule.

Table 5.02. B3LYP/6-311+G(d,p) calculated dipole moments and polarisabilities compared to literature experimental values where known.

Compound	***PA***	***IE***	***Dipole moment (μ_D) /Debye***		***Polarisability (α) /Å^3***	
	/kJ mol^{-1}	*/eV*	*Calculated* [a]	*Literature* [b]	*Calculated* [a]	*Literature* [b]
n-Butyl Methanoate	806.0	10.52	2.4	2.03	10.0	
n-Propyl Ethanoate	836.6	9.98	2.2	1.78	10.2	
n-Butyl Ethanoate		9.94	2.2	1.87	12.0	
i-Butyl Ethanoate		9.97	2.2	1.86	12.0	
s-Butyl Ethanoate		9.90	2.2	1.87	12.0	
t-Butyl Ethanoate		10.00[c]	2.1		11.6	
Methyl Propanoate[d]	830.2	10.15	1.8		8.1	8.97
Ethyl Propanoate[d]	813.3[c]	10.00	2.0	1.74	9.9	10.41
n-Propyl Propanoate		9.96	1.9		11.7	
i-Propyl Propanoate			1.9		11.7	
n-Butyl Propanoate			1.9		13.3	
t-Butyl Propanoate			1.9		13.3	
Ethyl Butanoate			1.8	1.74	12.0	
n-Propyl Butanoate			1.9		13.6	
i-Propyl Butanoate			1.9		13.6	
n-Butyl Butanoate			2.0		15.3	
i-Butyl Butanoate			2.0		15.3	

a) Values calculated using the Gaussian 03 suite of software.
b) Literature values sourced from the CRC handbook. [122]
c) Determined by CBS-4M calculations, using the G03W suite of software. See table 5.05.
d) Polarisability and dipole moments given in reference [36] for methyl and ethyl propanoate are based on estimates, and are not deemed to be accurate enough for a direct comparison.

But, the lowest energy molecular geometry, as calculated by B3LYP/6-311+G(d,p) is also the conformer that has the lowest dipole moment, and therefore the distortions that occur in the liquid phase will increase the observed dipole moment such that the dipole moment of the lowest energy conformer should be lower than the reported value. Only the lowest energy conformer is used for calculating the dipole moment in this study, and important effects may be ignored by this assumption.

The two literature values of polarisability given in table 5.02 are calculated by a parameterised method, but have been compared to experimental values and agree well within the quoted uncertainty. The values of polarisability calculated by quantum chemical methods in this study are found to be ~10% lower than the literature values. This observation is possibly attributed in this work to the use of a small basis set, and ignoring important conformers so as to minimise calculation time.

Table 5.03. Product ions observed from the reactions of the specified ion with the ester listed at 298 K and 0.5 Torr.

Compound	***m***	***H_3O^+***			***NO^+***			***$O_2^{\bullet+}$***		
	/g mol^{-1}	*Ion*	*m/z*	*BR*	*Ion*	*m/z*	*BR*	*Ion*	*m/z*	*BR*
n-Butyl Methanoate	102	$C_5H_{10}O_2H^+$	103	0.25	$C_5H_{10}O_2.NO^+$	132	0.80	$C_5H_{10}O_2^+$	102	0.05
		$C_4H_9^+$	57	0.75	$C_4H_9O^+$	73	0.15	$C_4H_9O^+$	73	0.05
					$C_4H_8^+$	56	0.05	$C_4H_8^+$	56	0.90
n-Propyl Ethanoate	102	$C_5H_{10}O_2H^+$	103	0.35	$C_5H_{10}O_2.NO^+$	132	0.30	$C_3H_5O_2^+$	73	0.10
		$C_5H_9O^+$	85	0.05	$C_5H_9O_2^+$	101	0.20	$C_2H_3O_2^+$	61	0.55
		$C_2H_3O_2H_2^+$	61	0.50	$C_5H_8O^+$	84	0.10	$C_3H_7O^+$	59	0.05
		$CH_3CO^+/C_3H_7^+$	43	0.10	$C_3H_7O^+$	59	0.10	$CH_3CO^+/C_3H_7^+$	43	0.20
					$CH_3CO^+/C_3H_7^+$	43	0.30	$CH_2CO^+/C_3H_6^+$	42	0.10
n-Butyl Ethanoate	116	$C_6H_{12}O_2H^+$	117	0.35	$C_6H_{12}O_2.NO^+$	146	0.65	$C_4H_8^+$	56	0.90
		$C_2H_3O_2H_2^+$	61	0.55	$C_6H_{11}O_2^+$	115	0.05	$CH_3CO^+/C_3H_7^+$	43	0.10
		$C_4H_9^+$	57	0.10	$C_4H_9O^+$	73	0.15			
					$CH_3CO^+/C_3H_7^+$	43	0.15			
i-Butyl Ethanoate	116	$C_6H_{12}O_2H^+$	117	0.20	$C_6H_{12}O_2.NO^+$	146	0.15	$C_4H_6O_2^+$	86	0.05
		$C_2H_3O_2H_2^+$	61	0.70	$C_6H_{11}O_2^+$	115	0.25	$C_4H_9O^+$	73	0.10
		$C_4H_{10}^+$	58	0.05	$C_4H_6O_2^+$	86	0.05	$C_2H_3O_2^+$	61	0.05
		$CH_3CO^+/C_3H_7^+$	43	0.05	$C_4H_9O^+$	73	0.30	$C_4H_8^+$	56	0.60
					$C_4H_8^+$	56	0.10	$CH_3CO^+/C_3H_7^+$	43	0.20
					$CH_3CO^+/C_3H_7^+$	43	0.15			
s-Butyl Ethanoate	116	$C_6H_{12}O_2H^+$	117	0.20	$C_6H_{12}O_2.NO^+$	146	0.35	$C_6H_{12}O_2^+$	116	0.05
		$C_2H_3O_2H_2^+$	61	0.75	$C_6H_{11}O_2^+$	115	0.05	$C_4H_9O^+$	73	0.05
		$C_4H_9^+$	57	0.05	$C_2H_4O_2.NO^+$	90	0.30	$C_2H_3O_2^+$	61	0.30
					$C_4H_8.NO^+$	86	0.15	$C_4H_8^+$	56	0.35
					$C_4H_9O^+$	73	0.15	$CH_3CO^+/C_3H_7^+$	43	0.25
t-Butyl Ethanoate	116	$C_6H_{12}O_2H^+$	117	0.05	$C_6H_{12}O_2.NO^+$	146	0.05	$C_5H_9O_2^+$	101	0.30
		$C_4H_9^+$	57	0.95	$C_2H_4O_2.NO^+$	90	0.45	$C_2H_3O_2^+$	59	0.10
					$C_4H_8.NO^+$	86	0.40	$C_4H_8^+$	56	0.60
					$C_4H_8^+$	56	0.10			
Methyl Propanoate[a]	88	$C_4H_8O_2H^+$	89	0.90 (0.95)	$C_4H_8O_2.NO^+$	118	0.45 (0.20)	$C_4H_8O_2^+$	88	0.35 (0.25)
		$C_2H_5CO^+$	57	0.10 (0.05)	$C_2H_5CO^+$	57	0.55 (0.80)	$C_2H_5CO^+$	57	0.65 (0.75)
Ethyl Propanoate[a]	102	$C_5H_{10}O_2H^+$	103	0.90 (0.95)	$C_5H_{10}O_2.NO^+$	132	0.55 (0.60)	$C_5H_{10}O_2^+$	102	0.25 (0.05)
		$C_3H_5O_2H_2^+$	75	0.05	$C_2H_5CO^+$	57	0.45 (0.40)	$C_3H_6O_2^+$	74	0.15 (0.05)
		$C_2H_5CO^+$	57	0.05 (0.05)				$C_2H_5CO^+$	57	0.40 (0.45)
								$C_2H_5O^+$	45	0.20 (0.15)
n-Propyl Propanoate	116	$C_6H_{12}O_2H^+$	117	0.40	$C_6H_{12}O_2.NO^+$	146	0.25	$C_3H_7O_2^+$	75	0.55
		$C_3H_5O_2H_2^+$	75	0.40	$C_6H_{12}O_2^+$	116	0.05	$C_3H_5O^+$	57	0.35
		$C_3H_5O^+$	57	0.10	$C_6H_{11}O_2^+$	115	0.10	$C_3H_7^+$	43	0.10
		$C_3H_7^+$	43	0.10	$C_3H_5O^+$	57	0.60			
i-Propyl Propanoate	116	$C_6H_{12}O_2H^+$	117	0.10	$C_6H_{12}O_2.NO^+$	146	0.35	$C_5H_9O_2^+$	101	0.05
		$C_3H_5O_2H_2^+$	75	0.75	$C_6H_{11}O_2^+$	115	0.40	$C_3H_7O_2^+$	75	0.40
		$C_3H_5O_2^+$	73	0.10	$C_4H_9O_2^+$	89	0.25	$C_3H_5O^+$	57	0.30
		$C_3H_7^+$	43	0.05				$C_2H_5O^+$	45	0.10
								$C_3H_7^+$	43	0.15
n-Butyl Propanoate	130	$C_7H_{14}O_2H^+$	131	0.40	$C_7H_{14}O_2.NO^+$	160	0.40	$C_3H_7O_2^+$	75	0.40
		$C_3H_5O_2H_2^+$	75	0.35	$C_7H_{13}O_2^+$	129	0.10	$C_4H_8^+$	56	0.60
		$C_4H_9^+$	57	0.25	$C_4H_8.NO^+$	86	0.10			
					$C_4H_9^+$	57	0.40			
t-Butyl Propanoate	130	$C_7H_{14}O_2H^+$	131	0.10	$C_7H_{14}O_2.NO^+$	160	0.05	$C_6H_{11}O_2^+$	115	0.10
		$C_3H_5O_2H_2^+$	75	0.10	$C_3H_6O_2.NO^+$	104	0.45	$C_3H_7O_2^+$	75	0.10
		$C_4H_9^+$	57	0.80	$C_4H_8.NO^+$	86	0.35	$C_4H_8^+$	56	0.80
					$C_4H_8^+$	56	0.15			
Ethyl Butanoate	116	$C_6H_{12}O_2H^+$	117	0.80	$C_6H_{12}O_2.NO^+$	146	0.30	$C_6H_{12}O_2^+$	116	0.10
		$C_4H_7O^+$	71	0.20	$C_4H_7O^+$	71	0.70	$C_4H_7O^+$	71	0.75
								$C_3H_7^+$	43	0.15

Table 5.03. Continued.

Compound	***m***	***H_3O^+***			***NO^+***			***$O_2^{\bullet+}$***		
	/g mol^{-1}	*Ion*	*m/z*	*BR*	*Ion*	*m/z*	*BR*	*Ion*	*m/z*	*BR*
n-Propyl Butanoate	130	$C_7H_{14}O_2H^+$	131	0.25	$C_7H_{14}O_2.NO^+$	160	0.05	$C_4H_9O_2^+$	89	0.60
		$C_4H_7O_2H_2^+$	89	0.30	$C_4H_7O^+$	71	0.85	$C_4H_7O^+$	71	0.30
		$C_4H_7O^+$	71	0.10	$C_3H_7^+$	43	0.10	$C_3H_7^+$	43	0.10
		$C_4H_9^+$	57	0.30						
		$C_3H_7^+$	43	0.05						
i-Propyl Butanoate	130	$C_4H_7O_2H_2^+$	89	0.45	$C_4H_7O^+$	71	0.30	$C_4H_9O_2^+$	89	0.15
		$C_3H_7O^+$	59	0.25	$C_3H_7O^+$	59	0.65	$C_4H_8O_2^+$	88	0.05
		$C_3H_7^+$	43	0.30	$C_3H_7^+$	43	0.05	$C_4H_7O^+$	71	0.15
								$C_3H_7O^+$	59	0.10
								$C_2H_5O^+$	45	0.35
								$C_3H_7^+$	43	0.20
n-Butyl Butanoate	144	$C_8H_{16}O_2H^+$	145	0.65	$C_8H_{16}O_2.NO^+$	174	0.25	$C_4H_7O^+$	71	0.25
		$C_4H_7O_2H_2^+$	89	0.35	$C_4H_7O^+$	71	0.75	$C_4H_8^+$	56	0.65
								$C_3H_7^+$	43	0.10
i-Butyl Butanoate	144	$C_8H_{16}O_2H^+$	145	0.20	$C_8H_{16}O_2.NO^+$	174	0.35	$C_4H_7O^+$	71	0.40
		$C_4H_7O_2H^+$	89	0.30	$C_8H_{15}O_2^+$	143	0.05	$C_4H_8^+$	56	0.60
		$C_4H_9^+$	57	0.50	$C_4H_7O^+$	71	0.60			

a) Comparable with literature values, where the literature branching ratios are given in parentheses. [36]

For ethyl propanoate, literature values for both the dipole moment and polarisability are known. When a collision limiting rate coefficient is calculated with the literature parameters, the values returned are approximately equal to the values determined when using the quantum chemically calculated dipole moment and polarisability. This observation is fortuitous and occurs because the discrepancy from the literature values of dipole moment and polarisability off-set one another. Due to this fortuity, the accuracy of the collision limiting rate coefficients presented here for the other esters are stated with reasonable confidence.

An ester molecule is divided into two side chains. With reference to reaction 5.01, R_1 is the carboxylic acid side chain and R_2 is the alcohol side chain. All molecules studied herein have linear carboxylic acid side chains, but some molecules studied have branched alcohol side chains. The definition of the nomenclature regarding the branched alcohol side chains used during the course of this chapter is given in figure 5.02.

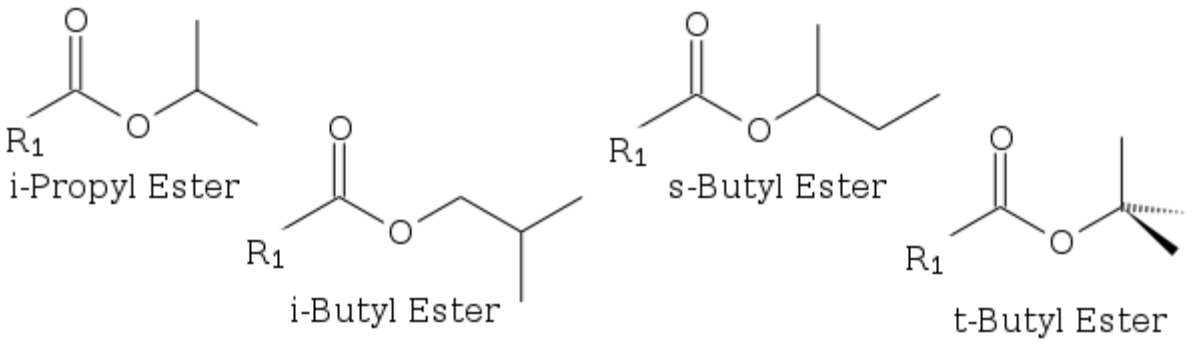

Figure 5.02. Nomenclature for naming alcohol side chains.

Also, for the remainder of this thesis, the oxygen that is doubly bound to the central carbon as part of the carbonyl group shall be referred to as the carbonyl oxygen, while the carbon that is directly bound to the alcohol side chain (R_2) shall be referred to as the alkoxy oxygen.

Reaction rate coefficients and product ion branching ratios for H_3O^+, NO^+ and $O_2^{\bullet+}$ reacting with ethyl and ethyl propanoate have been published previously by Spanel and Smith. [36] Repetition of these measurements is to ensure that there is consistency between them and measurements undertaken on the Voice100. Reactions of methyl and ethyl propanoate with H_3O^+ and NO^+ are found to yield very similar product ion branching ratios, however the rate coefficients of both NO^+ reactions are found to occur slightly slower in this study. This decrease in reaction rate is proposed to be an anomaly due the uncertainties in each measurement, and not the addition of argon to the carrier gas, as this difference should lead to the Voice100 measurements being greater than the previous data. The larger polarisability of argon compared to helium is known to generally increase the reaction efficiency of a termolecular reaction. [190] The reaction of H_3O^+ with ethyl propanoate yields a small product ion channel that was not observed previously at *m/z* 75. A mechanism for this pathway will be discussed at length later in this chapter. The reaction of $O_2^{\bullet+}$ with methyl propanoate gives very similar results to those published by Spanel and Smith, [36] however the reaction with ethyl propanoate was observed to give a larger product ion branching ratio of the molecular ion when compared to the previous investigation. This may indicate that the argon carrier gas is more effectively thermalising product ions which are formed with an excess of translational or vibrational energy compared to the helium only flow tube of Spanel and Smith. [36]

5.3 Discussion of Reaction Pathways

None of the alkyl esters studied in this chapter have known literature enthalpies of formation that are crucial for understanding the thermodynamics of the product ion channels. Therefore, where possible, some assumptions on the thermodynamics have been made, and quantum chemical calculations have been performed to give a more thorough understanding of the reactions studied.

5.3.1 H_3O^+ reactions

All 17 reactions were observed to proceed at or near the collision limiting rate coefficient, with proton transfer (the formation of $[M + H]^+$ ions) being the major product ion channel for 16 of the 17 reactions studied. When exergonic proton transfer is observed, experience has shown that the experimental reaction rate coefficient is expected to be equal to the collision-limiting rate coefficient.

Fragmentation pathways are also observed for all of the reactions of H_3O^+ with the studied alkyl esters. Where the alcohol side chain is propyl or butyl, the loss of the neutral carboxylic acid is observed leaving the charged alcohol side chain. Reaction 5.02 shows this type of pathway for n-butyl methanoate, but a similar reaction pathway is also observed for 11 other alkyl esters.

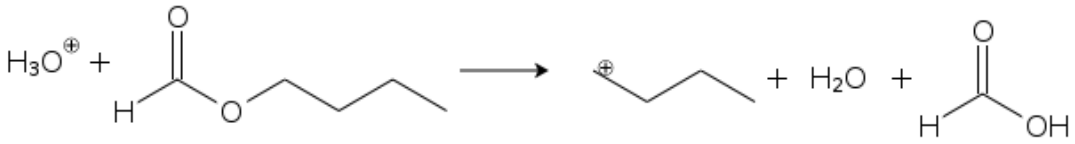

(5.02)

In two cases, an *m/z* 43 ion is observed, that could be attributed to the $C_3H_7^+$ ion (the isopropyl cation $\Delta H_f° = 799$ kJ mol^{-1}) or the CH_3CO^+ ion (ethanoyl cation $\Delta H_f° = 653$ kJ mol^{-1}). [191] For the case of n-propyl ethanoate, *m/z* 43 is observed in a 10% channel that could be attributed to either of the above ions as shown in reactions 5.03 and 5.04.

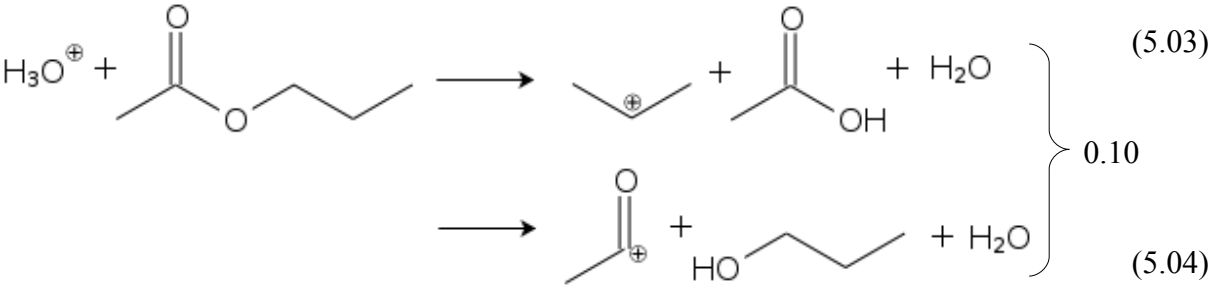

(5.03)

0.10

(5.04)

If it is assumed that the enthalpy of formation of the neutral product (acetic acid or propanol) is small compared to the enthalpy of formation of the cation, the ethanoyl cation will be the favoured product as its enthalpy of formation is the smaller of the two. [30] However, on consultation with the GIANT table (gas-phase ion and neutral thermochemistry) [191] it is discovered that the product heats of formation for 2-$C_3H_7^+$ (isopropyl cation $\Delta H_f° = 799$ kJ mol^{-1}) and CH_3COOH species (acetic acid $\Delta H_f° = 432$ kJ mol^{-1}) is 367 kJ mol^{-1} which is less than than 380.5 kJ mol^{-1}, the sum of the product heats of formation of the CH_3CO^+ ion

(ethanoyl cation $\Delta Hf° = 653$ kJ mol^{-1}) and the C_3H_7OH (propanol $\Delta H_f° = 272.5$ kJ mol^{-1}) species. Therefore the isopropyl cation is the more energetically favoured ion, although both are expected to be present.

For the case of n-propyl propanoate both the propanoyl cation (m/z 57) and the isopropyl cation (*m/z* 43) are observed as 10% channels. These two pathways can be resolved as the two ions appear at different masses. This observation suggests that a site specific protonation is occurring, such that when the ester is protonated at the carbonyl oxygen, a $C_3H_7^+$ cation is observed (as in reaction 5.03), and when the ester is protonated at the alkoxy oxygen, the neutral alcohol leaves and an ethanoyl or propanoyl cation remains (as in reaction 5.04).

An *m/z* 59 cation is observed from the reaction of H_3O^+ with i-propyl butanoate which does not follow the pattern observed in the two reactions discussed above. The *m/z* 59 is assigned to $C_3H_7O^+$, the 1-methyl ethoxy cation, and is proposed to be formed in the pathway given in reaction 5.05. However, formation of a protonated acetone product at *m/z* 59 due to an impurity in the analyte cannot be discounted.

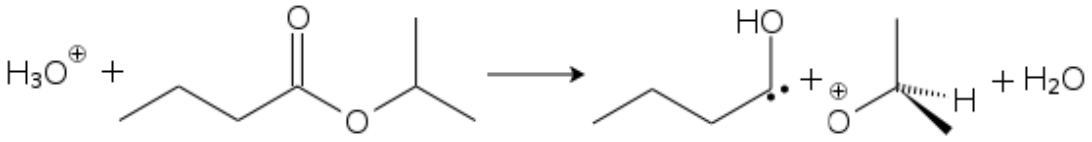

(5.05)

The pathway shown in reaction 5.05 leads to a neutral alcohol moiety that has a lone pair on the carbon previously part of the carbonyl group which has an enthalpy of formation of 825 kJ mol^{-1}. [191] Therefore it is expected that the neutral alcohol species will undergo further rearrangement that would give a more stable neutral species depending on the barrier.

The reaction of n-propyl ethanoate with H_3O^+ is observed to yield a minor product ion channel at *m/z* 85, that has been assigned the $C_5H_9O^+$ structure indicating after proton transfer, that a neutral water molecule is lost. Structurally, this neutral loss is difficult to visualise from a simple one step mechanism. However, as the product ion branching ratio for this channel is found to be only ~5%, a through investigation into the mechanistic pathway is not deemed necessary.

The final channel of interest is the formation of a protonated parent acid ion at *m/z* 61 for ethanoates, *m/z* 75 for propanoates and *m/z* 89 for butanoates. This pathway will be discussed at length in section 5.4.

5.3.2 $H_3O^+.(H_2O)_n$ Reactions (n = 1, 2, 3)

Raw rate coefficients measured on the Voice100 for $H_3O^+.(H_2O)_n$ reacting with the 17 alkyl esters discussed here were deconvoluted using the algorithm given in chapter 3. The algorithm used removes the effect of water clusters forming along the course of the reaction length using an iterative method and a Newton-Raphson optimisation. It is the deconvoluted rate coefficients that are listed in table 5.03.

As discussed in chapter 3, the uncertainty on a measurement of a hydronium ion-water cluster reaction increases as the cluster size increases, such that the uncertainty on $H_3O^+.H_2O$, $H_3O^+.(H_2O)_2$ and $H_3O^+.(H_2O)_3$ is ± 45%, ± 70% and ± 95% respectively. These large total uncertainties are due to the large uncertainty on each of the termolecular water clustering rate coefficients which are of the general form $H_3O^+.(H_2O)_{n-1} + H_2O + M \rightarrow H_3O^+.(H_2O)_n + M$. Because the uncertainties are so large, especially for the $H_3O^+.(H_2O)_3$ reactions, the rate coefficients given in table 5.03 are assumed to only be indicative of a reaction occurring at the collision limiting rate coefficient, or of no reaction at all.

All reactions of $H_3O^+.H_2O$ and $H_3O^+.(H_2O)_2$ are observed to occur within the quoted uncertainty of the collision limiting rate coefficient, and 9 of the 17 reactions of $H_3O^+.(H_2O)_3$ are observed to react at or near the collision rate coefficient. The remaining $H_3O^+.(H_2O)_3$ rate coefficients are concluded not to react with an appreciable rate coefficient ($<< 1 \times 10^{-9}$ cm^3 molecule^{-1} s^{-1}).

Table 5.02 lists the proton affinities of four of the 17 esters, all of which fall in the range of 800 – 840 kJ mol^{-1}. Therefore proton transfer from H_3O^+ (PA = 691 kJ mol^{-1}) is expected to be exergonic, while proton transfer will be exergonic for some $H_3O^+.H_2O$ (PA = 827 kJ mol^{-1}; see table 3.13) reactions. $H_3O^+.(H_2O)_2$ (PA = 911 kJ mol^{-1}) and $H_3O^+.(H_2O)_3$ (PA = 984 kJ mol^{-1}) will not proton transfer to any of the four esters that have listed proton affinities as this will be an endergonic process. However, in table 5.01, all four of the esters that have quoted proton affinities are observed to react with $H_3O^+.H_2O$ and $H_3O^+.(H_2O)_2$ at a rate coefficient that is within uncertainty of the collision limiting rate coefficient. Also, three of the four esters are found to react at, or very near, the collision limiting rate coefficient with $H_3O^+.(H_2O)_3$. Therefore these reactions are occurring through a pathway that is not proton transfer.

The proposed pathway for all $H_3O^+.(H_2O)_2$ and $H_3O^+.(H_2O)_3$ reactions is a metathesis reaction [192] also known as a ligand switching reaction. These types of reaction have been

proposed before by Spanel and Smith as a facile reaction pathway for the water clusters of H_3O^+. [40,71] As the reaction rate coefficients of all four water clusters of H_3O^+ are measured simultaneously, determining the product ions formed from each specific water cluster is a difficult task, and therefore the observed product ions have not been listed in a table. The metathesis pathway proposed below in reactions 5.06 – 5.09 show that the formation of the higher water clusters of an analyte occurs through a sequential pattern, where n = 1, 2, 3.

$$H_3O^+.(H_2O)_n + R_1COOR_2 \rightarrow R_1COOR_2.H_3O^+ + (n\text{-}1)H_2O \quad (5.06)$$

$$R_1COOR_2.H_3O^+ + H_2O + M \rightarrow R_1COOR_2.H(H_2O)_2^+ + M \quad (5.07)$$

$$R_1COOR_2.H(H_2O)_2^+ + H_2O + M \rightarrow R_1COOR_2.H(H_2O)_3^+ + M \quad (5.08)$$

$$R_1COOR_2.H(H_2O)_3^+ + H_2O + M \rightarrow R_1COOR_2.H(H_2O)_4^+ + M \quad (5.09)$$

The sequential pathway shown in reactions 5.06 – 5.09 cannot be resolved from the association reaction of a hydronium ion water cluster with the analyte as shown in reaction 5.10, however, direct association of a cluster ion with an analyte is not as entropically favourable as reaction 5.06.

$$H_3O^+.(H_2O)_n + R_1COOR_2 + M \rightarrow R_1COOR_2.H(H_2O)_{n+1}^+ + M \quad (5.10)$$

The sequential mechanism is supported by measurements of the reaction rate coefficients that are undertaken using different water number densities in the flow tube. Where the rates are measured with a low H_2O number density (~ 10^{12} molecules cm^{-3}), the distribution of the ions resulting from reactions 5.06 - 5.09 are very similar to that of the high H_2O number density (10^{13} molecules cm^{-3}), that indicates that reaction 5.06 is the rate limiting step, and the sequential water clustering reactions are rapid in comparison.

If a direct association pathway was occurring as a major channel, altering the number density of water in the flow tube will alter the relative intensities of the three hydronium ion water clusters (at *m/z* 37, 55 and 73) and therefore will alter the relative product ion branching ratio of each $R_1COOR_2.H(H_2O)_n^+$, where n = 1, 2, 3 or 4.

The actual system is expected to be a combination of the two mechanisms. Deuterium labelling studies would not substantially aid in determining the mechanism because of resonant proton transfer, and the kinetic isotope effect altering the distribution of product ions. [193]

5.3.3 NO^+ Reactions

NO^+ has been observed to react with the 17 alkyl esters by hydride abstraction (reaction 5.11) electron transfer (reaction 5.12) and association (reaction 5.13) pathways with a reaction efficiency of between 50% and 100% of the collision limiting rate coefficient.

$$NO^+ + R_1COOR_2 \rightarrow [R_1COOR_2 - H]^+ + NOH \quad (5.11)$$

$$NO^+ + R_1COOR_2 \rightarrow R_1COOR_2^+ + NO \quad (5.12)$$

$$NO^+ + R_1COOR_2 + M \rightarrow R_1COOR_2.NO^+ + M \quad (5.13)$$

The abstraction of H^- (reaction 5.11) is assumed to occur at the site that affords the highest degree of resonant stabilisation from the ester group, and does not lead to the formation of a primary carbocation. For n-propyl ethanoate, abstraction from the methyl group on the carboxylic acid side chain would lead to a primary carbocation, and therefore abstraction will occur from the carbon that is alpha to the alkoxy oxygen. This assumption is supported by the calculation of enthalpies of reaction for each site specific hydride abstraction pathway by the CBS-4M accurate energy compound method as shown in table 5.04. Calculations were undertaken using the Gaussian 03W suite of software to determine the hydride affinity of each site, where the hydride affinity is defined in reaction 5.14. The hydride affinity of NO^+ was determined using thermochemical parameters from the NIST Webbook [30,191] in an attempt to increase the accuracy of the calculation.

$$XH \rightarrow X^+ + H^- \qquad \textit{Hydride Affinity} = -\Delta H_r \quad (5.14)$$

It is apparent from table 5.04, that the most basic site (the site that can most easily donate a hydride) is the ethyl group which is bound to the alkoxy oxygen (the alpha carbon) and leads to an hydride abstraction pathway that is 161 kJ mol^{-1} exothermic for the reaction with NO^+. However, two other sites are also found to be exothermic, abstraction from the methyl group of the carboxylic acid side chain, and the beta carbon on the alcohol side carbon. It is assumed that hydride abstraction will occur at all three of the exothermic sites, but due to the quadrupole mass spectrometer resolution they are impossible to resolve.

Interestingly, when optimising the geometry of the structure where H^- has been abstracted from the methyl group on the carboxylic acid side chain, the guessed structure for the lowest energy configuration of the ion immediately rearranged to give a structure resembling a ketene, in that the remaining CH_2 group underwent a 1,2 migration. This rearrangement is clarified in reaction 5.15.

Table 5.04. Site specific enthalpies of reaction for abstraction of a hydride from n-propyl ethanoate. Calculated using the CBS-4M compound method to determine the hydride affinity. The hydride affinity of NO^+ was sourced from the NIST webbook and determined to be -1170.47 kJ mol^{-1}. [30,191]

Site	***Hydride Affinity /kJ mol^{-1}***	***ΔH_r /kJ mol^{-1}***
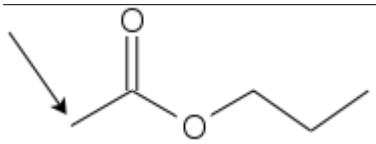	-1143.7	-26.8
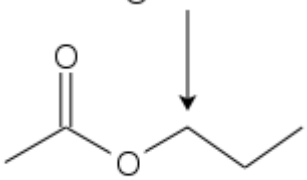	-1009.5	-161
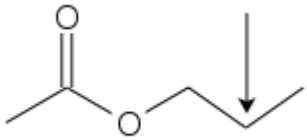	-1117.8	-52.7
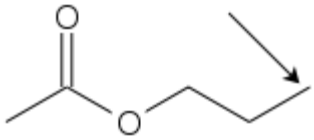	-1203.8	33.3

The 1,2 methylene shift affords the formation of a secondary carbocation, that is substantially more stable that the primary carbocation initially formed. 1,2-methylene shifts have been observed previously for $C_4H_8O^+$ ions in the gas phase [194] and are known to obey the Woodward-Hoffmann rules. [195]

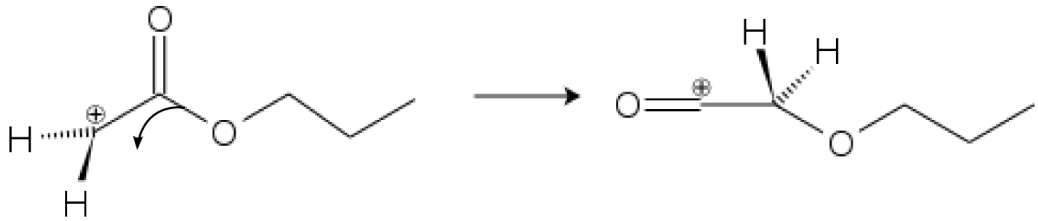

(5.15)

Because the 1,2-methylene shift shown in reaction 5.15 was observed to occur in the automated Newton-Raphson optimisation process used in the Gaussian 03W suite of software, [109] it is concluded that this rearrangement has a barrier which is small enough to ensure that all abstractions by NO^+ occurring at this site, will lead to structures that have the ketene configuration.

16 of the 17 alkyl esters studied were observed to have an association channel that was competitive with other channels such as electron transfer and/or hydride abstraction. The

competition between association reactions and other facile pathways has previously been discussed by Milligan, [76] who proposed a double well potential, which was similar to that of Mautner, [196] for the reaction of CH_2CHCN^+ with acrylonitrile as opposed to the traditional model of Brauman and co-workers. [197] The model proposed by Brauman and co-workers is also a double well potential, but of a different shape to that proposed by Milligan. Further investigation into which model was operating for the esters studied here requires research into the pressure dependence of the termolecular channel that is outside the scope of this research.

The ionisation potential of NO is 9.26 eV, [30] and therefore the majority of the alkyl esters studied here are not expected to react by electron transfer, because, where the ionisation potentials of the analytes are known, they are greater than 9.26 eV. However, a small channel (5%) attributable to electron transfer is observed for the reaction of NO^+ with n-propyl propanoate. It is possible that for n-propyl propanoate the *m/z* 116 product ion may arise from a small amount of excited NO^+, that is present during the reaction.

A range of fragmentation pathways are also observed in table 5.03 that presumably occur as dissociative hydride abstraction. A common reaction pathway observed is cleavage at the ester bond such as the formation of *m/z* 73 in a 15% channel in the reaction of NO^+ with n-butyl methanoate that is shown in reaction 5.16. The neutral products formed result from hydride abstraction. The electron transfer channel is not considered as it is known to be endothermic by 1.26 eV. The formation of *m/z* 73 via a hydride abstraction pathway requires that the methanoyl hydrogen (bound to the carbonyl) is the abstracted hydrogen, however this mechanism is only speculative and no supporting thermodynamic data is available for this mechanism.

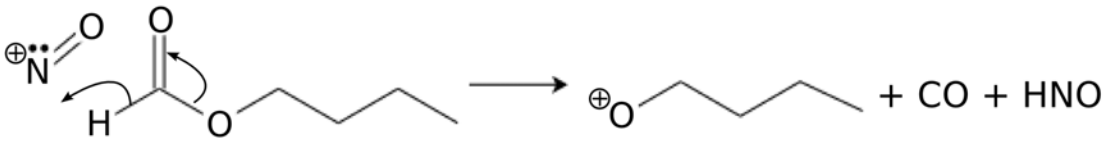

(5.16)

Also formed from the same reaction is *m/z* 56 in a 5% channel, which is proposed to be the $C_4H_8^+$ cation. A simple mechanism for the formation of this ion is the abstraction of a hydride by NO^+ from the alcohol side chain of n-butyl methanoate, followed by the neutral CO_2H group leaving.

Ambiguity again arises in assigning the peaks at *m/z* 43 for NO^+ reacting with n-propyl ethanoate and n-butyl ethanoate, as was the case for the H_3O^+ precursor. Again the thermodynamically more stable of the two product ions is the isopropyl cation, but ion

structure will depend on the site at which NO^+ attacks the neutral analyte.

The final pathway of interest is the ions that were observed to arise at *m/z* 90 for t-butyl and s-butyl ethanoate, and also *m/z* 104 for t-butyl propanoate. This pathway will be detailed in section 5.4.

5.3.4 $O_2^{\bullet+}$ Reactions

The reactions of $O_2^{\bullet+}$ with the alkyl esters studied here are found to give electron transfer and dissociative electron transfer as the major product ion channels. Nine out of the 17 alkyl esters have known literature ionisation energies, and all of these values fall between 9.9 and 10.6 eV. Because the ionisation energy of O_2 is 12.07 eV, [30] the majority of reactions between $O_2^{\bullet+}$ and the studied alkyl esters will occur with ~2 eV of excess energy. This excess energy leads to a large degree of fragmentation observed in the product ion channels. Some unexpected product ions have been observed that are proposed to be formed through complex rearrangements, such that rationalisation of all of the ion structures was found to be difficult. Needless to say, where possible, mechanisms for these rearrangements have been proposed, and supported by thermochemical data where available.

Hydride abstraction by $O_2^{\bullet+}$ does not generally occur in ion molecule chemistry, because the charge transfer channel is deemed to be a more facile process. [62] However, abstraction of a hydride by $O_2^{\bullet+}$ is a often a thermodynamically feasible process, where the hydride affinity (as defined in reaction 5.14) is 275 kJ mol^{-1} greater than that of NO^+. Having said that, in the current study, no hydride abstraction pathways to yield the $[M - H]^+$ ion have been observed using the $O_2^{\bullet+}$ precursor.

A wide range of dissociative electron transfer pathways have been observed. Where the alcohol side chain is a butyl group, the $C_4H_8^+$ ion is observed in all cases studied herein as a major product ion channel (> 30%), and not the $C_4H_9^+$ ion. The formation of $C_4H_8^+$ as a resultant fragment after electron transfer, requires that either an H atom is lost from the alcohol side chain, or that an H atom migrates onto one of the oxygen atoms of the ester group, such that the neutral carboxylic acid becomes the leaving group. For example the reaction of $O_2^{\bullet+}$ and t-butyl ethanoate will yield $C_4H_8^+$ and ethanoic acid as shown in reaction 5.17.

A concerted cyclo-reversion mechanism is proposed as the pathway to form the $C_4H_8^+$ ion. This type of reaction was first proposed by McLafferty, [198,199] who found that electron impact mass spectra of particular aldehydes and nitro-esters had product ions that

must be formed through cyclic rearrangement mechanisms. Known as McLafferty rearrangements, these cyclo-reversion mechanisms are common in solution phase chemistry, but are more rarely observed in the gas phase. [200,201] The mechanism shown in reaction 5.17 is further supported by the ionisation potentials of ethanoic acid and 2-methyl-1-butene, that are 10.65 and 9.22 eV respectively, such that 2-methyl-1-butene cation is the more stable of the two possible product ions. [30] The molecular ion at *m/z* 116 is not observed for the reaction of $O_2^{\bullet+}$ with t-butyl ethanoate.

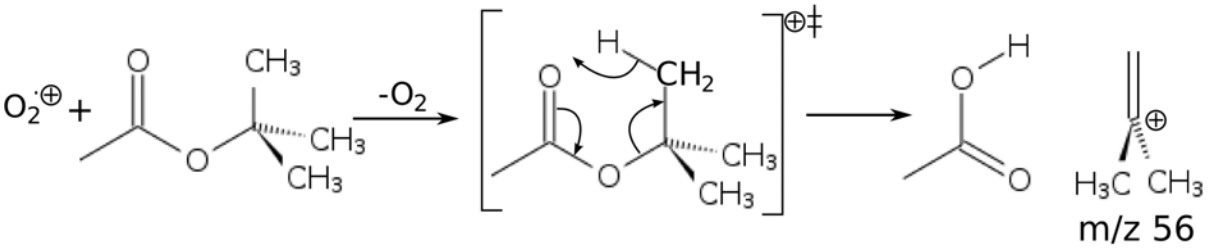

(5.17)

Compared to the situation above, when the alcohol side chain is propyl (as in propyl butanoate) the $C_3H_7^+$ (*m/z* 43) ion is observed. Because the $C_3H_7^+$ ion is observed and not the $C_3H_6^+$ ion, it is apparent that the McLafferty rearrangement mechanism shown in reaction 5.17 is not facile where the alcohol side chain is propyl. However, a minor channel at *m/z* 42 from the reaction of $O_2^{\bullet+}$ with n-propyl ethanoate could be attributed to $C_3H_6^+$, that may be indicative of the McLafferty rearrangement but unfortunately ambiguity exists with the CH_2CO^+ ion also at *m/z* 42 and differentiation is impossible without isotopic substitution.

The ester, n-butyl butanoate, affords insight into the fragmentation pattern of the carboxylic acid side chain. The $C_4H_8^+$ ion is observed, and as discussed above, is proposed to originate from the alcohol side chain, but the formation of $C_3H_7^+$ (*m/z* 43) is also observed in this reaction. The $C_3H_7^+$ ion is proposed to originate from the carboxylic acid side chain, where $C_4H_7O^+$ (*m/z* 71) that is formed initially undergoes a CO neutral loss. The situation is clarified further in reaction 5.18, where the ionisation step by electron transfer is assumed to have already occurred.

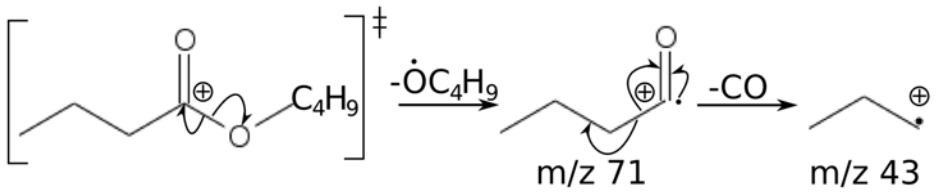

(5.18)

5.3.5 Secondary chemistry with H_2O

No product ions from table 5.03 were observed to proton transfer to water, that is

present in most SIFT-MS analytical samples at concentrations of between 0.1 and 6%. The reactions of $C_3H_6^+$, $C_3H_7^+$, $C_4H_8^+$ and $C_4H_9^+$ with water have been discussed at length in chapter 4, and shall not be discussed further. The protonated parent $[M + H]^+$ ions observed from proton transfer reactions were all found to cluster with 1 – 3 water molecules in the presence of water vapour and these ions must be monitored when measuring the concentration of the studied alkyl ester compounds.

5.4 Computational Mechanistic Studies of Gas-Phase Cyclo-Reversion

5.4.1 Introduction

On inspection of table 5.03, it might be concluded that most of the esters studied have large carboxylic acid impurities that are present due to solution phase hydrolysis of the alkyl ester occurring in the sample prior to entering the Voice100 flow tube. Ethanoate esters reacting with H_3O^+ often yield the *m/z* 61 ion corresponding to protonated ethanoic acid, all propanoate esters excluding methyl propanoate yield the *m/z* 75 ion (propanoic acid) and butanoic acid (*m/z* 89) is observed from the reaction of H_3O^+ with some butanoate esters. However, no methyl esters are found to yield this pathway. The reaction of ethyl propanoate with H_3O^+ is given as an example of this pathway in reaction 5.19.

Also, t-butyl ethanoate and s-butyl ethanoate reactions with NO^+ are found to form the $C_2H_4O_2.NO^+$ ion, and similarly t-butyl propanoate reacting with NO^+ is found to form $C_3H_6O_2.NO^+$.

$H_3O^+ +$ 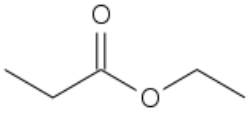 $\rightarrow$ $C_3H_5O_2H_2^+ + C_2H_4 + H_2O$ (*m/z* 75) 0.05 (5.19)

However, solution phase hydrolysis is not the source of these product ions. If solution phase hydrolysis were occurring, substantial signals of the alcohol would be expected to be present in the mass spectra, because the vapour pressure of an alcohol is generally much greater than that of a carboxylic acid. For instance, solution phase hydrolysis of n-butyl butanoate yields butanoic acid and butanol that have vapour pressures of 1.1 Torr and 6.6 Torr respectively at 298 K. [184] When this hydrolysed solution was passed into the flow tube and reacted with H_3O^+, *m/z* 89 (protonated butanoic acid) and *m/z* 57 (protonated butanol -H_2O) should be observed in a ratio of 1:6. [33,36] However, no *m/z* 57 is observed in the spectrum.

To ensure that solution phase hydrolysis was not occurring, rate coefficients and

product ion branching ratios were re-measured using new samples of some esters that were purchased from Sigma-Aldrich. The relative product ion branching ratios of the protonated carboxylic acids with H_3O^+, and NO^+ associated carboxylic acids were found to be the same as the previous measurements within the expected uncertainty. If solution phase hydrolysis was occurring, the branching ratio of the anomalous ions should change dependent on the length of storage time for the alkyl ester solution.

Finally, trap-to-trap purification was undertaken on n-propyl ethanoate to separate the highest boiling fraction, the ester (vapour pressure = 33.7 Torr at 298 K) from any propanol (vapour pressure = 21.1 Torr at 298 K) and ethanoic acid (vapour pressure = 15.9 Torr at 298 K). [184] Following the purification, no alteration was observed in the product ion branching ratio for *m/z* 61. It was therefore concluded that both the protonated carboxylic acid ions arising from reactions with H_3O^+, and ions resembling [NO^+.carboxylic acid] ions were formed from the reaction of the said ion with the neutral ester by a rearrangement mechanism.

The formation of a protonated carboxylic acid product ion is supported by Hopkinson *et al.*, [202] who studied small methanoate and ethanoate esters with a variety of reagent ions and supported the data with deuterium labelling studies, and Denekamp and Stanger, [203,204] who studied the collision-induced dissociation of alkyl benzoates. However, the presence of a benzene ring may allow electronic stabilisation of some transition states, and the mechanisms of Denekamp and Stanger may not necessarily apply to the alkyl esters presented here.

This study will first focus on the formation of the protonated parent carboxylic acid by H_3O^+, followed by the formation of the [NO^+.carboxylic acid] cation.

5.4.2 Hypotheses for rearrangement

The mechanism of formation of the protonated parent carboxylic acid cation was initially postulated to be similar to a solution phase hydrolysis reaction that is occurring in the gas phase. In the solution phase mechanism, H_3O^+ attacks the carbonyl oxygen transferring a proton to this site, then (or simultaneously) a separate water molecule adds to the carbonyl carbon, and finally following an intra-molecular proton migration, the neutral alcohol leaves and a protonated carboxylic acid group remains. [205] However, a reaction of this nature in the gas phase would require a stabilising collision with a carrier gas molecule (i.e. the reaction would be termolecular), and therefore it is unlikely that H_3O^+ "insertion" would be a facile competitive product ion channel when exergonic proton transfer is also observed, and the

reaction is occurring at the collision-limiting rate coefficient.

The second hypothesis for a mechanism to explain the formation of a protonated carboxylic acid parent ion relies on the formation of a six-membered cyclic transition state, where a hydrogen atom migrates from the carbon that is beta (β) to the alkoxy oxygen onto the carbonyl oxygen, which is a 1,5 migration. This explains the observation above that methyl esters (e.g. methyl propanoate (CH_3O-COC_2H_5) do not exhibit protonated carboxylic acid formation, because no β-carbon is present. The products formed from such a transition state would be a protonated carboxylic acid and a neutral alkene; therefore, this pathway is reminiscent of a solution-phase cyclo-reversion mechanism, or more formally a cyclo-elimination mechanism. [206] The postulated transition state structure, and the definition of the beta carbon are given in figure 5.03. For the [NO^+.carboxylic acid] case, the proton shown in figure 5.03 is expected to be replaced by NO^+.

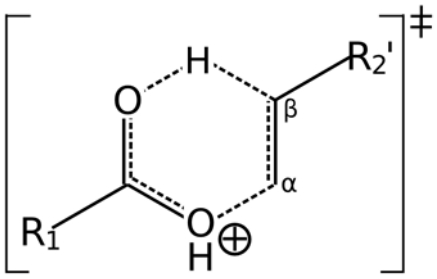

Figure 5.03. The postulated transition state structure leading to formation of a protonated carboxylic acid.

5.4.3 Computational methods

The reaction mechanisms studied here have been probed by the CBS-4M compound method of Petersson and co-workers, [97] using the Gaussian 03W suite of software, both chosen because they afford the calculation of the most accurate energies possible using the personal computer that has been used for quantum chemical calculations herein (P4, 2.4 GHz, 2 GB RAM). Transition state structures were obtained by Synchronous Transit guided Quasi Newton (STQN) methods such as QST2 or QST3. [207]

Two model chemistry test cases were chosen to study the mechanism of formation for the protonated carboxylic acid species: ethyl propanoate (C_2H_5O-COC_2H_5) and propyl ethanoate (C_3H_8O-$COCH_3$). These are two structural isomers, each with a molecular mass of 102 g mol^{-1}. Ethyl propanoate has a 5% channel leading to propanoic acid formation when reacted with H_3O^+ (reaction 5.19), and reaction 5.20 details the 50% channel to ethanoic acid that yields from the reaction of H_3O^+ with propyl ethanoate.

$H_3O^+ +$ 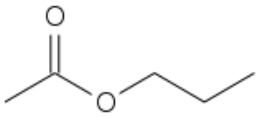 $\rightarrow$ $C_2H_3O_2H_2^+ + C_3H_6 + H_2O$ (*m/z* 61) 0.50 (5.20)

As the product ion channel for reaction 5.19 has a lower branching ratio than that of reaction 5.20, it is hypothesised that the barrier to rearrangement ($\Delta G^{\ddagger}$) is larger for the ethyl propanoate rearrangement than for the propyl ethanoate rearrangement.

The model chemistry chosen to study the formation of the [NO^+.carboxylic acid] ion is t-butyl ethanoate, as it is the smaller of the three esters where the product ion channel attributed to this pathway is observed.

5.4.4 Site dependent proton affinity

An alkyl ester affords two apparent sites that will accept a proton from H_3O^+, which are the carbonyl oxygen and the alkoxy oxygen. Protonation at the the carbonyl oxygen should be thermodynamically favoured because this site allows for the formation of a tertiary carbocation, whereas the alkoxy oxygen does not offer the same degree of resonant stabilisation.

The proton affinity and gas basicity of each site has been calculated by the CBS-4M method by determining the negative enthalpy of the protonation. For both the n-propyl ethanoate and ethyl propanoate cases the carbonyl oxygen is found to yield a more exothermic channel than the alkoxy oxygen. However, protonation at the alkoxy oxygen site by H_3O^+ (PA = 691 kJ mol^{-1}, GB = 660 kJ mol^{-1}) is still a thermodynamically feasible pathway. The calculated site-dependent proton affinities for both test cases are given as table 5.05. Table 5.05 also lists the experimental proton affinity of n-propyl ethanoate which was sourced from the NIST Webbook. [31]

Table 5.05. Site-dependent proton affinity and gas basicity at 298 K.

		CBS-4M /kJ mol^{-1}		***Experimental /kJ mol^{-1}***	
Molecule	*Protonation Site*	*PA*	*GB*	*PA*	*GB*
n-Propyl Ethanoate	Carbonyl oxygen	813.0	782.7	836.6[a]	805.6[a]
	Alkoxy oxygen	749.5	716.9		
Ethyl Propanoate	Carbonyl oxygen	813.3	782.2	Unknown	Unknown
	Alkoxy oxygen	748.3	719.3		

a) Ref [31]

For the n-propyl ethanoate case, there is a large discrepancy between the experimental thermochemical values, and the calculated values for protonation occurring at the carbonyl site. The observed difference between the two is 23.6 kJ mol^{-1} for proton affinity and 22.9 kJ mol^{-1} for gas basicity.

The CBS-4M method is known to give reasonably accurate energies at a low computational cost for small molecules which do not contain halogens, [97] such that when comparing the CBS-4M method to the G2/97† data set, the mean absolute deviation for proton affinity is 1.74 kcal mol^{-1} (7.27 kJ mol^{-1}) with a maximum observed error of 3.4 kcal mol^{-1} (14.2 kJ mol^{-1}). [208] However, because in the CBS-4M compound method, the ion geometry is optimised, and the zero point energy is found and using a low level HF/3-21G(d) calculation, geometries are sometimes found to be incorrect that leads to inaccuracy in the energy. [96] It is therefore assumed to be inaccuracies in the calculation of the lowest energy geometry that has led to the discrepancy in the calculation of the proton affinity/gas basicity. But, because the CBS-4M method is so inexpensive, such that a calculation on a $C_6H_{10}O_2^+$ molecule requires only 3 hours of computational time, the errors on the proton affinity seen here are deemed to be acceptable for a semi-quantitative study such as this. CBS-4M energies are assumed, therefore, only to be accurate to 20 – 30 kJ mol^{-1}.

As discussed above, protonation onto the carbonyl oxygen is observed to be a more thermodynamically favourable process than protonation at the alkoxy site. However, in an ester molecule, both sites are physically very close together (in n-propyl ethanoate the carbonyl oxygen is ~2.2 ≈ from the alkoxy oxygen) such that the approaching ion may possibly attack at either. A structural diagram of neutral n-propyl acetate, and its dipole vector are shown in figure 5.04.

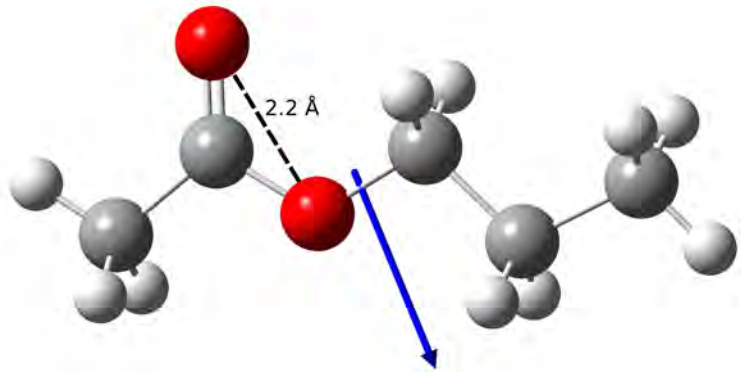

Figure 5.04. Dipole orientation of n-propyl acetate.

† The G2/97 data set is a collection of 125 atoms and molecules that have known experimental parameters (such as proton affinity) used to test the accuracy and precision of a quantum chemical method.

Average dipole orientation (ADO) theory [209] states that the average collision orientation will occur along the dipole vector, and the azimuthal angle between the dipole vector of the neutral species and the approach angle of a point charge will decrease as the distance (*r*) between the two species decreases. Therefore, with reference to figure 5.04, the majority of H_3O^+/n-propyl ethanoate collisions will occur along the dipole vector outlined in blue (using the calculated value of 2.2 Debye from table 5.02), that leads to the alkoxy site being exposed as the primary site for proton transfer to take place. However, it is assumed that proton transfer will still occur to some extent at the carbonyl oxygen site because it still carries increased electron density (i.e. is electronegative), and proton transfer is a facile process where the pathway is exothermic. [61]

Hydrogen atoms are known to migrate in a 1,3 fashion along the backbone of organic ions in the gas phase. [210] A migration of this nature would allow the hydrogen bound to either the alkoxy oxygen or carbonyl oxygen, to migrate between the two sites. Where the relative barrier (relative to the energies of the reagents) to this migration is low (≤ 0 kJ mol^{-1}), the carbonyl oxygen is expected to be the favoured site of protonation because any proton that binds at the alkoxy site will migrate onto the carbonyl site as rearrangement is a facile process (thermodynamic control). However, when the relative barrier to 1,3 migration is found to be large (> 0 kJ mol^{-1}) the proton is trapped at a specific site, and a statistical distribution of protonation at each site is expected to be observed (kinetic control).

5.4.5 Mechanism of protonated carboxylic acid formation

Figures 5.05 and 5.06 show that the barrier to 1,3- proton migration in both cases is greater than 0 kJ mol^{-1} (the sum of the electronic free energies of H_3O^+ and the neutral ester). However, both barriers lie at energies that approximate to zero within the uncertainty of the calculation. The barrier may be surmounted and 1,3-migration achieved by energy gained through collisions with carrier gas atoms, but the fraction expected to overcome the barrier is expected to be low in both the ethyl propanoate and n-propyl ethanoate cases. The protonation step in each case is therefore approximately under kinetic control such that a statistical distribution of protonation at the carbonyl and alkoxy sites based on dipole orientation is expected to be observed.

In both cases, where protonation occurs at the carbonyl oxygen, the $[M + H]^+$ ion or other pathways discussed in section 5.3.1 are expected to be observed. No exergonic or structurally feasible pathways were found that lead to the formation of a protonated

carboxylic acid product following protonation at this site. Other product ions such as *m/z* 85 and 43 from the n-propyl ethanoate reaction and *m/z* 57 from the ethyl propanoate reaction may form through the initial protonation step occurring at the carbonyl oxygen, however these pathways need further computational investigation.

If protonation occurs at the alkoxy oxygen site, the protonated carboxylic acid product ion can be formed. The rearrangement occurs through a transition state that is similar, but not the same as that proposed in figure 5.03. The structure in both test cases is a 6-membered cyclic transition state, but not in the expected chair conformation. The ring where the hydrogen migrates in a 1,5 fashion is planar, and the alkoxy C-O bond has elongated to 2.79 ≈. Figure 5.07 shows the geometry-optimised transition state structure determined for 1,5 migration for the n-propyl ethanoate test case.

The relative experimental product ion branching ratios for the protonated carboxylic acid product for each of the test cases are supported by the computational results. The barrier to 1,5-migration is greater in figure 5.05 (ethyl propanoate) than the barrier for the same rearrangement in figure 5.06 (n-propyl ethanoate), that is consistent with the experimental product ion branching ratios of each ester (0.05 and 0.50 respectively). For the ethyl propanoate case, the relative barrier is found to be -7.5 kJ mol^{-1}, which closely approximates zero within the uncertainty of the calculation, and is reflected by the product ion branching ratio for the $[M + H]^+$ ion of 90%. Conversely for n-propyl ethanoate, only a 35% channel is observed for the $[M + H]^+$ ion, because the relative barrier to 1,5 rearrangement (-25.2 kJ mol^{-1}) is much smaller than for the ethyl propanoate test case.

To ensure that the HF/3-21G geometry optimisation and frequency calculation used in the CBS-4M method was sufficient for calculating accurate energies for both the ground state and transition state structures, the 1,3-migration step for n-propyl ethanoate (shown in figure 5.06) has been repeated with the computationally more expensive G2(MP2,SVP) accurate energy compound method. The G2(MP2,SVP) method optimised structures to the MP2(Full)/6-31(d) level of theory that is expected to yield a more accurate lowest energy geometry. [100] Where the CBS-4M method found a barrier of 22.87 kJ mol^{-1} for 1,3-migration, the G2(MP2,SVP) method found a barrier of 27.72 kJ mol^{-1}, which is a difference of 4.85 kJ mol^{-1} (1.16 kcal mol^{-1}). The difference is well inside the quoted uncertainty of the two methods using the G2/97 data set. The barrier calculated by the G2(MP2,SVP) is larger than that calculated by the CBS-4M method but is consistent with the 1,3-migration step being under kinetic control.

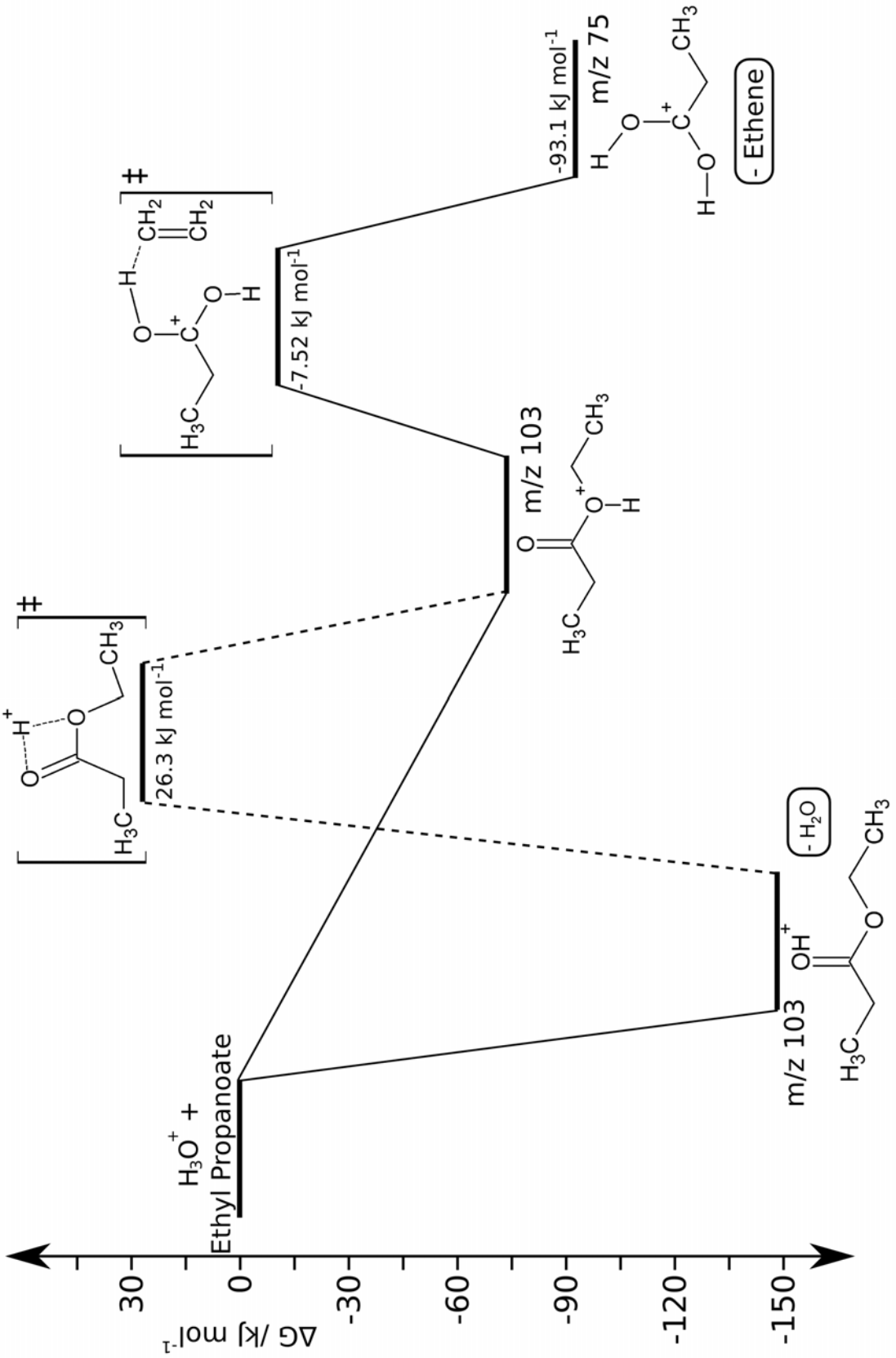

Figure 5.05. Mechanism of m/z 75 formation from protonated ethyl propanoate. The initial proton transfer step is scaled to the experimental gas basicity of n-propyl ethanoate. Free energies determined at 298 K.

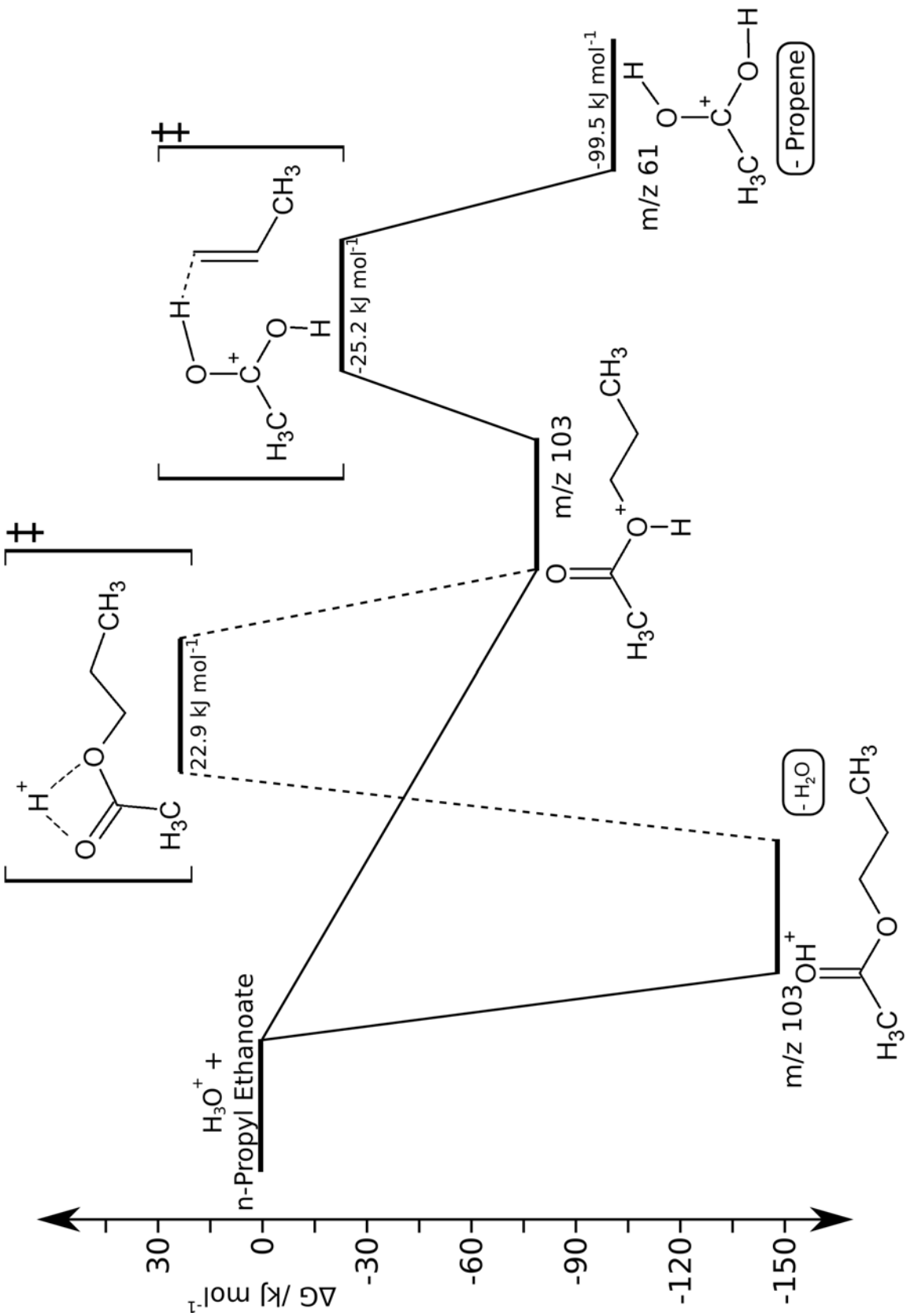

Figure 5.06. Mechanism of m/z 61 formation from protonated n-propyl ethanoate. The initial proton transfer step from H_3O^+ corresponds to the empirical gas basicity of n-propyl ethanoate. Free energies determined at 298 K.

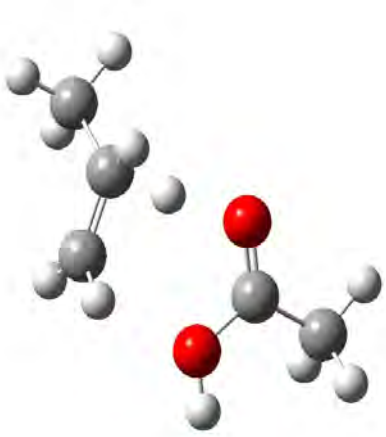

Figure 5.07. Geometry optimised transition state structure for the 1,5-migration of an H atom in n-propyl ethanoate after proton transfer to the alkoxy oxygen by H_3O^+.

Aprea and co-workers [211] observed similar product ions at the higher ion-neutral interaction energies of a proton transfer reaction mass spectrometry (PTR-MS). However, Aprea *et al.* have incorrectly assigned the mechanism as a McLafferty rearrangement, as they have not taken into account the effects of protonation at the alkoxy site. The structure that is assigned for the *m/z* 61 peak in the Aprea paper is not stable and immediately dissociates to the *m/z* 43 ion and water. The rearrangement proposed here is similar to a McLafferty rearrangement, [212] but is driven by protonation at the alkoxy oxygen.

5.4.6 Mechanism of [NO^+.carboxylic acid] formation

The mechanism of formation of the [NO^+.carboxylic acid] product ion from the reaction of NO^+ with an ester, is assumed to be via a similar transition state structure as shown in figure 5.03, except that the proton is replaced by an NO^+ group such that, at the first instance, NO^+ must form a collision complex with the alkyl ester that has an associated binding energy. t-Butyl ethanoate, s-butyl ethanoate and t-butyl propanoate reacting with NO^+ yield a product ion channel attributable to this pathway. In the interest of efficiency, only the t-butyl ethanoate case has been studied by computational methods.

The site specific NO^+ binding energies for the carbonyl and alkoxy oxygen sites of t-butyl ethanoate are found to be -116 and -36.2 kJ mol^{-1} respectively, such that the binding energy at the carbonyl site is ~80 kJ mol^{-1} stronger. However, the same argument as discussed above regarding the dipole orientation of the ester molecules applies; the alkoxy oxygen is more susceptible to nucleophilic attack than the carbonyl oxygen. If the barrier to 1,3-NO^+

migration is large, the NO^+ will exist at the site where it first binds, and therefore a statistical distribution of NO^+-bound sites based on the dipole orientation would be observed if this measurement were possible on a SIFT-MS.

The CBS-4M calculated pathway for the formation of an [NO^+.carboxylic acid] adduct is shown in figure 5.08 for the reaction of NO^+ with t-butyl ethanoate.

The barrier to 1,3-NO^+ migration is indeed very large (+390 kJ mol^{-1}) that places the system entirely under kinetic control. No interconversion between the carbonyl bound and alkoxy bound [NO^+.t-butyl ethanoate] will occur as the barrier is too high to be surmounted. No other NO^+ association sites were found to give a stationary point in the optimisation procedure without the presence of one or more negative frequencies.

As can be observed in figure 5.08, if association occurs at the carbonyl oxygen, a rearrangement can occur that leads to the formation of the [NO^+.ethanoic acid] product, where the transition state to this rearrangement is found to occur at -0.4 kJ mol^{-1} relative to the energies of the reactants. However, the products formed from the transition state are found to be higher in energy than both the transition state and the reactants at +0.9 kJ mol^{-1}, that approximates zero within the error of the the measurement. Therefore, formation of [NO^+.ethanoic acid] via association at the carbonyl oxygen is energetically feasible, but may not occur with a strong efficiency.

When association occurs at the alkoxy site, there is no barrier to the 1,5-H atom migration, and therefore this pathway will most likely occur in all cases when NO^+ associates at the alkoxy site, i.e. this will be a very facile process. This conclusion is supported by the observation of a large product ion channel at *m/z* 90 (45%). The transition state structure for this rearrangement is shown as figure 5.09, and is found to be very similar to the protonated structure for the same rearrangement shown in figure 5.07.

The [NO^+.carboxylic acid] pathway is only observed for alkyl esters that have a t-butyl or s-butyl group for the alcohol side chain as in t-butyl and s-butyl ethanoate and t-butyl propanoate. This observation is attributed to the number of β carbons available to donate an H atom to the carbonyl oxygen, which for molecules that have a t-butyl alcohol side chain, is three, the highest number possible. s-Butyl has two β carbons, and is found to yield the [NO^+.carboxylic acid] product ion in a lower branching ratio than both the t-butyl analytes. To reach the transition state shown in figure 5.09, a β methyl group must align with the carbonyl oxygen in a planar fashion.

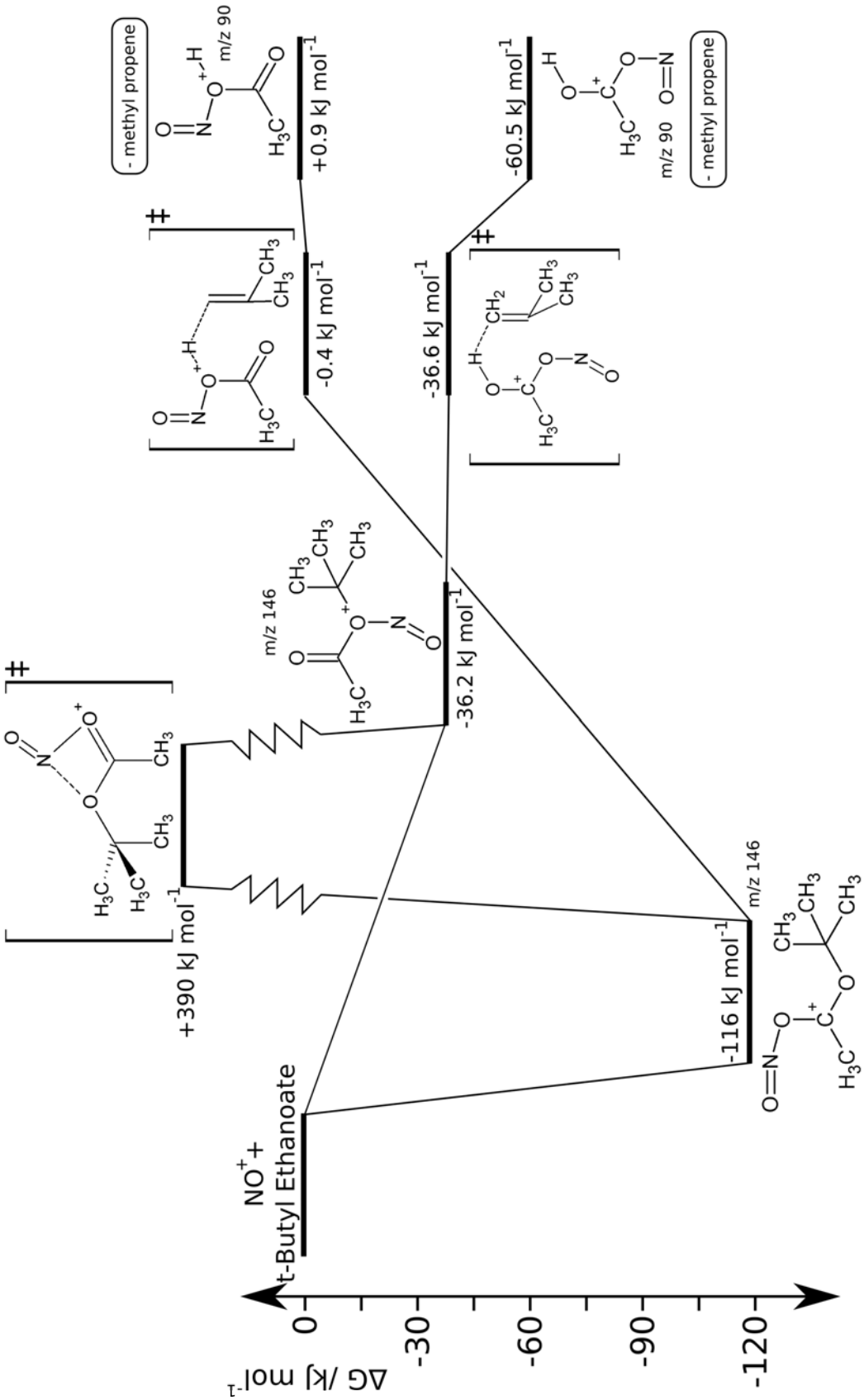

Figure 5.08. Mechanism of m/z 90 formation from the reaction of NO^+ with t-butyl ethanoate. Free energies determined at 298 K.

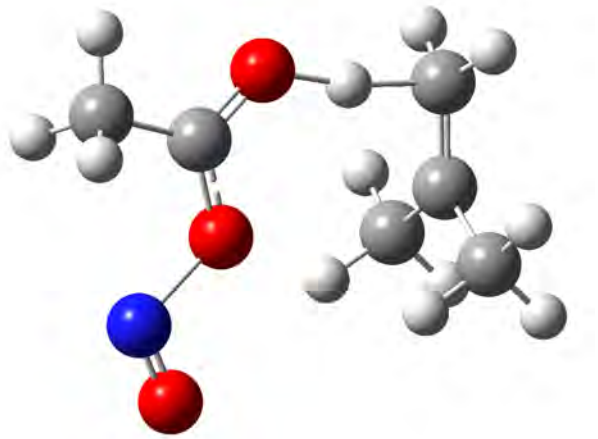

Figure 5.09. Optimised transition state structure for the 1,5-migration of an H atom in t-butyl ethanoate after NO^+ has associated at the alkoxy oxygen.

Because the t-butyl groups affords the highest chance orientating a methyl group towards the carbonyl oxygen that facilitates the rearrangement, the observation is not surprising.

Conversely, the [NO^+.carboxylic acid] product ion channel is not observed when the alcohol side chain is not t-butyl or s-butyl. Therefore, in this case, the [NO^+.ester] complex is proposed to be stabilised by collisions with carrier gas atoms before a β-carbon can orientate toward the carbonyl oxygen, which is a gauche geometry.

Figure 5.09 also shows that the methyl propene leaving group has already reached its approximate neutral conformation, and once the molecule has crossed the energy maxima at the transition state, very little conformation rearrangement is required by either the neutral or ionic species.

5.5 Detection of Alkyl Esters by SIFT-MS

The complex fragmentation pathways observed from the reactions of the SIFT-MS precursor ions with alkyl esters prohibits a simultaneous study of the entire suite of alkyl esters using the SIFT-MS technique. Fortunately, most "real-world" applications will not require every single alkyl ester to be quantified, instead, a particular group of esters may be of interest, and a particular analytical method can then be designed around this application.

5.5.1 Case study: Butyl ethanoates in Honeydew Melon

As an example of such an application, it may be of interest to differentiate the four butyl ethanoate isomers (n-, i-, s- and t-) in honeydew melon (cucumbis melo). Assuming that no other C_6 alkyl esters are present in the sample (as is known to be the case for Honeydew Melon), the total product ion intensity of butyl acetates can be found with the H_3O^+ and NO^+ precursors at *m/z* 117 and 146 respectively. The analyte origins of the two product ions can be expressed by equation 5.21, where the total product ion intensity at *m/z* 117 (H_3O^+) or *m/z* 146 (NO^+) is the sum of the product ion intensities I^p_j resulting from the isomer j.

$$Total\ \ Product\ \ Ion\ \ Intensity\ = I^p_{n\text{-}} + I^p_{i\text{-}} + I^p_{s\text{-}} + I^p_{t\text{-}} \tag{5.21}$$

The concentration of t-butyl ethanoate is resolved through its reaction with $O_2^{\bullet+}$ to give both the $C_5H_9O_2^+$ (*m/z* 101) and $C_2H_3O_2^+$ (*m/z* 59) ions that have product ion branching ratios of 0.30 and 0.10 respectively. Next, $I^p_{t\text{-}}$ from equation 5.21 for both the proton transfer reaction and NO^+ association reaction can be determined (as the number density of t-butyl ethanoate and the precursor intensities are known), using the rearranged concentration formula shown in equation 5.22, where I^I and I^p_j are the intensities of the precursor and product ion pair of interest (either NO^+ and *m/z* 146, or H_3O^+ and *m/z* 117) that has an associated branching ratio Br^p_j, *[B]* is the analyte concentration, and *t* is the reaction time.

$$I^P_j = k[B]tI^I Br^P_j \tag{5.22}$$

The reactions of both s-butyl and t-butyl ethanoate with NO^+ yield the *m/z* 90 ion as discussed in section 5.4.6. Using equation 5.22 the contribution to the ion intensity at *m/z* 90 from t-butyl ethanoate can be determined as the concentration is already known. A simple subtraction then gives the intensity at *m/z* 90 resulting from s-butyl ethanoate, such that the concentration can then be determined, and using the method above, the contribution to the product ion intensity for the proton transfer and NO^+ association reactions can also be easily found.

i-Butyl ethanoate is then resolved using its small product ion channel attributed to the $C_4H_{10}^+$ ion from its reaction with H_3O^+. Because the product ion branching ratio is small (5%) a substantial error in the accuracy of the measurement is introduced. A gas standard would be useful to calibrate the branching ratio to a known concentration, however a standard of this

nature was not obtained due to time constraints.

Finally the concentration of n-butyl ethanoate is determined by solving equation 5.22 for the intensity resulting at both the NO^+ association and proton transfer peaks. Because the method is of a subtractive nature, both the precision and the accuracy of the n-butyl ethanoate concentrations determined will suffer, however where the concentrations of the branched species are found to be substantially lower than the linear species, the accuracy and precision are acceptable for a measurement of this nature.

An example of a measurement of Honeydew Melon using the SIFT-MS technique is shown in figure 5.10 and 5.11. Slices of melon were placed inside a 1 L jar, and a headspace was allowed to form over a 30 minute period at 25 ºC. The headspace of the jar was then introduced into the flow tube through the sample inlet, where the concentrations were measured.

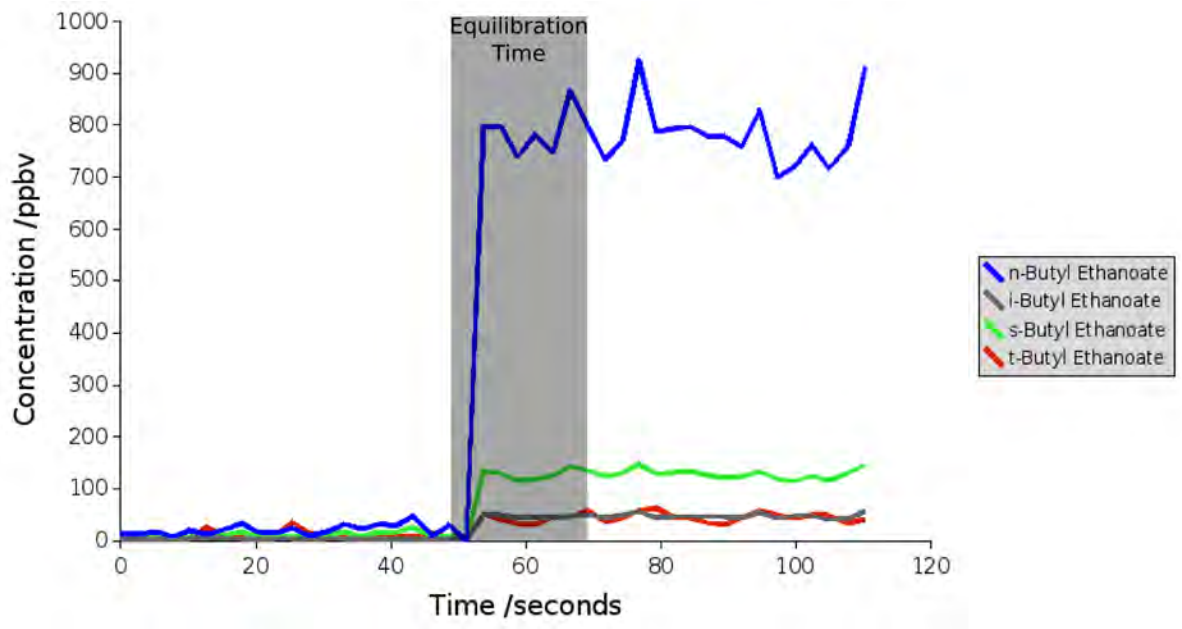

Figure 5.10. Concentrations of the four isomers of butyl ethanoate in Honeydew Melon as measured by the SIFT-MS technique. Between 0-50 seconds ambient air is passed into the flow to determine a chemical background, the sample inlet is then opened allowing the melon headspace to enter the flow tube.

The vapour pressures of both n-butyl and i-butyl ethanoate are known to be approximately 5 Torr at 298 K. [122] Therefore the relative vapour pressure of each analyte is not the dominant factor when observing the relative abundance.

The concentrations of the four butyl ethanoate esters in the headspace of Honeydew

Melon at 25 ºC are 790, 47, 120 and 57 ppbv for the n-, i-, s- and t- isomers respectively, and the total butyl ethanoate concentration is ~1 ppmv. The limit of detection (LOD) and limit of quantitation (LOQ) for each isomer and the total butyl ethanoate concentration, determined by the method prescribed by Milligan *et al.*, [58] are given in table 5.06. Further discussion regarding the LOD and LOQ calculations can be found in chapter 1.

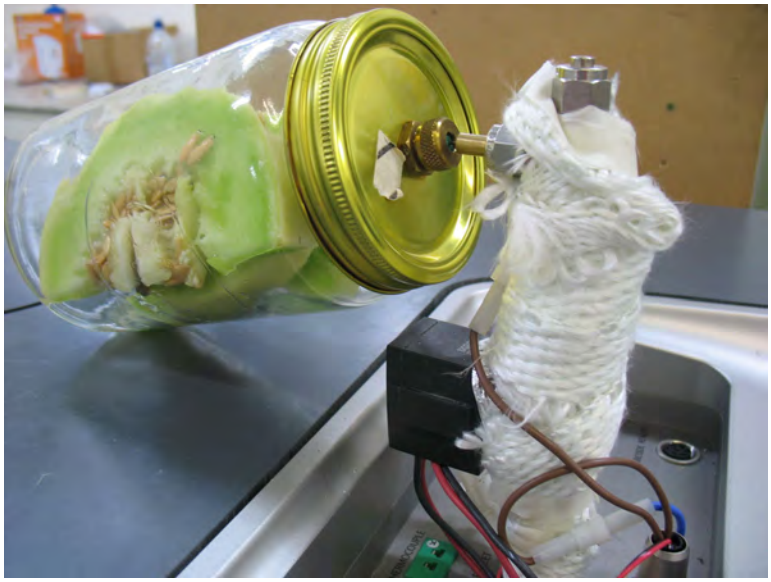

Figure 5.11. Melon headspace being introduced into the Voice100.

Table 5.06. Limits of detection and quantitation for the total butyl ethanoate concentration, and each individual isomer. LOD and LOQ of n- isomer cannot be calculated due to the subtractive method used to determine the concentration. b_μ is background ion intensity and s is the sensitivity of the measurement.

	b_μ / *cps*	***s*** *cps ppbv^{-1}*	***LOD_{ppbv}***	***LOQ_{ppbv}***	***Honeydew Melon Headspace /*** *ppbv*
Butyl Ethanoates	26.2	0.93	21.9	68.4	1010
t- isomer	1.46	0.30	15.8	101.	57
s- isomer	13.0	0.79	34.0	66.1	120
i- isomer	3.05	0.0376	184	684	47
n- isomer	-	-	-	-	790

It is apparent from table 5.06 that the total concentration of butyl ethanoates is substantially greater than the LOQ, however only the s- isomer was detectable above its limit of quantitation. i-Butyl ethanoate was not effectively detected above the limit of detection for the SIFT-MS instrument used.

The n- and s- isomers are found to be the highest in concentration, which is supported

by GC-MS experiments, [183] while the t- and i- isomers are known to be not strongly associated with Honeydew Melon aroma. Therefore the SIFT-MS measurements support the known data regarding these fruit.

5.6 Conclusions

The detection of alkyl esters by SIFT-MS is a non-trivial task due to the large degree of fragmentation observed in the reactions of the said analytes with any of the three SIFT-MS precursor ions and their respective water clusters. However, through understanding the reactions that are occurring in the Voice100 flow tube, resolution of individual alkyl esters can be achieved. Proton transfer, hydride abstraction, association and electron transfer pathways have been found to dominate for alkyl esters reacting in the Voice100 flow tube, where each of these pathways tend to lead to complex rearrangement mechanisms that have been discussed.

The rearrangement mechanisms of the studied alkyl esters are found to be complex, but two mechanisms have been determined using computational techniques with the CBS-4M compound method.

CHAPTER 6

CHEMICAL WARFARE AGENTS

6.1 Introduction

Chemical warfare agents (CWAs - also known as chemical weapons agents) are extremely toxic compounds that are "intended for use in military operations to, seriously injure, or incapacitate man because of physiological effects". [213] CWAs generally have a high vapour pressure such that dispersion through the atmosphere can be achieved.

In 1993, the Chemical Weapons Convention (CWC) was drafted by the Organisation for the Prohibition of Chemical Weapons. [214] The convention places a complete ban on the production, stockpiling, transport and use of chemical warfare agents, which is all encompassing across every country in the world. [215] In 1997, the CWC came into force, and at the current time 182 of the 195 nations recognized by the United Nations are party to the CWC. The CWC does not only control CWAs in their native form, but also places controls on the precursors used in the production of CWAs.

The CWC defines three schedules to place CWAs and their precursor compounds in, known as schedules I, II and III. [214]

- **Schedule I** contains compounds that have no legitimate usage, and may only be produced for research, medical, pharmaceutical or protective purposes.
- **Schedule II** relates to compounds that have no large scale industrial uses, but have some small scale use, such as dimethyl methyl phosphonate, a flame retardant.
- **Schedule III** contains compounds that have large scale commercial use, but may be considered CWAs in particular circumstances, such as chloropicrin a common fumigant.

CWAs are often produced by combining several precursor chemicals in specific ratios just prior to being deployed (known as binary technology), [216] as the CWA precursor compounds are less toxic and much easier to transport than their respective CWA. However, binary technology is only commonly used for specific classes of CWAs.

By their current definition, CWAs were first used in combat during World War I.

- In World War I, mustard gas (sulphur mustard), phosgene and chlorine gases resulted in the deaths of 1.3 million people. [217]
- Nerve agents (discussed further in section 6.1.1) were used against Kurdish rebels in the Iran-Iraq war between 1980 and 1988. [218]
- In October 2002, an incapacitation agent called fentanyl was pumped into a Moscow theatre to end a siege by Chechen rebels, The fentanyl killed approximately 120 people. [219]

However, since this original use, the organisations that have deployed CWAs have not necessarily been government agencies, but instead non-governmental organisations such as terrorist groups. For example in 1995, Aum Shinrikyo, a Japanese religious cult, [220] released packets containing sarin gas onto five subway trains in Tokyo resulting in the deaths of 12 people. [221]

Due to the aforementioned historical significance of CWAs, many analytical techniques have been developed for the detection of these highly toxic compounds, their precursor compounds, and decomposition products. [222] These techniques generally involve the chromatographic separation (in either the liquid [223] or gas phase [224]) of a compound of interest from a substrate such as soil, [218] groundwater [225] and even whole air. [226]

Ion mobility spectrometry (IMS) techniques have also been developed for rapid, 'on-line' detection of CWAs. The chemical agent monitor (CAM) [227] and rapid analysis in real time (RAID) [228] are hand-held IMS instruments specifically designed for direct CWA monitoring. However, IMS instruments are known to have short-comings regarding their selectivity for specific analytes, [229] and can be easily contaminated.

Chemical warfare agents come in a range of classes based on their chemical structure, toxicity and mode of biological action. The common classes are: nerve agents, asphyxiant/blood agents, vesicant/blister agents, choking/pulmonary agents, lachrymatory agents, incapacitants and cytotoxic proteins. A short description of each class and some relevant examples of compounds in that class shall now be given.

6.1.1 Nerve agents

Nerve agents act upon and inhibit the acetylcholinesterase pathway in the human body that alters neuron activity. Symptoms of nerve gas exposure are blurred vision and headaches at low concentrations of exposure, followed by respiratory problems and loss of consciousness at higher concentrations. Sarin, also known as isopropyl methylphosphonofluoridate, is the most common nerve agent that was mentioned above having been used in the Iran-Iraq war, and in the Tokyo subway attack.

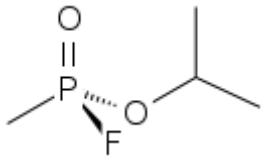

Figure 6.01. Structure of sarin also known as isopropyl methylphosphonofluoridate.

The structure of sarin is shown in figure 6.01, where the compound has an IDLH value† of 17 parts-per-billion-by-volume (ppbv).

6.1.2 Asphyxiant/Blood Agents

These agents react rapidly with the ferric species that is contained in the cytochrome oxidase enzyme of the human body. Through this mode of action, asphyxiant/blood agents inhibit the electron transport pathway in mitochondria (an intracellular organelle) that prevent the surrounding cell from using any oxygen arriving in the blood stream (known as hypoxia). [230] Therefore, because this 'aerobic respiration' pathway cannot be utilised, 'anaerobic respiration' begins in a human cell that leads to 'metabolic acidosis', a decreased blood pH.

Because of this mode of action, the skin of someone exposed to an asphyxiant/blood agent is often a bright red colour, although shortness of breath is rarely observed. Hydrogen cyanide (HCN) is a common asphyxiant/blood agent that has an IDLH value of 50 parts-per-million-by-volume (ppmv), three orders of magnitude greater than that of sarin.

---

† IDLH is an acronym for “Immediate Danger to Life and Health”. IDLH concentrations are concentrations “*that poses an immediate threat to life, would cause irreversible adverse health effects, or would impair an individual's ability to escape from a dangerous atmosphere.*” [231]

6.1.3 Vesicant/blister agents

As the name suggests, these agents cause severe blistering of both internal and external surfaces of the human body when exposed to the agent. [232] By forming covalent linkages with nucleophilic groups both in the cell wall, and on the the double helices of DNA, vesicant/blister agents leave large fluid filled sores at the areas where exposure has taken place. An example of a vesicant/blood agent is sulphur mustard (structure shown as figure 6.02) for which NIOSH (the US National Institute for Safety and Health) does not quote an IDLH value.

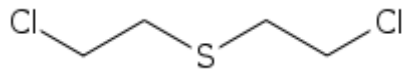

Figure 6.02. Structure of sulphur mustard also known as 1,1-thiobis(2-chloroethane).

6.1.4 Choking/pulmonary agents

Again, as the name suggests, choking/pulmonary agents lead to pulmonary oedema when inhaled. [233] Pulmonary oedema is a swelling and an increase of fluid in the lungs. This occurs by the choking/pulmonary agent molecule binding to and damaging essential cell components in the moist environment of the lungs. [234] A common choking/pulmonary agent is phosgene, also known as carbonyl dichloride (mentioned previously as being used in World War I), that has an IDLH of 2 ppmv.

6.1.5 Lachrymatory agents

These agents, also often called tear gases, are much less toxic than the aforementioned compounds. [235] By irritating the skin, eyes and upper respiratory tract, lachyromatory agents incapacitate subjects. Symptoms include stinging eyes, sneezing, vomiting and nausea. [234] A commonly used lachyromatory agent is chloroacetophenone (known as CN), that has an IDLH of 2.5 ppmv.

6.1.6 Incapacitants and cytotoxic proteins

Differing from lachrymatory agents, incapacitants cause incapacitation by altering the acetylcholine pathway for nervous response. [236] Cytotoxic proteins such as ricin are large non-volatile peptide chains that initiate a biological response. [237] However, neither of these two types of CWA are discussed further in this thesis.

6.1.7 SIFT-MS and CWAs

The current study looks at the capabilities of SIFT-MS to detect two schedule I nerve agents (sarin and ethyl sarin) and a schedule I vesicant agent (sulphur mustard). To complement these three compounds, a selection of less toxic chemical warfare agents (such as phosgene), surrogate compounds and precursor compounds have also been studied. Surrogate compounds are less toxic structural analogs of CWAs that are commonly used by other detection technologies (such as ion mobility spectrometry) to ensure the correct functioning of the instrument with a minimised risk of exposure to extreme toxicity. [238] The CWA surrogate compounds have been studied to more fully demonstrate the detection limits expected for real CWAs.

The detection of the three native chemical warfare agents was a collaborative work between the author, Syft Technologies and the Australian Defence Science and Technology Organisation (Melbourne, Australia).

6.2 Measurement of Kinetic Parameters – Precursors and Surrogates

The reactions of 15 compounds relevant to chemical warfare agents with the precursor ions H_3O^+, NO^+ and $O_2^{\bullet+}$ have been studied using a Voice100 SIFT-MS instrument. This instrument was discussed in detail in chapter 2. As well as the aforementioned reactions, the reactions of 11 of the 15 chemical warfare related compounds with the three sequential water clusters of H_3O^+ have also been studied.

Of the 15 compounds studied in the current section, ten are restricted by the CWC as precursors to native chemical warfare agents. The majority of these precursor compounds are phosphonate and phosphite compounds that are used in the synthesis of organophosphorus

nerve agents such as sarin. [239,240] Thiophosphoryl chloride and 2-chloroethyl ethyl sulphide are studied, and these are surrogate compounds for sarin and sulphur mustard respectively. [241] Methyl salicylate and trimethyl phosphate are ion mobility spectrometry CWA surrogate compounds, and these are included for completeness.

6.2.1 Experimental

All rate coefficients and branching ratios discussed in this chapter were measured on a Voice100 instrument (discussed in detail in chapter 2) using the carrier gas flows stated in chapter 3. To reiterate, the carrier flows employed in the Voice100 are 15 Torr L s^{-1} of helium through the inner annulus and 25 Torr L s^{-1} of argon through the outer hole inlet. These parameters result in a flow tube pressure of 0.5 Torr at 298 K and an ion transit time through the reaction region of approximately 3.8 ms. Helium and argon carrier gases were sourced from Southern Gas Services (Christchurch, New Zealand), each having a stated purity of 99.995%. Neither gas was purified further.

Three methods have been employed for determining the rate coefficients and branching ratios of the 15 CWA compounds studied. These methods were discussed in the experimental chapter, and shall therefore only be mentioned for pertinence. For compounds with high vapour pressures (greater than 2.5 torr at 20 °C), rate coefficients and branching ratios were determined by the semi-logarithmic plot of ion intensity against an absolute measurement of neutral flow, known as 'absolute kinetics'. For compounds with vapour pressures found to be less than 2.5 Torr, rate coefficients could only be measured relative to the H_3O^+ collision-limiting rate coefficient, using mixtures of the analyte in dry nitrogen. Branching ratios were determined where possible by diluting the analyte concentration, and extrapolating the product ion intensity to zero flow. This 'relative with dilutions' method was used for compounds that had partial vapour pressures less than 2.5 Torr, but greater than 50 ppmv (~0.04 Torr partial vapour pressure).

The third method was dictated because of safety issues concerning transport. Phosgene could not be transported readily and instead of synthesising the compound, a permeation tube (Kin-Tek Laboratories, Inc., 504 Laurel Dr., LaMarque, TX, USA) was used that creates an accurate dynamic dilution in the single digit parts-per-million-by volume concentration range. The permeation tube was used in conjunction with a Dynacalibrator 150 (VICI Metronics

Inc., Poulsbo, WA, USA) permeation oven. This combination with the known concentration release of phosgene enables the rate coefficient and branching ratio to be found.

The method of determining rate coefficients of the water clusters ($H_3O^+.H_2O$ m/z 37, $H_3O^+.(H_2O)_2$ m/z 55 and $H_3O^+.(H_2O)_3$ m/z 73) reacting with a neutral analyte was described in chapter 3.

Table 6.01 lists the methods of measuring the kinetic parameters, and their estimated absolute uncertainties, as well as the governing body that restricts the use and transportation of each compound.

Table 6.01. CWA related compounds, their thermodynamic parameters, measurement methods and uncertainties.

Compound	***CAS No.***	***Mass***	***Type***[a]	***PA / IE /***		***Method***[b]	***Uncertainty***[c]	
				kJ mol^{-1}	*eV*		k_{exp}	*BR*
Thiophosphoryl chloride	3983-91-0	169.41	Surrogate			Absolute	± 15%	± 20%
2-Chloroethyl ethyl sulfide	693-07-2	124.63	Surrogate			Absolute	± 15%	± 20%
Diethyl ethanolamine	100-37-8	117.19	CWC 2.11	1005[d]	8.6	Absolute	± 15%	± 20%
Dimethyl methyl phosphonate	756-79-6	124.08	CWC 2.4		10.0	Absolute	± 15%	± 20%
Phosgene (carbonyl dichloride)	75-44-5	98.92	CWC 3.1	669.5[e]		Permeation tube	± 15%	± 20%
Dimethyl ethyl phosphonate	6163-75-3	138.10	CWC 2.4			Relative with dilutions	± 25%	± 30%
Diethyl methyl phosphonate	683-08-9	152.13	CWC 2.4			Relative with dilutions	± 25%	± 30%
Diethyl ethyl phosphonate	78-38-6	166.16	CWC 2.4			Relative with dilutions	± 25%	± 30%
Diethyl phosphite	762-04-9	138.10	CWC 3.11			Relative with dilutions	± 25%	± 30%
Diisopropyl phosphite	1809-20-7	166.16	CWC 3.11			Relative with dilutions	± 25%	± 30%
Triisopropyl phosphite	116-17-6	208.24	CWC 3.11			Relative with dilutions	± 25%	± 30%
Methyl Salicylate	119-36-8	152.05	Surrogate		7.7	Relative with dilutions	± 25%	± 30%
Trimethyl Phosphate	512-56-1	140.02	Surrogate	890.6	10.5	Relative with dilutions	± 25%	± 30%
(Diisopropylamino) ethanol	96-80-0	145.12	CWC 2.11	971.4[d]		Relative without dilutions	± 25%	± 30%
Chloroacetophenone	532-27-4	154.29	Tear Gas		9.6	Relative without dilutions	± 25%	± 30%

a) Refers to the schedule of the CWC that restricts the compound, or whether the compound is a surrogate. Chloroacetophenone is a lachrymatory compound (CN) that is neither restricted, nor a surrogate, but is included for completeness.
b) Definitions discussed in text.
c) k_{exp} refers to the uncertainty of the experimental rate coefficients of H_3O^+, NO^+ and O_2^+ reacting with the neutral analyte. The uncertainty on each of the $H_3O^+.(H_2O)_n$ (n = 1, 2, 3) cations for the absolute measurements is listed in table 3.15. The uncertainty on the same cluster ions for the relative measurements is at least 10% greater per water cluster. BR refers to the uncertainty on the measurement of the branching ratio.
d) Proton affinities calculated by the CBS-4M [97] accurate energy compound method using the Gaussian 03W suite of software.
e) The proton affinity of phosgene was calculated by the G4 [106] accurate energy compound method using the Gaussian 03W suite of software. All other thermochemical parameters are sourced from the NIST database. [30,31]

The collision-limiting rate coefficients have been calculated using the method of Su. [108] Dipole moments and polarisabilities have been obtained by quantum chemical

calculations using the Gaussian 03W suite of software at the B3LYP/6-311+G(d,p) level of theory. As some of the studied molecules are quite large with many degrees of torsional freedom, there is possibility that more than one conformer may be long-lived in the gas phase. Individual conformers have differing dipole moments and polarisabilities. It therefore becomes necessary to take a Boltzmann average of the dipole moment and polarisability over each of these conformers.

The determination of a collision-limiting rate coefficient was undertaken in four steps, where the approach taken here is similar to the approach taken by Schoon *et al.*, [242] however the current method is optimised for use with a desktop computer (P4 - 2.4GHz - 2GB RAM).

- The initial conformational analysis was undertaken using an MM2/MM3 potential energy surface scan, by altering a range of torsional angles. [243,244]
- All conformers that were determined to be within 20 kJ mol^{-1} of the lowest energy conformer were then optimised to the B3LYP/3-21G level of theory and the Hessian calculated to ensure each conformer was a true minimum.
- All true minima were then re-optimised using the 6-311+G(d,p) basis set.
- Collision-limiting rate coefficients were determined for each conformer, and then Boltzmann averaged across all conformers using the standard enthalpy also determined from the same quantum chemical calculations.

As mentioned above, phosgene was sourced in a permeation tube with a known permeation rate uncertainty of ± 2% (a NIST calibrated standard). Methyl salicylate and trimethyl phosphate were donated by the Australian Defence Science and Technology Organisation (Fishermans Bend, Melbourne, Australia). All other compounds were purchased from Sigma Aldrich (Sydney, Australia), with the purity of all compounds being 95% or greater. Compounds that were measured by the method of absolute kinetics were further purified by freeze-pump-thaw cycling.

6.2.2 Results

Table 6.02 lists the experimental rate coefficients and calculated collision-limiting rate coefficients for each of the 15 compounds. Where an experimental rate coefficient is not given

for H_3O^+, the 'relative with dilutions' method (discussed in section 6.2.1) has been used and the collision-limiting rate coefficient is assumed. However, where an experimental rate coefficient is not given for $H_3O^+.(H_2O)_n$ the collision-limiting rate coefficient cannot be assumed as the process of proton transfer may not be exothermic. Table 6.03 lists the product ions observed and the relative branching ratios for each ion reacting with the 15 compounds of interest. The branching ratios of all molecules containing chlorine and sulphur atoms were observed with the expected isotopic ratios.

The assignment of product ion structures in table 6.03 is more tentative than product ions discussed in previous chapters of this thesis as they are based mainly on the product ion mass. There is also a lack of information in the literature regarding the rearrangement mechanisms of phosphorus-containing molecules in the gas-phase, although these rearrangement mechanisms are known to be highly complex. [245] Furthermore, time constraints placed upon the current research did not allow for computational mechanistic studies.

Table 6.02. Rate coefficients of 15 chemical warfare related compounds reacting with the SIFT-MS precursor ions measured at 298 K and 0.5 Torr.

Compound	μ_D [a] /	α [a] /	k_{exp} [k_c] [b,c] /10^{-9} cm^3 $molecule^{-1}$ s^{-1}					
	Debye	*Å³*	H_3O^+	$H_3O^+.H_2O$	$H_3O^+.(H_2O)_2$	$H_3O^+.(H_3O)_3$	NO^+	$O_2^{\bullet+}$
Thiophosphoryl chloride	0.85	11.81	2.3 [2.3]	0.32 [1.7]	0.06 [1.4]	0.06 [1.3]	1.1 [1.8]	1.7 [1.8]
2-Chloroethyl ethyl sulfide	2.25	12.38	3.5 [3.4]	2.8 [2.6]	- [2.2]	- [2.0]	2.7 [2.8]	2.7 [2.7]
Diethyl ethanolamine	1.94	13.60	2.9 [3.2]	2.6 [2.4]	- [2.1]	- [2.0]	2.3 [2.6]	2.2 [2.5]
Dimethyl methyl phosphonate	2.27	10.05	3.3 [3.3]	3.5 [2.5]	- [2.2]	- [2.0]	0.7 [2.7]	1.5 [2.7]
Phosgene (carbonyl dichloride) [d]	1.22	5.77	0.2 [2.1]	<0.01 [1.6]	<0.01 [1.4]	<0.01 [1.3]	<0.01 [1.7]	0.9 [1.7]
Dimethyl ethyl phosphonate	2.04	11.74	[3.2]	2.1 [2.4]	- [2.1]	- [1.9]	2.1 [2.6]	2.1 [2.5]
Diethyl methyl phosphonate	2.25	13.66	[3.4]	1.8 [2.6]	- [2.2]	- [2.0]	2.1 [2.8]	2.2 [2.7]
Diethyl ethyl phosphonate	2.05	15.36	[3.3]	1.8 [2.5]	- [2.1]	- [1.9]	2.0 [2.7]	2.1 [2.6]
Diethyl phosphite	2.22	13.06	[3.5]	3.2 [2.6]	- [2.3]	- [2.1]	2.8 [2.8]	2.8 [2.8]
Diisopropyl phosphite	2.64	15.28	[3.9]	3.1 [2.9]	2.6 [2.5]	- [2.2]	2.8 [3.2]	2.7 [2.7]
Triisopropyl phosphite	2.37	19.58	[3.8]	2.8 [2.8]	2.0 [2.4]	1.4 [2.1]	3.1 [3.1]	3.0 [3.0]
Methyl Salicylate	3.32	15.45	[4.5]	- [3.4]	- [2.9]	- [2.6]	2.1 [3.7]	2.7 [3.6]
Trimethyl Phosphate	3.87	10.34	[4.8]	- [3.6]	- [3.1]	- [2.8]	2.0 [4.0]	2.2 [3.9]
(Diisopropylamino) ethanol	0.93	14.28	[2.5]	- [1.9]	- [1.6]	- [1.5]	1.3 [2.0]	0.9 [2.0]
Chloroacetophenone	4.85	15.87	[6.0]	- [4.5]	- [3.9]	- [3.5]	4.4 [4.9]	2.8 [4.8]

a) All dipole moments and polarizabilities are the Boltzmann averaged value across lowest energy conformers as discussed in the experimental section.
b) Collision-limiting rate coefficients calculated by method of Su.[108]
c) Where the experimental rate coefficient is blank assume the collision-limiting rate coefficient, where the value is a hyphen "-" the rate was not measurable and the collision-limiting rate cannot be assumed.
d) Phosgene has known literature values of dipole moment (1.17 Debye) and polarizability (7.92 ≈[3]) as discussed in the text. [122]

Table 6.03. Product ion branching ratios measured at 298 K and 0.5 Torr. The product ions arising from the ion-molecule reaction of the listed reagent ion with each analyte.

Compound	***H_3O^+***			***NO^+***			***$O_2^{\bullet+}$***		
	Ion	*m/z*	*BR*	*Ion*	*m/z*	*BR*	*Ion*	*m/z*	*BR*
Thiophosphoryl chloride	$PS\ ^{37}Cl_2\ ^{35}ClH^+$	173	0.10	$PS\ ^{37}Cl_2\ ^{35}Cl.NO^+$	202	0.15	$PS\ ^{37}Cl_2\ ^{35}Cl^+$	172	0.05
	$PS\ ^{37}Cl\ ^{35}Cl_2H^+$	171	0.25	$PS\ ^{37}Cl\ ^{35}Cl_2.NO^+$	200	0.40	$PS\ ^{37}Cl\ ^{35}Cl_2^+$	170	0.20
	$PS\ ^{35}Cl_3H^+$	169	0.30	$PS\ ^{35}Cl_3.NO^+$	198	0.45	$PS\ ^{35}Cl_3^+$	168	0.20
	$P\ ^{37}Cl\ ^{35}Cl_2H^+$	139	0.05				$PS\ ^{37}Cl\ ^{35}Cl^+$	135	0.10
	$P\ ^{35}Cl_3H^+$	137	0.05				$PS\ ^{35}Cl_2^+$	133	0.10
	$PS\ ^{37}Cl\ ^{35}Cl^+$	135	0.05				$P\ ^{37}Cl\ ^{35}Cl^+$	103	0.15
	$PS\ ^{35}Cl_2^+$	133	0.10				$P\ ^{35}Cl_2^+$	101	0.20
	$P\ ^{37}Cl\ ^{35}Cl^+$	103	0.05						
	$P\ ^{35}Cl_2^+$	101	0.05						
2-Chloroethyl ethyl sulfide	$C_4H_9\ ^{32}S\ ^{37}ClH^+$	127	0.05	$C_4H_9\ ^{32}S\ ^{37}Cl^+$	126	0.15	$C_4H_9\ ^{32}S\ ^{35}Cl^+$	124	0.05
	$C_4H_9\ ^{32}S\ ^{35}ClH^+$	125	0.20	$C_4H_9\ ^{32}S\ ^{35}Cl^+$	124	0.40	$C_4H_9\ ^{32}S^+$	89	0.15
	$C_4H_9\ ^{34}S^+$	91	0.05	$C_4H_9\ ^{32}S^+$	89	0.40	$C_3H_7\ ^{32}S^+$	75	0.75
	$C_4H_9\ ^{32}S^+$	89	0.65	$C_3H_7\ ^{32}S^+$	75	0.05	$C_2H_6\ ^{32}S^+$	62	0.05
	$C_3H_7\ ^{32}S^+$	75	0.05						
Diethyl ethanolamine	$C_6H_{14}NOH_2^+$	118	0.85	$C_6H_{14}NOH^+$	117	0.05	$C_5H_{12}N^+$	86	1.00
	$C_6H_{14}N^+$	100	0.05	$C_6H_{14}NO^+$	116	0.05			
	$C_4H_9NOH_2^+$	89	0.10	$C_5H_{12}N^+$	86	0.75			
				$C_4H_{10}N^+$	72	0.15			
Dimethyl methyl phosphonate	$C_3H_9PO_3H^+$	125	0.90	$C_3H_9PO_3.NO^+$	154	1.00	$C_3H_9PO_3^+$	124	0.35
	$C_2H_6PO_2H^+$	94	0.05				$C_2H_7PO_2^+$	94	0.55
	$C_2H_6PO_2^+$	93	0.05				$CH_4PO_2^+$	79	0.10
Phosgene	$CO\ ^{37}Cl.H_2O^+$	83	0.15	No Reaction			$CO\ ^{37}Cl^+$	65	0.75
(carbonyl dichloride)	$CO\ ^{35}Cl.H_2O^+$	81	0.35				$CO\ ^{35}Cl^+$	63	0.25
	$CO\ ^{37}Cl^+$	65	0.15						
	$CO\ ^{35}Cl^+$	63	0.35						
Dimethyl ethyl phosphonate	$C_4H_{11}PO_3H^+$	139	1.00	$C_4H_{11}PO_3.NO^+$	168	1.00	$C_4H_{11}PO_3^+$	138	0.30
							$C_2H_7PO_3^+$	110	0.70
Diethyl methyl phosphonate	$C_5H_{13}PO_3H^+$	153	1.00	$C_5H_{13}PO_3.NO^+$	182	1.00	$C_5H_{13}PO_3^+$	152	0.20
							$C_3H_{10}PO_3^+$	125	0.55
							$C_3H_9PO_2^+$	108	0.10
							$CH_3PO_3H_3^+$	97	0.10
							$C_2H_5O^+$	45	0.05
Diethyl ethyl phosphonate	$C_6H_{15}PO_3H^+$	167	1.00	$C_6H_{15}PO_3.NO^+$	196	1.00	$C_3H_{10}PO_3^+$	125	0.80
							$C_3H_9PO_2^+$	108	0.20
Diethyl phosphite	$C_4H_{11}PO_3H^+$	139	1.00	$C_4H_{11}PO_3.NO^+$	168	1.00	$C_4H_{11}PO_3^+$	138	0.20
							$C_2H_8PO_3^+$	111	0.75
							$PO_3H_4^+$	83	0.05
Diisopropyl phosphite	$C_6H_{15}PO_3H^+$	167	1.00	$C_6H_{15}O_3P.NO^+$	196	0.95	$C_6H_{15}O_2^+$	119	0.10
				$C_3H_7O^+$	59	0.05	$C_6H_{13}O^+$	101	0.40
							$C_6H_{11}^+$ /$PO_3H_4^+$	83	0.50

Table 6.03. Continued.

Compound	***H_3O^+***			***NO^+***			***$O_2^{\bullet+}$***		
	Ion	*m/z*	*BR*	*Ion*	*m/z*	*BR*	*Ion*	*m/z*	*BR*
Triisopropyl phosphite	$C_9H_{21}PO_3H^+$	209	0.50	Unable to measure[a]			$C_9H_{21}PO_3^+$	208	0.15
	$C_6H_{14}PO_2^+$	149	0.50				$C_6H_{14}PO_2^+$	149	0.25
							$C_3H_9PO_3^+$	124	0.60
Methyl Salicylate	$C_8H_8O_3H^+$	153	1.00	$C_8H_8O_3^+$	152	1.00	$C_8H_8O_3^+$	152	0.60
							$C_7H_6O_3^+$	138	0.40
Trimethyl Phosphate	$C_3H_9PO_4H^+$	141	1.00	$C_3H_9PO_4.NO^+$	170	1.00	$C_3H_9PO_4^+$	140	0.30
							$C_3H_8PO_4^+$	139	0.70
(Diisopropylamino) ethanol	$C_8H_{19}NOH^+$	146	0.95	$C_8H_{19}NO.NO^+$	175	0.35	$C_7H_{16}NO^+$	130	0.10
	$C_8H_{18}N^+$	128	0.05	$C_8H_{19}NO^+$	145	0.25	$C_7H_{16}N^+$	114	0.60
				$C_7H_{16}N^+$	114	0.35	$C_5H_{12}NO^+$	102	0.15
				$C_5H_{12}NO^+$	102	0.05	$C_4H_{10}N^+$	72	0.15
Chloroacetophenone	$C_8H_7O\,^{37}ClH^+$	157	0.25	$C_8H_7O\,^{37}Cl.NO^+$	186	0.25	$(C_6H_5)CO^+$	105	1.00
	$C_8H_7O\,^{35}ClH^+$	155	0.75	$C_8H_7O\,^{35}Cl.NO^+$	184	0.75			

a) The association product is at the limit of the Voice100 mass range. The $[M.NO]^+$ ion is the expected product ion.

The calculated value of the dipole moment for phosgene (1.22 Debye) is approximately equal to the literature value of 1.17 Debye (± 0.02). [122] However, the B3LYP/6-311+G(d,p) value for polarizability calculated here (5.77 $\approx^3$) is approximately 20% lower than the literature value (7.29 $\approx^3$) tabulated by Maryott and Buckley. [246] The discrepancy may be attributed to the the 6-311+G(d,p) basis set not correctly modelling the large chlorine atoms, and/or the uncertainty (which is unknown) on the literature value.

Using both literature values for dipole moment and polarisability, the value for the collision-limiting rate coefficient for H_3O^+ is only 5% larger than the value determined using calculated parameters, which is an acceptable discrepancy. Boltzmann averaging of the dipole moment and polarisability over the lowest energy conformers (refer to section 6.2.1) was found to affect the calculated collision-limiting rate coefficient for four molecules: diethyl ethanolamine, diethyl phosphite, triisopropyl phosphite and methyl salicylate, where the largest perturbation was found for diethyl phosphite. The dipole moment of diethyl phosphite is substantially perturbed by the contributions from two conformers that are not global minima. The lowest energy conformer gave a dipole moment of 2.84 Debye, however contributions from conformers at +0.8 kJ mol^{-1} and +3.64 kJ mol^{-1} (compared to the global minima) decreased this value to 2.22 Debye. This decrease in dipole moment led to a decrease in the collision-limiting rate coefficients for diethyl phosphite of 15%.

6.2.3 Reactions of H_3O^+

Proton transfer was observed to occur for all rate coefficients measured by the relative kinetics method, and therefore H_3O^+ was assumed to react at the calculated collision-limiting rate coefficient. [61] In support of this assumption, for all measured absolute rate coefficients H_3O^+ was found to proton transfer at, or very near to, the empirical collision-limiting rate coefficient. Only phosgene (measured using a permeation apparatus) was observed to react slower than the collision-limiting rate coefficient with a reaction efficiency of ~10% and this is indicative of the reported proton affinity of phosgene being less than the proton affinity of H_2O.

On initial measurement, the reaction of H_3O^+ with phosgene gave rise to product ions corresponding to proton transfer (m/z 99, 101 and 103) with the experimental rate coefficient being substantially less than the collision-limiting rate coefficient (3×10^{-10} cm^3 $molecule^{-1}$ s^{-1}). The G4 'accurate energy' compound method [106] was employed to determine an accurate proton affinity/gas basicity of phosgene in an attempt to explain the observations. Proton affinities and gas basicities for both the carbonyl (oxygen bound) and chloride sites have been determined, and are given as figure 6.03. However, as figure 6.03 illustrates, even with the contribution from entropy, protonation at neither the carbonyl nor the chloride site will be an exergonic process with H_3O^+ (PA = 691 kJ mol^{-1}, GB = 660 kJ mol^{-1}). [31] The observation of the protonated phosgene species is attributed to the presence of small amounts of ArH^+ present in the flow tube. The ArH^+ is formed by excited H_3O^+ species entering the flow tube, and colliding with an argon atom before all the excitation energy has been dissipated by collisions with helium atoms. The effect of ArH^+ reacting with phosgene was subtracted from the measured rate coefficient to yield a final rate coefficient of 2×10^{-10} cm^3 $molecule^{-1}$ s^{-1}.

Table 6.03 shows that generally all phosphonate, phosphite and phosphate compounds reacting with H_3O^+ give the protonated molecular ion, with very little or no fragmentation observable. Trimethyl phosphate has a literature proton affinity of 890.6 kJ mol^{-1}, [31] and therefore a reaction with H_3O^+ would yield a protonated molecular ion with ~200 kJ mol^{-1} excess energy. As only the protonated molecular ion is observed, it must be concluded that trimethyl phosphate with 17 atoms has sufficient degrees of freedom to survive long enough without dissociation so that the excess energy is ultimately removed by collisions with the carrier gas.

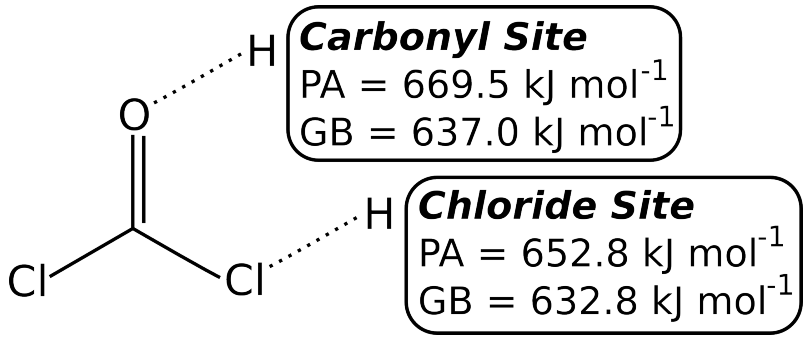

Figure 6.03. Site specific proton affinity (PA) and gas basicity (GB) for the carbonyl and chloride sites of phosgene.

6.2.4 Reactions of $H_3O^+.(H_2O)_n$ (n = 1, 2, 3)

To measure the reaction rate coefficients of an analyte with the water cluster ions, significant analyte vapour must be generated such that the drop in the intensity of the precursor ions is large enough to be measurable. These conditions have resulted in the ability to measure rate coefficients for only 11 of the 15 CWA precursor or surrogate analytes with $H_3O^+.(H_2O)$. Furthermore, due to an inability to generate significant analyte vapour, the rate coefficients of $H_3O^+.(H_2O)_2$ and $H_3O^+.(H_2O)_3$ with only four analytes have been measured.

Thiophosphoryl chloride was observed to react at the collision-limiting rate coefficient with H_3O^+, at approximately 20% reaction efficiency with $H_3O^+.H_2O$, and at less than 5% reaction efficiency for the higher water clusters of the hydronium ion. Because of the observed decrease in reaction efficiency as the number of water molecules attached to H_3O^+ increases, it is not unreasonable to bracket the proton affinity of thiophosphoryl chloride as greater than that of H_2O (691 kJ mol^{-1}), but less than 827 kJ mol^{-1}, the total of the proton affinity of H_2O and the enthalpy of reaction of H_2O clustering with H_3O^+. [31]

6.2.5 Reactions of NO^+

As expected, the reactions of NO^+ precursor ions with the 15 CWA related compounds are found to generally proceed via an association pathway. However, the two analytes that have listed ionisation energies which are less than 9.24 eV (the ionisation energy of NO [30])

are found to yield a channel attributed to electron transfer. 2-Chloroethyl ethyl sulphide and diisopropylamino ethanol are also found to proceed via an electron transfer pathway to give a range of $[M]^+$ ions, and therefore their ionisation energy must be less than that of NO.

Diisopropylamino ethanol is found to have competing association, electron transfer and fragmentation pathways. The fragmentation pathways are assumed to result from dissociative electron transfer as the same product ions are observed from the more energetic electron transfer reactions of $O_2^{\bullet+}$ with the same analyte. The proposed fragmentation pathways are given in reactions 6.01 and 6.02.

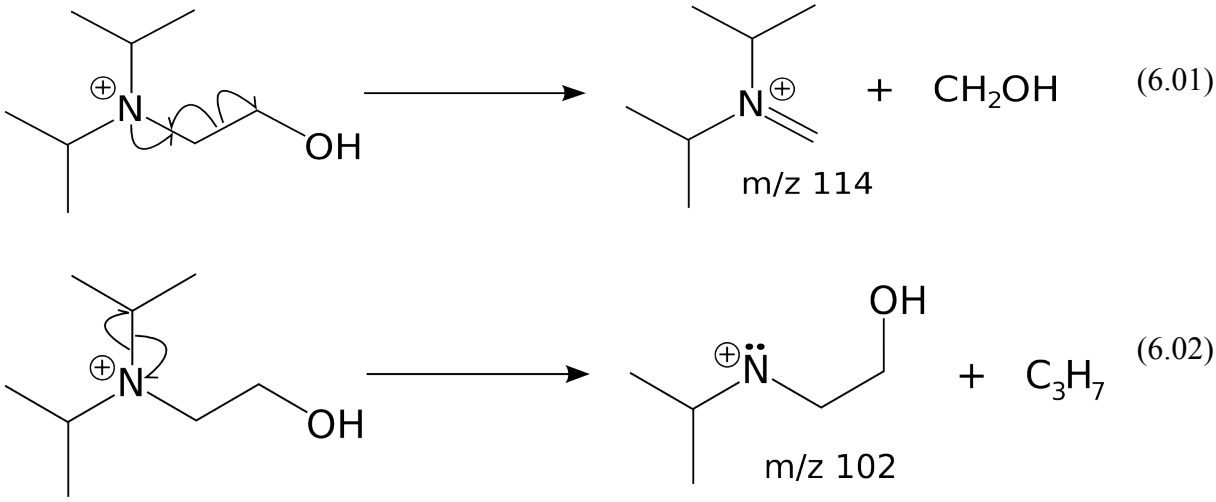

Pressure dependent studies may infer more information regarding the mechanism of competition between the association and electron transfer channels, [76] however, this is outside the scope of the current research.

Diethyl ethanolamine is found to yield a small channel to hydride abstraction, that is assumed to be due to the presence of the alcohol group affording a facile abstraction site.

6.2.6 Reactions of $O_2^{\bullet+}$

As mentioned above, the gas-phase rearrangement mechanisms of phosphorus containing molecules are known to be very complex, [245] and therefore without the aid of computational methods few conclusions can be easily drawn.

Dimethyl methyl phosphonate (commonly known as DMMP), an organophosphorus nerve agent precursor, is observed to yield ions at m/z 94 and m/z 79 in both a chemical

ionisation reaction time-of-flight mass spectrometer (CIR-TOF-MS) [247] and an H_2/O_2 flame. [248] The structure and formation pathway for each of these product ions is given as reaction 6.03. The structure of the product ion for m/z 94 differs from that proposed by Korobeinichev *et al.* [248] in that a formally +3 (excluding the charge) phosphorus is proposed here, whereas Korobeinichev *et al.* give details of a formally +5 ion (shown in figure 6.04).

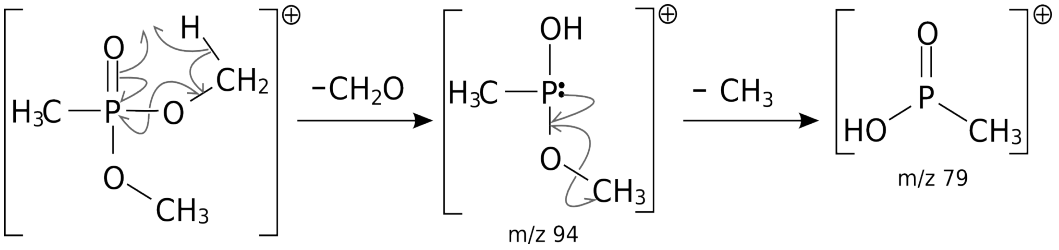

(6.03)

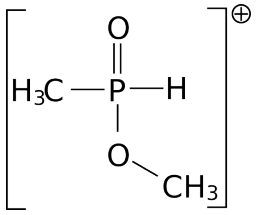

Figure 6.04. Structure of m/z 94 proposed by Korobeinichev et al. [248]

The ionic structure proposed here is favoured due to the ability of a phosphorus atom to facilitate a 5-membered cyclic transition state. The 5-membered cyclic transition state easily allows the phosphorus atom to formally oxidise to the +3 oxidation state.

The structure proposed by Korobeinichev *et al.* is formed via a radical mechanism at the highly elevated temperatures of combustion and not the thermal regime at which a SIFT flow tube operates. To form the ion shown in figure 6.04 in the gas-phase, from the reaction of $O_2^{\bullet+}$ and dimethyl methyl phosphonate, would require a 1,3 migration of an H atom, that due to the steric restrictions is assumed to be less favoured than a 1,4 migration. It is apparent that computational quantum chemical calculations would substantially aid in the differentiation of these two product ion structures.

The reaction of diethyl methyl phosphonate with $O_2^{\bullet+}$ yields an ion at m/z 108 that is proposed to form via the same pathway shown in reaction 6.03, however in this case an acetaldehyde moiety is expected to be the neutral leaving group and not formaldehyde.

The product ions observed for $O_2^{\bullet+}$ reacting with 2-chloroethyl ethyl sulphide are similar to those reported by Cordell *et al*. [247] in a CIR-TOF-MS.

Many product ions shown in table 6.03 from the reactions of $O_2^{\bullet+}$ and the CWA related compounds have been assigned speculative ion formulae. These ions are proposed to be thermodynamic minima that have undergone complex rearrangement processes due to the presence of the phosphorus atom, which can exist in multiple oxidation states.

6.2.7 Limits of detection and quantitation

The limit of detection (LOD) and limit of quantitation (LOQ) using the SIFT-MS technique have been defined by Milligan *et al*. [58] and were also discussed in detail during chapter 1 of this thesis. The LOD is the minimum concentration or 'weight of analyte' that can be detected at a known confidence level (as defined in equation 1.31), and the LOQ is defined as a signal with a precision that satisfies an expected value (defined in equation 1.34).

The limits of detection and limits of quantitation (in parts-per-*trillion*-by-volume) for each CWA related analyte with the optimum precursor ion over a 10 second background sampling time and 20 second analyte sampling time are given in table 6.04. Values of b_μ (the mean background product ion intensity in counts s^{-1}) and s (the sensitivity in counts s^{-1} $ppbv^{-1}$) were determined on the Voice100 instrument used for the majority of the research presented here. These values are typical of a standard Voice100 instrument. LOQ_{pptv} values are found to be less the 8 hour time-weighed-average (TWA) values for safe exposure for the each of the three compounds that have these safety thresholds. [249]

The data presented in table 6.04 can be compared with other CWA detection technologies that have published limits of detection. Black and Read [250] quoted the limit of detection for diisopropylamino ethanol on an LC-APCI-MS (liquid chromatography – atmospheric pressure ionisation – mass spectrometer) to be ≤1200 pptv (≤10 ng ml^{-1} of analyte in water), that is ~5 times worse than measured for a Voice100 in this study. Chen *et al*. [251] measured dimethyl methyl phosphonate using ESI-MS-MS (electrospray ionisation mass spectrometry with collision induced dissociation), and determined the limit of detection to be in the low ppbv range. Patel *et al*. [252] measured the same compound using a chemicapacitative microsensor and found the limit of detection to be 180 ppbv (180,000 pptv), which is three orders of magnitude worse than determined here. The Voice100 is

therefore found to be a very sensitive instrument for the detection of chemical warfare precursor and surrogate compounds when compared to other technologies currently available.

Table 6.04. The limits of detection and quantitation in parts-per-trillion-by-volume for all 15 measured CWA related analytes.

	Ions						
Analyte	***Precursor***	***Product***	b_μ [a]	***s*** [b]	LOD_{pptv}	LOQ_{pptv}	TWA_{pptv} [c]
Thiophosphoryl chloride	H_3O^+	$PS\ ^{35}Cl_3H^+$	4.2	1.4	1400	2100	
2-Chloroethyl ethyl sulfide	NO^+	$C_4H_9\ ^{32}S\ ^{35}Cl^+$	0.50	9.1	75	180	
Diethyl ethanolamine	H_3O^+	$C_6H_{14}NOH_2^+$	1.8	5.0	250	450	2×10^6
Dimethyl methyl phosphonate	NO^+	$C_3H_9PO_3.NO^+$	0.83	2.4	360	760	
Phosgene (carbonyl dichloride)	$O_2^{\bullet+}$	$CO\ ^{37}Cl^+$	46	1.8	3600	4600	2×10^4
Dimethyl ethyl phosphonate	NO^+	$C_4H_{11}PO_3.NO^+$	0.65	7.0	110	250	
Diethyl methyl phosphonate	NO^+	$C_5H_{13}PO_3.NO^+$	0.35	7.0	80	220	
Diethyl ethyl phosphonate	NO^+	$C_6H_{15}PO_3.NO^+$	0.10	6.7	45	200	
Diethyl phosphite	NO^+	$C_4H_{11}PO_3.NO^+$	0.65	9.4	81	180	
Diisopropyl phosphite	NO^+	$C_6H_{15}PO_3.NO^+$	0.10	9.4	32	140	
Triisopropyl phosphite	H_3O^+	$C_9H_{21}PO_3H^+$	0.05	3.8	55	340	
Methyl Salicylate	NO^+	$C_8H_8O_3^+$	0.65	7.0	110	250	
Trimethyl Phosphate	NO^+	$C_3H_9PO_4.NO^+$	1.35	6.7	160	310	
(Diisopropylamino) ethanol	H_3O^+	$C_8H_{19}NOH^+$	1.36	4.9	230	420	
Chloroacetophenone	NO^+	$C_8H_7O\ ^{35}Cl.NO^+$	0.70	11.1	72	160	5×10^4

a) b_μ (in units of counts s^{-1}) measured over 10 seconds of sampling chemical background.
b) s (in units of counts s^{-1} $ppbv^{-1}$) determined at the representative H_3O^+, NO^+ and $O_2^{\bullet+}$ precursor ion intensities of 6×10^5, 1×10^6, and 8×10^5 counts s^{-1} respectively.
c) The TWA is a health and safety related 8 hour time-weighted average value (as discussed in the text) that is given where available.

An example of the quantitation of diisopropyl phosphite in dry air in the parts-per-trillion-by-volume (pptv) concentration range is given as figure 6.05. The measured concentration was found to be 150 pptv, with a chemical background of less than 10 pptv. The equilibration time listed in figure 6.05 is required to remove any analytes that have absorbed to the seats of the solenoid valves used in the sample inlet manifold.

Clearly, it has been shown that the SIFT-MS technique can quantify compounds related to the manufacture of chemical warfare agents, and surrogate compounds for chemical warfare agents, in a concentration regime that is substantially lower than the prescribed TWA health and safety levels. However, it is apparent from the literature that the detection of schedule I CWAs in whole air samples is also of interest. [253]

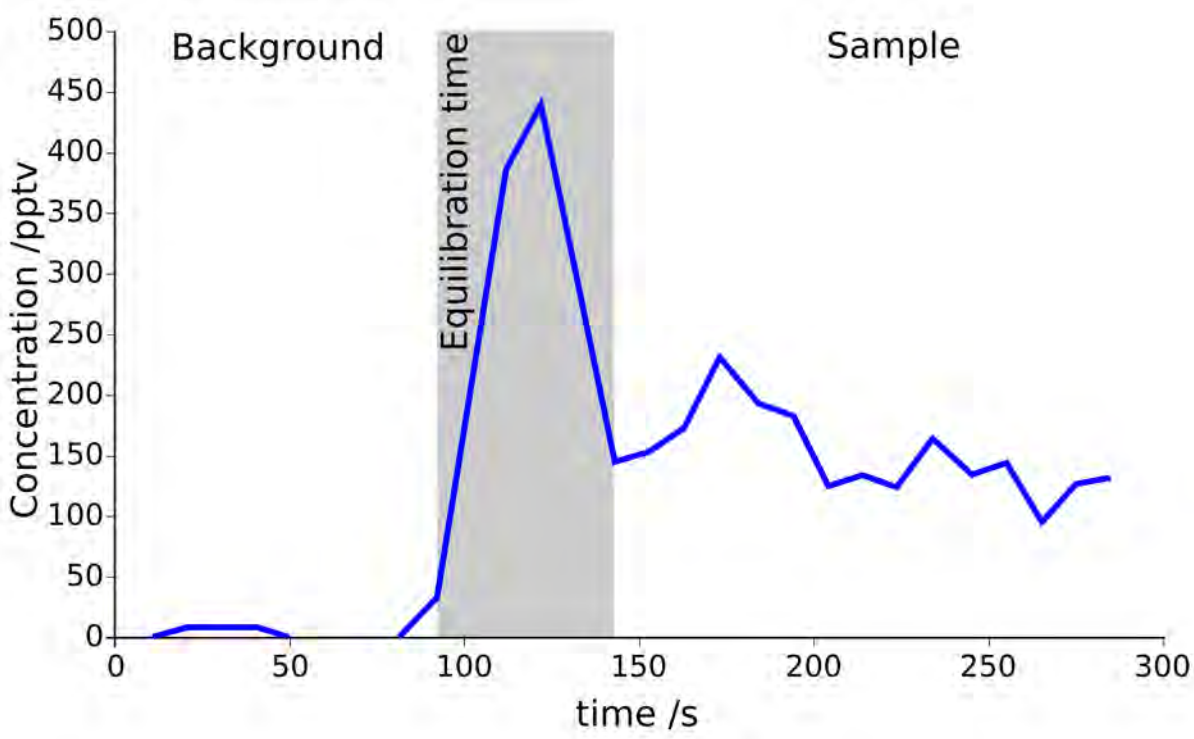

Figure 6.05. Detection of diisopropyl phosphite in the parts-per-trillion-by-volume concentration range.

6.3 Semi-Quantitative Detection of Native Schedule I CWAs

Three schedule I chemical warfare agents have been detected using a Voice100 SIFT-MS instrument. The detection took place in the licensed chemical warfare agent laboratory at the Australian Department of Defence Science and Technology (DSTO) at Fisherman's Bend, Melbourne, Australia.

6.3.1 Experimental

A Voice100 instrument was transported to Melbourne, Australia, and installed beside a constant vapour generator (CVG) apparatus. The CVG (shown in figure 6.06) is used to create dynamic dilutions of chemical warfare agents and the apparatus is similar in design to that reported by Eiceman *et al*. [254] In the CVG, a CWA is heated (using a light bulb) to a temperature slightly above ambient such that an appreciable amount of vapour is created. Vapour from the primary containment chamber is swept into the secondary containment

chamber by a constant flow of dry air. Dual levels of containment are used to minimise any risk of human exposure to CWAs. In the secondary containment region, a second diluent gas is added such that accurate control of the CWA vapour concentration can be achieved. Finally after a mixing region, the CWA vapour is expelled from the CVG into a large fumehood.

A 1 metre long stainless steel sampling arm, connected to the sample inlet on the Voice100, was positioned in the outlet of the CVG, such that the generated vapour could be sampled and measured by the Voice100. The sampling arm was heated to >100 °C to minimise any CWAs adsorbing to the surface of the stainless steel. After sampling CWAs, all O-rings, rubber tubing and pump oil that may have been exposed to CWAs were safely disposed of.

Three native, schedule I CWAs were studied: sarin (figure 6.01), ethyl sarin (a sarin derivative, where the phosphorus bound methyl group in figure 6.01 is replaced by an ethyl group) and sulphur mustard (figure 6.02). Due to an inability to create an accurate and known concentration from the CVG, only semi-quantitative data were obtainable. The data is deemed to be semi-quantitative, not qualitative, as collision-limiting rate coefficients can be applied to provide approximate concentrations.

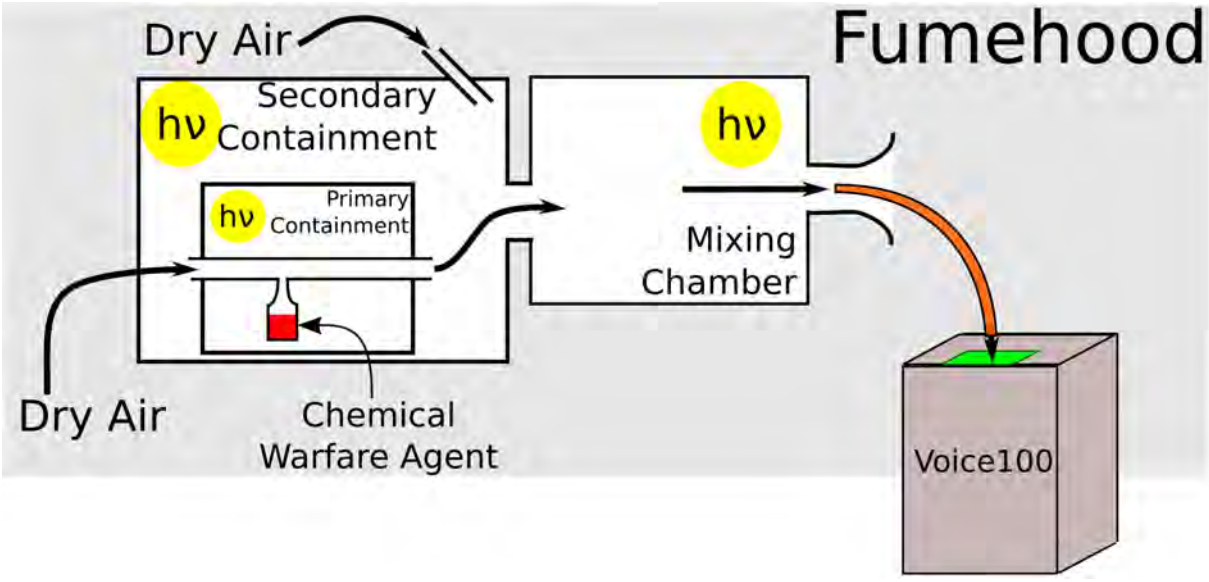

Figure 6.06. Diagram of the DSTO constant vapour generator (CVG) integrated with the Voice100 SIFT-MS. The symbol "hυ" refers to a lightbulb that is used as a heat source.

6.3.2 Detection of sarin

Figure 6.07-A shows a mass scan of sarin vapour that was sampled from the CVG. Sarin, which has a neutral mass of 140 g mol^{-1} is observed to react with H_3O^+ by proton transfer forming the $[M + H]^+$ ion at m/z 141. Due to the dry nature of the vapour generated from the CVG, very little secondary clustering of water molecules is observed.

NO^+ is observed to rapidly associate with sarin giving a peak at m/z 170. The association is known to be rapid as the peak height of the NO^+ association peak is much larger than the $[M + H]^+$ arising from proton transfer from H_3O^+. However, the $[M + H]^+$ is assumed not to contain the entire product ion population resulting from the H_3O^+ + sarin reaction, as secondary clustering of another sarin molecule is proposed to occur giving the $[M_2 + H]^+$ cluster (the proton bound dimer). This $[M_2 + H]^+$ ion was not observed as it occurs at m/z 281 and is outside the mass range of a Voice100 instrument.

$O_2^{\bullet+}$ is observed to react by dissociative electron transfer yielding the $[M - CH_3]^+$ ion at m/z 125. No product ions attributable to the non-dissociative channel are detectable.

An impurity was also observed in the sarin spectra, that was attributed to methylfluorophosphonic acid, a precursor compound used in the synthesis of sarin. [239] The structure of methylfluorophosphonic acid is given in figure 6.07-A. The impurity was found to react by proton transfer with H_3O^+, and association with NO^+. $O_2^{\bullet+}$ was found to react and give an $[Imp + H]^+$ ion (where "Imp" is an impurity), that is assumed to form via non-dissociative electron transfer, followed by a secondary hydride abstraction reaction with another methylfluorophosphonic acid molecule.

6.3.3 Detection of ethyl sarin

Figure 6.07-B shows a mass scan of ethyl sarin vapour that was sampled from the CVG. Comparing this mass scan to the sarin mass scan in figure 6.07-A, the signal to noise ratio is substantially reduced, however, important product ion peaks are still identifiable.

H_3O^+ was observed to proton transfer to ethyl sarin resulting in an $[M + H]^+$ ion at m/z 155. A substantial fraction (approximately 0.3) of the $[M + H]^+$ ions were found to add a water molecule, however ambiguity arises in determining whether the clustering is via a primary reaction or through secondary chemistry occurring.

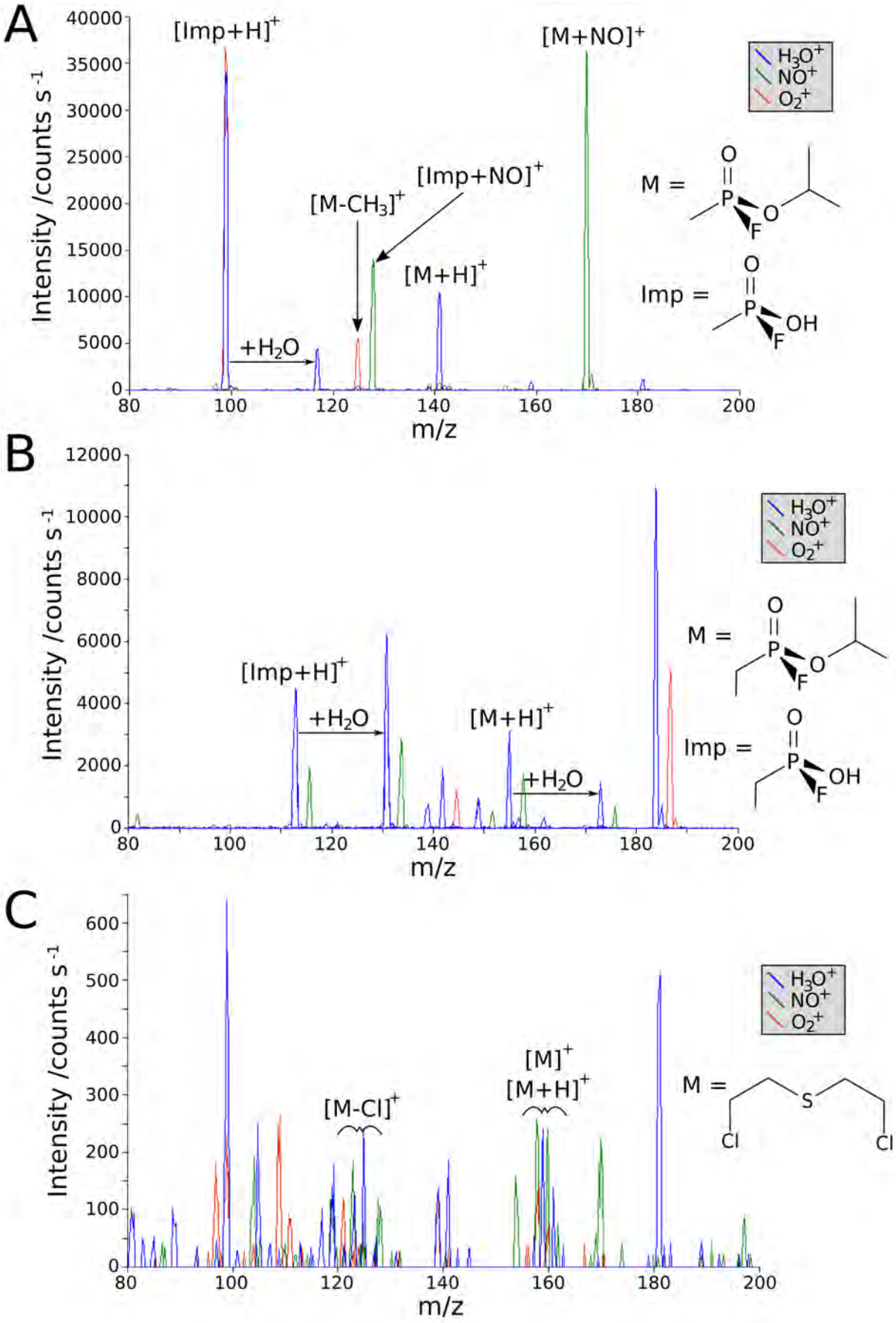

Figure 6.07. Mass scans of native CWAs. A) Sarin, B) ethyl sarin, C) sulphur mustard.

Reactions of NO^+ and $O_2^{\bullet+}$ with ethyl sarin were not found to yield assignable product ions. In comparion to the case of sarin, where NO^+ association was found to be rapid, ethyl sarin is not observed to yield any product ions to an association channel from NO^+. However, similar spectrum taken during the course of the experiments did show some evidence of an NO^+ association channel yielding a product ion at m/z 184. Further research is required to support this observation.

An ethylfluorophosphonic acid impurity can be observed in figure 6.07-B at m/z 113, which is assigned as an $[Imp + H]^+$ ion due to proton transfer from H_3O^+. The structure of ethylfluorophosphonic acid is given in figure 6.07-B. The $[Imp + H]^+$ ion is found to rapidly add a water molecule giving a large peak at m/z 131. However again, it is impossible to confirm that the m/z 131 ion is formed through secondary chemistry, and not via direct association. The largest peak in the mass spectrum shown as figure 6.07-B is found at m/z 183 with the H_3O^+ precursor, that is 28 amu greater in mass than the protonated ethyl sarin cation. This ion at m/z 183 is deemed to be an impurity ion that has two extra CH_2 units in the molecular structure, however no further information regarding structure is obtainable.

No other ions observed in the spectra given as figure 6.07-B were attributable to ethyl sarin or obvious impurities.

6.3.4 Detection of sulphur mustard

Figure 6.07-C shows a mass scan of sulphur mustard vapour that was sampled from the CVG. It is apparent from figure 6.07-C that the amount of sulphur mustard vapour produced from the CVG was very low, which is reflective of the low relative partial vapour pressure (PVP) of sulphur mustard ($PVP_{Sulphur\ Mustard}$ = 0.069 Torr at 20 °C, PVP_{Sarin} = 1.5 Torr at 20 °C). [255] However, even with the very low vapour, and minimal signal, peaks attributable to sulphur mustard were still identifiable. Three sets of peaks are shown in figure 6.07-C that are attributed to sulphur mustard, these are

- the $[M + H]^+$ peaks that are due to proton transfer from H_3O^+,
- the $[M]^+$ peaks resulting due to non-dissociative electron transfer from both the NO^+ and $O_2^{\bullet+}$ precursor ions.
- and the $[M - Cl]^+$ peaks resulting from either proton transfer from H_3O^+ followed by neutral hydrochloric acid loss, or electron transfer from NO^+ or $O_2^{\bullet+}$ with

an ensuing $Cl^{\bullet}$ neutral loss.

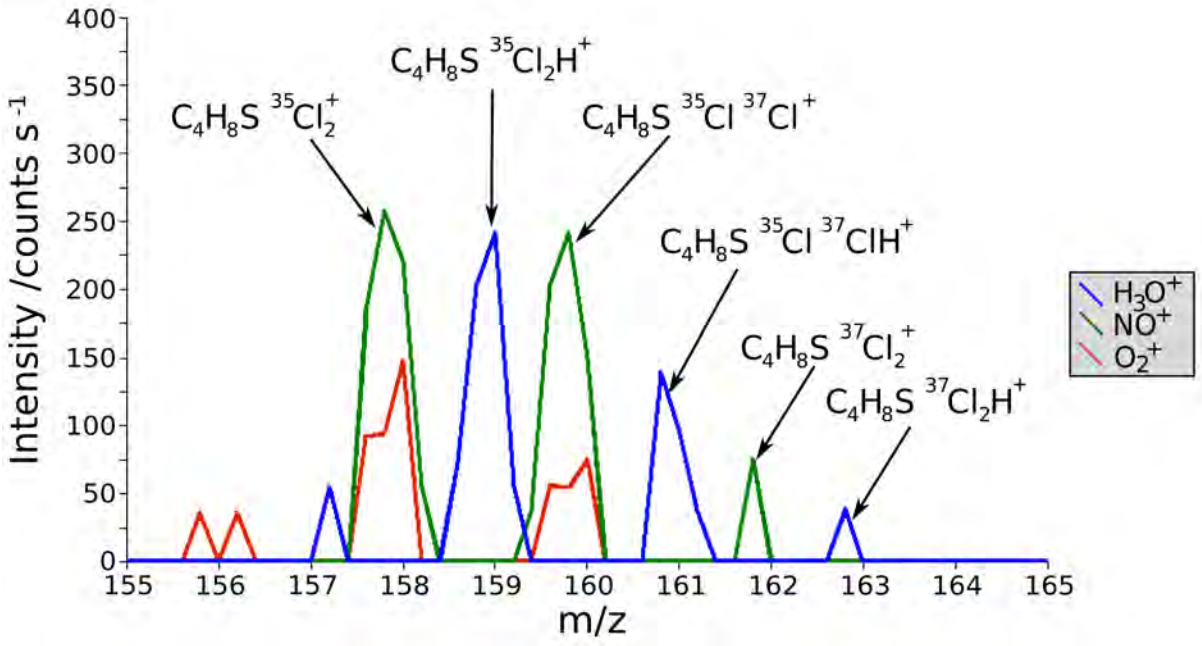

Figure 6.08. Expanded region of the sulphur mustard mass spectrum detailing the observed ions.

Figure 6.08 is an expanded mass spectrum of figure 6.07-C detailing the region where the peaks identified as the $[M + H]^+$ and $[M]^+$ ions were found. The isotopic ratios of each of these two sets of peaks are found to approximately reflect the expected natural isotopic abundance of a dichloro- species. The natural abundance for the three major molecular ion isotopes is approximately 10:6:1.

6.3.5 Collision limiting rate coefficients

The collision limiting rate coefficients for each of the three native CWAs discussed above with the three common SIFT-MS precursor ions and three water cluster ions $H_3O^+.(H_2O)_n$ have been calculated by the method discussed in section 6.2.1. The resulting data from the calculations are listed in table 6.05.

For both sarin and ethyl sarin, three conformers were found to be local minima. However, the only variation between each conformer was the orientation of the isopropyl group, which was not observed to markedly alter the electronic energy, dipole moment or polarisability of the molecule. The only stable conformer found for sulphur mustard was the

linear structure.

Table 6.05. Collision-limiting rate coefficients for the studied schedule I CWAs.

Compound	***μ_D /***	***α /***	***k_c /10^{-9} cm^3 molecules^{-1} s^{-1} – B3LYP/6-311+G(d,p)***					
	Debye	*Å^3*	*H_3O^+*	*$H_3O^+.H_2O$*	*$H_3O^+.(H_2O)_2$*	*$H_3O^+.(H_3O)_3$*	*NO^+*	*$O_2^{\bullet+}$*
Sarin	2.25	13.4	3.4	2.6	2.2	2.0	2.8	2.8
Ethyl Sarin	3.31	13.0	4.4	3.3	2.8	2.6	3.6	3.6
Sulphur Mustard	0.74	14.3	2.4	1.8	1.5	1.4	2.0	1.9

Assuming that the only product ion from the reaction of NO^+ with sarin is the adduct, and that the adduct formation occurs at the collision limiting rate (neither are unreasonable assumptions based on the data presented in tables 6.02 and 6.03) a detection limit for sarin can be calculated. Figure 6.07-A shows the [NO^+.sarin] peak at m/z 170 to have an intensity of 38000 counts s^{-1}. These ions resulted from a NO^+ precursor ion intensity of 1 x 10^6 counts s^{-1} (the NO^+ intensity is not shown in the spectrum). Therefore, applying the standard Voice100 parameters discussed in chapters 1 to 3, the concentration of sarin expelled from the CVG is found to be 4.45 ppmv, and the sensitivity is then 7.87 counts s^{-1} $ppbv^{-1}$. From table 6.04 the background intensity at m/z 170 is known to be 1.35 counts s^{-1}, such that the limit of detection for sarin is 140 pptv and the limit of quantitation is 440 pptv.

The calculated LOQ for sarin is found to approximately 38 times lower than its IDLH value of 17 ppbv as discussed in section 6.1.1. Therefore sarin can be easily quantitated on a Voice100 instrument at a concentration that does not pose immediate danger to life and health.

6.4 Conclusions

The work presented in this chapter shows that the SIFT-MS technique and the Voice100 instrument can be applied to the detection and quantitation of a range of compounds related to chemical warfare. The compounds discussed were CWA reagents (precursor compounds), surrogate compounds and native chemical warfare agents that are restricted by schedule I of the Chemical Weapons Convention 1993.

The quantitation of the CWA reagent and surrogate compounds was enabled by the measurement of rate coefficients and product ion branching ratios for each compound with the three common SIFT-MS precursor ions and a further three water cluster ions $H_3O^+.(H_2O)_n$.

Sarin, ethyl sarin and sulphur mustard were then detected semi-quantitatively, and an estimate for the LOQ for sarin was found to be 440 pptv.

CHAPTER 7

HAZARDOUS AIR POLLUTANTS

7.1 Introduction

For a compound to be toxic to a human, it must first be ingested, inhaled or absorbed through the skin. [256] However, due to the diffusive nature of volatile compounds in the air, inhalation is a more ubiquitous method of poisoning than either ingestion or absorption. Also, because the average human inhales between 10000 and 20000 litres of air each day, even very low concentrations of harmful chemicals may lead to an accumulation of that chemical in the lungs and blood stream.

Volatile Organic Compounds (VOCs) are chemicals that are primarily formed by anthropogenic means (human activity) and are significant air pollutants. Many VOCs are toxic to the natural environment, are known to cause serious health effects in humans and contribute to secondary effects such as ozone production in photochemical smog. [231,257] Therefore, it is of importance to monitor the concentrations of VOCs in the air that we breath to ensure that it is clean and pure. [258] To that end, the United States of America implemented an amendment to the Clean Air Act in 1990, that lists 188 different compounds as 'hazardous air pollutants', (HAPs) also known as 'air toxics'. [259,260] Monitoring of HAP compounds is an important issue for occupational safety and health and NIOSH (the United States National Institute for Occupational Safety and Health) has developed a range of guidelines to which workplaces in the USA must conform. [231]

The compound-specific safety limit for an exposure to a HAP is usually defined as an eight hour time-weighted-average (TWA), that is the maximum value *"for (*a*) normal 8-hour work day and a 40-hour work week to which nearly all workers may be repeatedly exposed, day after day, without adverse effect*". [261] Where concentrations are above the TWA limit, it becomes unsafe to be working in such an environment. [231] The short-term exposure limit (STEL) is also often quoted for a particular compound and this value is always a higher concentration than the TWA. The STEL concentration is defined as a 15 minute exposure limit that should not be exceeded. [261] Furthermore, there should be 60 mins between successive exposures to HAPs that are at the STEL and exposure to an STEL value should not

occur more than four times in a single day.

The US EPA (Environmental Protection Agency) has then described a range of methods for the analysis of these 188 HAPs, by a range of different analytical techniques and sampling methodologies and many analytical laboratories perform analyses by these prescribed methods on a daily basis. The TO-14A [262] and TO-15 [263] (where TO stands for Toxic Organic) are two analytical methods written by the US EPA, where each method contains a list of target compounds that are suitable for analysis by that method. A short description of each of these two methods will now be given. A range of different 'TO' methods have been described by the US EPA (total of 17), however the TO-14A and TO-15 are most widely used in current literature. [264-267]

7.1.1 TO-14A analytical method

The TO-14A method [262] outlines sampling and quantitative detection criteria for 41 VOCs, most of which are halogenated hydrocarbons. Here, samples are collected into rigid stainless steel canisters that have an approximate volume of 6 L. Traditionally SUMMA™ canisters have been used, but a range of approved canisters are listed in the method. On arrival at a laboratory, the sample is removed from the canister, separated by gas chromatography and detected by either a mass spectrometer or by multi-detector techniques such as the flame ionisation detector, nitrogen-phosphorus detector and electron capture detector. The TO-14A method is designed for the simultaneous detection of all 41 VOCs.

7.1.2 TO-15 analytical method

The TO-15 method [263] is similar to the TO-14A method in that it is an analytical method for the quantitative measurement of compounds sampled into rigid stainless canisters such as SUMMA™ canisters. However, the focus of the TO-15 method is on 97 of the most volatile VOCs from the 188 HAPs in the Clean Air Act. Furthermore, the method is designed such that the 97 compounds listed in the method can be divided into subsets based on the application requirement, as opposed to the TO-14A which is for simultaneous detection of all 41 compounds.

GC-MS (gas chromatography – mass spectrometry) is the prescribed technique for the

separation and detection of the VOCs. Other detection techniques (such as the flame ionisation detector) are deemed to be too unspecific for the TO-15 method.

7.1.3 Application to SIFT-MS

As the TO-14A and TO-15 methods have become commonplace in many analytical laboratories, they constitute the current standards for analysis. Therefore, from a commercial aspect, before SIFT-MS can become a competitor to GC-MS in the ambient air monitoring field it is necessary to develop the technique to quantify HAP compounds.

One advantage of the SIFT-MS technique is that it allows for real-time analysis of compounds in whole air samples and therefore compounds that are deemed to be HAPs by the US EPA can be constantly monitored using this technique. Currently, neither the TO-14A nor TO-15 methods are constant monitoring methods because GC-MS is not a technique that allows for real-time analysis. Therefore, the application of the SIFT-MS technique to the monitoring of HAPs will reduce the response time from as long as days (if an air sample must be sent to a contract laboratory) down to seconds. This improvement has an obvious advantage for ambient air monitoring in the workplace.

The following study has been undertaken with a goal of enabling SIFT-MS to quantitatively measure air toxic compounds in air. The rate coefficients and branching ratios are presented for the reactions of three important SIFT-MS precursor ions and three $H_3O^+.(H_2O)_n$ hydrates with 17 compounds deemed to be HAPs and listed on either the TO-14A or TO-15 methods. Limits of detection and limits of quantitation are then given for each compound outlining the ability of SIFT-MS and the Voice100 instrument to quantitatively detect HAP compounds at concentrations near or below 1 part-per-billion-by volume (ppbv).

7.2 Experimental

All rate coefficients and branching ratios discussed in this chapter were measured on a Voice100 instrument (discussed in detail in chapter 2) using the carrier gas flows stated in chapter 3. To reiterate, the carrier flows employed in the Voice100 are 15 Torr L s^{-1} of helium through the inner annulus and 25 Torr L s^{-1} of argon through the outer hole inlet. These parameters result in a flow tube pressure of 0.5 Torr at 298 K and an ion transit time through

the reaction region of approximately 3.8 ms.

Two methods have been employed for determining the rate coefficients and branching ratios of the 17 HAP compounds that are studied herein. Both of these methods were discussed in the experimental chapter, and shall therefore only be mentioned for pertinence. For compounds with high vapour pressures (greater than 2.5 Torr at 20 °C), rate coefficients and branching ratios were determined by the semi-logarithmic plot of ion intensity against an absolute measurement of neutral flow, known as absolute kinetics. For compounds with vapour pressures less than 2.5 Torr, rate coefficients could only be measured relative to the H_3O^+ collision limiting rate coefficient, using mixtures of the analyte in dry nitrogen. Branching ratios were determined where possible by diluting the analyte concentration, and extrapolating the product ion intensity to zero flow. This 'relative' kinetics method was used for compounds that had partial vapour pressures less than 2.5 Torr, but greater than 50 ppmv (~0.04 Torr partial vapour pressure). The method of determining rate coefficients of the water clusters ($H_3O^+.H_2O$ m/z 37, $H_3O^+.(H_2O)_2$ m/z 55 and $H_3O^+.(H_2O)_3$ m/z 73) reacting with a neutral analyte was described in chapter 3.

Table 7.01 lists the methods of measuring the kinetic parameters, and their estimated absolute uncertainties, as well as the governing body that restricts the use of each compound. The collision limiting rate coefficients have been calculated using the method of Su. [108] Dipole moments and polarisabilities have been obtained by quantum chemical calculations using the Gaussian 03W suite of software at the B3LYP/6-311+G(d,p) level of theory. Due to the small size and rigidity of the molecules studied in the current chapter, dipole moments and polarisabilities were not averaged across the lowest energy conformers as per the method discussed in chapter 6.

All chemicals were purchased from Sigma Aldrich, and all had listed purities of > 95%. The compounds that were studied by the absolute method were purified further by freeze-pump-thaw cycling. A mixture of *E* and *Z* 1,2-dichloroethene isomers was used due to the lack of availability of a single stereoisomer. For the purposes of determining collision rate coefficients and and ionisation energy, the *E* and *Z* stereoisomers are assumed to be in a 1:1 mixture. Helium and argon carrier gases were sourced from Southern Gas Services (Christchurch, New Zealand), each having a stated purity of 99.995%. Neither gas was purified further.

Table 7.01. A selection of compounds from the TO-14A and TO-15 methods, their thermodynamic parameters, measurement methods and uncertainties.

Compound	***CAS No.***	***TO*** [a]	***Mass***	***VP*** /[b]	***PA*** /[c]	***IE*** /[d]	***Method*** [e]	***TWA*** [f]	***Uncertainty*** [g]	
				Torr	*kJ mol*$^{-1}$	*eV*		*ppmv*	k_{exp}	*BR*
1,1-Dichloroethene	75-35-4	15	96.94	500	606.8	9.8	Absolute	100	± 15%	± 20%
1,2-(E/Z)-Dichloroethene [h]		14A	96.94	335	619.5	9.7	Absolute	200	± 15%	± 20%
Vinyl acetate	108-05-4	15	86.09	83.0	813.9	9.2	Absolute	8.5	± 15%	± 20%
1,4-Dioxane	123-91-1	15	88.11	37.0	797.4	9.2	Absolute	25	± 15%	± 20%
Methyl methacrylate	80-62-6	15	100.1	28.1	831.4	10.0	Absolute	100	± 15%	± 20%
Epichlorohydrin	106-89-8	15	92.52	12.0		10.6	Absolute	5	± 15%	± 20%
Cumene	98-82-8	15	120.2	3.2	791.6	8.7	Absolute	50	± 15%	± 20%
N,N-Dimethylformamide	68-12-2	15	73.09	2.7	887.5	9.1	Absolute	10	± 15%	± 20%
2-Chloroethyl ether	111-44-4	15	143.0	0.71			Relative	5	± 25%	± 30%
Chloroacetic Acid	79-11-8	15	94.50	0.69	765.4	10.8	Relative	0.3 [i]	± 25%	± 30%
Urethane	51-79-6	15	89.09	0.54		10.2	Relative	1.3 [j]	± 25%	± 30%
Acrylamide	76-06-1	15	71.08	0.53	870.7	9.8	Relative	0.1	± 25%	± 30%
N,N-Dimethylaniline	121-69-7	15	121.2	0.50	941.1	7.1	Relative	5	± 25%	± 30%
Isophorone	78-59-1	15	138.2	0.38	893.5	9.1	Relative	25	± 25%	± 30%
Styrene oxide	96-09-3	15	120.2	0.30		9.1	Relative	-	± 25%	± 30%
1,2,4-Trichlorobenzene	120-82-1	Both	181.5	0.18		9.0	Relative	5	± 25%	± 30%
Nitrobenzene	98-95-3	15	123.1	0.15	800.3	9.9	Relative	1	± 25%	± 30%

a) 'TO' refers to the method of which the compound is a member of either the TO-14A, the TO-15 or both. Each method is discussed in the text.
b) VP is the partial vapour pressure of the analyte in Torr. The vapour pressures are sourced from the TO-14A and TO-15 method documents. [262] [263]
c) Proton affinities sourced from the NIST Webbook. [31]
d) Ionisation energies also sourced from the NIST Webbook. [30]
e) Definitions discussed in text.
f) The definition of TWA is discussed in the text, however the specific value here is the US NIOSH/OSHA workplace safety value. [261]
g) 'k_{exp}' refers to the uncertainty of the experimental rate coefficients of H_3O^+, NO^+ and O_2^+ reacting with the neutral analyte. The uncertainty on each of the $H_3O^+.(H_2O)_n$ (n = 1, 2, 3) cations for the absolute measurements is listed in table 3.15. The uncertainty on the same cluster ions for the relative measurements is at least 10% greater per water cluster. 'BR' refers to the uncertainty on the measurement of the branching ratio.
h) The compound studied was a mixture of both the *E* and *Z* stereoisomers. CAS number of the *E* isomer is 156-60-5 and the CAS number of the *Z* isomer is 156-59-2. The vapour pressure listed is a linear combination of both isomers in a 1:1 mixture.
i) The Great Britian TWA value has been used as the US TWA value is not defined.
j) Texas, USA 30 min ambient air safety limit has been used as the USA TWA value is not defined.

7.3 Results and Discussion

Table 7.02 lists the experimental rate coefficients and calculated collision limiting rate coefficients for each of the 17 compounds. Where an experimental rate coefficient is not given for H_3O^+, the relative with dilutions method has been used and the collision limiting rate

coefficient is assumed. However, where an experimental rate coefficient is not given for $H_3O^+.(H_2O)_n$ the collision limiting rate coefficient cannot be assumed as the process of proton transfer may not be exothermic. Table 7.03 lists the product ions observed and the relative branching ratios for each ion reacting with the 17 compounds of interest. The experimental branching ratios of all molecules containing chlorine atoms were observed to occur with the expected isotopic ratios.

Where noted, experimental values of the dipole moment and polarisability have been used when calculating the collision limiting rate coefficient. These values have been sourced from the CRC Handbook of Chemistry and Physics. [122]

Table 7.02. Rate coefficients of 17 hazardous air pollutant compounds reacting with the SIFT-MS precursor ions and $H_3O^+.(H_2O)_n$ ions measured at 298 K and 0.5 Torr.

Compound	μ_D [a] /	α [a] /	k_{exp} [k_c] [b,c] /10^{-9} cm^3 $molecule^{-1}$ s^{-1}					
	Debye	*Å³*	H_3O^+ [d]	$H_3O^+.H_2O$	$H_3O^+.(H_2O)_2$	$H_3O^+.(H_2O)_3$	NO^+	$O_2^{\bullet+}$
1,1-Dichloroethene	1.62	7.78	2.4 [2.6]	<0.01 [2.0]	<0.01 [1.8]	<0.01 [1.6]	0.03 [2.2]	1.9 [2.1]
(*E*/*Z*)-1,2-Dichloroethene [e]	1.11	7.78	0.3 [2.2]	<0.01 [1.7]	<0.01 [1.5]	<0.01 [1.3]	0.01 [1.8]	1.5 [1.8]
Vinyl acetate	1.83	8.47	3.2 [2.9]	- [2.2]	- [2.0]	- [1.8]	2.8 [2.4]	2.6 [2.4]
1,4-Dioxane [f]	0.00	8.12	2.4 [1.7]	- [1.3]	- [1.1]	- [1.0]	1.7 [1.4]	1.7 [1.4]
Methyl methacrylate	3.13	10.0	3.2 [3.0]	- [2.3]	- [2.0]	- [1.9]	1.9 [2.5]	2.3 [2.5]
Epichlorohydrin	0.65	7.43	2.2 [1.8]	- [1.4]	- [1.2]	- [1.1]	0.34 [1.5]	1.8 [1.5]
Cumene [g]	0.79	16.0	2.4 [2.6]	- [2.0]	- [1.7]	- [1.5]	1.2 [2.1]	1.7 [2.1]
N,N-Dimethylformamide	3.82	7.24	3.4 [5.1]	- [4.0]	- [3.6]	- [3.3]	2.5 [4.3]	2.9 [4.3]
Bis(2-Chloroethyl) ether	0.53	11.6	[2.1]	1.9 [1.6]	1.8 [1.4]	1.8 [1.3]	1.4 [1.7]	1.6 [1.7]
Chloroacetic Acid	1.71	5.49	[2.5]	2.0 [2.0]	1.7 [1.6]	1.6 [1.3]	1.1 [2.1]	1.8 [2.0]
Urethane	2.43	7.01	[3.4]	3.0 [2.6]	3.2 [2.3]	3.3 [2.1]	2.4 [2.8]	2.6 [2.8]
Acrylamide	3.58	6.29	[4.8]	3.6 [3.8]	3.3 [3.4]	3.9 [3.1]	3.7 [4.1]	3.2 [4.0]
N,N-Dimethylaniline	2.00	15.6	[3.3]	2.9 [2.5]	2.8 [2.2]	2.8 [2.0]	2.4 [2.8]	2.5 [2.7]
Isophorone	4.62	16.06	[5.8]	5.2 [4.4]	5.0 [3.7]	5.0 [3.4]	4.3 [4.8]	4.3 [4.7]
Styrene oxide	1.93	15.42	[3.3]	3.9 [2.4]	2.8 [2.2]	2.8 [2.0]	2.5 [2.7]	2.5 [2.6]
1,2,4-Trichlorobenzene	1.36	15.64	[2.8]	0.9 [2.1]	0.6 [1.8]	0.5 [1.6]	2.3 [2.3]	2.2 [2.2]
Nitrobenzene [g]	4.22	14.7	[5.4]	- [4.1]	- [3.5]	- [3.2]	3.9 [4.4]	4.7 [4.3]

a) All dipole moments and polarizabilities are the Boltzmann averaged value across lowest energy conformers as discussed in the experimental section.
b) Collision limiting rate coefficients calculated by method of Su. [108]
c) Where a "-" is given, a rate coefficient has not been measured and the collision-limiting rate coefficient can be assumed.
d) Where a value of k_{exp} is not listed for H_3O^+ reactions, the collision rate is assumed.
e) The listed dipole moment of (*E*/*Z*)-1,2-Dichloroethene is determined assuming a 1:1 mixture of the *E* and *Z* isomers. Therefore the listed dipole moment is half of the dipole moment determined for the *Z* isomer.
f) Dipole moment and polarisability determined for the chair conformer.
g) Both the dipole moment and polarisability were sourced from the CRC Handbook. [122]

Table 7.03. Product ion branching ratios measured at 298 K and 0.5 Torr. The product ions arising from the ion-molecule reaction of the listed reagent ion with each analyte.

Compound	***H_3O^+***			***NO^+***			***$O_2^{\bullet+}$***		
	Ion	*m/z*	*BR*	*Ion*	*m/z*	*BR*	*Ion*	*m/z*	*BR*
1,1-Dichloroethene	$C_2H_2{}^{37}Cl_2H^+$	101	0.05	$C_2H_2{}^{35}Cl_2.NO^+$	130	0.05	$C_2H_2{}^{37}Cl_2^+$	100	0.05
	$C_2H_2{}^{37}Cl{}^{35}ClH^+$	99	0.35	$C_2H_2{}^{37}Cl{}^{35}Cl.NO^+$	128	0.35	$C_2H_2{}^{37}Cl{}^{35}Cl^+$	98	0.35
	$C_2H_2{}^{35}Cl_2H^+$	97	0.55	$C_2H_2{}^{35}Cl_2.NO^+$	126	0.60	$C_2H_2{}^{35}Cl_2^+$	96	0.60
	$C_2H_2{}^{35}Cl^+$	61	0.05						
(*E*/*Z*)-1,2-Dichloroethene	$C_2H_2{}^{37}Cl{}^{35}ClH^+$	99	0.15	$C_2H_2{}^{35}Cl_2.NO^+$	130	0.05	$C_2H_2{}^{37}Cl_2^+$	100	0.05
	$C_2H_2{}^{35}Cl_2H^+$	97	0.20	$C_2H_2{}^{37}Cl{}^{35}Cl.NO^+$	128	0.35	$C_2H_2{}^{37}Cl{}^{35}Cl^+$	98	0.35
	$C_2H_2{}^{37}Cl.H_2O^+$	81	0.10	$C_2H_2{}^{35}Cl_2.NO^+$	126	0.60	$C_2H_2{}^{35}Cl_2^+$	96	0.60
	$C_2H_2{}^{35}Cl.H_2O^+$	79	0.40						
	$C_2H_2{}^{35}Cl^+$	61	0.15						
Vinyl acetate	$C_4H_6O_2H^+$	87	0.45	$C_4H_6O_2^+$	86	0.05	$C_4H_6O_2^+$	86	0.05
	$C_2H_3O^+$	43	0.55	$C_2H_3O^+$	43	0.95	$C_2H_3O^+$	43	0.95
1,4-Dioxane	$C_4H_8O_2H^+$	89	0.95	$C_4H_8O_2^+$	88	0.50	$C_4H_8O_2^+$	88	0.55
	$C_2H_4OH^+$	45	0.05	$C_4H_7O_2^+$	87	0.50	$C_3H_6O^+$	58	0.35
							$C_2H_4^+$	28	0.10
Methyl methacrylate	$C_5H_8O_2H^+$	101	0.90	$C_5H_8O_2.NO^+$	130	0.20	$C_5H_8O_2^+$	100	0.60
	$C_4H_5O^+$	69	0.10	$C_4H_5O^+$	69	0.80	$C_5H_7O_2^+$	99	0.05
							$C_4H_5O_2^+$	85	0.05
							$C_4H_5O^+$	69	0.30
Epichlorohydrin	$C_3H_5O{}^{37}ClH^+$	95	0.10	$C_3H_5O{}^{37}Cl.NO^+$	124	0.15	$C_3H_5O{}^{35}Cl^+$	92	0.05
	$C_3H_5O{}^{35}ClH^+$	93	0.35	$C_3H_5O{}^{35}Cl.NO^+$	122	0.35	$C_3H_5O^+$	57	0.75
	$C_3H_5O^+$	57	0.15	$C_3H_4O{}^{37}Cl^+$	93	0.15	$C_2H_5^+$	29	0.10
	$C_2H_5^+$	29	0.40	$C_3H_4O{}^{35}Cl^+$	91	0.35	$C_2H_4^+$	28	0.10
Cumene	$C_9H_{12}H^+$	121	0.70	$C_9H_{12}^+$	120	0.60	$C_9H_{12}^+$	120	0.05
	$C_8H_{11}^+$	107	0.05	$C_9H_{11}^+$	119	0.15	$C_8H_{10}^+$	106	0.05
	$C_8H_9^+$	105	0.10	$C_8H_{10}^+$	106	0.05	$C_8H_9^+$	105	0.65
	$C_7H_9^+$	93	0.05	$C_8H_9^+$	105	0.05	$C_3H_7^+$	43	0.25
	$C_3H_7^+$	43	0.10	$C_3H_7^+$	43	0.15			
N,N-Dimethylformamide	$C_3H_7NOH^+$	74	0.95	$C_3H_7NO.NO^+$	103	0.10	$C_3H_7NO^+$	73	0.95
	CHO^+	29	0.05	$C_3H_7NO^+$	73	0.45	$C_3H_7^+$	43	0.05
				$C_3H_6NO^+$	72	0.45			
Bis(2-Chloroethyl) ether	$C_4H_8O{}^{37}Cl_2H^+$	147	0.05	$C_4H_8O{}^{37}Cl{}^{35}Cl.NO^+$	174	0.10	$C_3H_6{}^{37}ClO^+$	95	0.25
	$C_4H_8O{}^{37}Cl{}^{35}ClH^+$	145	0.35	$C_4H_8O{}^{35}Cl_2.NO^+$	172	0.15	$C_3H_6{}^{35}ClO^+$	93	0.70
	$C_4H_8O{}^{35}Cl_2H^+$	143	0.60	$C_4H_7O{}^{37}Cl_2^+$	145	0.05	$C_2H_4{}^{35}Cl^+$	63	0.05
				$C_4H_7O{}^{37}Cl{}^{35}Cl^+$	143	0.25			
				$C_4H_7O{}^{35}Cl_2^+$	141	0.35			
				$C_4H_8O{}^{35}Cl^+$	107	0.10			
Chloroacetic Acid	$C_2H_3O_2{}^{37}ClH^+$	97	0.25	$C_2H_3O_2{}^{37}Cl.NO^+$	126	0.25	$C_2H_3O_2{}^{37}Cl^+$	96	0.10
	$C_2H_3O_2{}^{35}ClH^+$	95	0.75	$C_2H_3O_2{}^{35}Cl.NO^+$	124	0.75	$C_2H_3O_2{}^{35}Cl^+$	94	0.30
							$CH_3{}^{37}Cl^+$	52	0.15
							$CH_3{}^{35}Cl^+$	50	0.45
Urethane	$C_3H_7NO_2H^+$	90	1.00	$C_3H_7NO_2.NO^+$	119	1.00	$C_3H_7NO_2^+$	89	0.05
							$CH_4NO_2^+$	62	0.70
							$C_2H_5O^+$	45	0.25

Table 7.03. Continued.

Compound	***H_3O^+***			***NO^+***			***$O_2^{\bullet+}$***		
	Ion	*m/z*	*BR*	*Ion*	*m/z*	*BR*	*Ion*	*m/z*	*BR*
Acrylamide	$C_2H_3NH_2COH^+$	72	1.00	$C_2H_3NH_2CO.NO^+$	101	1.00	$C_2H_3NH_2CO^+$	71	0.55
							$NHCO^+$	43	0.45
N,N-Dimethylaniline	$C_8H_{11}NH^+$	122	1.00	$C_8H_{11}N^+$	121	1.00	$C_8H_{11}N^+$	121	0.65
							$C_8H_{10}N^+$	120	0.35
Isophorone	$C_9H_{14}OH^+$	139	1.00	$C_9H_{14}O.NO^+$	168	0.75	$C_9H_{14}O^+$	138	1.00
				$C_9H_{14}O^+$	138	0.25			
Styrene oxide	$C_8H_8OH^+$	121	0.90	$C_8H_8O^+$	120	0.20	$C_8H_8O^+$	120	0.15
	$C_7H_7O^+$	107	0.10	$C_8H_8^+$	104	0.40	$C_8H_7O^+$	119	0.30
				$C_7H_8^+$	92	0.20	$C_8H_8^+$	104	0.05
				$C_7H_7^+$	91	0.20	$C_7H_8^+$	92	0.20
							$C_7H_7^+$	91	0.30
1,2,4-Trichlorobenzene	$C_6H_3{}^{37}Cl_2{}^{35}ClH^+$	185	0.10	$C_6H_3{}^{37}Cl_2{}^{35}Cl^+$	184	0.10	$C_6H_3{}^{37}Cl_2{}^{35}Cl^+$	184	0.10
	$C_6H_3{}^{37}Cl{}^{35}Cl_2H^+$	183	0.40	$C_6H_3{}^{37}Cl{}^{35}Cl_2^+$	182	0.40	$C_6H_3{}^{37}Cl{}^{35}Cl_2^+$	182	0.40
	$C_6H_3{}^{35}Cl_3H^+$	181	0.50	$C_6H_3{}^{35}Cl_3^+$	180	0.50	$C_6H_3{}^{35}Cl_3^+$	180	0.50
Nitrobenzene	$C_6H_5NO_2H^+$	124	1.00	$C_6H_5NO_2.NO^+$	153	1.00	$C_6H_5NO_2^+$	123	1.00

The reactions of 1,4-dioxane with H_3O^+, NO^+ and $O_2^{\bullet+}$ are observed to react with experimental collision rate coefficients that are approximately 40% faster than the collision limiting rate coefficients determined by the method of Su. [108] The uncertainty on each experimental rate coefficient is ± 15% and the uncertainty on the polarisability is known not to exceed ± 5%. [268] Furthermore, 1,4-dioxane does not have an appreciable dipole moment as the two principal dipole vectors in the lowest energy conformer (chair structure) [269] are of the same magnitude, but opposing direction. Therefore, assuming Langevin theory [270] accurately models the situation, the overall discrepancy between k_c and k_{exp} should not substantially exceed ± 20%. The observed discrepancy of 40% is therefore an anomalously large value.

The first postulated theory to explain the aforementioned discrepancy is that a contribution from the boat and/or twist boat conformers that have non-zero dipole moments may be increasing the experimental rate coefficient. However, the Gibbs free energy barrier to ring inversion ($\Delta G^{\ddagger}$) between the chair and boat conformers is 10.1 kcal mol^{-1} (42.3 kJ mol^{-1}), which is 17 times greater than thermal energy at room temperature and will not occur in the gas-phase. [269,271]

Khajehpour and Kauffman [272] found that in the solution-phase 1,4-dioxane behaves like a polar solvent, even though the molecule has a very low dielectric constant. The

researchers attributed this observation to 1,4-dioxane having a large non-ideal quadrupole moment that arises due to the distribution of electron density throughout the molecule and that 1,4-dioxane is not axially symmetric. In the gas-phase, a large quadrupole moment may influence the long-range Coulombic attraction between a cation and a neutral molecule, however no literature was obtainable that either supports or denies this hypothesis. Furthermore, no current theory is available for calculating gas-phase ion-molecule collision-limiting rate coefficients that takes into account the effects of quadrupole moments. The experimental rate coefficients that have been observed in the current study are in support of the findings of Khajehpour and Kauffman [272] in as far as 1,4-dioxane is found to exhibit the chemistry of a molecule which is more polar than the structure would suggest.

N,N-dimethylformamide is observed to react 35% slower than the calculated collision-limiting rate coefficient for each of the SIFT-MS precursor ions. The dipole moment of 3.82 Debye is a literature value sourced form the CRC Handbook of Chemistry and Physics. [122] It is the magnitude of this dipole moment that leads to the very fast collision-limiting rate coefficients. [108] The additive uncertainties of the experimental rate coefficient (± 15%) and the calculation of the collision limiting rate coefficient (± 20%) spans the observed discrepancy between the two values.

7.3.1 Reactions of H_3O^+

Proton transfer was observed to occur for all reactions measured by the relative kinetics method and therefore H_3O^+ was assumed to react at the calculated collision rate coefficient. [61] Furthermore, proton transfer was observed to occur from H_3O^+ to all analytes in table 7.03 at the collision limiting rate coefficient except for (*E/Z*)-1,2-dichloroethene.

1,1- and 1,2-dichloroethene differ only by the connectivity of one chlorine atom, yet on observation of table 7.02 and 7.03, each is found to react with H_3O^+ via quite markedly different pathways. The 1,1- isomer reacts by proton transfer at the collision limiting rate coefficient (k_c) whereas the 1,2- isomer is observed to react at approximately 10% of k_c, with a range of product ions, some of which are attributed to proton transfer. To further complicate the situation, the 1,2-dichloroethene solution is a mixture of *E* and *Z* stereoisomers. Both the 1,1- and 1,2- isomers have known experimental literature ionisation energies, [30] but the proton affinities of neither isomer are known. Therefore, in an attempt to understand the reaction mechanisms that are operating, the proton affinities and gas basicities for the three

isomers of $C_2H_4Cl_2$ have been calculated using quantum mechanical methods. Each value has been calculated using the G3 accurate energy compound method [101] in the Gaussian 03W suite of software. [109] At each step the Hessian matrix was evaluated to ensure all structures found were energetic minima.

The G3 calculated ionisation energies are found to accurately reproduce experimental data which was sourced from the NIST webbook. [30] The largest discrepancy found was for the *Z*-1,2- isomer which was 0.05 eV when including the experimental uncertainty. This discrepancy is approximately equal to the average deviation of G3 theory from the G2/97 data set of experimental values. [101]

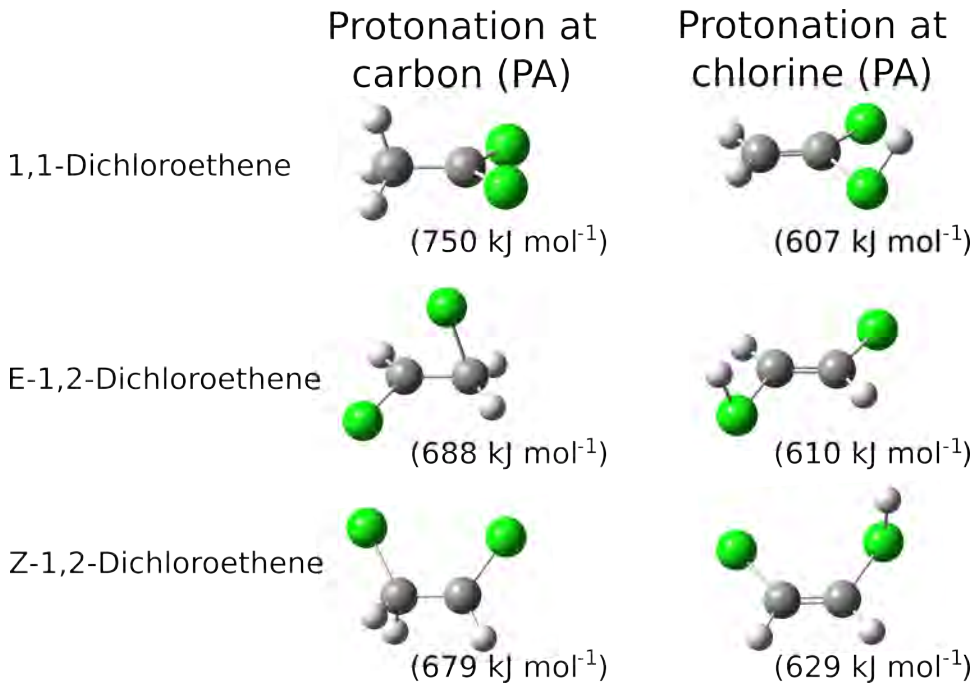

Figure 7.01. Structures and site-specific proton affinities of dichloroethene isomers.

Each isomer of dichloroethene was found to afford two sites for protonation: one at a chlorine atom and the other at an ethyl carbon. All three isomers of dichloroethene were found to yield a more stable structure when protonation occurred at an ethyl carbon atom rather than a chlorine atom. The calculated structures and site-specific proton affinities are given as figure 7.01. Furthermore, table 7.04 reports the G3 calculated proton affinities and gas basicities for protonation at the more stable ethyl carbon, as well as the calculated and experimental ionisation energy.

The proton affinity and gas basicity of water are known to be 691 and 660 kJ mol^{-1} respectively. [31] Therefore based on the values presented in table 7.04, proton transfer from H_3O^+ will occur to the 1,1- isomer, but will not occur with unit efficiency to either of the 1,2-isomers. 1,1-dichloroethene is found experimentally to react at the collision rate and therefore the computational findings support the experimental data.

Table 7.04. Proton affinities (PA), gas basicities (GB) and ionisation energies (IE) for each isomer of $C_2H_4Cl_2$.

	G3[a] PA / *kJ mol^{-1}*	***G3[a] GB /*** *kJ mol^{-1}*	***G3[a] IE /*** *eV*	***Literature[b] IE (±) /*** *eV*
1,1-dichloroethene	750	721	9.80	9.81 (0.04)
E-1,2-dichloroethene	688	659	9.60	9.64 (0.02)
Z-1,2-dichloroethene	679	650	9.62	9.66 (0.01)

a) Values calculated using the G3 compound method. [101]
b) Literature values sourced from the NIST Webbook. [30]

The transfer of a proton from H_3O^+ to *E*-1,2-dichloroethene is found to be approximately 3 kJ mol^{-1} endothermic and 1 kJ mol^{-1} endergonic (with inclusion of the entropy term). A similar case applies for the *Z*-1,2- isomer, however the magnitude of the endothermicity and endergonicity is larger (12 and 10 kJ mol^{-1} respectively).

Applying the Arrhenius equation, approximately 30% of H_3O^+ + *E*-1,2-dichloroethene collisions should surmount the energy barrier of 3 kJ mol^{-1} and lead to proton transfer products. In comparison, less than 1% of H_3O^+ + *Z*-1,2-dichloroethene collisions will lead to proton transfer according to the same relationship. As the compound used in the current study is a mixture of *E* and *Z* isomers, the Arrhenius calculated reaction efficiency is deemed to be an average of the two isomers, which is 15%. By multiplying this calculated reaction efficiency by the collision rate yields an expected experimental rate coefficient for the proton transfer channel of 3.4 x 10^{-10} cm^3 $molecule^{-1}$ s^{-1}, which is very similar to the experimental rate coefficient presented in table 7.02. This is concluded to be somewhat fortuitous, as the activation energy term in the Arrhenius equation is only approximated by the endothermicity of the reaction.

Mikhailov *et al.* [273] have measured rate coefficients and product ion branching ratios for the two individual isomers of 1,2-dichloroethene and found that both isomers react with

similar experimental rate coefficients of 3 x10^{-10} and 4 x 10^{-10} cm^3 $molecule^{-1}$ s^{-1} for the E and Z isomers respectively.

To ensure that the reactions of H_3O^+ ions in the Voice100 flow tube are occurring at or very near to thermal energy and the observed reactions of 1,2-dichloroethene are not aided by energetic H_3O^+ ions, the reaction of H_3O^+ with cyclohexane was studied. The proton affinity of cyclohexane is 686.9 kJ mol^{-1} and the reaction of H_3O^+ with cyclohexane is known to yield only association products. [274] The experimental reaction rate coefficient was found to be << 1 x 10^{-12} cm^3 $molecule^{-1}$ s^{-1} which correlates with the data measured by Spanel *et al.* [274] It is therefore apparent that the vast majority of H_3O^+ ions in the Voice100 flow tube are in the ground vibrational state, as the first excited vibrational state is 525.82 cm^{-1} (6.3 kJ mol^{-1}) higher in energy. [275] The fact that the experimental observations of Mikhailov *et al*. [273] differ from the results predicted by the G3 proton affinities for each of the dichloroethene isomers is probably a reflection of the uncertainty in the calculations, and not due to energetic collisions.

Epichlorohydrin yields a major product ion channel at m/z 29. This ion could be assigned as either the ethyl cation ($C_2H_5^+$) or the formyl cation (CHO^+). The two pathways are shown as reactions 7.01 and 7.02 where the neutral products are proposed based on mass balance and the two other product ions observed from the same reaction that are presented in table 7.03.

$$H_3O^+ + C_3H_5OCl \rightarrow C_2H_5^+ + HCl + H_2O + CO + 52.9 \text{ kJ mol}^{-1} \quad (7.01)$$

$$\rightarrow CHO^+ + HCl + H_2O + C_2H_4 - 200 \text{ kJ mol}^{-1} \quad (7.02)$$

It is apparent from the two reactions shown above that the formation of $C_2H_5^+$ is thermodynamically feasible and the formation of CHO^+ is not. Therefore only the $C_2H_5^+$ ion is given in table 7.03. The enthalpies of formation were sourced from the NIST Webbook. [191]

Styrene oxide is observed to yield a 10% product ion channel corresponding to a CH_2 loss from the molecular ion. A pathway that is proposed for the formation of this ion is shown as reaction 7.03. The proposed reaction is facilitated by the benzene ring that affords multiple resonance structures stabilising the ion listed as m/z 107.

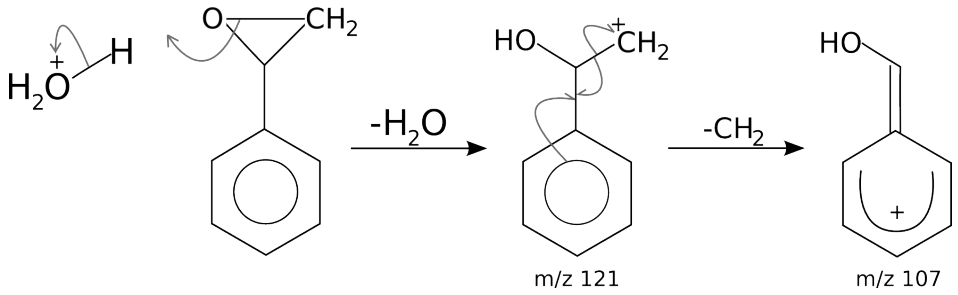

(7.03)

7.3.2 Reactions of $H_3O^+.(H_2O)_n$ (n = 1, 2, 3)

All compounds (excluding 1,1- and 1,2-dichloroethene) that have experimental H_3O^+ rate coefficients were measured before the method prescribed in section 3.4 (for the determination of water cluster rate coefficients) was designed. Therefore, no rate coefficients for the $H_3O^+.(H_2O)_n$ reactions with these analytes are given. However, the absolute $H_3O^+.(H_2O)_n$ rate coefficients for 1,1- and 1,2-dichloroethene are given as these reactions were revisited after the method prescribed in section 3.4 was designed. For the nine reactions where an experimental H_3O^+ rate coefficient is not given (determined by the 'relative with dilutions' method), relative rate coefficients for the $H_3O^+.(H_2O)_n$ cluster ions were determined.

In general, where measured, the experimental $H_3O^+.(H_2O)_n$ reaction rate coefficients were found to be slightly faster than the calculated collision limiting rate coefficients, although the differences are well within the established uncertainties of the experimental method (see section 3.4). The observed trend ($k_{exp} > k_c$) may be indicative of a water clustering rate coefficient used in the deconvolution process being inaccurate.

7.3.3 Reactions of NO^+

Reactions of the 17 toxic organic analytes were found to proceed via the association, electron transfer and hydride abstraction pathways. Dissociative electron transfer and dissociative hydride transfer were also observed, however in general, these ions are minor product ion channels.

A small amount of excited NO^+, which is formed in the ion source, is not thermalised through collisions with carrier gas atoms. Midey *et al.* [276] observed that approximately 2% of the NO^+ ions in their SIFT flow tube are in an excited state and react with N_2 via exothermic electron transfer yielding N_2^+. A similar concentration of excited NO^+ ions are

observed in the Voice100 when studying the same reaction. The excited NO^+ ion is postulated to be in the $^3\Sigma^+$ state, as opposed to the $^1\Sigma^+$ ground state. [277] As a transition between a triple and singlet state is spin-forbidden, the excited NO^+ ($^3\Sigma^+$) species is long-lived in a SIFT flow tube. The effects of this excited NO^+ were subtracted from the reactions involving 1,1- and 1,2-dichloroethene where the rate coefficient was found to be very slow.

1,4-dioxane has an experimental literature ionisation potential of 9.19 eV, [31] such that electron transfer from NO^+ (IE = 9.24 eV) is at least 0.045 eV endothermic. However, a 50% channel to electron transfer is observed in table 7.03. The Arrhenius equation determines that 18% of the ions will surmount the endothermicity of the reaction and yield molecular product ions. The discrepancy of 32% is deemed to be due to inaccuracies in the measurement of the product ion branching ratio and in the measurement of the ionisation energy of 1,4-dioxane.

7.3.4 Reactions of $O_2^{\bullet+}$

$O_2^{\bullet+}$ is observed to react via electron transfer and dissociative electron transfer with all 17 analytes. This finding is not surprising as the ionisation energy of O_2 is 12.07 eV, which is higher than that of all analytes that have ionisation energies listed in table 7.01.

A major product ion channel from the reaction of $O_2^{\bullet+}$ with 1,4-dioxane is observed at m/z 58, which is deemed to be a neutral loss of a formaldehyde moiety (CH_2O). The m/z 58 ion is assumed not to be due to an acetone impurity as the H_3O^+ and NO^+ spectra yield no product ions at peaks that would correspond to the presence of acetone. The ion structure that is formed is proposed to be the oxetane (1,3-epoxypropane) cation, which is formed via a electrocyclic transition state. The proposed mechanism is shown in reaction 7.04, where the ionisation step from $O_2^{\bullet+}$ is assumed to have already occurred, however the excess energy from the reaction has not yet been dissipated by collisions with carrier gas atoms.

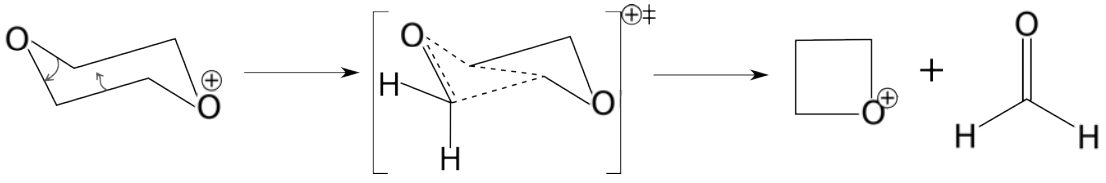

(7.04)

The enthalpy of reaction 7.04 plus the excess energy from the ionisation of 1,4-dioxane is -114.6 kJ mol^{-1}, however the barrier to the rearrangement is unknown. For the mechanism

proposed as reaction 7.04 to proceed, the barrier to rearrangement must be less than 2.87 eV (276 kJ mol^{-1}), which is the difference in ionisation energy between O_2 and 1,4-dioxane. As the upper-limit for the barrier to rearrangement is large, it is not unreasonable to conclude that the reaction proceeds through this pathway.

7.4 Quantitative Detection of Toxic Air Pollutants

The limit of detection (LOD) and limit of quantitation (LOQ) using the SIFT-MS technique have been defined by Milligan *et al*. [58] and were also discussed in detail during chapter 1 of this thesis. The LOD is the minimum concentration or 'weight of analyte' that can be detected at a known confidence level (as defined in equation 1.31), and the LOQ is defined as a signal with a precision that satisfies an expected value (defined in equation 1.34).

Table 7.05. The limits of detection and quantitation in parts-per-trillion-by-volume for all 17 measured analytes that are classed as hazardous air pollutants.

	Ions						
Analyte	***Precursor***	***Product***	b_μ [a]	s [b]	LOD_{pptv}	LOQ_{pptv}	TWA_{pptv} [c]
1,1-Dichloroethene	$O_2^{\bullet+}$	$C_2H_2{}^{35}Cl_2^+$	26	2.9	1600	2100	1 x 10^8
1,2-(E/Z)-Dichloroethene	$O_2^{\bullet+}$	$C_2H_2{}^{35}Cl_2^+$	26	3.1	1600	2100	2 x 10^8
Vinyl acetate	H_3O^+	$C_4H_6O_2H^+$	55	3.7	1900	2400	8.5 x 10^6
1,4-Dioxane	H_3O^+	$C_4H_8O_2H^+$	11	5.9	530	740	2.5 x 10^7
Methyl methacrylate	H_3O^+	$C_5H_8O_2H^+$	17	7.4	530	720	1 x 10^8
Epichlorohydrin	H_3O^+	$C_3H_5{}^{37}ClH^+$	35	0.6	9900	1.3 x 10^5	5 x 10^6
Cumene	H_3O^+	$C_9H_{12}H^+$	15	4.3	850	1200	5 x 10^7
N,N-Dimethylformamide	NO^+	$C_3H_7NO.NO^+$	6.7	1.1	2300	3300	1 x 10^7
2-Chloroethyl ether	H_3O^+	$C_4H_8O{}^{35}Cl_2H^+$	12	3.3	1000	1400	5 x 10^6
Chloroacetic Acid	NO^+	$C_2H_3O_2{}^{35}Cl.NO^+$	5.0	3.6	600	900	3 x 10^5 [d]
Urethane	H_3O^+	$C_3H_7NO_2H^+$	1.4	8.8	130	240	1.3 x 10^6 [e]
Acrylamide	H_3O^+	$C_2H_3NH_2COH^+$	23	12	370	490	1 x 10^5
N,N-Dimethylaniline	NO^+	$C_8H_{11}NH^+$	1.2	10	100	190	5 x 10^6
Isophorone	$O_2^{\bullet+}$	$C_9H_{14}O^+$	8.1	15	180	260	2.5 x 10^7
Styrene oxide	H_3O^+	$C_8H_8OH^+$	15	7.7	480	980	-
1,2,4-Trichlorobenzene	H_3O^+	$C_6H_3{}^{35}Cl_3^+$	0.4	3.6	170	430	5 x 10^6
Nitrobenzene	H_3O^+	$C_6H_5NO_2^+$	3.6	14	130	200	1 x 10^6

a) b_μ (in units of counts s^{-1}) measured over 10 seconds of sampling chemical background.
b) s (in units of counts s^{-1} $ppbv^{-1}$) determined at the representative H_3O^+, NO^+ and $O_2^{\bullet+}$ precursor ion intensities of 6 x 10^5, 1 x 10^6, and 8 x 10^5 counts s^{-1} respectively.
c) The TWA is a health and safety related 8 hour time-weighted average value (as discussed in the text) that is provided for all analytes.
d) The Great Britian TWA value has been used as theUS TWA value is not defined.
e) Texas, USA 30 min ambient air safety limit has been used as the US TWA value is not defined.

The LODs and LOQs have been calculated (in parts-per-*trillion*-by-volume) for each hazardous air pollutant with the optimum precursor ion over a 10 second background sampling time and a 20 second analyte sampling time. These values are presented in table 7.05. Values of b_μ (the mean background product ion intensity in counts s^{-1}) and s (the sensitivity in counts s^{-1} $ppbv^{-1}$) were determined on the Voice100 instrument that was used for the majority of the research presented here. These values are typical of a standard Voice100 instrument. Table 7.05 also reiterates the TWA values presented in table 7.01, however for the current situation, the values are in the units of pptv for direct comparison to the LOD and LOQ. [261]

Limits of quantitation for all compounds in table 7.05 (except epichlorohydrin) are found to be at least two orders of magnitude lower than the listed TWA value. [261] Epichlorohydrin has a higher LOD and LOQ due to large backgrounds at all product ion masses and a slow rate coefficient with NO^+ inhibiting the use of that precursor for detection.

Because the Voice100 instrument used in the current study can detect the listed HAPs at concentrations substantially lower than the safety limit, greater confidence in the constant monitoring procedure is achieved. Furthermore, where a concentration is observed to rise but is yet to reach the TWA limit, preventative measures can be put in place to lower the concentration in the ambient air and protect worker health and safety.

7.5 Conclusions

The work presented in this chapter shows that the SIFT-MS technique and the Voice100 instrument can be applied to the detection and quantitation of a range of compounds related to ambient air monitoring and the detection of hazardous air pollutants. The compounds that were discussed are listed in the United States Clean Air Act as compounds which are harmful to human health above specified concentrations. The hazardous air pollutant compounds that have been studied are currently measured using the TO-14A and TO-15 methods which are prescribed by the US-EPA. The research presented chapter outlines the ability of the SIFT-MS technique to not only compete, but to replace gas chromatography as the most suitable technique for ambient air monitoring of hazardous air pollutants.

The quantitation of the 17 compounds discussed in the current chapter was enabled by the measurement of rate coefficients and product ion branching ratios for each compound with

the three common SIFT-MS precursor ions and a further three water cluster ions $H_3O^+.(H_2O)_n$.

CHAPTER 8

CONCLUDING REMARKS AND SUGGESTIONS FOR FUTURE WORK

The following is a summary of the research presented in this thesis and an offering of some suggestions for future work that may develop upon and/or strengthen the arguments presented in the preceding chapters.

8.1 A Summary of the Preceding Research

SIFT-MS is an emerging technology for the quantitative detection of analytes in whole air samples. However, the number of compounds that can currently be monitored by SIFT-MS, on the grounds of their known kinetic parameters, number less than 500. It is therefore important to increase this database of knowledge. In the preceding research, the rate coefficients of product ion branching ratios of 58 new analytes with SIFT-MS precursor ions has been presented. The 58 analytes are grouped into four separate applications. The limits of detection and quantitation are discussed for each application. Concurrently, new instrumentation has been optimised and verified.

8.1.1 Consequences of instrument design changes

The Voice100 instrument is a small-scale selected ion flow tube designed particularly for the quantitative analysis of trace analytes in whole air samples. Two novel factors have been integrated into the Voice100 distinguishing it from earlier versions of SIFT-MS equipment and also minimising the size of the instrument, while increasing the overall number of ions transmitted to the particle multiplier. These novel factors are a flow tube that is bent through 180° and the mixing of two carrier gases, helium and argon. Because these two novel factors are associated with the flow tube, the carrier gas dynamics of the Voice100 flow tube were investigated to determine the optimum operating conditions. These conditions

are required to yield large ion signals while minimising turbulent flow. By comparing a calculated ion arrival time in laminar flow with an experimental ion time-of-flight, a deviation from laminar flow was determined for a range of carrier gas flows. The optimum condition (the least deviation from laminar flow) was found to occur with a helium flow of 15 Torr L s^{-1} through the inner annular inlet and an argon flow of 25 Torr L s^{-1} through the outer hole inlet, where both carrier inlets are on the Venturi plate. At these conditions the flow tube pressure was found to be approximately 0.5 Torr and the ion time-of-flight along the reaction length 3.63 ms. Furthermore, an end correction was measured, resulting in a 2.8 cm decrease in reaction length.

8.1.2 Diffusion in mixed carrier gases

The calculation of an ionic mobility and diffusion coefficient for an ion in a single carrier gas is well understood for a simple system. [111] However, the calculation of a diffusion coefficient of an ion in a mixed carrier gas system is a more difficult task. Both a range of computational methods and an experimental method have been employed to calculate the diffusion coefficients of a range of ions often encountered in SIFT-MS measurements that are diffusing through a helium/argon mixture. The computational methods applied previously published theory to the Voice100 instrument. [120,121] The experimental method involved subtracting the downstream ion-detection chamber mass discrimination function from the overall instrument mass discrimination function. However, a large discrepancy was found between the experimental and computational methods. The discrepancy was concluded to be due to a momentum (and therefore mass) dependent discrimination factor occurring at the ion orifice where ions are sampled from the flow tube into the downstream ion-detection chamber. The region near the sampling orifice is not a field-free region, but the theories used to calculate ionic mobility and diffusion in SIFT flow tubes assume that the entire flow tube is field-free. The momentum-dependent parameter has been coined M_P and a range of values have been measured for different ions of different mass. The factor M_P leads to an agreement between theory and experiment.

8.1.3 Problems with water

All analytical samples that are encountered when using the SIFT-MS technique contain some water vapour. H_3O^+ is known to react with water vapour to form a series of cluster ions $H_3O^+.(H_2O)_n$ (n = 1, 2, 3) and each of these cluster ions can react in turn with other analytes present in the flow tube where the thermodynamics permit. To be able to accurately measure the concentrations of analytes in the presence of water vapour, the rate coefficients for each of the sequential water clusters of H_3O^+, reacting with the analyte, must be known. However, the water cluster ions are formed (and reacted away) along the course of the flow tube, as they cannot be individually injected from the upstream ion-selection chamber. Furthermore, the concentration of an $H_3O^+.(H_2O)_n$ ion is dependent on the concentration of the $H_3O^+.(H_2O)_{n-1}$ ion. Therefore, to measure the rate coefficients for each water cluster ion reacting with a particular analyte, deconvolution of the observed rate coefficients is required. This has been achieved using two methods. Firstly, the rate law has been solved by analytical means using the Mathematica package, leading to four integrated rate expressions. However, as these expressions are cumbersome, a simpler iterative method has been proposed that arrives at the same solution as the more cumbersome method, by dividing the flow tube into a series of shorter steps and recalculating the individual ion concentrations at each step. The uncertainty upon the deconvoluted $H_3O^+.(H_2O)_2$ and $H_3O^+.(H_2O)_3$ rate coefficients was determined to be greater than ± 50%. This uncertainty is deemed to be acceptable, due to the ease of performing the calculation. Both of these methods have been verified against literature values for the reactions of $H_3O^+.(H_2O)_n$ with both ethanol and acetone and were found to reproduce the literature values to within the expected uncertainty.

8.1.4 GeoVOC applications

Quantitative detection of small hydrocarbons using the SIFT-MS technique has been previously hindered by the secondary reactions of product ions arising in the primary reactions, subsequently reacting with water vapour. To help unravel this secondary chemistry, the rate coefficients and product ion branching ratios of the $C_1 - C_9$ linear hydrocarbons with $O_2^{\bullet+}$ and H_3O^+ have been studied on the University of Canterbury FA-SIFT where the flow tube carrier gases were a mixture of helium and argon. The majority of reactions that were presented have been published previously and excellent correlation is observed between parameters measured in “helium only” flow tubes and the “helium/argon system” presented

here. Furthermore, the rate coefficients and product ion branching ratios for 21 hydrocarbon ions reacting with water vapour have been measured. Each of the reactions studied have facilitated the development of a method for the quantitation of $C_1 - C_9$ linear hydrocarbons by the SIFT-MS technique. Furthermore, the detection of hydrocarbons has been demonstrated by integrating a Nafion™ dryer system into a Voice100 instrument. The Nafion™ selectively removes water vapour from non-polar hydrocarbon mixtures. By removing the water vapour, quantitative measurement of ethane and propane becomes viable, as the primary product ions are not depleted by reactions with water vapour. When comparing the method (coined GeoVOC) to a range of certified standards, the RMS error for humidified samples was found to be 4.1% and slightly skewed toward under-measurement. In support of the method, two case studies have been presented, the first determines the optimum depth for gas extraction from a gas well, while the second discusses a preliminary study of hydrocarbon micro-seepage in the North Island of New Zealand.

8.1.5 Food and flavour applications – alkyl esters

The rate coefficients and product ion branching ratios of 17 alkyl esters with the SIFT-MS precursor ions have been presented. These esters are known to be important contributors to the characteristic odour of certain fruits. Many of the ester analytes are observed to fragment when reacted with H_3O^+, NO^+ and $O_2^{\bullet+}$ and yield unexpected product ion structures. Of particular note was the observation of a protonated parent carboxylic acid ion, which was found to be formed as a primary ion from the reaction of particular alkyl esters with H_3O^+. The rearrangement pathways of two of these esters, ethyl propanoate and n-propyl ethanoate, have been studied by computational methods employing the CBS-4M compound method. The formation of the protonated parent carboxylic acid was found to occur by site-specific protonation at the alkoxy site followed by a 1,5-H atom migration. The lowest energy pathway for the 1,5-H atom migration was found to occur from a carbon that is β to the alkoxy oxygen onto the carbonyl oxygen. The barrier to 1,5-H atom migration was found to be larger for ethyl propanoate than for n-propyl ethanoate that was supported by the magnitude of the experimental product ion channels at m/z 75 and m/z 61 respectively. Furthermore a similar channel in the NO^+ spectrum was observed yielding an $[NO^+.\text{carboxylic acid}]^+$ ion. A thermodynamically feasible pathway was also determined for this channel using t-butyl ethanoate as a model chemistry. Finally, using the rate coefficients and product ion

branching ratios that had been determined for each of the alkyl esters, the quantitative measurement of four butyl ethanoate isomers in Honeydew Melon has been demonstrated.

8.1.6 Chemical warfare applications

Chemical warfare agents (CWAs) are extremely toxic compounds that are restricted by the Chemical Weapons Convention. [214] Due to the extreme toxicity of CWAs, it is often prudent to transport the precursor compounds (which are used to synthesis the chemical warfare agents) and not the agents themselves. To that end, the rate coefficients and product ion branching ratios of 10 CWA precursor compounds and five CWA surrogate compounds with SIFT-MS precursor ions have been measured. These measurements allow for the quantitative detection of many of the compounds by the SIFT-MS technique in the parts-per-trillion-by-volume concentration regime. To complement the precursor and surrogate compounds, three native CWAs have been detected semi-quantitatively at the Australian Defence Science and Technology laboratory in Melbourne, Australia. The measurements are deemed to be semi-quantitative as the collision-limiting rate coefficients not the experimental rate coefficients have been used to calculated the concentrations of the three CWAs. The collision-limiting rate coefficients were calculated using the Gaussian 03W suite of software.

8.1.7 Environmental applications

The 1996 amendment to the United States Clean Air Act lists 188 compounds that are deemed to be hazardous air pollutants (HAPs). [260] Each pollutant has an associated safety limit that, when exceeded, becomes a health hazard. Therefore it is of importance to be able to accurately measure the concentrations of these volatile compounds in ambient air in real time. The rate coefficients and product ion branching ratios of 17 HAPs reacting with SIFT-MS precursor ions has been presented. One of the studied analytes, 1,2-dichloroethene, was found to react with H_3O^+ by proton transfer with a reaction efficiency less than unity. Approximately 10% of all collisions of 1,2-dichloroethene with H_3O^+ were found to proceed via proton transfer. G3 calculated site-specific proton affinities and gas basicities confirmed that the reaction with H_3O^+ is approximately thermoneutral. Conversely, 1,4-dioxane was found to react with an experimental rate coefficient that was approximately 40% faster than the

collision-limiting rate coefficient. The discrepancy was postulated to be due to the large quadrupole moment associated with 1,4-dioxane. Finally, the limits of detection and limits of quantitation for each compound have been determined. The limits of quantitation for 16 of the 17 HAPs are found to be at least two orders of magnitude less than the safety threshold defined by the National Institute of Occupational Safety and Health. [231]

8.1.8 General comments

During the course of this thesis, Voice100 SIFT-MS has been shown to be a very useful tool for solving real-time analytical problems. Analytical chemistry should benefit enormously from applications that have been presented here. Furthermore, particular industries will benefit from the applications that relate to their field. These industries are: the oil exploration industry, can now rapidly screen soil, water and gas samples for small hydrocarbons; the food and flavour industry that, for the purposes of quality control, can quantitatively detect alkyl esters in food products; border and homeland security can now measure the concentrations in real-time of many analytes related to chemical warfare; and any industry that is involved with hazardous chemicals benefits from the ability to monitor the ambient concentrations of these chemical and improve workplace safety.

Two new technologies DESI (desorption electrospray ionisation) and DART (direct analysis in real-time) are mass spectrometry techniques that do not require sample preparation and are known as direct mass spectrometry. [278,279] Both of these techniques are in competition to the SIFT-MS technique. However, SIFT-MS has two major advantages over DESI and DART.

- SIFT-MS does not require a calibration to known standards to be able to measure analyte concentrations. However, neither the DESI nor the DART technique can utilise the well understood gas-phase kinetic parameters to measure concentrations, as the precursor ion signal is unknown and reaction conditions are poorly controlled.

- Each of the DESI and DART techniques require a beam of either ions or metastable molecules to encounter a compound of interest on a substrate for detection to occur. For instance, to detect sarin in a suitcase, the beam of either ions or metastable molecules must encounter sarin molecules which are adsorbed to the

surface of the suitcase. Therefore a large surface may be required to be tested by either DESI or DART. However, because SIFT-MS detects volatile molecules in the gas-phase into the parts-per-trillion-by-volume concentration range, sarin vapour that is near the suitcase can be detected by SIFT-MS without the need for scanning large surfaces.

8.2 Suggestions For Future Work

The discrepancy observed between experimental and calculated diffusion coefficients (discussed in chapter 3) was deemed to be due to a momentum-dependent discrimination in the non-field-free region near the downstream sampling orifice. However, this was only postulated and no literature was available to support the claim. Ion trajectory studies using SIMION^{TM} or similar software across a range of masses (momenta) may afford more insight into the interaction. Furthermore, experimental studies using apparatus specifically designed for such an experiment would also be useful. Such an apparatus would be a low-field flow/drift tube operating in the range of 0 – 100 V cm^{-1} where the diffusion and mass discrimination in low fields can be easily studied.

The addition of a field into the flow tube of a SIFT-MS instrument may also be pursued with a goal to minimise the water cluster formation from H_3O^+ while not substantially altering the bimolecular kinetics. However, the low field would affect the termolecular processes often observed from the reactions of NO^+, such that the field would need to be variable to ensure that the pseudo bimolecular rate coefficients of these reactions would not be perturbed.

PTR-MS (proton transfer reaction – mass spectrometer) instruments have recently incorporated linear and Paul ion traps as well as time-of-flight (TOF) mass spectrometers. [280-282] The integration of each of these mass separation techniques can allow for greater analyte specificity. TOF mass spectrometers give accurate mass information that can yield molecular formulae, however, a TOF tube does not lead to information regarding structural isomers. For instance a TOF tube may separate $C_2H_3O^+$ (m/z 43.184) from $C_3H_7^+$ (m/z 43.054) but will not able to separate acetaldehyde from oxirane (both form the molecular ion $C_2H_4OH^+$ when reacted with H_3O^+). Ion trap instruments allow for collision-induced-dissociation (CID) of an ion inside the ion trap that may yield further information regarding an ion's structure.

However, two issues arise from the use of ion traps. The first issue is an inability to efficiently trap low mass ions, such as the SIFT-MS precursor ions. This inefficiency leads to lower limits of detection for many analytes as observed by Steeghs *et al.* [281] for their proton transfer reaction instrument. Secondly, many ions of interest may fragment by CID, however the appearance energy of these fragments is often larger than the amount of collision energy created in the ion trap. In these cases such fragments will not be observed.

As noted in chapter 3, the end correction is dependent on the carrier gas flow. However, the end correction may also be dependent on the flow through the sample inlet. Where a sample is known to have a very high concentration of analyte, it is often applicable to lower the flow through the sample inlet. Changing the sample flow may alter the end correction and in turn alter the effective reaction time, which is crucial to measuring concentrations by the SIFT-MS technique. Therefore, a more effective way of lowering the concentration of an analyte is to create a dynamic dilution system that allows for a constant flow through the sample inlet. It is suggested that this research avenue be pursued. A dynamic dilution system is immediately applicable to the GeoVOC method, where concentrations of hydrocarbons often exceed the linear range of a standard Voice100 instrument (0 – 50 ppmv). In conjunction with a dynamic dilution apparatus, improvements to the sample inlet system, such as integration of passivated (silicate coated) tubing and fittings, would yield better limits of detection for compounds that may absorb to the surface of current inlet system.

As discussed in section 8.1, the SIFT-MS compound database is small, and even with the research that has been presented herein, the database requires further expansion. A short summary of suggested research pursuits related to the current applications is now discussed, however many other applications may be pursued.

- The GeoVOC method is currently able to quantitatively detect linear hydrocarbon compounds from C_1 – C_9. It may be of interest to expand this application to include higher mass hydrocarbons that are often found in crude oil.

- Alkyl esters were investigated in chapter 5, however only acyclic, linear, non-saturated compounds were discussed. It may be of interest to research the reactions of the SIFT-MS precursor ions with saturated, branched and cyclic esters as many of these compounds are found in fruits, vegetables and fragrances.

- There is a large scope for expansion in the area of chemical warfare agents. Experimental rate coefficients and product ion branching ratios are yet to be

determined for the three Schedule I CWAs that were discussed in chapter 6. Furthermore, research into many other CWAs that have not been discussed here (such as lewisite, nitrogen mustard and VX) is of interest both commercially and academically. Also, the kinetic parameters of many CWA precursor compounds are yet to be measured and these should be pursued to expand the method.

- Finally, only 17 of the 188 HAPs defined in the US Clean Air Act were discussed in chapter 7. By measuring the rate coefficients and product ion branching ratios for the remaining HAP compounds that are not yet in the SIFT-MS database, the application becomes much more commercially viable.

The SIFT-MS compound database may also be expanded more rapidly by development of a generalisation which, based on an analyte's functional groups, predicts the product ions that may be observed from the reaction of that analyte with a particular precursor ion. A general algorithm of this type, in conjunction with the calculation of collision-limiting rate coefficients, would allow for rapid addition of a compound to the database without the need for measuring experimental rate coefficients and product ion branching ratios. However a general algorithm such as this would yield only semi-quantitative results.

APPENDIX A

DERIVATION OF EQUATIONS 3.12 – 3.16

The derivation which is discussed in this thesis is adapted from chapter 5 of *Transport Properties of Ions in Gases* by Mason and McDaniel. [111]

The basis of momentum-transfer theory, which was developed by Maxwell in 1860, [283] is that the momentum gained by an ion in a field must be balanced by losses through collisions with neutral molecules. Determining the gained momentum is a trivial task, as *eE* (where *e* is the ionic charge and *E* the field strength) is equal to the momentum gained from the field per unit time. However, determining the momentum lost to collision is a much more difficult undertaking. The simplest approach to calculating this parameter is to determine the average energy lost per collision, multiplied by the average number of collisions per unit time and then summed over all possible collisions.

Firstly, we determine ρ, the relative momentum transferred to the gas per collision. This is defined in equation A.01 where v_d is the drift velocity due to the field, μ is the reduced mass of the ion-neutral collision pair and θ is the relative deflection angle of the collision. [111]

$$\rho = \mu\, v_d (1 - \cos\theta) \tag{A.01}$$

Then, the average number of collisions an ion encounters per unit time (usually in seconds) between the angles θ and $\theta + d\theta$ is defined in equation A.02. Here, N is the number density of carrier gas and v_r is the average relative collision velocity, $\sigma(\theta, v_r)$ is the collision cross section.

$$Collision\ \ frequency = N\, v_r\, 2\pi\, \sigma(\theta, v_r) \sin\theta\, d\theta \tag{A.02}$$

Combining A.01 to A.02 and integrating over all deflection angles affords an expression for momentum loss, A.03. This equation determines the overall momentum loss integrated over all collision energies and collision angles.[111]

$$Momentum\ Loss = \mu\, v_d\, N v_r 2\pi \int_0^{\pi} (1 - \cos\theta)\, \sigma(\theta, v_r) \sin\theta\, d\theta \tag{A.03}$$

The expression for momentum loss can be reduced by defining a momentum transfer

cross section Q_D in equation A.04 at a particular energy ε, where ε is defined in equation A.05 as the mean relative energy of a collision.

$$Q_D(\varepsilon) = 2\pi \int_0^{\pi} (1-\cos\theta)\, \sigma(\theta, v_r) \sin\theta\, d\theta \tag{A.04}$$

$$\varepsilon = \frac{1}{2} \mu\, v_r^2 \tag{A.05}$$

Furthermore, the collision frequency $v(\varepsilon)$ for the ion-neutral pair (from equation A.02) can be simplified to equation A.06.

$$v(\varepsilon) = N\, v_r\, Q_D(\varepsilon) \tag{A.06}$$

Therefore a formula can now be written for the momentum balance between the momentum gained from the electric field and then lost to collisions which is defined as equation A.07.

$$eE = \mu\, v_d\, v(\varepsilon) \tag{A.07}$$

By substituting A.06 into A.07, we arrive at an expression for the momentum balance based on the drift velocity v_d and relative collision velocity v_r.

$$eE = \mu\, v_d\, N\, v_r Q_D(\varepsilon) \tag{A.08}$$

Equation A.08 determines the momentum transferred for any ion which is in a carrier gas composed of a single species. However, the current derivation is directed at the mobility and diffusion of ions through mixed carrier gases.

The sum of the momenta transferred to each species in the mixture equals the total momentum transferred. However, the collision frequency of an ion with a pure carrier gas j is not necessarily equal to the collision frequency of the same ion with a mixture of carrier gases. This is because the relative drift velocity is different in each case. A quantity that represents an average in a mixture is defined as "$< >_{mix}$". The momentum-balance equation for an ion in a mix of carrier gases is then defined as equation A.09

$$eE = < v_d >_{mix} \sum_j \mu_j N_j < v_{r,j} >_{mix} Q_{D,j}(< \varepsilon_j >_{mix}) \tag{A.09}$$

If we define χ_j as the mole fraction of the carrier gas j (where $\chi_j = N_j / N$) and $<v_j(\varepsilon_j)>_{mix}$ as the collision frequency of an ion with the carrier gas j in a mixture, A.09 can be simplified to A.10. For the case of the Voice100, j is related to either helium or argon.

$$eE = \langle v_d \rangle_{mix} \sum_j \chi_j \mu_j \langle v_j(\varepsilon_j) \rangle_{mix} \quad \text{(A.10)}$$

As the drift velocity is defined as $v_d = K.E$ (where K is the ionic mobility) and therefore $\langle v_d \rangle_{mix} = K_{mix}.E$, an expression for ionic mobility in a mixture of carrier gases can be found from A.10. [111] This expression is given as equation A.11.

$$\frac{1}{K_{mix}} = \frac{\sum_j \chi_j}{K_j} \frac{\langle v_j(\varepsilon_j) \rangle_{mix}}{v_j(\varepsilon_j)} \quad \text{(A.11)}$$

For the case where the fields are very low, A.11 approximates to Blanc's Law which was shown as equation 3.11. However, it is the diffusion coefficient in a mix of carrier gases which is of interest here and this requires that the temperature of the ions in both the transverse (radial) and longitudinal (axial) directions is known. The temperature in the axial direction is defined as T_A and in the radial direction as T_R.

Skullerud [284] defined these temperatures for a single gas and it is not unreasonable to expand these equations to a mixture, where the mass of the carrier gas in the mixture is defined is $\langle M \rangle_{mix}$ and the drift velocity in the mixture is $\langle v_d \rangle_{mix}$. These expressions are provided as equation A.12 and A.13 where m is the mass of an ion, v is the velocity in the given direction which is either x, y, z or d (the drift velocity) and k_B is Boltzmann's constant.

$$k_B \langle T_A \rangle_{mix} \equiv m\left(v_z^2 - v_z^2\right) \equiv k_B T + \frac{1}{3}\left(\frac{4m + \langle M \rangle_{mix}}{2m + \langle M \rangle_{mix}}\right) \langle M \rangle_{mix} \langle v_d^2 \rangle_{mix} \quad \text{(A.12)}$$

$$k_B \langle T_R \rangle_{mix} \equiv m v_x^2 \equiv m v_y^2 \equiv k_B T + \frac{1}{3}\left(\frac{m + \langle M \rangle_{mix}}{2m + \langle M \rangle_{mix}}\right) \langle M \rangle_{mix} \langle v_d^2 \rangle_{mix} \quad \text{(A.13)}$$

Mason and McDaniel [111] have then suggested an extension to Skullerud's equations which adjust the reduced mass relationship to more accurately reproduce experimental values. These adjusted expressions are given in equation A.14- A.18. [111]

$$\langle T_{R,A} \rangle_{mix} = T + \frac{\langle \zeta_{R,A} \rangle_{mix} \langle M \rangle_{mix} \langle v_d \rangle_{mix}^2 \left(1 + 0.5 \langle \beta_{R,A} \rangle_{mix}\right)}{k_B} \quad \text{(A.14)}$$

$$\langle \zeta_R \rangle_{mix} = \frac{0.85(m + \langle M \rangle_{mix})}{4m + 3(0.85)\langle M \rangle_{mix}} \quad \text{(A.15)}$$

$$<\zeta_A>_{mix}=\frac{4m-0.85(2m-<M>_{mix})}{4m+3(0.85)<M>_{mix}} \tag{A.16}$$

$$<\beta_R>_{mix}\approx 0 \tag{A.17}$$

$$<\beta_A>_{mix}\approx\frac{m}{m+<M>_{mix}}+\frac{m<M>_{mix}}{(m+<M>_{mix})^2} \tag{A.18}$$

The Nernst-Townsend-Einstein relationship was discussed in chapter 3 and presented as equation 3.05. Einstein expanded on equation 3.05 and defined what is now known as the Generalised Einstein Relationship (GER). The GER takes advantage of the fact that $v_d = K.E$. This equation is presented as equation A.19, where $D_{R,A}$ is the diffusion coefficient in either the radial or axial direction. [111]

$$D_{(R,A)}=\frac{k_B T_{R,A}}{e}\left(\frac{dv_d}{dE}\right)_{R,A} \tag{A.19}$$

In a mixture of carrier gases, equation A.19 becomes equation A.20.

$$<D_{(R,A)}>_{mix}=\frac{k_B<T_{R,A}>_{mix}}{e}\left(\frac{d<v_d>_{mix}}{dE}\right)_{R,A} \tag{A.20}$$

By then rearranging equation A.20 and substituting into equation A.11, the diffusion coefficients in either the axial or radial directions can be found for a specific temperature. This equation is shown as equation A.21, where γ_R is 0, γ_A is 1.

$$\frac{<T_{R,A}>_{mix}}{<D_{R,A}>_{mix}}(1+0.5\gamma_{R,A})=\sum_j \chi_j\frac{(T_{R,A})_j}{(D_{R,A})_j}\frac{<v_j>_{mix}}{v_j}(1+0.5\gamma_{R,A}) \tag{A.21}$$

Equation A.21 is the same equation reported in chapter 3 as equation 3.12.

APPENDIX B

ANALYTICAL SOLUTIONS TO THE $H_3O^+.(H_2O)_n$ INTEGRATED RATE LAWS

Consider the following reactions B.01-B.07 and their respective rate coefficients:

$H_3O^+ + H_2O$	→	$H_3O^+.H_2O$	k_0	(B.01)
$H_3O^+.H_2O + H_2O$	→	$H_3O^+.(H_2O)_2$	k_1	(B.02)
$H_3O^+.(H_2O)_2 + H_2O$	→	$H_3O^+.(H_2O)_3$	k_2	(B.03)
$H_3O^+ + A$	→	Products	k_{A0}	(B.04)
$H_3O^+.H_2O + A$	→	Products	k_{A1}	(B.05)
$H_3O^+.(H_2O)_2 + A$	→	Products	k_{A2}	(B.06)
$H_3O^+.(H_2O)_3 + A$	→	Products	k_{A3}	(B.07)

The pseudo-first order rate equations for the decay in concentration of H_3O^+, $H_3O^+.H_2O$, $H_3O^+.(H_2O)_2$ and $H_3O^+.(H_2O)_3$ are then defined as equations B.08-B.11.

$$\frac{d[H_3O^+]}{dt} = -k_{A0}[H_3O^+] - k_0[H_3O^+] \tag{B.08}$$

$$\frac{d[H_3O^+.H_2O]}{dt} = -k_{A1}[H_3O^+.H_2O] - k_1[H_3O^+.H_2O] + k_0[H_3O^+] \tag{B.09}$$

$$\frac{d[H_3O^+.(H_2O)_2]}{dt} = -k_{A2}[H_3O^+.(H_2O)_2] - k_2[H_3O^+.(H_2O)_2] + k_1[H_3O^+.H_2O] \tag{B.10}$$

$$\frac{d[H_3O^+.(H_2O)_3]}{dt} = -k_{A3}[H_3O^+.(H_2O)_3] + k_2[H_3O^+.(H_2O)_2] \tag{B.11}$$

If the initial H_3O^+ intensity detectable before addition of water or analyte is R_0, the above equations can be solved for each of the four water cluster concentrations, where $W = [H_2O]$ and $A = [A]$. These equations are presented as equations B.12-B.15.

$$[H_3O^+] = e^{-t\,(A\,kA0+k0\,W)}\,Ro \tag{B.12}$$

$$[H_3O^+.H_2O] = -\frac{(e^{-t\,(A\,kA0+k0\,W)} - e^{-t\,(A\,kA1+k1\,W)})\,k0\,Ro\,W}{A\,(kA0-kA1)+(k0-k1)\,W} \tag{B.13}$$

$$[H_3O^+.(H_2O)_2] = \frac{\begin{array}{l}(e^{-t\,(A\,(kA0+kA1+kA2)+(k0+k1+k2)\,W)}\,k0\,k1\,Ro\,W^2\\ \quad(A\,(e^{t\,(A\,(kA0+kA1)+(k0+k1)\,W)}\,(kA0-kA1)+e^{t\,(A\,(kA1+kA2)+(k1+k2)\,W)}\,(kA1-kA2)+e^{t\,(A\,(kA0+kA2)+(k0+k2)\,W)}\,(-kA0+kA2))+\\ \quad\quad(e^{t\,(A\,(kA0+kA1)+(k0+k1)\,W)}\,(k0-k1)+e^{t\,(A\,(kA1+kA2)+(k1+k2)\,W)}\,(k1-k2)+e^{t\,(A\,(kA0+kA2)+(k0+k2)\,W)}\,(-k0+k2))\,W))\end{array}}{\begin{array}{l}((A\,(kA0-kA1)+(k0-k1)\,W)\,(A\,(kA0-kA2)+(k0-k2)\,W)\\ \quad(A\,(kA1-kA2)+(k1-k2)\,W))\end{array}} \tag{B.14}$$

$$[H_3O^+.(H_2O)_3] = \frac{\begin{array}{l}-(e^{-A\,kA3\,t}\,k0\,k1\,k2\,Ro\,W^3\\ \quad(A^3\,(kA0^2\,((-1+e^{-t\,(A\,kA2-A\,kA3+k2\,W)})\,kA1+kA2-e^{-t\,(A\,kA1-A\,kA3+k1\,W)}\,kA2+(e^{-t\,(A\,kA1-A\,kA3+k1\,W)}-e^{-t\,(A\,kA2-A\,kA3+k2\,W)})\,kA3)+\\ \quad\quad e^{-t\,(A\,(2\,kA0+kA1+kA2-3\,kA3)+(2\,k0+k1+k2)\,W)}\,(-e^{t\,(A\,(2\,kA0+kA1+kA2-3\,kA3)+(2\,k0+k1+k2)\,W)}\,kA1\,(kA1-kA2)\,kA2+\\ \quad\quad\quad e^{t\,(A\,(kA0+kA1+kA2-2\,kA3)+(k0+k1+k2)\,W)}\,(kA1-kA2)\,(kA1-kA3)\,(kA2-kA3)+e^{t\,(A\,(2\,kA0+kA1-2\,kA3)+(2\,k0+k1)\,W)}\,kA1\\ \quad\quad\quad(kA1-kA3)\,kA3-e^{t\,(A\,(2\,kA0+kA2-2\,kA3)+(2\,k0+k2)\,W)}\,kA2\,(kA2-kA3)\,kA3)+kA0\,((1-e^{-t\,(A\,kA2-A\,kA3+k2\,W)})\,kA1^2+\\ \quad\quad(-1+e^{-t\,(A\,kA1-A\,kA3+k1\,W)})\,kA2^2+(-e^{-t\,(A\,kA1-A\,kA3+k1\,W)}+e^{-t\,(A\,kA2-A\,kA3+k2\,W)})\,kA3^2))+\\ \quad A^2\,(e^{-t\,(A\,(kA0+kA1-2\,kA3)+(k0+k1)\,W)}\,k2\,(e^{t\,(A\,(kA0+kA1-2\,kA3)+(k0+k1)\,W)}\,(kA0-kA1)\,(kA0+kA1-2\,kA2)-\\ \quad\quad e^{t\,(A\,(kA0-kA3)+k0\,W)}\,(kA0-kA3)\,(kA0-2\,kA2+kA3)+e^{t\,(A\,(kA1-kA3)+k1\,W)}\,(kA1-kA3)\,(kA1-2\,kA2+kA3))+\\ \quad\quad e^{-t\,(A\,(kA1+kA2-2\,kA3)+(k1+k2)\,W)}\,k0\,(e^{t\,(A\,(kA1+kA2-2\,kA3)+(k1+k2)\,W)}\,(kA1-kA2)\,(-2\,kA0+kA1+kA2)-\\ \quad\quad\quad e^{t\,(A\,(kA1-kA3)+k1\,W)}\,(kA1-kA3)\,(-2\,kA0+kA1+kA3)+e^{t\,(A\,(kA2-kA3)+k2\,W)}\,(kA2-kA3)\,(-2\,kA0+kA2+kA3))+\\ \quad\quad e^{-t\,(A\,(kA0+kA2-2\,kA3)+(k0+k2)\,W)}\,k1\,(-e^{t\,(A\,(kA0+kA2-2\,kA3)+(k0+k2)\,W)}\,(kA0-kA2)\,(kA0-2\,kA1+kA2)+\\ \quad\quad\quad e^{t\,(A\,(kA0-kA3)+k0\,W)}\,(kA0-kA3)\,(kA0-2\,kA1+kA3)-e^{t\,(A\,(kA2-kA3)+k2\,W)}\,(kA2-kA3)\,(-2\,kA1+kA2+kA3)))\,W+\\ \quad A\,(k1^2\,kA0-k2^2\,kA0-2\,k0\,k1\,(kA0-kA1)+2\,e^{-t\,(A\,(kA2-kA3)+k2\,W)}\,k0\,k1\,(kA0-kA1)-k0^2\,kA1-\\ \quad\quad 2\,k1\,k2\,kA1+k2^2\,kA1+2\,k0\,k2\,(kA0-kA2)-2\,e^{-t\,(A\,(kA1-kA3)+k1\,W)}\,k0\,k2\,(kA0-kA2)+\\ \quad\quad k0^2\,kA2-k1^2\,kA2+2\,k1\,k2\,kA2+e^{-t\,(A\,(kA2-kA3)+k2\,W)}\,(k0^2\,(kA1-kA3)+k1^2\,(-kA0+kA3))+\\ \quad\quad e^{-t\,(A\,(kA0-kA3)+k0\,W)}\,(2\,k1\,k2\,(kA1-kA2)+k1^2\,(kA2-kA3)+k2^2\,(-kA1+kA3))+\\ \quad\quad e^{-t\,(A\,(kA1-kA3)+k1\,W)}\,(k2^2\,(kA0-kA3)+k0^2\,(-kA2+kA3)))\,W^2+\\ \quad(e^{-t\,(A\,kA0+k0\,W)}\,(e^{A\,kA3\,t}-e^{A\,kA0\,t+k0\,t\,W})\,k1\,(k1-k2)\,k2+k0^2\,((-1+e^{-t\,(A\,kA2-A\,kA3+k2\,W)})\,k1+k2-e^{-t\,(A\,kA1-A\,kA3+k1\,W)}\,k2)+\\ \quad\quad k0\,((1-e^{-t\,(A\,kA2-A\,kA3+k2\,W)})\,k1^2+(-1+e^{-t\,(A\,kA1-A\,kA3+k1\,W)})\,k2^2))\,W^3))\end{array}}{\begin{array}{l}((A\,(kA0-kA3)+k0\,W)\,(A\,(kA0-kA1)+(k0-k1)\,W)\,(A\,(kA1-kA3)+k1\,W)\\ \quad(A\,(kA0-kA2)+(k0-k2)\,W)\\ \quad(A\,(kA1-kA2)+(k1-k2)\,W)\\ \quad(A\,(kA2-kA3)+k2\,W))\end{array}} \tag{B.15}$$

The above solutions are outputs from a Mathematica file in which the 'dsolve' and 'simplify' function have been used. By then assuming values of k_n, k_{An}, $[H_2O]$, and R_0 across a range of $[A]$ values, the observable reaction rate coefficient k_{eff} can be calculated. Conversely, where the values of k_n and k_{eff} are known, the 'solver' function in Excel can be employed to determine the actual values of k_{An} as per the method discussed in section 3.4

REFERENCES

[1] P. Spanel and D. Smith. *Med. & Biol. Eng. & Comp.*, **34**:409-419, 1996.

[2] N.G. Adams and D. Smith in *Techniques for the Study of Ion/Molecule Reactions*. J. Wiley and Sons, New York, Vol 4, p.165-220, 1988.

[3] A.L. Schmeltekopf and H.P. Broida. *J. Chem. Phys.*, **39**:1261-1268, 1963.

[4] P.H. Dawson. *Quadrupole Mass Spectrometry*. Elsevier Science, Amsterdam, 1976.

[5] E.E. Ferguson, F.C. Fehsenfeld, and A.L. Schmeltekopf in *Advances in Atomic and Molecular Physics*, Academic Press, New York, Vol. 5, p. 1-56, 1969.

[6] F.C. Fehsenfeld, A.L. Schmeltekopf, P.D. Goldan, H.I. Schiff, and E.E. Ferguson. *J. Chem. Phys.*, **44**(11):4087-4094, 1966.

[7] P.D. Goldan, A.L. Schmeltekopf, F.C. Fehsenfeld, H.I. Schiff, and E.E. Ferguson. *J. Chem. Phys.*, **44**(11):4095-4103, 1966.

[8] F.C. Fehsenfeld, E.E. Ferguson, and A.L. Schmeltekopf. *J. Chem. Phys.*, **45**(5): 1844-1845, 1966.

[9] J.A. Burt, J.L. Dunn, M.J. McEwan, M.M. Sutton, A.E. Roche, and H.I. Schiff. *J. Chem. Phys.*, **52**(12):6062-6075, 1970.

[10] N.G. Adams, M.J. Church, and D. Smith. *J. Phys. D: Appl. Phys.*, **8**:1409-1422, 1975.

[11] M.J. McEwan in *Advances in Gas Phase Ion Chemistry*, N.G. Adams, L.M. Babcock (Eds.), J.A.I. Press, Greenwich, Vol. 1, p. 1, 1992.

[12] R.N. Bhave and R. Cooper, *Aust. J. Phys.*, **48**:503-513, 1995.

[13] M. Numano, J.R. Cussenot, M. Fabry, and M. Felden. *J Quant. Spectrosc. Rad.*, **15**:1007-1016, 1975.

[14] N.G. Adams and D. Smith. *Int. J. Mass Spectrom. Ion Phys.*, **21**:349-359, 1976.

[15] P.M. Solomon and W. Klemperer. *Astrophys. J.*, **178**:389-421, 1972.

[16] E. Herbst and W. Klemperer. *Astrophys. J.*, **185**:505-533, 1973.

[17] D. Smith and N.G. Adams. *Mon. Not. R. Astr. Soc.*, **197**:377-384, 1981.

[18] A.A. Viggiano, F. Howorka, D.L. Albritton, F.C. Fehsenfeld, N.G. Adams, and D. Smith. *Astrophys. J.*, **236**:492-497, 1980.

[19] G.I. Mackay, G.D. Vlachos, D.K. Bohme, and H.I. Schiff. *Int. J. Mass Spectrom. Ion Phys.*, **36**:259-270, 1980.

[20] D. Smith and N.G. Adams. *Adv. Atom. Mole. Phys.*, **24**:1-49, 1988.

[21] V.N. Fishman and J.J. Grabowski. *Int. J. Mass Spectrom.*, **177**:175-186, 1998.

[22] D.B. Milligan, D.A. Fairley, C.G. Freeman, and M.J. McEwan. *Int. J. Mass Spectrom.*, **202**:351-361, 2000.

[23] A.A. Viggiano and J.F. Paulson. *J. Chem. Phys.*, **79**:2241-2245, 1983..

[24] C.H. DePuy, J.M. Van Doren, S. Gronert, S.R. Kass, E.L. Motell, G.B. Ellison, and V.M. Bierbaum. *J. Org. Chem.*, **54**:1864-1850, 1989.

[25] R.J. Shul, R. Passarella, B.L. Upschulte, R.G. Keesee, and A.W. Castleman Jr. *J. Chem. Phys.*, **86**(8):4446-4451, 1987.

[26] M. Lin and J.J. Grabowski. *Int. J. Mass Spectrom.*, **237**:149-165, 2004.

[27] G.K. Koyanagi, V.I. Baranov, S.D. Tanner, and D.K. Bohme. *J. Anal. At. Spectrom.*, **15**:1207-1210, 2000.

[28] G.K. Koyanagi, V.I. Baranov, S.D. Tanner, J. Anichnia, M.Y. Jarvis, S. Feil, and D.K. Bohme. *Int. J. Mass Spectrom.*, **265**:295-301, 2007.

[29] P. Spanel and D. Smith. *J. Chem. Phys.*, **104**(5):1893-1899, 1996.

[30] S.G. Lias, "Ionization Energy Evaluation" in **NIST Chemistry WebBook, NIST Standard Reference Database Number 69**, Eds. P.J. Linstrom and W.G. Mallard, June 2005, National Institute of Standards and Technology, Gaithersburg MD, 20899 (http://webbook.nist.gov).

[31] E.P. Hunter and S.G. Lias, "Proton Affinity Evaluation" in **NIST Chemistry WebBook, NIST Standard Reference Database Number 69**, Eds. P.J. Linstrom and W.G. Mallard, June 2005, National Institute of Standards and Technology, Gaithersburg MD, 20899 (http://webbook.nist.gov).

[32] Y. Ikezoe, S. Matsuoka, M. Takebe, and A.A. Viggiano. *Gas Phase Ion-Molecule Reaction Rate Constants Through 1986*. Ion Reaction Research Group of the Mass Spectrometry Society of Japan, 1986.

[33] P. Spanel and D. Smith. *Int. J. Mass Spectrom. Ion Proc.*, **167/168**:375-388,1997.

[34] P. Spanel, Y. Ji, and D. Smith. *Int. J. Mass Spectrom. Ion Proc.*, **165/166**:25-37, 1997.

[35] P. Spanel and D. Smith. *Int. J. Mass Spectrom.*, **181**:1-10, 1998.

[36] P. Spanel and D. Smith. *Int. J. Mass Spectrom.*, **172**:137-147, 1998.

[37] P.F. Wilson, *Experimental Studies of Gas-Phase Ion-Molecule Reactions*, Ph.D. Thesis, University of Canterbury, New Zealand, 1994.

[38] R.A. Kennedy, C.A. Mayhew, R. Thomas, and P. Watts. *Int. J. Mass Spectrom.*, **223/224**:627-637, 2003.

[39] D. Smith and P. Spanel. *Mass Spec. Rev.*, **24**:661-700, 2005.

[40] P. Spanel, S. Davies, and D. Smith. *Rapid Commun. Mass. Spectrom.*, **12**:763-766, 1998.

[41] P. Spanel, S. Davies, and D. Smith. *Rapid. Commun. Mass. Spectrom.*, **13**:1733-1738, 1999.

[42] A.M. Diskin, P. Spanel, and D. Smith. *Physiol. Measure.*, **24**:191-199, 2003.

[43] W. Cao and Y. Duan. *Clin. Chem.*, **52**(5):800-811, 2006.

[44] S. Davies, P. Spanel, and D. Smith. *Nephrology Dialysis Transplant*, **16**:836-839, 2001.

[45] P. Spanel, A.M. Diskin, S.M. Abbott, T. Wang, and D. Smith. *Rapid. Commun. Mass. Spectrom*., **16**:2148-2153, 2002.

[46] R.A. Allardyce, V.S. Langford, A.L. Hill, and D.R. Murdoch. *J. Microbiol. Methods*, **65**:361-365, 2006.

[47] J.M. Scotter, R.A. Allardyce, V.S. Langford, A. Hill, and D.R. Murdoch. *J. Microbiol. Methods*, **65**:628-631, 2006.

[48] D. Smith, P. Cheng, and P. Spanel. *Rapid. Commun. Mass. Spectrom.*, **16**:1124-1134, 2002.

[49] D. Smith, P. Spanel, D. Dabill, J. Cocker, and B. Rajan. *Rapid. Commun. Mass. Spectrom.*, **18**:2830-2838, 2004.

[50] W.K. Anger, L. Moody, J. Burg, W.S. Brightwell, B.J. Taylor, J.M. Russo, N. Dickerson, J.V. Setzer, B.L. Johnson, and K. Hicks. *Neurotoxicology*, **7**(3):137-156, 1986.

[51] G.J. Francis, D.B. Milligan and M.J. McEwan. *J. Phys. Chem. A*, **111**:9670-9679, 2007.

[52] R.C. Bolden, R.S. Hemsworth, M.J. Shaw, and N.D. Twiddy. *J. Phys. B: Atom. Molec. Phys.*, **3**:45-60, 1970.

[53] P. Spanel, K. Dryahina, and D. Smith. *Int. J. Mass Spectrom.*, **249/250**:230-239, 2006.

[54] C.G. Freeman and M.J. McEwan. *Aust. J. Chem.*, **55**:491-494, 2002.

[55] V.G. Anicich. *An Index of the Literature for Bimolecular Gas Phase Cation-Molecule Reaction Kinetics*, JPL Publication 03-19. NASA, November 2003.

[56] W.M.A. Niessen. *Current Practice of Gas Chromatography - Mass Spectrometry*, Chromatographic Science Series. Marcel Dekker, New York, Vol. 86, 2001.

[57] I. Lavagnini and F. Magno. *Mass Spec. Rev.*, **26**:1-18, 2007.

[58] D.B. Milligan, G.J. Francis, B.J. Prince, and M.J. McEwan. *Anal. Chem.*, **79**:2537-2540, 2007.

[59] D.A. Skoog. *Principles of Instrumental Analysis.* Saunders College Publishing, Philadelphia, PA, USA, 3rd edition, 1985.

[60] G.L. Long, E.G. Voigtman, M.A. Kosinski, and J.D. Winefordner. *Anal. Chem.*, **55**:1432-1434, 1983.

[61] D.K. Bohme. *The Kinetics and Energetics of Proton Transfer*, in *NATO Adv. Study Inst. Ion Molecule Interaction*, Plenum Press, p. 489-504, 1975.

[62] S.G. Lias, J.E. Bartmess, J.F. Liebman, J.L. Holmes, R.D. Levin, and W.G. Mallard. *J. Phys. Chem. Ref. Data*, **17**:1-861, 1988.

[63] E.P.L. Hunter and S.G. Lias. *J. Phys. Chem. Ref. Data*, **27**(3):413-656, 1998.

[64] M. Meot ner (Mautner). *Int. J. Mass Spectrom.*, **227**:525-554, 2003.

[65] D. Smith, T. Wang, and P. Spanel. *Int. J. Mass Spectrom.*, **230**:1-9, 2003.

[66] S.T. Arnold, A.A. Viggiano, and R.A. Morris. *J. Phys. Chem. A*, **102**:8881-8887, 1998.

[67] V.G. Anicich and W.T. Huntress Jr. *Astrophys. J. Suppl. Ser.*, **62**:553-672, 1986.

[68] D.R. Bates and E. Herbst. *Radiative Association* in *Reaction Rate Coefficients in Astrophysics*, T.J. Miller and D.A. Williams (Eds), Reidel, Dordrecht, 1988.

[69] A. Gapeev and R.C. Dunbar. *J. Am. Soc. Mass Spectrom.*, **13**:477-484, 2002.

[70] M. M. Meot-Ner (Mautner) and S. G. Lias, "Binding Energies Between Ions and Molecules, and The Thermochemistry of Cluster Ions" in **NIST Chemistry WebBook, NIST Standard Reference Database Number 69**, Eds. P.J. Linstrom and W.G. Mallard, June 2005, National Institute of Standards and Technology, Gaithersburg MD, 20899 (http://webbook.nist.gov).

[71] P. Spanel and D. Smith. *Rapid Commun. Mass. Spectrom.*, **14**:1896-1906, 2000.

[72] J.S. Knight, *Selected Ion Flow Tube Studies of Some Gaseous Ion-Molecule Reactions*, Ph.D. Thesis, University of Canterbury, New Zealand, 1986.

[73] S.A.H. Petrie, *A Selected Ion Flow Tube Study of Some Gas-Phase Ion-Molecule Reactions of Relevance to the Chemistry of Dense Interstellar Clouds*, Ph.D. Thesis, University of Canterbury, New Zealand, 1991.

[74] G.B.I. Scott, *Experimental Studies of Astronomical Ion-Atom and Ion-Molecule Reactions*, Ph.D. Thesis, University of Canterbury, New Zealand, 1997.

[75] D.A. Fairley, *Selected Ion Flow Tube Drift Tube (SIFDT) Studies of Reactive Ion-Neutral Encounters*, Ph.D. Thesis, University of Canterbury, New Zealand, 1998.

[76] D.B. Milligan, *Selected Reactions of Ions and Molecules in a Flowing Afterglow Selected Ion Flow/Drift Tube (FA-SIFDT)*, Ph.D. Thesis, University of Canterbury, New Zealand, 2000.

[77] D. Smith and N.G. Adams. *J. Phys. D: Appl. Phys.*, **13**:1267-1273, 1980.

[78] J.M. Van Doren, S.E. Barlow, C.H. DePuy, and V.M. Bierbaum. *Int. J. Mass Spectrom. Ion Proc.*, **81**:85-100, 1987.

[79] F.C. Fehsenfeld, K.M. Evenson, and H.P. Broida. *NBS Report 8701*, US National Bureau of Standards Report, November 1964.

[80] G. Dupeyrat, B.R. Rowe, D.W. Fahey, and D.L. Albritton. I*nt. J. Mass Spectrom. Ion Phys.*, **44**:1-18, 1982.

[81] B.L. Upschulte, R.J. Shul, R. Passarella, R.G. Keese, and A.W. Castleman Jr. *Int. J. Mass Spectrom. Ion Proc.*, **75**:27-45, 1987.

[82] P. Spanel, E.F.H. Hall, C.T. Workman, and D. Smith. *Plasma Sources Sci. Technol.*, **13**:282-284, 2004.

[83] P. Spanel, K. Dryahina, D.Smith, *Int. J. Mass Spectrom.* **267**:117-124, 2007.

[84] P. Rummel and T.A. Grotjohn. *J. Vac. Sci. Technol. A*, **20**(2):536-543, 2002.

[85] W.M. Brubaker in *Advances in Mass Spectrometry*, Elsevier Science, England, Vol. 6, p. 293, 1968.

[86] R.E. Pedder, *Fundamental studies in Quadrupole Ion Trap Mass Spectrometry,* Ph.D. Thesis, University of Florida, USA 1992.

[87] R.E. Pedder, *Practical quadrupole theory: Quadrupole acceptance characteristics* in Proceedings of the 52nd ASMS Conference on Mass Spectrometry and Allied Topics, May 2004.

[88] R.E. March and J.F.J. Todd, (Eds). *Practical Aspects of Ion Trap Mass Spectrometry: Fundamentals*. CRC Press, Boca Raton, FL, USA, Vol. 1, 1995.

[89] N. Rott. *Ann. Rev. Fluid Mech.*, **22**:1-11, 1990.

[90] J.V. Seeley, J.T. Jayne, and M.J. Molina. *J. Phys. Chem.*, **100**:4019-4025, 1996.

[91] C.E. Kolb, J.T. Jayne, D.R. Worsnop, M.J. Molina, R.F. Meads, and A.A. Viggiano. *J. Am. Chem. Soc.*, **116**:10314-10315, 1996.

[92] A.E. O'Keefe and G.C. Ortman. *Anal. Chem.*, **38**:760-763, 1966.

[93] F.P. Scaringelli, A.E. O'Keefe, E. Rosenburg, and J.P. Bell. *Anal. Chem.*, **42**:871-876, 1970.

[94] VICI Metronics Inc., Poulsbo, WA, USA. *Generating Calibration Gas Standards,* 2004. (http://www.vici.com)

[95] V.N. Fishman and J.J. Grabowski. *J. Phys. Chem. A*, **103**:4879-4884, 1999.

[96] J.W. Ochterski, G.A. Petersson, and J.A. Montgomery Jr. *J. Chem. Phys.*, **104**(7): 2598-2619, 1996.

[97] J.A. Montgomery Jr., M.J. Frisch, J.W. Ochterski, and G.A. Petersson. *J. Chem. Phys.*, **112**(15):6532-6542, 2000.

[98] G.A. Petersson and M.J. Frisch. *J. Phys. Chem. A*, **104**:2183-2190, 2000.

[99] L.A. Curtiss, K. Raghavachari, and J.A. Pople. *J. Chem. Phys.*, **98**(5):1293-1298, 1993.

[100] L.A. Curtiss, P.C. Redfern, B.J. Smith, and L. Radom. *J. Chem. Phys.*, **104**(13): 5148-5152, 1996.

[101] L.A. Curtiss, K. Raghavachari, P.C. Redfern, V. Rassolov, and J.A. Pople. *J. Chem. Phys.*, **109**(18):7764-7776, 1998.

[102] L.A. Curtiss, P.C. Redfern, K. Raghavachari, V. Rassolov, and J.A. Pople. *J. Chem. Phys.*, **110**(10):4703-4709, 1999.

[103] L.A. Curtiss, P.C. Redfern, K. Raghavachari, and J.A. Pople. *J. Chem. Phys.*, **114**(1):108-117, 2001.

[104] L.A. Curtiss, P.C. Redfern, K. Raghavachari, and J.A. Pople. *Chem. Phys. Let.*, **358**:390-396, 2002.

[105] L.A. Curtiss, P.C. Redfern, and K. Raghavachari. *J. Phys. Chem.*, **123**:124107-124119, 2005.

[106] L.A. Curtiss, P.C. Redfern, and K. Raghavachari. *J. Chem. Phys.*, **126**:84108-84120, 2007.

[107] T. Su and W.J. Chesnavich. *J. Chem. Phys.*, **76**(10):5183-5185, 1982.

[108] T. Su. *J. Chem. Phys.*, **88**:5355, 1988.

[109] *Gaussian 03*, Revision C.02, M.J. Frisch, G.W. Trucks, H.B. Schlegel, G.E. Scuseria, M.A. Robb, J.R. Cheeseman, J.A. Montgomery, Jr., T.Vreven, K.N. Kudin, J.C. Burant, J.M. Millam, S.S. Iyengar, J. Tomasi, V. Barone, B. Mennucci, M. Cossi, G. Scalmani, N. Rega, G.A. Petersson, H. Nakatsuji, M. Hada, M. Ehara, K. Toyota, R. Fukuda, J. Hasegawa, M. Ishida, T. Nakajima, Y. Honda, O. Kitao, H. Nakai, M. Klene, X. Li, J.E. Knox, H.P. Hratchian, J.B. Cross, V. Bakken, C. Adamo, J. Jaramillo, R. Gomperts, R.E. Stratmann, O. Yazyev, A.J. Austin, R. Cammi, C. Pomelli, J.W. Ochterski, P.Y. Ayala, K. Morokuma, G.A. Voth, P. Salvador, J.J. Dannenberg, V.G. Zakrzewski, S. Dapprich, A.D. Daniels, M.C. Strain, O. Farkas, D.K. Malick, A.D. Rabuck, K. Raghavachari, J.B. Foresman, J.V. Ortiz, Q. Cui, A.G. Baboul, S. Clifford, J. Cioslowski, B.B. Stefanov, G. Liu, A. Liashenko, P. Piskorz, I. Komaromi, R.L. Martin, D.J. Fox, T. Keith, M.A. Al-Laham, C.Y. Peng, A. Nanayakkara, M. Challacombe, P.M.W. Gill, B. Johnson, W. Chen, M.W. Wong, C. Gonzalez, and J.A. Pople, Gaussian, Inc., Wallingford CT, 2004.

[110] D. Smith and P. Spanel in *Experimental Methods in the Physical Sciences*. Academic Press Inc., Vol. 29A, p. 273-298, 1995.

[111] E.A. Mason and E.W. McDaniel. *Transport Properties of Ions in Gases*. John Wiley and Sons, New York, 1988.

[112] R.W. Barber and D.R. Emerson. *A numerical investigation of low reynolds number gaseous slip flow at the entrance of circular and parallel plate micro-channels.* ECCOMAS, Computational Fluid Dynamics Conference, September 2001.

[113] G.A. Eiceman and Z. Karpas. *Ion Mobility Spectrometry*. CRC Press, 2nd edition, 2005.

[114] J. Panda. *J. Fluid Mech.*, **378**:71-96, 1999.

[115] P. Spanel and D. Smith. *J. Am. Soc. Mass Spectrom.*, **12**:863-872, 2001.

[116] K.V. Wood, A.H. Grange, and J.W. Taylor. *Anal. Chem.*, **50**:1652-1654, 1978.

[117] P. Coxon and G. Canadas. *Int. J. Mass Spectrom. Ion Phys.*, **37**:177-183, 1981.

[118] J. Renn. *Ann. Phys. Leipzig*, **14**:23-37, 2005.

[119] H.W. Ellis, R.Y. Pai, E.W. McDaniel, E.A. Mason, and L.A. Viehland. *Atom. Data Nucl. Data Tables*, **17**:177-210, 1976.

[120] L.A. Viehland, E.A. Mason, W.F. Morrison, and M.R. Flannery. *Atom. Data Nucl. Data Tables*, **16**:495-514, 1975.

[121] K. Dryahina and P. Spanel. *Int. J. Mass Spectrom.*, **244**:148-154, 2005.

[122] D.R. Lide, (Ed.) *CRC Handbook of Chemistry and Physics*. CRC Press, 86th edition, 2006.

[123] J.A. de Gouw, M. Krishnamurthy, V.M. Bierbaum, and S.R. Leone. *Int. J. Mass Spectrom. Ion Proc.*, **167/168**:281-289, 1997.

[124] J.H. Whealton, E.A. Mason, and R.E. Robson. *Phys. Rev. A*, **9**(2):1017-1020, 1974.

[125] D.B. Milligan, P.F. Wilson, C.G. Freeman, M. Meot ner (Mautner), and M.J. McEwan. *J. Phys. Chem. A*, **106**:9745- 9755, 2002.

[126] A.J. Midey, S. Williams, S.T. Arnold, and A.A. Viggiano. *J. Phys. Chem. A*, **106**:11726-11738, 2002.

[127] V. G. Anicich, *J. Phys. Chem. Ref. Data*, **22**:1469-1562 ,1993.

[128] S.T. Arnold, J.M. Thomas, and A.A. Viggiano. *Int. J. Mass Spectrom.*, **179/180**:243-251, 1998.

[129] P. Spanel and D. Smith, *Int. J. Mass Spectrom. Ion Proc.*, **176**:167-176, 1998.

[130] V.M. Bierbaum, M.F. Golde, and F. Kaufman. *J. Chem. Phys.*, **65**(1):2715-2724, 1976.

[131] D.Smith, A.M. Diskin, Y. Ji, and P. Spanel, *Int. J. Mass Spectrom.*, **209**:81-97, 2001.

[132] Daniel Milligan, Private Communication.

[133] L.A. Viehland and E.A. Mason. *Atom. Data Nucl. Data Tables*, **60**:37-95, 1995.

[134] C.E. Young, D. Edelson, and W.E. Falconer. *J. Chem. Phys.*, **53**(11):4295-4302, 1970.

[135] A. Good, D.A. Durden, and P. Kebarle. *J. Chem. Phys.*, **52**(1):212-221, 1970.

[136] A. Good, D.A. Durden, and P. Kebarle. *J. Chem. Phys.*, **52**(1):222-229, 1970.

[137] A.A. Viggiano, F. Dale, and J.F. Paulson. *J. Chem. Phys.*, **88**(4):2469-2477, 1988.

[138] X. Yang, X. Zhang, A.W. Castleman Jr. *Int. J. Mass Spectrom. Ion Proc.*, **109**:33-354, 1991.

[139] E.W. Owen. *Trek of the Oil Finders: A History of Exploration for Petroleum.* The American Association of Petroleum Geologists, Tulsa, Oklahoma, USA, 1975.

[140] C.F. Conaway. *The Petroleum Industry: A Non-technical Guide.* PennWell, Tulsa, Oklahoma, USA, 1999.

[141] B.P. Tissot and D.H. Welte. *Petroleum Formation and Occurrence.* Springer-Verlag, Berlin, Germany, 2nd edition, 1984.

[142] M.A. Abrams in *Hydrocarbon Migration and its Near Surface Expression*, D. Schmacher and M.A. Abrams (Eds.), AAPG, Tulsa, Oklahoma, USA, Memoir 66, Chapter 1, 1996.

[143] M.D. Matthews in *Hydrocarbon Migration and its Near Surface Expression*, D. Schmacher and M.A. Abrams (Eds.), AAPG, Tulsa, Oklahoma, USA, Memoir 66, Chapter 11, 1996.

[144] J. Toth in *Hydrocarbon Migration and its Near Surface Expression*, D. Schmacher and M.A. Abrams (Eds.), AAPG, Tulsa, Oklahoma, USA, Memoir 66, Chapter 20, 1996.

[145] J. Thrasher, A.J. Fleet, S.J. Hay, M. Hovland, and S. Duppenbecker in *Hydrocarbon Migration and its Near Surface Expression*, D. Schmacher and M.A. Abrams (Eds.), AAPG, Tulsa, Oklahoma, USA, Memoir 66, Chapter 17,1996.

[146] D. Schumacher. *The Leading Edge*, **March 2000**:258-261, 2000.

[147] L.M. Dowling, C.J. Boreham, J.M. Hope, A.P. Murray, and R.E. Summons. *Org, Geochem.*, **23**:729-737, 1995.

[148] O.K. Bazhenova, O.A. Arefiev, and E.B. Frolov. *Org, Geochem.*, **29**:421-428, 1998.

[149] Z. Berger. *Satellite Hydrocarbon Exploration: Interpretation and Integration Techniques.* Springer-Verlag, Berlin, Germany, 1994.

[150] M.J. Davidson. *Oil & Gas Journal*, **102**(23):35-38, 2004.

[151] D.M. Richers, V.T. Jones, M.D. Matthews, J. Maciolek, R.J. Pirkle, and W.C. Sidle. *Am. Assoc. Pet. Geol. Bull.*, **70**:869-887, 1986.

[152] V.T. Jones and R.J. Drozd. *Am. Assoc. Pet. Geol. Bull.*, **67**(6):932-952, 1983.

[153] K.F.M. Thompson. *Geochimica et Cosmochimica Acta*, **47**:303-316, 1983.

[154] K.F.M. Thompson. *Org, Geochem.*, **11**(6):573-590, 1987.

[155] P.P. Ballesta, R. Field, and E. De Saeger. *Atmospheric Environment*, **35**:5729-5740, 2001.

[156] J. Slemr, F. Slemr, H. D'Souza, and R. Partridge. *J. Chromatogr. A*, **1061**:75-84, 2004.

[157] G.J. Francis, P.F. Wilson, D.B. Milligan, V.S. Langford, and M.J. McEwan. *Int. J. Mass Spectrom.*, **268**:38-46, 2007.

[158] I. Dotan, F.C. Fehsenfeld, and D.L. Albritton. *J. Chem. Phys.*, **68**(12):5665-5666, 1978.

[159] D. Smith, N.G. Adams, and T.M. Miller. *J. Chem. Phys.*, **69**(1):308-318, 1978.

[160] M. Durup-Ferguson, H. Bohringer, D.W. Fahey, F.C. Fehsenfeld, and E.E. Ferguson. *J. Chem. Phys.*, **81**:2657-2666, 1984.

[161] J.M. Van Doren, S.E. Barlow, C.H. DePuy, V.M. Bierbaum, I. Dotan, and E.E. Ferguson. *J. Phys. Chem.*, **90**:2772-2777, 1986.

[162] S.E. Barlow, J.M. Van Doren, C.H. DePuy, V.M. Bierbaum, I. Dotan, and E.E. Ferguson. *J. Chem. Phys.*, **85**(7):3851-3859, 1986.

[163] P.F. Wilson, C.G. Freeman, and M.J. McEwan. *Int. J. Mass Spectrom.*, **229**:143-149, 2003.

[164] W. Lindinger, D.L. Albritton, M. McFarland, F.C. Fehsenfeld, A.L. Schmeltekopf, and E.E. Ferguson. *J. Chem. Phys.*, **62**(10):4101-4110, 1975.

[165] S. Matsuoka and Y. Ikezoe. *J. Phys. Chem.*, **92**:1126-1133, 1988.

[166] L. Talrose and E.L. Frankevitch. *J. Am. Chem. Soc.*, **80**:2344-2345, 1958.

[167] W.T. Huntress Jr. *Astrophys. J. Suppl. Ser.*, **33**:495-514, 1977.

[168] L.W. Sieck and S.K. Searles. *J. Chem. Phys.*, **53**(7):2601-2605, 1970.

[169] J.J. DeCorpo, M.V. McDowell, and F.E. Saalfeld. *J. Phys. Chem.*, **76**:1517-1519, 1972.

[170] S.T. Arnold, A.A. Viggiano, and R.A. Morris. *J. Phys. Chem. A*, **101**:9351-9358, 1997.

[171] NIST Computational Chemistry Comparison and Benchmark Database, **NIST Standard Reference Database Number 101**, Release 12, Aug 2005, Russell D. Johnson III (ed). (http://srdata.nist.gov/cccbdb)

[172] V.G. Anicich, P.F. Wilson, and M.J. McEwan. *J. Am. Soc. Mass Spectrom.*, **14**:900-915, 2003.

[173] P.M. Hierl, I. Dotan, J.V. Seeley, J.M. Van Doren, R.A. Morris, and A.A. Viggiano. *J. Chem. Phys.*, **106**:3540-3544, 1997.

[174] K.A. Mauritz and R.B. Moore. *Chem. Rev.*, **104**:4535-4585, 2004.

[175] W. Janicki, L. Wolska, W. Wardencki, and J. Namiesnik. *J. Chromatogr. A*, **654**(2): 279-285, 1993.

[176] K. Brendow. *Oil Shale*, **20**(1):81- 92, 2003.

[177] Stephen McCormick. *Innovative logging techniques for Taranaki*, in *New Zealand Petroleum Conference Proceedings*, 7-10 March 2004. (http://www.crownminerals.govt.nz)

[178] T.R. Naish, B.C. Field, H. Zhu, A. Melhuish, R.M. Carter, S.T. Abbott, S. Edwards, B.V. Alloway, G.S. Wilson, F. Niessen, A. Barker, G.H. Browne, and G. Maslen. *J. Roy. Soc. New Zealand*, **35**:91-122, 2005.

[179] A. Latrasse. *Fruits III*, in *Volatile Compounds in Foods and Beverages*. H. Maarse (Ed), Marcel Dekker, New York, NY, USA, 1991.

[180] D.J. Rowe. *Aroma chemicals I: C, H, O Compounds*, in *Chemistry and Technology of Flavors and Fragrances*. D.J. Rowe (Ed), CRC Press, Boca Raton, FL, USA, 2005.

[181] Gary Reineccus. *Flavor Chemistry and Technology*. CRC Press, Boca Raton, FL, USA, 2nd edition, 2006.

[182] P.E. Shaw. Fruits I. In H. Maarse, editor, Volatile Compounds in Foods and Beverages. Marcel Dekker, New York, NY, USA, 1991.

[183] R.G. Berger. *Fruits I*, in *Volatile Compounds in Foods and Beverages*. H. Maarse (Ed), Marcel Dekker, New York, NY, USA, 1991.

[184] "Phase Change Data" in NIST Chemistry WebBook, **NIST Standard Reference Database Number 69**, Eds. P.J. Linstrom and W.G. Mallard, June 2005, National Institute of Standards and Technology, Gaithersburg MD, 20899 (http://webbook.nist.gov).

[185] J.H.T. Luong, P. Bouvrette, and K.B. Male. *Trends in Biotechnology*, **15**:369-377, 1997.

[186] L. Huber. *Validation and Qualification in Analytical Laboratories*. CRC Press, Boca Raton, FL, USA, 1999.

[187] *Importation and Clearance of Fresh Fruit and Vegetables into New Zealand*, MAF Biosecurity New Zealand Standard **152.02**, August 2007.

[188] F.M. Benoit and A.G. Harrison. *J. Am. Chem. Soc.*, **99**:3980-3984, 1977.

[189] M. Meot-ner (Mautner). *J. Phys. Chem.*, **84**:2716, 1980.

[190] F.C. Fehsenfeld, M. Mosesman, and E.E. Ferguson. *J. Chem. Phys.*, **55**(5): 2120-2125, 1971.

[191] S. G. Lias, J. E. Bartmess, J. F. Liebman, J. L. Holmes, R. D. Levin, and W. G. Mallard, "**Gas-Phase Ion and Neutral Thermochemistry**," *J. Phys. Chem. Ref. Data*, **16**:Suppl. 1, 1988.

[192] M.J. McEwan, P.F. Wilson, G.J. Francis and T.H. Morton, *Int. J. Mass. Spectrom.*, **267**:81-88, 2007.

[193] K.B. Wiberg and L.H. Slaugh. *J. Am. Chem. Soc.*, **80**:3033-3039, 1958.

[194] C.E. Hudson and D.J. McAdoo. *Int. J. Mass Spectrom.*, **199**:41-57, 2000.

[195] R.B. Woodward and R. Hoffmann. *J. Am. Chem. Soc*., **87**:365-367, 1965.

[196] M. Meot ner (Mautner). *J. Am. Chem. Soc.*, **101**:2389-2395, 1979.

[197] W.N. Olmstead, M. Lev-on, D.M. Golden, and J.I. Brauman. *J. Am. Chem. Soc.*, **99**:992-998, 1977.

[198] F.W. McLafferty. *Anal. Chem.*, **28**:306-313, 1956.

[199] N.M.M. Nibbering. *J. Am. Soc. Mass Spectrom.*, **15**:956-958, 2004.

[200] F. Grandinetti, G. Occhiucci, M.E. Crestoni, S. Fornarini, and M. Speranza. *Int. J. Mass Spectrom. Ion Proc.*, **127**:137-146, 1993.

[201] L.E. Gusel'nikov. *Coord. Chem. Rev.*, **244**:149-240, 2003.

[202] A.C. Hopkinson, G.I. Mackay, and D.K. Bohme. *Can. J. Chem.*, **57**:2996-3004, 1979.

[203] C. Denekamp and A. Stanger. *Chem. Comm.*, **2002**:236-237, 2002.

[204] C. Denekamp and A. Stanger. *J. Mass Spectrom.*, **37**:336-342, 2002.

[205] J. Clayden, N. Greeves, S. Warren, and P. Wothers. *Organic Chemistry.* Oxford University Press, Oxford, UK, 2001.

[206] A.D. McNaught and A. Wilkinson. *Compendium of Chemical Terminology.* Blackwell Science, Boston, USA, 1997.

[207] C. Peng, P.Y. Ayala, H.B. Schlegel, and M.J. Frisch. *J. Comp. Chem.*, **17**(1):49-56, 1996.

[208] L.A. Curtiss, K. Raghavachari, P.C. Redfern, and J.A. Pople. *J. Chem. Phys.*, **106**:1063-1080, 1997.

[209] T. Su and M.T. Bowers. *J. Chem. Phys.*, **58**(7):3027-3038, 1973.

[210] C.E. Hudson and D.J. McAdoo. *Int. J. Mass Spectrom.*, **219**:295-303, 2002.

[211] E. Aprea, F. Biasioli, T.D. Mark, and F. Gasperi. *Int. J. Mass Spectrom.*, **262**:114-121, 2007.

[212] M.L. Gross. *J. Am. Soc. Mass Spectrom.*, **15**:951-955, 2004.

[213] U.S. Department of the Army. *NATO Handbook on the Medical Aspects of NBC Defensive Operations*. Part 3; **1-1**, 1996.

[214] United States Control and Disarmament Agency, *Convention on the Prohibition of the Development, Stockpiling and use of Chemical Weapons and on their Destruction*. Washington, DC, 1993.

[215] Blix. H. *Weapons of Terror: Freeing the World of Nuclear, Biological and Chemical Arms*. Weapons of Mass Destruction Commission, Stockholm, 2006.

[216] Cirincione J, Wolfsthal J, and Rajkumar M. *Deadly Arsenals: Tracking Weapons of Mass Destruction*. Carnegie Endowment for International Peace, Washington, 2002.

[217] D. Noort, H.P. Benschop, and R.M. Black. *Tox. App. Pharma.*, **184**:116-126, 2002.

[218] R.M. Black, R.J. Clarke, R.W. Read, and M.T.J. Reid. *J. Chromatogr. A*, **662**:301-321, 1994.

[219] R.M. Coupland. *Lancet*, **362**:1346, 2003.

[220] A.L. Smithson and L.A. Levy. *Ataxia: The chemical and biological terrorism threat and the US response.* **Technical Report 35**, The Henry L. Stimson Center, Washinton D.C. October 2000.

[221] C. Bismuth, S.W. Borron, F.J. Baud, and P. Barriot. *Tox. Let.*, **149**:11-18, 2004.

[222] S. Kendler, A. Zifman, N. Gratziany, A. Zaltsman, and G. Frishman. *Anal. Chim. Acta*, **548**:58-65, 2005.

[223] J.R. Smith and M.L. Shih. *J. Appl. Toxicol.*, **21**(Sup. 1):S27-S34, 2001.

[224] R.M. Black and R.W. Read. *J. Chromatogr. A*, **794**:233-244, 1998.

[225] G.A. Sega, B.A. Tomkins, and W.H. Griest. *J. Chromatogr. A*, **790**:143-152, 1997.

[226] I.N. Stan'kov, A.A. Sergeeva, V.B. Sitnikov, I.D. Derevyagina, O.T. Morozova, S.N. Mylova, and V.B. Forov. *J. Anal. Chem*, **59**(5):447-451, 2004.

[227] A.A. Urbas and P.B. Harrington. *Anal. Chim. Acta*, **446**:393-412, 2001.

[228] R. Pozzi, F. Pinelli, P. Bocchini, and G.C. Galletti. *Anal. Chim. Acta*, **504**:313-317, 2004.

[229] K.O. Fultz. *Aviation security: Technology's role in addressing vulnerabilities*. **Technical Report 96-262**, United States General Accounting Office, 1996.

[230] A.M. Calafat and S.B. Stanfill. *J. Chromatogr. B*, **772**:131-137, 2002.

[231] U.S. Department of Health and Human Services. *Pocket Guide To Chemical Hazards, number 90-117*. National Institute for Occupational Safety and Health (NIOSH), June 1990.

[232] P. Rice. *Medicine*, **35**(10):578-579, 2007.

[233] ScA.M. Sciuto. *Tox. Let.*, **95**:151, 1998.

[234] L. Karalliedde, H. Wheeler, R. Maclehose, and V. Murray. *Public Health*, **114**:238-248, 2000.

[235] F.T. Fraunfelder. *Brit. J. Med.*, **320**:458-459, 2000.

[236] Force Health Protection and Readiness. *Operation Tall Timber. In SHAD Tests*. US Veterans Affairs, September 2002.

[237] S. Bradberry. *Medicine*, **35**(10):576-577, 2007.

[238] A.B. Kanu, P.E. Haigh, and H.H. Hill. *Anal. Chim. Acta*, **553**:148-159, 2005.

[239] R. Norlin and G. Lindberg. *J. Label. Compd. Radiopharm*., **46**:599-604, 2003.

[240] A.W. Abu-Qare and M.B. Abou-Donia. *Food and Chemical Toxicology*, **40**:1327-1333, 2002.

[241] B. Muir, H.B. Duffy, and M.C. Moran. *J. Chromatogr. A*, **1038**:183-187, 2004.

[242] N. Schoon, C. Amelynck, E. Debie, P. Bultinck, and E. Arjis. *Int. J. Mass Spectrom.*, **263**:127-136, 2007.

[243] N.L. Allinger. *J. Am. Chem. Soc.*, **99**:8127-8134, 1977.

[244] N.L. Allinger, Y.H. Yuh, and J.H. Lii. *J. Am. Chem. Soc.*, **111**:8551-8556, 1989.

[245] R.L. Smith, A. Schweighofer, H. Keck, W. Kuchen, and H.I. Kenttamaa. *J. Am. Chem. Soc.*, **118**:1408-1412, 1996.

[246] A.A. Maryott and F. Buckley. *A tabulation of dipole moments, dielectric constants, and molar refractions measured between 1910 and 1952*. U.S. National Bureau of Standards Circular, **Number 537**, 1953.

[247] R.L. Cordell, K.A. Willis, K.P. Whyce, R.S. Blake, A.M. Ellis and P.S. Monks. *Anal. Chem.*, **79**:8359-8366, 2007.

[248] O.P. Korobeinichev, S.B. Ilyin, T.A. Bolshova, V.M. Shavartsberg, and A.A. Chernov. *Combustion and Flame*, **121**:593-609, 2000.

[249] New Zealand Department of Labour, Occupational Safety and Health Service, *Workplace Exposure Standards*. January 2002. (http://www.osh.dol.govt.nz)

[250] R.M. Black and R.W. Read. *J. Chromatogr. A*, **759**:79-92, 1997.

[251] H. Chen, X. Zheng, and R.G. Cooks. *J. Am. Soc. Mass Spectrom.*, **14**:182-188, 2003.

[252] S.V. Patel, T.E. Mlsna, B. Fruhberger, E. Klaassen, S. Cemalovic, and D.R. Baselt. *Sensors and Actuators B*, **96**:541, 2003.

[253] P.G. Georgopoulos, P. Fedele, P. Shade, P.J. Lioy, M. Hodgson, A. Longmire, M. Sands, and M.A. Brown. Am. *J. Industrial Med.*, **46**(5):432-445, 2004.

[254] G.A. Eiceman, D. Preston, G. Tiano, J. Rodriguez, and J.E. Parmeter. *Talanta*, **45**:57-74, 1997.

[255] United States Center for Disease Control. *NIOSH Emergency Response Cards*, 2007. (http://www.bt.cdc.gov/agent/).

[256] S. Penny and S. Bell. *Toxic Chemicals and You.* Random House, Auckland, New Zealand, 2005.

[257] R.A. Freeze. *The Environmental Pendulum: A Quest for the Truth about Toxic Chemicals*, Human Health, and Environmental Protection. University of California Press, Berkeley, 2000.

[258] K.D. Berry. *Environ. Sci. Tech.*, **20**:647-651, 1986.

[259] United States Environmental Protection Agency. *The Plain English Guide to the Clean Air Act.* Triangle Park, North Carolina, April 2007.

[260] United States Environmental Protection Agency. *Clean Air Act.* Washington DC, 1990.

[261] M. Sittig. *World-Wide Limits for Toxic and Hazardous Chemicals in Air, Water and Soil.* Noyes Publications, New Jersey, 1994.

[262] United States Environmental Protection Agency. *Compendium method TO-14A* in *Compendium of methods for the determination of toxic organic compounds in ambient air.* 2nd edition. Cincinnati, Ohio. January 1999.

[263] United States Environmental Protection Agency. *Compendium method TO-15* in *Compendium of methods for the determination of toxic organic compounds in ambient air.* 2nd edition. Cincinnati, Ohio. January 1999.

[264] G.C. Pratt, D. Bock, T.H. Stock, M. Morandi, J.L. Adgate, G. Ramachandran, S.J. Mongin, and K. Sexton. *Environ. Sci. Tech.*, **39**:3261-3268, 2005.

[265] J.L Wang, C. Chew, S.W. Chen, and S.W. Kuo. *Environ. Sci. Tech.*, **34**:2243- 2248, 2000.

[266] Y.M. Kim, S. Harrad, and R.M. Harrison. *Environ. Sci. Tech.*, **33**:4342-4345, 1999.

[267] M.D. Hays, C.D. Geron, K.J. Linna, N.D. Smith, and J.J. Schauer. *Environ. Sci. Tech.*, **36**:2281-2295, 2002.

[268] J. Applequist, J.R. Carl, and K.K. Fung. *J. Am. Chem. Soc.*, **94**:2952-2960, 1972.

[269] D.M. Chapman and R.E. Hester. *J. Phys. Chem. A*, **101**:3382-3387, 1997.

[270] P. Langevin. *Ann. Chim. Phys.*, **5**:245-248, 1905.

[271] F.R. Jensen and R.A. Neese. *J. Am. Chem. Soc.*, **93**:6329-6330, 1971.

[272] M. Khajehpour and J.F. Kauffman. *J. Phys. Chem. A*, **105**:10316-10321, 2001.

[273] V.A. Mikhailov, M.A. Parkes, R.P. Tuckett, and C.A. Mayhew. *J. Phys. Chem. A*, **110**:5760-5771, 2006.

[274] P. Spanel and D. Smith. *J. Phys. Chem.*, **99**:15551-15556, 1995.

[275] D.J. Liu and T. Oka. *Phys. Rev. Lett.*, **54**(16):1787-1789, 1985.

[276] A.J. Midey, S. Williams, and A.A. Viggiano. *J. Phys. Chem. A*, **105**:1574-1578, 2001.

[277] K.P. Huber. *Can. J. Phys.*, **46**:1691-1695, 1968.

[278] R.G. Cooks, Z. Ouyang, Z. Takats, and J.M. Wiseman. *Science*, **311**:1566-1570, 2006.

[279] R.B. Cody, J.A. Laramee, and H.D. Durst. *Anal. Chem.*, **77**:2297-2302, 2005.

[280] C.J. Ennis, J.C. Reynolds, B.J. Keely, and L.J. Carpenter. *Int. J.Mass Spectrom.*, **247**:72-80, 2005.

[281] M.M.L. Steeghs, C. Sikkens, E. Crespo, S.M. Cristescu, and F.J.M. Harren. *Int. J. Mass Spectrom.*, **262**:16-24, 2007.

[282] L.H. Mielke, D.E. Erickson, C. Doerge, A. Wisthaler, A. Hansel, S.A. McLuckey, P.B. Shepson. *Eos Trans. AGU*, **87**(52), Fall Meet. Suppl. Abstract A23A-0939, 2006.

[283] J.C. Maxwell. *Philos. Mag.*, **20**:21-33, 1860.

[284] H.R. Skullerud. *J. Phys.*, **B9** 535-546, 1976.